Advanced techniques for numerical contact analysis in spiral bevel gears

Mathijs Vivet

Supervisors:
Prof. dr. ir. W. Desmet
Prof. dr. ir. D. Mundo
   (Università della Calabria)

Dissertation presented in partial fulfillment
of the requirements for the degree of
Doctor of Engineering Science (PhD):
Mechanical Engineering

July 2019

Advanced techniques for numerical contact analysis in spiral bevel gears

Mathijs VIVET

Examination committee:
Prof. dr. ir. Y. Willems, chair
Prof. dr. ir. W. Desmet, supervisor
Prof. dr. ir. D. Mundo, supervisor
  (Università della Calabria)
Dr. ir. T. Tamarozzi, co-supervisor
Prof. dr. ir. D. Vandepitte
Prof. dr. ir. K. Meerbergen
Prof. dr. ir. F. Gagliardi
  (Università della Calabria)
Prof. dr. ir. A. Artoni
  (Università di Pisa)
Prof. dr. ir. S. Theodossiades
  (Loughborough University)

Dissertation presented in partial fulfillment
of the requirements for the degree of
Doctor of Engineering Science (PhD):
Mechanical Engineering

July 2019

Acknowledgments

This PhD dissertation is the result of about four and a half years of research that I conducted both at KU Leuven and the University of Calabria (UNICAL). It has been an amazing experience that has given me so much more than just the technical realizations. I am grateful for having had the opportunity to move from Belgium to Italy twice, the chance to work at universities and in industry but most importantly the fortune to meet many amazing people along the way.

But to begin, I would like to thank the institutions that made this work possible. My gratitude goes out to University of Calabria and KU Leuven for the support during the first and final years. I also gratefully acknowledge the European Commission for its support through the FP7-DEMETRA Marie Curie project, which allowed me to interweave both academic and industrial experiences within the research. Finally, I would like to thank the Agency for Innovation and Entrepreneurship (VLAIO) for their support in numerous R&D projects.

First and foremost, I would like to thank my promotors, Prof. Wim Desmet and Prof. Domenico Mundo, for all their support. Wim, I still remember your enthusiastic response when we discussed my PhD plans back in 2014 at LMS. It is this boundless enthusiasm and the trust that you place in your researchers, which were of great motivation to me. Especially in times when I doubted my work. Thank you for the chance to be part of such an amazing group that is the *Noise and Vibration Research Group*. I greatly appreciate the freedom and the support that you have given me to explore and prepare a future after the PhD. Domenico, I don't know where to start when expressing my gratitude to you. From day one, it was clear that you do your utmost best to guarantee that all your PhD researchers can have success stories. Thank you for the warm, Italian hospitality with which you welcomed a Belgian stranger into your group, for your close guidance during the two-year period at UNICAL and for the calls to hear how I was doing during my periods "abroad". Your availability and unwavering support made setbacks feel like no big deal, while you were often more excited than myself when successes arrived. More I could not wish for.

Tommaso, your influence on my work goes far beyond being co-promotor. You were the person who introduced me to research back when you mentored Laurens and I during our Master's thesis. I was happy to meet you again as my supervisor during my secondment in Siemens. Thank you for the many methodological discussions we have had. Your drive for excellence not only helped me to critically evaluate my work, it also inspired me with many ideas. I am also very grateful for how you now promote my work within the company. And I look forward to the many interactions that will hopefully come.

I would like to extend my gratitude to the remaining members of my examination committee. Prof. Dirk Vandepitte and Prof. Karl Meerbergen, as members of my supervisory committee, you provided me with valuable feedback over the course of my PhD. Thank you for the precise and critical view with which you have evaluated this dissertation. Prof. Francesco Gagliardi, I very much enjoyed our interactions during my stay in Calabria and the interesting comments you made during the preliminary defense. Prof. Alessio Artoni and Prof. Stephanos Theodossiades, it is an honor to have my work examined by two esteemed gear researchers as yourselves. Your positive feedback genuinely means a lot to me. I also would like to express my appreciation to Prof. Yves Willems for ensuring that everything went smoothly, as the chair of the examination committee.

I want to thank Prof. David Dooner (University of Puerto Rico at Mayagüez) for the many, many email conversations that we have had on the topic of bevel and hypoid gear design. Enthusiastic as ever, you explained me your research, while providing me with better insights in both gear geometry and the industry.

I also would like to express my thanks to the colleagues and friends at Siemens, in particular the multibody research group. Ali, Sara, Roberta, Marco, Shadi, Elias and Tuur, thank you for being great colleagues. Daehyun, the knowledge that you have on gears, is incredible. Thank you for the many discussions on bevel and hypoid gears, and for the enthusiasm you always show for my work. Pavel, you create quality of life within the team. Interacting with you has given a tremendous boost to my coding skills. Thank you for that and for the crazy talks on the latest video games, we played. Stijn, I have really enjoyed interacting with you during these years. Thank you for all the precious advice and encouragement that you gave when I started, but also for the time that you have invested in preparing me for future adventures. The lessons you have taught me on project writing are invaluable. Lotte, thank you for always going the extra mile whenever someone in the team needs something.

Leoluca, the ease with which you have combined the bearing developments and your research, is truly inspiring. Conversations with you on research, life or cycling are always a pleasant distraction from work. Thanks for the many laughs during the coffee breaks or the beers together with Rocco in Oude Markt.

Summary

The research presented in this dissertation treats the subject of efficient gear contact simulation and is applied to the contact analysis of spiral bevel gears.

In today's competitive environment getting better products to market faster is essential to win a customer's interest and loyalty. Therefore, engineers are evermore in need of the correct solutions to rapidly predict, analyze and improve their designs if they want to meet the tight development schedules and budgets. Within the current development cycle of mechanical transmissions, computerized *tooth contact analysis* (TCA) has proven to be an invaluable tool to predict a gear pair's key contact performance characteristics, while reducing the need for expensive physical prototyping and labor-intensive experimental testing. However, the geometrical complexity of the gear teeth still pose significant computational challenges to the tooth contact simulation for spiral bevel gears. Correctly capturing the spatial nature of the motion transfer and the resulting contact load distribution requires a three-dimensional gear contact model. Finite element method (FEM) based contact simulations are usually conducted, especially in an industrial context, while various tailor-made solutions also exist. When performing the contact detection, many of these solutions tend to apply a general contact detection method (e.g. node-to-surface) that treats the contacting gear teeth flanks as arbitrary surfaces. Not realizing that the gear flanks are designed to transmit motion in a near-conjugate way, leads to inefficient contact searches for which the associated computational cost not only limits TCA's application to static component-level analysis but also hinders extension towards full-system level analysis or dynamic gear contact simulation.

Building upon the existing concept of the *surface of roll angles* to efficiently detect contact, this dissertation develops a new *penetration-based contact model* to compute the three-dimensional contact loads from the actual position and orientation of the real tooth surfaces, whether misaligned or not. The proposed methods show to correctly predict component behavior at a computational cost that enables further application in system-level or dynamic analyses.

An accurate description of the spiral bevel gear tooth surfaces is deep-rooted in the presented methodologies, since this proves vital to precisely describe the gear pair kinematics but also to correctly include all the relevant complex contact phenomena. However, a reference tooth profile, similar to the involute for cylindrical gears, does not exist for spiral bevel gears. Therefore, a mathematical model that simulates the cutting kinematics of the manufacturing process, proves to be indispensable to correctly capture both the gear teeth's macro- and microgeometry. In this work the five-cut *face-milling* cutting process is adopted to create a representative geometry of a face-milled spiral bevel gear set.

Contact detection based on the tooth flank's surface of roll angles, combined with the *ease-off topography*, has been proposed in the gear literature to reduce the computational load, associated with the contact search. Yet, the ease-off topography, which quantifies the geometrical mismatch of a pair of contacting gear tooth surfaces, shows to hold limitations when moving beyond component-level contact analysis, as it is sensitive to the instantaneous gear pair installment. With the underlying idea of potential application of the presented methodologies within multibody system simulation, the usage of ease-off topography concept for contact detection is abandoned and replaced by a penetration-based contact model. An analytical compliance model is formulated to translate the detected penetrations into appropriate contact loads. The compliance model separates the linear gear tooth deflection components from a tooth pair's local nonlinear deformation, which arises around the contact zone.

The developed gear contact model with surfaces of roll angles, computed for the gear pair's actual tooth flanks in the absence of misalignments, is then shown to be well capable of predicting a misaligned gear pair's contact performance. In contrast, ease-off based contact models would require an update of the (misaligned) ease-off topography, each time the gear pair's configuration changes (e.g. due to system-induced deflections), reducing their otherwise excellent computational efficiency. The proposed penetration-based gear contact model identifies the contact locations based on the surface of roll angles but computes the flank mismatch based on the instantaneous position and orientation of the real gear tooth surfaces, showing to be more robust to configurational changes. Finally, a strategy to parametrically redefine the gear contact model's surfaces of roll angles in function of the instantaneous misaligned state of the gear pair, is proposed to further increase the accuracy of the contact detection.

A prototype toolchain is created around the presented techniques for contact modeling, covering the various analyses for unloaded and loaded tooth contact analysis that are an essential part of today's spiral bevel gear design process. Automated finite element model creation routines are developed to support the validation of the methods against nonlinear FEM-based contact simulations. These tools will greatly support future research into methodological advances.

Samenvatting

Deze verhandeling behandelt de ontwikkeling van numeriek efficiënte methodes voor de simulatie van het tandcontact in kegeltandwielen met spiraalvertanding.

In de huidige competitieve markt is het sneller lanceren van nieuwe producten voor elk bedrijf essentieel om aan klantenvertrouwen te winnen. Ingenieurs moeten daarom op steeds kortere tijd oplossingen bedenken die het product zowel verbeteren als ook binnen het geplande budget en productietijd blijven. In de ontwikkeling van moderne transmissies is *tandcontactanalyse* (TCA) een waardevol instrument voor het voorspellen van de mechanische prestaties van tandwielparen, zonder te moeten steunen op dure prototypes en experimenten. De geometrische complexiteit van kegeltandwielen met spiraalvormige tanden vormt echter een actuele rekenkundige uitdaging voor de TCA-methode. Om accuraat de bewegingsoverbrenging en de krachtverdeling in het contactgebied te voorspellen, is het gebruik van een driedimensionaal contactmodel noodzakelijk. Vandaag wordt de tandcontactanalyse voornamelijk gesimuleerd met behulp van de *eindige-elementenmethode* (FEM), hoewel ook andere meer specifieke oplossing bestaan. De meeste van deze FEM-oplossingen gebruiken generieke methodes (bijv. *node-to-surface*) om de contactgebieden te bepalen, waarbij de tandoppervlakken vanwege hun complexiteit als willekeurig worden beschouwd. Het niet in acht nemen dat de tandflanken ontworpen zijn om de beweging over te brengen op een bijna geconjugeerde wijze, vertaalt zich voor tandwielen echter in een zeer inefficiënte contactdetectie. De bijgevolg hoge rekenlast beperkt TCA in haar toepassing tot statische componentanalyse en verhindert uitbreidingen tot dynamische analyses of tot de simulatie van transmissies als systemen.

Bouwend op concepten zoals het *oppervlak van rolhoeken* en de *interpenetratie* van de tandflanken, ontwikkelt deze verhandeling een nieuw driedimensionaal contactmodel voor kegeltandwielen, die al dan niet uitlijnfouten vertonen. De methodologie voorspelt het correcte contactgedrag van het tandwielpaar aan een lagere rekenkost die de weg effent voor toekomstige toepassingen in de statische of dynamische analyse van systemen met spiraalvormige kegeltandwielparen.

Een nauwkeurige beschrijving van de tandoppervlakken van de spiraalvormige kegeltandwielen is essentieel om zowel de kinematica te beschrijven als ook alle complexe contactfenomenen correct in rekening te brengen. Het ideale profiel, gelijkaardig aan het evolvente tandprofiel voor cilindrische tandwielen, bestaat echter niet voor spiraalvormige kegeltandwielen. Een wiskundig model is daarom vereist om de kinematica van het snijproces te simuleren en zo de macro- en microgeometrie van de tand te modelleren. In dit onderzoek wordt het verspaningsproces, genaamd *five-cut face-milling* (frezen), gebruikt om de geometrie van een spiraalvormige kegeltandwielpaar virtueel te genereren.

Een methode, die in de literatuur wordt geponeerd om de rekenkost van de contactdetectie te reduceren, combineert het oppervlak van de rolhoeken met het concept van *ease-off topografie*. Deze topografie kwantificeert het gebrek aan geometrische conformiteit van een paar tandflanken in contact. Toch heeft deze methode haar beperkingen met het oog op de analyse van tandwielsystemen, daar de ease-off topografie sterk gevoelig is aan optredende uitlijnfouten. Daarom verruilt de ontworpen methodologie het ease-off concept met een contactmodel dat berust op de interpenetratie van de tandflanken, zodat deze toepasbaar is in een meer systeemgeoriënteerde methode zoals de *meerlichamensimulatie*. Een analytisch model wordt geformuleerd om de interpenetratie tussen de tandflanken te vertalen naar contactkrachten. De vervorming van een tandpaar in contact is beschreven als de som van twee componenten: een lineaire voor de globale tandvervorming en een niet-lineaire voor de contactvervorming.

De ontwikkelde methodologie kan de prestaties van een verkeerd uitgelijnd tandwielpaar voorspellen, vertrekkende van de rolhoekoppervlakken die berekend zijn voor de tandflankparen in afwezigheid van de uitlijnfouten. Een op ease-off gebaseerde methode moet echter de topografie herberekenen telkens de uitlijning van het tandwielpaar verandert (bijv. door systeemgeïnduceerde verplaatsingen). Hierdoor vermindert haar anders uitstekende numerieke efficiëntie sterk. Het op interpenetratie gebaseerde contactmodel identificeert het contact door middel van het rolhoekoppervlak maar brengt het gebrek aan geometrische conformiteit in rekening via de ogenblikkelijke positie en oriëntatie van de tandoppervlakken. Hierdoor is de accuraatheid van de methode minder afhankelijk van uitlijnfouten. Een strategie om de rolhoekoppervlakken parametrisch te herdefiniëren in functie van de ogenblikkelijke uitlijnfout wordt ook geopperd om de nauwkeurigheid van de contactdetectie nog verder te verbeteren.

Een *toolchain* prototype is gecreëerd die alle gepresenteerde technieken omvat, inclusief methodes voor onbelaste en belaste tandcontactanalyse. Deze zijn in feite essentieel in het huidige ontwerpproces van spiraalvormige kegeltandwielen. Routines voor het automatisch creëren van FEM modellen zijn ontwikkeld om zo de methodes te valideren bij middel van niet-lineaire FEM contactsimulaties. Dit alles ondersteunt toekomstig onderzoek naar methodologische verbeteringen.

Sommario

Il seguente lavoro di ricerca tratta l'efficienza di simulazioni di fenomeni di contatto per ruote dentate, in particolare alle ruote coniche a denti spiroidali.

Al giorno d'oggi per ogni azienda è fondamentale sviluppare i propri prodotti in modo più veloce possibile, al fine di sfidare la concorrenza e di ottenere la fedeltà del cliente. Gli ingegneri hanno dunque la necessità di proporre, nel minor tempo possibile, soluzioni corrette per migliorare il design dei prodotti così da rientrare nel budget e nei tempi prestabiliti. Nello sviluppo delle moderne trasmissioni meccaniche, la *tooth contact analysis* (TCA), rappresenta un prezioso strumento per predire le prestazioni meccaniche delle coppie di ruote dentate, senza dover ricorrere a costosi prototipi ed impegnativi test sperimentali. Tuttavia, la complessità geometrica delle ruote coniche a denti spiroidali pone costanti sfide computazionali al metodo della TCA. Al fine di simulare correttamente la trasmissione del moto e la distribuzione del carico nella zona di contatto, è necessario utilizzare un modello tridimensionale. Oggigiorno le simulazioni del contatto fra i denti sono analizzate attraverso metodi agli elementi finiti (FEM), nonostante esistano altre soluzioni più specifiche. Nella maggior parte di questi metodi FEM, approcci generici (es *node-to-surface*) sono utilizzati per captare le zone di contatto, considerando le superfici dei denti come arbitrarie. Inoltre, trascurare che le superfici dei denti sono progettate per trasmettere il moto in maniera quasi coniugata, porta ad una inefficiente ricerca del contatto. Di conseguenza, l'onere computazionale associato limita l'utilizzo della TCA alle analisi statiche dei componenti, impedendo l'estensione del metodo a simulazioni di trasmissioni come sistemi o ad analisi dinamiche.

Il lavoro di tesi sviluppa un nuovo modello di contatto tridimensionale, basato sulla compenetrazione dei denti reali. Esso si basa sul concetto di *surface of roll angles* per identificare il contatto in modo efficiente. La metodologia mostra una corretta previsione dell'interazione tra i componenti in contatto ad un costo computazionale ridotto, aprendo la strada a future applicazioni per l'analisi statiche o dinamiche di sistemi con ruote dentate spiroidali.

Una descrizione accurata della superficie dei denti spiroidali è fondamentale. Questa si dimostra essenziale per definire la cinematica delle coppie di denti, ma anche per includere correttamente tutti i complessi fenomeni relativi al contatto. Tuttavia, un profilo del dente simile all'evolvente per ruote cilindriche non esiste per le ruote coniche a denti spiroidali. Di conseguenza, un modello matematico in grado di simulare la cinematica del processo di taglio è necessario al fine di identificare correttamente la macro e microgeometria del dente. Nel lavoro di tesi il processo di *five-cut face milling* (fresatura) è utilizzato per creare la geometria di una coppia di ruote coniche a denti spiroidali.

In letteratura, vari metodi sono proposti sulla base della *surface of roll angles* in combinazione con la topografia *ease-off* per ridurre il carico computazionale associato alla ricerca del contatto. Questa topografia quantifica la mancata corrispondenza geometrica di una coppia di superfici arbitrarie a contatto. Essa mostra di avere limiti quando ci si sposta verso l'analisi di sistemi con ruote dentate in contatto. In consapevolezza di ciò, la metodologia sviluppata sostituisce il concetto di *ease-off* con un modello basato sulla compenetrazione dei denti e diviene compatibile con ambienti di simulazione di tipo *multibody*. Un modello analitico è formulato per tradurre la compenetrazione fra denti in carichi di contatto. Esso descrive la deflessione di una coppia di denti in contatto come somma di una componente lineare ed una non-lineare.

Il modello sviluppato è in grado di prevedere le prestazioni di una coppia di ruote disallineate, partendo dalle *surfaces of roll angles* ottenute per i fianchi della coppia di denti in assenza di disallineamenti. Al contrario, se cambiasse la configurazione della coppia di ingranaggi (ad esempio a causa di deflessioni indotte dal sistema), i modelli basati su *ease-off* dovrebbero effettuare un aggiornamento relativo al disallineamento introdotto, riducendo così la loro altrimenti eccellente efficienza computazionale. Il modello di contatto basato sulla compenetrazione, identifica le posizioni del contatto in base alla *surface of roll-angles*, ma calcola la mancata corrispondenza dei fianchi in base alla posizione e all'orientamento istantaneo delle superfici dei denti. In tal modo si mostra una maggiore versatilità ai cambiamenti di configurazione. Infine, una strategia per ridefinire parametricamente il modello con le *surfaces of roll angle*s in funzione del disallineamento istantaneo della coppia di ingranaggi, è proposto per aumentare la precisione del rilevamento del contatto.

Un prototipo di *toolchain* è creato attorno alle tecniche presentate, includendo le varie analisi per il contatto fra denti con e senza carichi applicati. Queste analisi sono infatti una parte essenziale dell'attuale processo di progettazione degli ingranaggi conici a denti spiroidali. Le routine sono sviluppate per supportare la creazione automatizzata di modelli FEM, al fine di validare i metodi a confronto con simulazioni basate su FEM non lineari. Questi strumenti supporteranno attivamente la ricerca futura sui progressi metodologici.

List of Abbreviations

2D	two-dimensional
3D	three-dimensional
AGMA	American Gear Manufacturers Association
CAD	computer-aided design
CAE	computer-aided engineering
CFD	computational fluid dynamics
CNC	concave
CNV	convex
CPP	contact point path
DAE	differential-algebraic equations
DOF	degree of freedom
DTE	dynamic transmission error
EHL	elastohydrodynamic lubrication
EO	ease-off
FE	finite element
FEA	finite element analysis
FEM	finite element method
FH	face-hobbing
FM	face-milling
GCFE	gear contact force element
ICP	instantaneous contact point
ISO	International Organization for Standardization

LTCA   loaded tooth contact analysis
LTE   loaded transmission error

MB   multibody
MBSD   multibody system dynamics
MOO   multi-objective optimization

NL-FEA   nonlinear finite element analysis
NTS   node-to-surface
NVH   noise, vibration and harshness

ODE   ordinary differential equations

pRS   parametric surface of roll angles

RMSE   root mean square error
RS   surface of roll angles

STE   static transmission error

TCA   tooth contact analysis
TE   transmission error

UDF   user-defined force (routine)
UTCA   unloaded tooth contact analysis
UTE   unloaded transmission error

List of Symbols

Latin symbols

A	Axial offset along the gear rotational axis.
$\mathbf{A}_a$	Rotation matrix from S_a to S_G.
a	Half contact width.
B	Width of a gear slice
$\boldsymbol{b}$	The curve binormal vector.
b	Half contact length.
$\mathcal{C}$	Spatial curve.
C_2	2nd roll constant of modified roll.
C_3	3rd roll constant of modified roll.
d_b	Bending component of the global tooth compliance.
d_c	Local contact compliance.
d_g	Global tooth compliance.
d_f	Body foundation component of the global tooth compliance.
d_s	Shear component of the global tooth compliance.
d_t	Total deformation of a pair of teeth.
E	The Young's modulus of a material.
E_H	Hypoid offset, the offset between the gear rotational axes.
E_M	Blank offset.

$\mathcal{E}_\delta$ Ease-off topography in length units.

$\mathcal{E}_\theta$ Ease-off topography in angular units.

$\boldsymbol{e}_{max}$ The direction of the maximum principal curvature κ_{max}.

$\boldsymbol{e}_{min}$ The direction of the minimum principal curvature κ_{min}.

F_c Magnitude of the contact force.

f_N Nodal contact force between a slave node and a master element.

$\boldsymbol{G}$ Constraint residual vector.

$\mathbf{G}_{\boldsymbol{q}}$ Constraint Jacobian matrix.

g_N Nodal gap function between a slave node and a master element.

h_C Distance from the contact point to center of the tooth profile.

$\mathbf{L}_{ba}$ Rotational matrix from S_a to S_b.

L_c Length of the contact curve/line.

l_c Length of the contact curve/line on a tooth slice.

$\mathbf{M}$ Mass matrix.

m_{21} Gear ratio of the gear pair.

m_{gC} Ratio of roll (velocity ratio) between gear blank and the head cutter.

$\boldsymbol{N}$ Surface normal vector.

N_T Maximum number of teeth considered for contact detection.

$\boldsymbol{n}$ Curve normal vector.

$\boldsymbol{O}$ Vector of the origin of the reference frame S.

P_C Point width between two cutter blades.

p_0 Maximum Hertzian contact pressure.

$\boldsymbol{Q}$ Vector of generalized forces.

$\boldsymbol{Q}_{cont}$ Vector of generalized contact forces.

$\boldsymbol{Q}_e$ Vector of generalized external forces.

$\boldsymbol{Q}_v$ Vector of generalized quadratic velocity forces.

$\boldsymbol{q}$	Vector of generalized coordinates.
q	Angle of rotation of the cradle.
q_0	Angle of the initial (basic) rotation of the cradle.
$\boldsymbol{R}$	Position vector of the origin of a reference frame.
R	Radius of a (spatial) circle.
R_A	Cutter point radius of the blade.
R_C	Radius of the cutter head.
R_F	Radius of the cutter point.
$R_{p,eq}$	Pitch radius of an equivalent spur gear.
R_{proj}	Projected radius of the gear flank onto the projection plane.
$\mathcal{R}_\phi$	Surface of roll angles
$\boldsymbol{r}$	Position vector of a point in Cartesian coordinates.
$\bar{\boldsymbol{r}}$	Position vector of a point in homogeneous coordinates.
$\mathcal{S}$	Surface
S	Reference frame.
S_R	Radial setting of the cradle.
s_M	Normal tooth height where contact force is applied.
s_F	Normal tooth height at the bottom of the active flank .
s_T	Normal tooth height at the top of the active flank.
$\mathbf{T}_{ba}$	Homogeneous transformation matrix from S_a to S_b.
$\boldsymbol{t}$	Curve tangent vector.
t_F	Normal tooth thickness at the bottom of the active flank.
t_T	Normal tooth thickness at the top of the active flank.
u	Curvilinear coordinate that describes surface $\mathcal{S}(u,v)$.
u_A	Curvilinear coordinate along the blade's straight edge.
u_F	Curvilinear coordinate along the blade's circular arc.

v	Curvilinear coordinate that describes surface $\mathcal{S}(u,v)$.
w	Constraint function $w(g_N, \lambda)$.
w_s	Width of a tooth slice
X_B	Translational misalignment parameter w.r.t. S_B.
X_D	Machine-center-to-root.
X_F	Center of the cutter point.
X_{SB}	Sliding base.
Y_B	Translational misalignment parameter w.r.t. S_B.
Z	Number of gear teeth.
Z_B	Translational misalignment parameter w.r.t. S_B..
Z_{proj}	Axial coordinate of the gear flank onto the projection plane.

Greek symbols

α_A	Profile angle of the (active part of the) cutter blade.
α_n	Normal pressure angle of the tooth flank.
α_t	Transverse pressure angle of the tooth flank.
Γ	Angle between surface normal vector and curve normal vector.
γ	Shaft angle of the gear pair.
γ_M	Machine-root angle.
δ	Penetration measured between a pair of rigid flank slices.
δ_e	Elastic approach, an assumed elastic deformation under load.
ϵ_N	User-defined parameter in the constraint-function method.
ϵ_P	Penalty factor in the penalty method.
ϵ_α	Profile contact ratio.
ϵ_β	Face contact ratio.
ϵ_γ	Total contact ratio.

θ_C Angle of rotation of the cutter head.

θ_c Angle of direction between two spatial curves.

θ_{proj} Angle of rotation onto the projection plane.

θ_t Angle of direction between $\boldsymbol{t}$ and $\boldsymbol{e}_{max}$.

$\kappa_{\mathcal{C}}$ Curvature of a spatial curve.

κ_n Normal curvature of a surface $\mathcal{S}$.

κ_{max} Maximum principal curvature.

κ_{min} Minimum principal curvature.

$\boldsymbol{\lambda}$ Vector of Lagrange multipliers.

λ Lagrange multiplier.

ν Poisson's coefficient of a material.

ρ Radius of curvature

$\rho_{\mathcal{C}}$ Radius of curvature of a spatial curve.

ρ^* Relative radius of curvature between two surfaces.

$\boldsymbol{\rho}_B$ Vector of the rotational moment in the equation of meshing.

τ Angular pitch of a gear.

τ_g Surface torsion (or surface warping) of a surface $\mathcal{S}$.

Φ_x Anglular misalignment parameter w.r.t. S_B.

Φ_y Anglular misalignment parameter w.r.t. S_B.

ϕ_g Angle of rotation about the gear blank's rotational axis.

ϕ_x Angle of rotation about x-axis of S_B.

ϕ_y Angle of rotation about y-axis of S_B.

ϕ_z Angle of rotation about z-axis of S_B.

$\boldsymbol{\omega}$ Angular velocity vector.

ω Angular velocity magnitude.

Superscript symbols

$\bullet^{(1)}$ Refers to real flank of gear 1.

$\bullet^{(1c)}$ Refers to ideal flank of gear 1, conjugate to real flank of gear 2.

$\bullet^{(2)}$ Refers to real flank of gear 2.

$\bullet^{(2c)}$ Refers to ideal flank of gear 2, conjugate to real flank of gear 1.

$\bullet^{(cont)}$ Refers to the contact point.

$\bullet^{(g)}$ Refers to the gear.

$\bullet^{(M)}$ Refers to the master surface.

$\bullet^{(S)}$ Refers to the slave surface.

Subscript symbols

$\bullet_1$ Refers to gear 1 (usually the pinion element).

$\bullet_2$ Refers to gear 2 (usually the gear element).

$\bullet_B$ Refers to the Base reference frame.

$\bullet_C$ Refers to the Cutter reference frame.

$\bullet_f$ Refers to gear tooth flank that is considered.

$\bullet_G$ Refers to the Global reference frame.

$\bullet_i$ Refers to a (general) loop index.

$\bullet_s$ Refers to gear tooth slice that is considered.

$\bullet_t$ Refers to gear tooth flank pair that is considered.

Operators and Miscellaneous symbols

$\tilde{\bullet}$ Refers to the nominal configuration.

$\dot{\bullet}$ The first derivative to time.

$\ddot{\bullet}$ The second derivative to time.

$[\bullet]^{-1}$ Matrix inverse.

$[\bullet]^{T}$ Matrix transpose.

$\lceil x \rceil$ Rounds x ($x \in \mathbb{R}$) to the least integer greater than or equal to x.

Contents

List of Figures

List of Tables

Chapter 1

Introduction

The level of technological advancement in today's world would have been unrealizable without the existence of gears; from the toys, with which we played as kids, over the cars that we drive to work as adults, the planes, which we take to go on holidays [96]. In nearly all applications where power transfer is required, gears play an essential role. However, the gear industry has recognized that significant technological challenges lie ahead and should be overcome if it wants to remain the preferred solution for power transmission in the near future [4]. More than ever does the industry need to integrate consumers' unceasing desire for increased performance into their products, while complying to increasingly stringent regulations regarding energy consumption and emissions. Still, the rising environmental awareness in our society provides companies with opportunities for added-value, increased competitiveness and brand identification through sustainable design [91]. Meanwhile, emerging markets continue to invest heavily in the development of new technologies and products, providing the developed markets with a drive for increased cost-effectiveness and a focus towards innovation.

It is within this mind-set of continuous pursuit for innovation, improved performance and shorter time-to-market cycles that the development of new key technologies for design and analysis can play a decisive role. In the past, design has often been treated as a *"trial and error"* process during which multiple physical prototypes of a new product were built. Experimental test campaigns were then conducted to assess the performance of a prototype with respect to given design criteria (e.g. noise, durability, efficiency, ...) and if needed the design was altered until the provided criteria were met satisfactorily. The introduction and further development of *computer-aided engineering* (CAE)

platforms during the second part of the last century provided engineers with powerful alternatives to evaluate their design choices. No longer do they have to rely solely on information obtained through the laborious and costly creation of physical prototypes. Methodologies, such as *finite element analysis* (FEA), *computational fluid dynamics* (CFD), *multibody system dynamics* (MBSD) or *multi-objective optimization* (MOO) now provide the means to create physics-based virtual prototypes and analyze the influence of design modifications relatively early in the development cycle.

For these CAE methodologies to fit within the design process, it is essential that the underlying mathematical models approximate the real-life behavior as accurately as desired, while maintaining a reasonable computational efficiency. The growing complexity of today's mechanical power transmission systems make that an optimal system design through optimization of individual components becomes progressively harder to maintain. Driven partially out of necessity but also supported by continuous advances in computational power, the last decade has seen a noticeable shift towards the use of CAE methods for the study and optimization of component behavior as part of a larger system. Still, as the complexity of the numerical models increases, the need for accurate and computational efficient algorithms remains.

1.1 On the importance of accurate spiral bevel gear models, applicable to system-level analysis

1.1.1 A growing need for system-level simulations

Following global environmental concerns, one of the focal points for industry has been a reduction of fuel consumption through a combination of lightweight design, downsizing and improved efficiency. Depending on the type, mechanical transmissions can be a source of significant energy losses in automotive or aerospace applications, leading to an overall efficiency of generally 85-94% [88]. When it comes to optimization and design, two viable approaches are often pursued to increase the transmission efficiency.

Gear manufacturers aim at improving the mechanical efficiency of the individual gear pairs, in the hope to optimize the (efficiency of the) system by optimizing the individual components. An example of such a component-based approach is the decision, taken in 2004 by the *American Gear Manufacturers Association* (AGMA) to improve the mechanical efficiency of gears with 50% by 2020 [4]. The ambitiousness of such a task should not be underestimated, given that the mechanical efficiency of current gear pairs is high. With an efficiency

of well-above 99%, spur and helical gears (parallel axes) show to be one of the most efficient ways to transfer power between rotating axes [55, 88]. The mechanical efficiency of bevel (intersecting axes) and hypoid (crossed axes) is lower due to higher frictional losses that go with the higher total load for a given tangential load and the higher sliding velocities at the localized contact. Still, a well-made bevel gear set generally reaches a mechanical efficiency of 98-99% [96], whereas hypoid gears have an efficiency of 90-97% [67, 139]. The lower efficiency for hypoid gears results from the higher sliding velocities across the teeth faces, which are inherent to all motion transfer between crossed rotational axes [31, 96]. With regard to further optimization on component-level, numerous research studies are devoted to accurately modeling of the different mechanical phenomena that occur during contact.

Transmission and gearbox designers on the other hand are ever more challenged to unite conflicting design requirements of increased power density and mechanical efficiency, while maintaining or further enhancing *noise, vibration and harshness* (NVH) and durability characteristics [47, 108]. Notwithstanding the importance of improvements towards gear pair efficiency, they realize that consumers attach more importance to transmission efficiency than to efficient gears. Moreover, consumers consider other system performance characteristics, such as NVH and durability, equally important. While, recent studies [55, 82] document the potential of significant gains towards transmission efficiency, they do not include the impact of the loss phenomena on other system-level performance characteristics. For example, friction can be beneficial in dampening out undesired drivetrain vibrations, thus improving the overall NVH performance [85]. Neglecting the impact of design choices on the system's behavior can lead to later problems during the manufacturing process, where they prove to be more time-consuming and highly expensive to correct. Consequently, manufacturers have indicated a need for adequate simulation tools that can correctly capture the system-level dynamics of their systems [94]. The necessity for these system-level models within the transmission design process is also reflected in the recent literature, as a growing number of researchers explore methodologies to integrate models that simulate the behavior of transmission components, such as bearings [39, 83, 103, 136], cylindrical gears [16, 22, 38, 104, 120] and bevel and hypoid gears [25, 58, 95, 133, 140], within multibody dynamics simulations. However, while high-fidelity models for bearings and cylindrical gears are starting to be integrated in system-level models, the geometrical complexity of the gear teeth makes that dynamic models for bevel and hypoid gears often start from precomputed tooth contact results.
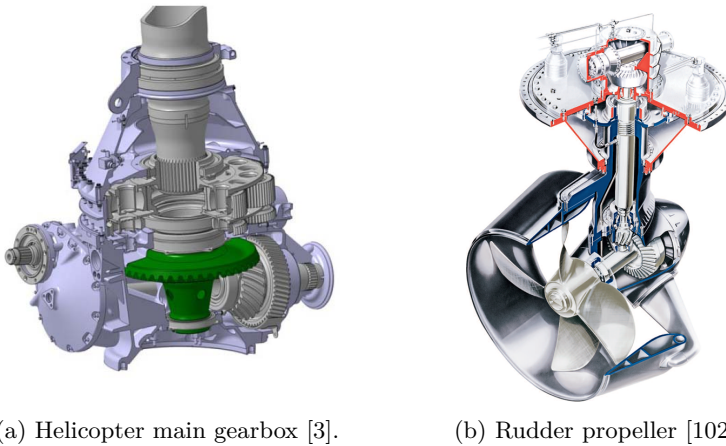
(a) Helicopter main gearbox [3].

(b) Rudder propeller [102].

Figure 1.1: Examples of spiral bevel gear applications.

1.1.2 On the importance of numerically efficient and accurate contact models for spiral bevel gears

Bevel gears play an essential role when it comes to motion transfer between intersecting rotating axes. While in most cases the motion transfer takes place between perpendicular axes, they can also be designed to transmit motion under acute or obtuse shaft angles. Based on the tooth shape, bevel gears are usually categorized into different subgroups (e.g. straight, skew, spiral, ...), of which spiral bevel gears have the most complex tooth shape, manufacturing process and contact characteristics.

Spiral bevel gears have found application in a wide variety of sectors, ranging from general industry to aerospace (Fig. 1.1a) and marine (Fig. 1.1b). The presence of the tooth spiral (length-wise curvature) causes the characteristically curved and oblique teeth, while also providing a more gradual tooth engagement and better load-carrying capacity, compared to other bevel gears of the same size. This allows them to be used for highly loaded applications that run at high operating speeds.

Even though spiral bevel gears produce less noise, compared to most of the other gear types, noise and vibration problems can still arise from the periodic engagement and disengagement of the gear teeth. Although it has no direct impact on the transmissions lifetime, gear whine is often considered to be undesired, due to its tonal sound that occurs at the mesh frequency and its
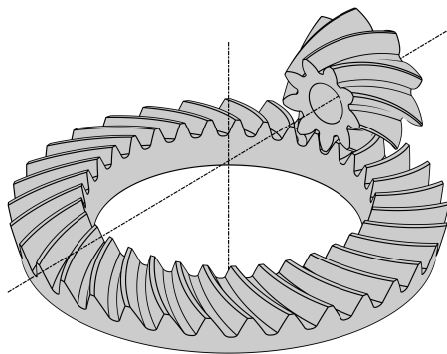
Figure 1.2: An example of a face-milled spiral bevel gear pair.

harmonics [51]. Imperfect motion transfer between the mating gears can be identified as the main cause for gear whine. This motion transfer is mainly governed by the contact properties of the mating gear tooth flanks so that the local tooth flank geometry, the tooth stiffness and tribological effects play an important role. Moreover, as spiral bevel gears are usually part of a larger system, these component characteristics are also affected by the interactions with the other components to which they are connected (e.g. gear-bearing interactions). As time-varying forces that arise from contact between the gear teeth, can cause additional shaft and bearing deflections, the relative orientation of the gear pair will also be altered, thus changing the local contact conditions. Consequently, this shows that models for spiral bevel gears cannot overlook the local contact phenomena that are at play on a component-level, if they want to accurately predict the behavior on a system-level.

The complexity of the gear tooth geometry (Fig. 1.2) often forms an obstacle in the development process of spiral bevel gear pairs. As both the macroscopic (e.g. tooth shape and curvature) and microscopic (e.g. flank modifications) properties of the tooth geometry are directly affected by the manufacturing process, the machine settings have a significant impact on the contact location and the error in motion transfer. Besides the tooth surface geometry, the gear pair's mounting conditions also influence the quality of motion transmission, since the latter is the direct result of interactions between the mating flanks.

Contact between meshing gear teeth is highly nonlinear in nature, as visualized in Fig. 1.3 through the Von Mises stress distribution for a spiral bevel gear pair in mesh. Over the course of a mesh cycle (indexing of one gear tooth) tooth engagement and disengagement occurs, changing the number of gear

teeth that carry the contact at a given point. The resulting nonlinear and time-varying nature of the mesh stiffness is often identified as a source for gear pair vibrations and is tightly linked to the quality of motion transfer. In the proximity of the contact zone the tooth deformation and the resulting contact stresses also show to be vary nonlinearly as a function of the loading conditions. To reduce vibrations at a given operational load, gear designers usually include a certain amount of flank mismatch into the spiral bevel gear pair's design to counterbalance tooth deflections under load. This causes the local (dry-)contact deformation, which resembles that of a point load for lightly loaded gears, to develop into a line load for increased loading conditions, while potentially bringing neighboring teeth into contact due to additional tooth deflections.

While just a few important aspects were discussed, it allows to form a clear idea about the importance of component-based spiral bevel gear models. Tribological (e.g. friction or lubrication), thermal or durability related (e.g. pitting) effects were left out of the discussion, although they can have an important impact on the behavior of the components as well as the system. Due to the amount of variables, it becomes difficult to comprehend upfront which effects will dominate the behavior. Without neglecting possible influences by the system, it is therefore essential that component models unite a sufficiently accurate description of the phenomena that govern a component's behavior with an acceptable amount of computational time. A component model of a spiral bevel gear pair should for example be able to account for changes in relative configuration due to system compliance. In conclusion, it is considered to be good-practice to first establish an accurate description of the structural behavior (static, then dynamic) of the mechanical components and then to augment the model fidelity, depending on the phenomena that one wants to study.
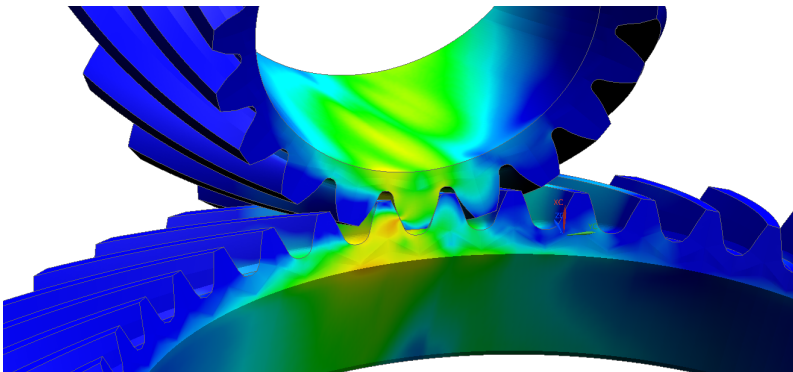
Figure 1.3: The Von Mises stress distribution for spiral bevel gears in mesh is here used to visualize the nonlinear nature of the tooth contact.

1.2 Problem statement and research objectives

1.2.1 Problem statement

In light of a growing need for accurate gear models that integrate into a system-level design process for mechanical transmissions, a clear difference can be identified when comparing simulation technology for cylindrical involute gearing with what exists today for bevel gears. While the models for spur and helical involute gears have evolved from analytical models [20, 53, 70, 92] to component-based models that allow to predict contact performance of lightweight gear designs within (flexible) multibody simulations [17, 22, 97, 142], the dynamic models for spiral bevel gears [85, 95, 133, 140] depend on pre-computed and averaged tooth contact data to approximate the time-varying mesh stiffness over the mesh cycle. One important basis that explains why the simulation technology for bevel gears has not yet caught up, points to the geometry of spiral bevel gear teeth and the resulting complexity of the contact phenomena.

For cylindrical gears, involute tooth profiles - introduced by Euler - have become today's standard, when motion transmission is required. Involute tooth geometry is relatively simple and can be described analytically. Moreover, meshing involute gear teeth also have additional beneficial properties. Unloaded and unmodified involute gear teeth have so-called conjugate flanks, i.e. they are able to guarantee perfect motion transmission. They also offer a good sensitivity to gear pair misalignments. However, their most important property for this discussion is that the contact between involute gear teeth can be expressed analytically through the *line* (2D) or *plane* (3D) *of action*. This allows to derive the contact points and the direction of the contact forces directly from the instantaneous rotation of each gear element [38, 54]. In contrast, a *face-milling* (FM) or *face-hobbing* (FH) process is used to create the required tooth geometry that allows for near-conjugate motion transfer in spiral bevel gears. The complexity of the tooth geometry does not allow for an analytical expression but requires the numerical simulation of the actual manufacturing process. Moreover, due to the three-dimensional nature of the motion transfer, the contact will take place along a *surface of action*, for which an analytical solution is not generally available.

As a consequence, a lot of research efforts (see Chapter 2) have gone into the analysis and optimization of individual spiral bevel gear pairs, either by experimental testing or by computerized *tooth contact analysis* (TCA). Through simulation of the gear meshing process, TCA aims at providing answers about key performance characteristics of the gear pair without a need for expensive prototyping and experimental testing. The performance of a spiral bevel gear

pair is typically classified based on the quality of the *transmission error* (TE), the *contact point path* (CPP) on the gear flanks, the (overall) contact zone under load and the sensitivity of these characteristics w.r.t. configurational misalignments [76]. While *unloaded tooth contact analysis* (UTCA) focuses mainly on determining the geometrical mismatch (referred to as ease-off topography) between two mating tooth profiles and the resulting *unloaded transmission error* (UTE), *loaded tooth contact analysis* (LTCA) predicts the contact behavior under load. Both types of TCA have integrated the simulation of the manufacturing process into their methodology to obtain an accurate description of the mating tooth flanks. TCA is often extended with *nonlinear FEA* (NL-FEA) of the meshing process to determine tooth bending and contact stresses under load. To handle the geometrical complexity of the gear teeth, the mating tooth surfaces are usually considered to be arbitrary and a general contact detection method, such as *continuous tangency* (in TCA) or *node-to-surface* (in FEA), is used to detect contact. The high computational requirements that come with the generality of such an approach make it impractical for parameter studies or optimization campaigns and have lead to its application being mostly limited to the study of component behavior.

Perhaps one of the most applicable methods to the system-level analysis of spiral bevel and hypoid gears, is the contact detection methodology that was proposed by KOLIVAND and KAHRAMAN to improve the computational efficiency of TCA [63]. Their contact detection and load distribution model proved useful in studies regarding the tooth flank optimization [9], efficiency analysis [67], and wear prediction [93]. Rather than imposing contact between the real teeth flanks, they simplified the contact detection by determining contact between the (chosen) real pinion flank and a (computed) theoretical flank that is conjugate to the pinion, while using the *ease-off topography* (EO) to account for difference between the conjugate to the pinion and the real gear flank. Using the so-called *surface of roll angles* or *roll surface* (RS), this methodology allows to compute contact lines between the real pinion flank and its conjugate in a numerically efficient way. This assumption is justified for flanks that transmit motion in a nearly conjugate manner, since the differences between the real gear flank and the conjugate to the real pinion flank are only a few micrometers and thus do not affect the location nor the shape of the contact region.

A direct translation of the model that was proposed by KOLIVAND, to a system-level model is however not without its difficulties. Since the ease-off topography does not only depend on the gear tooth flank geometry but also on the relative installment of the gear pair, the main drawback is directly related to changes in the mounting conditions (due to system compliance) that can occur during time simulation. Any variation in the nominal mounting conditions does not only directly affect the ease-off topography but also the contact locations (surface

of roll angles). Additionally, the gear-based *projection plane* method, as it is defined by KOLIVAND, requires a detailed knowledge about the manufacturing process to compute the 3D surface points of the gear teeth flanks. While such a requirement is less relevant to the core of the methodology, it does make the approach less applicable to predefined spiral bevel gear pair models for which such information is not (directly) available.

Apart from detecting contact it is equally important to correctly translate the detected deformation into accurate contact forces. System-level models for cylindrical gearing show that current gear and transmission design still calls for models with different levels of fidelity. While the development of more advanced, often *finite element* (FE) based, contact models [5, 22, 38, 97, 121] is driven by the present trend of lightweight design, analytical mesh stiffness models [20, 53, 70] still have their place within the design process. When it comes to TCA of spiral bevel gears, analytical mesh stiffness models are rarely used. This is attributed to the fact that analytical models can sometimes introduce significant approximations due to the complexity of the tooth geometry. Since linear and nonlinear FEA methods have shown to be effective modeling tools that allow for an accurate analysis of complex structures, FE-based methodologies for TCA are commonly used [6, 37, 40, 46, 77]. The increase in computational costs that comes with such an increase of model fidelity, also becomes easier to accept in the absence of a computationally efficient contact detection method. However, with efforts being done to improve the computational efficiency of contact detection algorithms, accurate analytical mesh stiffness models for spiral bevel gears can provide engineers with an additional powerful tool for quick evaluation of design alternatives.

1.2.2   Existing solutions

Different software solutions are commercially available to assist designers of transmissions with their design and simulation. Without any claim on completeness, it is reasonable to group the following list of available solutions into four product families. While originally each of these simulation approaches might have targeted a specific phase in the design cycle, over recent years synergies between the product families have emerged to compensate for individual weak points or to provide a mutual integrated solution.

The first family covers gearbox design (e.g. Romax [98], KISSoft [60], ...), integrating a lot of gearbox design know-how with simulation tools that allow for strength calculations, design optimization and some level of simulation capabilities for durability and NVH analysis.

A second family comprises of NL-FEA software (e.g. Simulia Abaqus [28], LMS Samcef Mecano [109], NX Nastran [111], ...), which can be situated at the highest end of the spectrum when it comes to solution accuracy. However, the price for high accuracy is often paid in terms of increased simulation time. This is particularly true for NL-FEA contact simulations with sliding or rolling surfaces, which require finely meshed contact interfaces to accurately represent the contacting geometry and to describe the arising contact stress distributions. In practice, these solutions are typically applied in the detailed static analysis of components, as system-level analysis or time-domain simulations prove too computationally expensive.

The third family governs products that are specifically created for the contact analysis of geared transmission components (e.g. Gleason CAGE [45], CALYX [127], BECAL [122], LDP and HAP [43], ...). Especially for spiral bevel and hypoid gear design, most of these solutions have become a reference in the field of TCA, as they provide the required tools for the optimization of tooth flank geometry through both UTCA and LTCA. Compared to a general-purpose NL-FEA software, these dedicated solutions are able to provide accurate results at a lower computational cost. This is often achieved through an integration of FE-based methods that describe the global behavior of the component with analytical or integral solutions that model the local deformation of the contact interface [37, 126].

The final product family covers the general-purpose multibody simulation software (e.g. Simcenter Motion [110], Simulia SIMPACK [29], ...). They excel at the simulation of system dynamics by representing the system as a set of interconnected elements (bodies, joints, forces, ...) but inherently offer less transmission design know-how or automated processes. To complement the modeling process, recent developments have therefore pursued either the integration of third-party software (of the first or third product family) or the creation of dedicated programs (so-called verticals) that support an automated process for multibody transmission creation [108]. The simulation tools that fit in this product family, emphasize on predicting nonlinear (system) dynamics within a reasonable time-frame and up to a sufficiently accurate level that makes the analysis of NVH and durability performance feasible. Still, thanks to the inclusion of advanced model order reduction techniques [22], current state-of-the-art models for cylindrical gears [120] have reached a level of fidelity that allows them to compete in terms of accuracy with solutions from the third and even second product family. Multibody contact models for spiral bevel and hypoid gears have not yet reached this level but are often included through simplified models or tessellation-based contact [86]. Alternatively, *user-defined force* (UDF) routines offer the possibility to create TCA-based contact models [100], by means of precomputed look-up tables, as is described in [95].

1.2.3 Research objectives

This dissertation aspires to establish foundation for gear contact modeling in spiral bevel gears. Its goal is to develop advanced gear contact models that accurately predict component behavior at a computational cost that enables further application within system-level analysis. Not only do the contact models have to efficiently predict the precise locations of contact, they also have to provide an accurate estimate for the resulting deformation and contact loads. Building on the thoughts of the previous sections, a successful modeling strategy should therefore meet the following requirements:

- *Numerically efficient, thanks to correct gear pair kinematics.* In practice, the real gear geometry only approximates the ideal transmission ratio due to errors that result from a combination of geometrical mismatch and contact deformation under external loading. An important step towards simplifying the contact detection between mating spiral bevel gear flanks and improving its numerical efficiency, lies in providing an accurate description of the gear pair kinematics for both the installment configuration of the gear pair and variable misaligned configurations.

  The envisioned gain in computation time for a single contact simulation, when compared to state-of-the-art methods, has to be significantly high (e.g. seconds vs. hours) to support usage in system-oriented applications.

- *Accurate, thanks to geometrical correctness.* A precise description of the contacting interfaces is of the utmost importance when developing an accurate 3D-contact model. While current manufacturing techniques allow for the creation of nearly-conjugate spiral bevel gears, the tooth's (macro-) geometry can differ significantly, depending on both the cutting process and gear parameters. Moreover, since the nonlinear contact behavior is predominantly influenced by the local surface geometry in contact, the geometrical models have to accurately capture the tooth's micro-geometry. Furthermore, a correctly defined tooth geometry also benefits the accuracy with which the gear pair's mesh stiffness is predicted.

  The methodology's accuracy is evaluated based on established criteria such as transmission error, contact pattern and contact pressure distribution. Static FEM-based contact simulations are used as a source of reference to assess whether the targeted accuracy is achieved against these metrics. The accurate prediction of the unloaded contact is deemed required to illustrate the contact detection methodology's effectiveness, together with a correct representation of the trends in loaded gear contact behavior. Considering that numerous loads are analyzed, differences in averaged model behavior that are in a range 10-15%, are thought to be permissible.

- *Modular design.* Providing different levels of model complexity can prove advantageous when designing systems. Depending on the application, simplified models that make correct assumptions, are often able to provide good impressions at a fraction of the computational cost. Moreover, having the option to include or remove more complex effects such as gear pair misalignments, friction, lubrication or the flexibility of a (lightweight) gear blank provides transmission design engineers with the appropriate tools to investigate the influences of such phenomena on the design.

  While this dissertation does not aim to provide a spiral bevel gear contact model that includes all these effects, the model should be developed in such a way that a future inclusion of more complex effects remains feasible.

1.3   Research approach and methodology

To successfully create a basis for the development of advanced gear contact models for spiral bevel gears, this research focuses on the design of innovative strategies for accurate and numerically efficient contact detection of both aligned and misaligned gear pairs. The methodologies, described in this dissertation, have been integrated in a MATLAB framework for the simulation of spiral bevel gear contact, that covers the creation of accurate tooth geometry, unloaded and loaded tooth contact analysis and validation of the proposed methods.

The presented methods for contact detection rely on concepts that originate from Differential Geometry, such as the *equation of meshing*, to predict the gear pair kinematics and optimize the contact search. They are therefore not restricted to the analysis of spiral bevel gears but can in general be applied to components that are designed to transmit rotational motion in a close-to-conjugate manner. Yet, an accurate description of the contacting tooth surfaces is required to capture effects on both a macro- and a microscopic scale. Various methods have been developed to make production of bevel and hypoid gears economically viable (see Chapter 3) but the mathematical models of these cutting processes, which are required to define the final gear tooth surface geometry, are not as accurately described in the literature for each of the processes. Within the scope of this research the first requirement is to create a sufficiently complex tooth surface geometry that is representative of a spiral bevel gear pair, rather than to investigate the contact performance of a gear pair that is created by one specific manufacturing method. Therefore, this work uses the *five-cut* method, a historically relevant face-milling method with an in the literature well-described model, to create a virtual prototype of a spiral bevel gear with accurately defined gear tooth surfaces.

The developed methods for contact detection and contact modeling in spiral bevel gears are presented over the course of the remaining chapters. At the end of each chapter, the different methods are applied to the analysis of an in-the-literature-described spiral bevel gear pair, created by the five-cut process. Simulation and analysis of this gear pair's contact performance under different operating conditions will provide sufficient data to evaluate the various aspects of the proposed methodology. The results from the performed unloaded or geometrical analysis (Chapter 4) can be compared with those published in the literature. The loaded tooth contact behavior of the aligned gear pair (Chapter 5) and of the misaligned gear pair (Chapter 6) are extensively correlated against the results of detailed static FEM-based contact simulations. The validation of the contact performance is achieved based on well-defined criteria for transmission error, contact pattern and contact pressure distribution.

To determine the contact loads, a modeling approach that separates the total gear tooth deflection into a global and a local deformation component, is adopted. Separating both effects creates a modular gear contact compliance model of which each component can be modeled with a different level of accuracy, depending on the application. Within the scope of this research, it is investigated if an analytical compliance model can be developed to accurately model the global tooth deformation, while using a Hertzian contact model to describe the local contact deformation under the assumption of a dry, frictionless contact. Advances in model fidelity, e.g. the inclusion of a FEM-based global compliance model or of friction models, are retained as possible future extensions.

Potential application within a multibody simulation environment should be a central idea during the development. Given the complexity of the various effects that arise during the gear contact, the dissertation emphasizes on an incremental validation of the unloaded and (statically) loaded contact behavior to build confidence in the modeling methodology. Simulation and analysis of the dynamic contact performance are kept as next steps for future research.

1.4   Outline and contributions

The modeling and simulation strategy for contact in spiral bevel gears is outlined in seven chapters. Each chapter addresses a specific aspect of the methodology, while shifting the focus from state-of-the-art methods to novel contributions.

1.4.1   Thesis outline

The equation of meshing, together with the ideas for TCA, formulated by KOLIVAND [63], will prove essential in the development of an efficient penetration-based contact detection algorithm. Consequently, **Chapter 2** discusses the state-of-the-art TCA methods that are available to analyze spiral bevel gears.

Chapter 3 covers the basic models, that are used to simulate the manufacturing process of spiral bevel gears. The process for creating face-milled spiral bevel gears is described in details, since it is used to create the gear pair under study in the following chapters. A general method to determine the principal curvatures of the contact surfaces is provided.

Spiral bevel gear pair kinematics and the theory of conjugate surfaces are discussed in **Chapter 4**. KOLIVAND's methodology for UTCA is modified and extended to construct conjugate surfaces, surfaces of roll angles and gear-based ease-off topography from predefined tooth flanks of the pinion and gear elements without the need for additional knowledge about the manufacturing process.

Chapter 5 proposes a multibody approach to LTCA. Using the surfaces of roll angles, an efficient contact detection algorithm that detects contact over multiple tooth pairs, is developed. Tooth deflections under load are computed by using a penetration-based contact model that applies a slicing technique to compute the individual tooth slice deformation, based on Hertzian contact and beam theory. The chapter concludes with a validation of the proposed analytical model against results, obtained by NL-FEA.

Chapter 6 proposes the novel idea of interpolating a new surface of roll angles that is a function of the actual gear pair misalignment. Using this methodology the developed multibody gear contact model is extended to simulate continuously varying gear pair misalignments that can occur due to system compliance. The developed methodology is again validated against NL-FEA results.

Finally, **Chapter 7** draws the main conclusions of the presented research, while also drafting a blueprint for improvements and future work.

To provide the reader with a clear understanding of how these different chapters come together, the proposed modeling strategy for spiral bevel gears is provided at the end of Chapter 2 (Section 2.4), following a concise overview of the state-of-the-art methods for tooth contact analysis.

1.4.2   Thesis contributions

The main contributions, which have resulted from these research efforts and which are described in this dissertation, can be summarized as follows:

- **Modification of an existing methodology for unloaded TCA.** Rather than incorporating the equations that govern the manufacturing process into the process, the developed UTCA methodology starts from a discrete description of the meshing gear tooth surfaces. The UTCA methodology is based on the surface of roll angles and gear-based ease-off topography but applies these concepts, combined with interpolation methods, directly to a predefined geometry for which the manufacturing process should not necessarily be known. A description of the tooth flanks in terms of surface coordinates and surface normal vectors in combination with a specification about the gear pair kinematics will prove sufficient.

- **Application of an existing contact detection strategy within a multibody framework.** A gear contact force element, suitable for multibody applications, is developed that uses the concept of the surface of roll angles to compute the contact curves for multiple teeth pairs in contact. The computed penetration is then translated into contact loads to simulate the contact behavior of a spiral bevel gear pair, while a static load is applied. The resulting gear contact force element could also be applied to the simulation of the dynamic gear contact.

- **Development of an analytical mesh stiffness model for spiral bevel gears.** To translate the occurring penetration into accurate contact loads, it is assumed that the detected penetration between rigid flanks reflects the tooth deformation of gear teeth, if they were flexible. The local contact deformation between two flanks is computed with an analytical expression that is derived from Hertzian contact theory. To approximate the global deformation of each gear tooth in contact, an involute tooth profile is fitted onto a local segment of the spiral bevel tooth. A set of analytical expressions, developed based on beam theory, are used to model the deformation of each tooth segment.

- **Development of a numerically efficient strategy to accurately detect contact under varying misalignments.** The surface of roll angles is dependent on the actual gear pair configuration. When the configurational states of the gear pair change, the original surface of roll angles will become less capable of accurately detecting the contact locations. The developed approach proposes to update the surface of roll angles by interpolating precomputed surfaces of roll angle based on the

actual configuration, so that the newly-created surface of roll angles better represents the misaligned configuration.

- **Validation of the developed methods.** For validation purposes, a virtual model of a spiral bevel gear pair that has been extensively described in the literature, is created and analyzed with the different developed techniques. In addition a FEM-based model of this gear pair is also created with one of the developed tools and a FEA-based contact simulations are performed for both aligned and misaligned configurations. A commercially available NL-FEA software package is used to perform these reference calculations. Besides creating different data sets to which the developed contact model is validated, the generated reference results can also be of use for the validation of future research.

- **Creation of dedicated toolchain for the contact analysis of spiral bevel gears.** An automated toolchain is created in MATLAB that combines all of the developed methods to cover: (i) accurate description of the gear tooth flank geometry through either simulation of the cutting process or importing existing cloud-of-point data. (ii) automated FE-model creation, (iii) automated computation of the required data for contact detection (preprocessing), (iv) UTCA and (v) LTCA.

Chapter 2

State-of-the-art in tooth contact analysis of spiral bevel gears

Computerized TCA has significantly aided the development of spiral bevel gears, since it allows to characterize a gear pair's performance without the need for prototyping and experimental testing. Depending on whether the kinematic or static performance of the gear pair is of interest, either unloaded (UTCA) or loaded (LTCA) tooth contact analysis is applied during the gear pair's design process. As a result, tailor-made TCA solutions have been developed to facilitate the simulation of the gear meshing process in both unloaded and loaded conditions. To obtain an accurate description of the gear geometry under analysis, many of these solutions integrate a numerical simulation of the manufacturing process into their functionality. This makes them particularly useful when it comes to the identification of optimized machine settings, as a function of desired contact characteristics. At the same time general purpose NL-FEA-based simulations are also performed when a deeper understanding of the arising contact and tooth bending stresses are required.

This chapter's main goal is to provide an overview of the different methodologies that have been developed for the contact detection and mesh stiffness calculation within TCA. Although it is possible to analyze any gear type using TCA, only those solutions that are used for spiral bevel gears will be of interest. Additionally, the key concepts for contact simulation using NL-FEA are provided and some interesting multibody models for spiral bevel gears are discussed.

2.1   Models for unloaded tooth contact analysis

Historically, the first computerized simulation methodologies that were developed for tooth contact analysis focused on a kinematic investigation of the gear pair's meshing performance. Without the consideration of external loads, UTCA's main attention goes to providing an accurate description of the geometrical mismatch between the mating rigid tooth flanks. Two fundamentally different methodologies for UTCA have been proposed in the literature: contact can be detected by directly imposing the contact conditions or through the concept of ease-off topography. Independently from the applied methodology, the goal of UTCA is to determine: (i) the unloaded transmission error (UTE), (ii) the path of instantaneous contact points (CPP), and (iii) the contact bearing pattern that provides an idea of how the contact develops under load. The bearing pattern is usually established based on the concept of the *elastic approach* δ_e, which represents an artificial deformation threshold [76].

2.1.1   Conventional approach to contact detection in TCA

The groundwork for most of today's methods for geometry, manufacturing and tooth contact analysis for spiral bevel and hypoid gears has been laid by WILDHABER [137] and BAXTER [14]. In the following years significant advancements were made by the researchers of the GLEASON WORKS [69] and KLINGELNBERG-OERLIKON [61]. Their efforts resulted in the creation of commercial TCA solutions for spiral bevel and hypoid gears.

In the early 1980s, LITVIN and GUTMAN presented their work on the geometrical analysis of FM spiral bevel gears in a triplet of papers [78, 79, 80]. Their work introduced the concept of local synthesis as a method to determine the machine settings, starting from predetermined contact characteristics for the gear pair at a predefined point. In later publications by LITVIN, FUENTES and ARGRYIS this methodology was adopted again to further optimize the manufacturing parameters for spiral bevel gear sets [6, 40, 77]. Their methodology for determining the contact between the meshing flanks under no-load conditions was based on the *principle of continuous tangency* between the mating flanks. It became a generally accepted method for contact detection in UTCA.

Methodology

The condition of continuous tangency is obtained by imposing the contact conditions between the mating flanks. Mathematically, this translates to

identifying the contact locations as those surface points ($\boldsymbol{r}^{(1)}$ and $\boldsymbol{r}^{(2)}$) on the corresponding flanks that become coincident and whose surface normal vectors ($\boldsymbol{N}^{(1)}$ and $\boldsymbol{N}^{(2)}$) become collinear in case of contact [76]:

$$\boldsymbol{r}^{(1)} = \boldsymbol{r}^{(2)} \tag{2.1a}$$

$$-\boldsymbol{N}^{(1)} = \boldsymbol{N}^{(2)} \tag{2.1b}$$

As a result, computerized programs for TCA, which make use of this methodology, usually have the following assumptions built-in to determine a solution to the contact problem: (i) the equations that define the pinion and gear tooth flanks are known, (ii) the gear pair installment is known and constant during the simulation, and (iii) the meshing tooth flank surfaces are conjugate in a specified point (point M).

A mathematical description of the individual gear tooth flanks can be obtained from the equations that govern the kinematics of the gear cutting process in combination with the equation of meshing (See Chapter 3). Given that this information is available, it becomes possible to define the position vector of each point $\boldsymbol{r}_1^{(1)}(u^{(1)}, v^{(1)})$ and corresponding surface normal vector $\boldsymbol{N}_1^{(1)}(u^{(1)}, v^{(1)})$ on the pinion tooth surface $\mathcal{S}_1$ (*gear 1*) as a function of two independent curvilinear coordinates $u^{(1)}$ and $v^{(1)}$. Similarly it is possible to define the position vector $\boldsymbol{r}_2^{(2)}(u^{(2)}, v^{(2)})$ and corresponding surface normal vector $\boldsymbol{N}_2^{(2)}(u^{(2)}, v^{(2)})$ on the gear tooth surface $\mathcal{S}_2$ (*gear 2*) as a function of the two independent curvilinear coordinates $u^{(2)}$ and $v^{(2)}$. In addition to the local reference frames S_1 and S_2, which are used to express the teeth surfaces of respectively the pinion and the gear element, a third reference frame can be introduced to define the gear pair installment and misalignments. These misalignments can be seen as variations about the nominal installment configuration (see Chapter 6). In this work, this auxiliary reference frame is referred to as the *Base* frame S_B. To satisfy the contact conditions at the point M (see Fig. 2.1a) both the pinion and the gear element are allowed to rotate about their respective rotational axes (z-axis of each local frame), while the gear pair's installment parameters are considered to remain constant during the simulation. From Eq. (2.1) the conditions for contact between the pinion and gear flanks is then defined in the frame S_B by:

$$\mathbf{T}_{B1}(\phi_z^{(1)})\,\bar{\boldsymbol{r}}_1^{(1)}(u^{(1)}, v^{(1)}) = \mathbf{T}_{B2}(-\phi_z^{(2)})\,\bar{\boldsymbol{r}}_2^{(2)}(u^{(2)}, v^{(2)}) \tag{2.2a}$$

$$-\mathbf{L}_{B1}(\phi_z^{(1)})\,\boldsymbol{N}_1^{(1)}(u^{(1)}, v^{(1)}) = \mathbf{L}_{B2}(-\phi_z^{(2)})\,\boldsymbol{N}_2^{(2)}(u^{(2)}, v^{(2)}) \tag{2.2b}$$

In Eq. (2.2) the angles $\phi_z^{(1)}$ and $\phi_z^{(2)}$ represent the pinon and gear rotations about their respective rotational axes. To simplify the operations when dealing with numerous rotation and translation transformations, the coordinates of the

contact points on the pinion and gear surfaces, given by the vectors $\boldsymbol{r}_1^{(1)}$ and $\boldsymbol{r}_2^{(2)}$ in their respective local frames S_1 and S_2, are written in their homogeneous forms $\bar{\boldsymbol{r}}_1^{(1)}$ and $\bar{\boldsymbol{r}}_2^{(2)}$ (See also Appendix B: Eqs. (B.1) and (B.2)). The homogeneous transformation matrices $\mathbf{T}_{B1}$ and $\mathbf{T}_{B2}$ are then used to represent the gear pair's installment (translation and rotation) w.r.t. the Base frame S_B. The matrices $\mathbf{L}_{B1}$ and $\mathbf{L}_{B2}$ are sub-matrices of $\mathbf{T}_{B1}$ and $\mathbf{T}_{B2}$, respectively, that represent the orientation of the contact flanks w.r.t. the Base frame S_B.

While Eq. (2.2) defines the contact locations in terms of six unknown variables $(\phi_z^{(1)}, u^{(1)}, v^{(1)}, \phi_z^{(2)}, u^{(2)}$ and $u^{(2)})$, it comprises only five independent nonlinear equations [76]. Because of the collinearity of the surface normal vectors at the contact point, the components of Eq. (2.2b) are further related by:

$$\left\| \boldsymbol{N}_B^{(1)} \right\| = \left\| \boldsymbol{N}_B^{(2)} \right\| = 1 \tag{2.3}$$

Consequently, the user has to specify either $\phi_z^{(1)}$ or $\phi_z^{(2)}$ in order to solve the system of equations for the remaining five unknowns. In addition, accurate guess values are also required to guarantee a correct solution. When applied successfully, the methodology of continuous tangency allows to determine the UTE, based on the resulting pinion rotation angle $\phi_z^{(1)}$ and gear rotation angle $\phi_z^{(2)}$, using the general equation for transmission error:

$$TE = \left(\phi_z^{(2)} - \phi_{z0}^{(2)} \right) - \frac{Z_1}{Z_2} \left(\phi_z^{(1)} - \phi_{z0}^{(1)} \right) \tag{2.4}$$

Here $\phi_{z0}^{(1)}$ and $\phi_{z0}^{(2)}$ correspond to the initial angular displacement of the pinion and the gear that are required to position the mating tooth flanks in contact (as close as possible) at the start of the simulation, while Z_1 and Z_2 correspond to the number of teeth for the pinon and gear, respectively [36].

Solving the system of equations, given by Eq. (2.2), for each of the selected angular configurations of the mesh cycle, allows to establish the path of instantaneous contact points on both the pinion and the gear flank. To estimate how the contact pattern develops when a light load is applied, a potential contact line is computed for each point of the CPP. It is assumed that the instantaneous contact line develops along the direction for which the distance between the two contact surfaces (i.e. the pinion and the gear surface) is minimal [75, 76, 134]. This direction also corresponds to the direction that minimizes the relative normal curvature between the two surfaces at the *instantaneous contact point* (ICP) M. To compute the relative curvature, the contacting surfaces are locally approximated as two contacting ellipsoids, centered around the contact point M, as shown in Fig. 2.1. When viewed in the tangent plane T, the resulting contact pattern resembles that of an ellipse for which the size and orientation
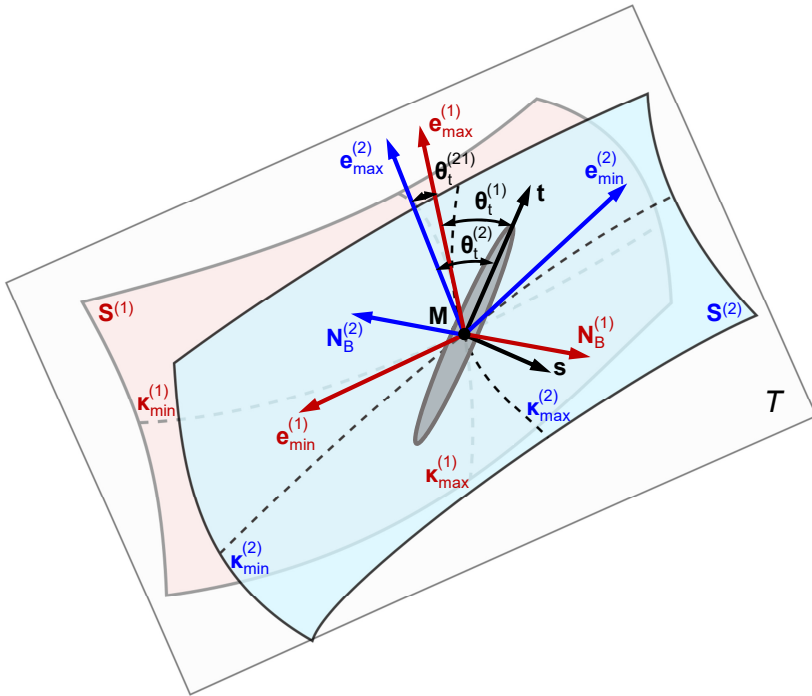
(a) Continuous tangency condition and the assumed contact ellipse.
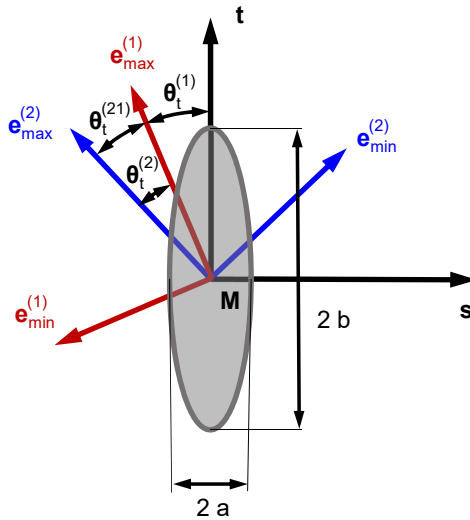
(b) The insantaneous contact ellipse.

Figure 2.1: Illustration of continuous tangency condition and the assumed instantaneous contact ellipse.

are determined by the minor axis s and major axis t. Since the direction of the contact ellipse's major axis t represents the direction of the contact line, the normal curvature along t has to be determined for both surfaces.

When the principal curvatures of both the pinion surface ($\kappa_{min}^{(1)}$ and $\kappa_{max}^{(1)}$) and the gear surface ($\kappa_{min}^{(2)}$ and $\kappa_{max}^{(2)}$) and their corresponding principal directions ($e_{min}^{(1)}$, $e_{max}^{(1)}$, $e_{min}^{(2)}$ and $e_{max}^{(2)}$) are known, Euler's formula, given in Eq. (2.5), allows to compute the normal curvature along any direction t.

$$\kappa_n^{(g)} = \kappa_{max}^{(g)} \cos^2\left(\theta_t^{(g)}\right) + \kappa_{min}^{(g)} \sin^2\left(\theta_t^{(g)}\right) \qquad (g = 1, 2) \qquad (2.5)$$

The angle $\theta_t^{(g)}$ is defined as the angle between the direction t and the direction of maximum principal curvature $e_{max}^{(g)}$ for a surface g, as shown in Fig. 2.1b.

Correspondingly, Eqs. (2.6) and (2.7) allow to compute the normal curvature along t for respectively a pinion ($i = 1$) and a gear surface ($i = 2$). The relative orientation of both surfaces is taken into account through $\theta_t^{(21)} = \theta_t^{(2)} - \theta_t^{(1)}$, which allows the relative normal curvature $\kappa_n^{(21)}$ along t to be expressed as a function of $\theta_t^{(1)}$.

$$\kappa_n^{(1)} = \kappa_{max}^{(1)} \cos^2\left(\theta_t^{(1)}\right) + \kappa_{min}^{(1)} \sin^2\left(\theta_t^{(1)}\right) \qquad (2.6)$$

$$\kappa_n^{(2)} = \kappa_{max}^{(2)} \cos^2\left(\theta_t^{(1)} + \theta_t^{(21)}\right) + \kappa_{min}^{(1)} \sin^2\left(\theta_t^{(1)} + \theta_t^{(21)}\right) \qquad (2.7)$$

$$\kappa_n^{(21)} = \kappa_n^{(2)} - \kappa_n^{(1)} \qquad (2.8)$$

Assuming that the contact ellipse occurs along the direction of minimum relative normal curvature $\kappa_n^{(21)}$, its orientation is found by computing the value of $\theta_t^{(1)}$ that minimizes Eq. (2.8). From $\frac{d\kappa_n^{(21)}}{d\theta_t^{(1)}} = 0$, one obtains [76]:

$$\tan\left(2\theta_t^{(1)}\right) = \frac{g_{\mathcal{S}}^{(2)} \sin\left(2\theta_t^{(21)}\right)}{g_{\mathcal{S}}^{(1)} - g_{\mathcal{S}}^{(2)} \cos\left(2\theta_t^{(21)}\right)} \qquad (2.9)$$

In order to compact the notation, the following expressions are introduced:

$$\kappa_{\mathcal{S}}^{(g)} = \kappa_{max}^{(g)} + \kappa_{min}^{(g)}, \qquad g_{\mathcal{S}}^{(g)} = \kappa_{max}^{(g)} - \kappa_{min}^{(g)} \qquad (g = 1, 2) \qquad (2.10)$$

With the orientation of the contact ellipse determined, it is also possible to estimate the length of the contact line along t as $L_c = 2b$ and the width of the contact along s as $2a$ (see Fig. 2.1b), using Eq. (2.11) [76].

$$2a = 2\left|\frac{\delta_e}{A}\right|^{1/2}, \qquad\qquad 2b = 2\left|\frac{\delta_e}{B}\right|^{1/2} \qquad (2.11)$$

where:

$$A = \frac{1}{4} \left[\kappa_{\mathcal{S}}^{(1)} - \kappa_{\mathcal{S}}^{(2)} + \left[\left(g_{\mathcal{S}}^{(1)} \right)^2 - 2 g_{\mathcal{S}}^{(1)} g_{\mathcal{S}}^{(2)} \cos \left(2\theta_t^{(21)} \right) + \left(g_{\mathcal{S}}^{(2)} \right)^2 \right]^{1/2} \right] \quad (2.12)$$

$$B = \frac{1}{4} \left[\kappa_{\mathcal{S}}^{(1)} - \kappa_{\mathcal{S}}^{(2)} - \left[\left(g_{\mathcal{S}}^{(1)} \right)^2 - 2 g_{\mathcal{S}}^{(1)} g_{\mathcal{S}}^{(2)} \cos \left(2\theta_t^{(21)} \right) + \left(g_{\mathcal{S}}^{(2)} \right)^2 \right]^{1/2} \right] \quad (2.13)$$

In practice, the elastic approach δ_e, which is used in Eq. (2.11) to estimate the size of the contact ellipse, corresponds to the thickness of the marking compound that is applied to the gear teeth when an experimental TCA test is performed. In case of a light load, the resulting tooth deformation can be considered negligible. Therefore, the marking component that is removed due to friction, indicates the minimum distance between the engaging tooth flanks. Experimental results have shown that this thickness is usually between 4-7 μm [76, 134]. Alternatively, an estimated value for the overall tooth deflection can also be chosen to predict the emerging contact pattern under load.

Challenges

The conventional approach to TCA considers the contacting teeth flanks to be arbitrary, while imposing the condition of continuous tangency at each step of the mesh cycle by solving a system of nonlinear equations (Eqs. (2.2a) and (2.2b)). Finding an accurate solution to this problem is complicated as convergence to points in the proximity of the true contact point can occur due to the high level of conformity (similarity) between the mating flanks. The solution also shows to be very sensitive to the initial guesses, which are not straightforward to determine [63]. Consequently, dedicated strategies for automatic determination of appropriate guess values have been proposed for both general TCA [81] and TCA in the presence of misalignments [49].

The condition of continuous tangency also shows limitations when contact occurs at the edges of the teeth flanks (edge contact) or when the mating teeth surfaces are in a perfect line contact [72, 99]. In case of an edge contact the methodology might fail at solving the contact problem, if a common direction for the contact surface normal cannot be identified. When the flanks show to be in line contact for unloaded conditions, multiple solutions to the contact problem exist and the accuracy of the methodology might be low, depending on the chosen solution. In addition, the assumption of a contact ellipse, equally distributed around the instantaneous contact point M, does not account for a change in relative flank curvature along the contact direction but rather
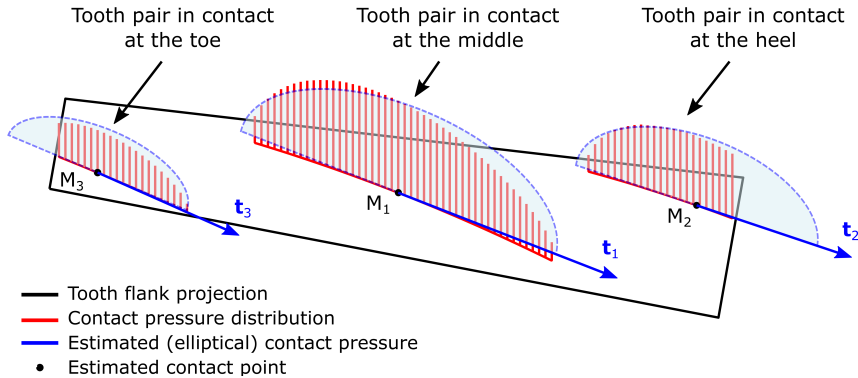
Figure 2.2: Comparison between the actual contact distribution and the estimated elliptical contact distribution that is centered around contact point.

assumes a constant relative curvature along the contact direction. Such an approximation can lead to incorrect estimates for the contact length and contact pressure distribution at narrow (toe) and wide (heel) end of the teeth flanks. A comparison between the assumed elliptical contact pressure distribution and the contact pressure distribution, that was computed using the methodology of Chapter 5, is provided in Fig. 2.2. The three instantaneous contact curves and pressure distributions (for different tooth flank pairs) are projected onto a common projection of the tooth flank for better visualization.

Different solutions are proposed in the literature to overcome these problems. SIMON developed a methodology for TCA, which he applied to the analysis of spiral bevel gears [114, 115] and hypoid gears [112, 113, 116], for which he optimized contact pressure and transmission error. While detecting the ICP through the concept of continuous tangency, he introduced the separation function to compute the instantaneous contact lines. By assuming that under load the contact point would evolve into a line load, he was able to compute the direction of the contact curves through minimization of the separation functions. This procedure avoided the computation of the relative curvatures [114, 115] and allowed him to demonstrate that the assumption of an elliptical contact zone, centered around the ICP, can lead to significant errors when the contact occurs near the toe and heel sections of the teeth (see Fig. 2.2) [112]. To overcome problems related to edge or line contacts, VIJAYAKAR proposed to discretize the tooth surfaces and to solve the contact detection problem by finding the points of minimum distance between the discretized surfaces, similar to the node-to-surface method (see Sec. 2.2.3). He combined this approach with an adaptive grid refinement strategy to increase the accuracy with which candidate contact points are identified [126]. LIN also adopted a numerical approach to

TCA [72], for which he discretized the tooth surface. Rather than solving for the contact location that satisfies both contact conditions, his methodology focuses on the computation of the smallest rotational angle, required to bring the gear into contact with the pinion. During the analysis the pinion element with finely meshed tooth flanks is kept fixed, while the gear with initially coarsely meshed flanks is allowed to rotate about its rotational axis. At each step of the mesh cycle an adaptive mesh refinement procedure is performed in order to identify a converged value for the smallest gear rotational angle. Building on the same ideas, SANCHEZ-MARIN recently proposed a geometric approach to TCA that relies on discretization and adaptive refinement of all the contact surfaces [99]. To show the robustness of the method he analyzed spur and helical gears in both aligned (line contact) and misaligned (edge contact) configurations.

All of the described methods in this sections have a common drawback: they consider the mating flanks as arbitrary surfaces. While some of these methods have proven to be robust for contact detection, they fail to benefit from the fact that the contacting surfaces are designed to transmit motion in a nearly conjugate manner. As a result their computational cost tends to be relatively high compared to methods that can include such information.

2.1.2   Ease-off based contact detection in TCA

STADTFELD introduced the concept of ease-off (EO) topography to TCA in [117] and used it in a later study to optimize the shape of the UTE by applying flank modifications to reduce impacts and lower the noise of the gear pair [118]. His definition for ease-off topography includes the effects of flank form corrections and misalignments, applied to either pinion or gear, that cause a mismatch between the mating flanks and thus a non-conjugate behavior of the gear pair.

KOLIVAND and KAHRAMAN developed a novel methodology for TCA which is based on the ease-off concept. During the UTCA they construct the surface of roll angles (RS) and ease-off topography from the gear pair installment, whether misaligned or not. Through the combination of the surface of roll angles and the ease-off topography they are able to compute potential contact curves and unloaded transmission error in an elegant way [63, 64]. In their developed approach the ease-off topography is defined w.r.t. the gear element.

Given that the ideas behind the TCA methodology of [63] serve as a starting point for the contact detection techniques that are developed in this work, the different concepts are introcuded in this section and KOLIVAND's method for UTCA is briefly discussed. A detailed description on how these ideas contribute to this work's methodology for UTCA and penetration-based contact detection is given in Chapters 4 and 5.

Background

Two contacting surfaces are considered to be mathematically conjugate when they have line contact. A gear pair is said to be conjugate when the contacting tooth flanks have line contact for each position of the mesh cycle [62]. For unloaded conditions or when rigid flanks are considered, a conjugate gear pair provides motion transfer as prescribed by the (instantaneous) gear ratio and thus yields zero UTE throughout the mesh cycle.

In practice, a gear pair does not only need to transmit rotational motion in a continuous manner, it also needs to transmit power between the rotating axes. Under operational loading the contact forces that arise between the conjugate teeth cause deformation of both contacting and neighboring gear teeth, causing teeth to come into contact sooner than designed. When this happens the tooth engagement is characterized by shocks and high contact pressure concentrations at the flank edges, which is detrimental for a gear pair's NVH and durability performance. In addition the transmitted torque also causes housing and shaft deflections that introduce configurational misalignments, which in turn affects the error of motion transmission and edge contacts. Therefore, flank form modifications, e.g. lengthwise and profile crowning, are typically applied to one (usually the pinion) or both gear elements by removing a microscopic amount of material (up to a few hundred micrometers). The purpose of these modifications is to create enough space for the tooth to deform under a given design load or to allow smooth motion transmission for a range of misaligned configurations. However, the definition of the flank form modifications for spiral bevel and hypoid gears is far more complicated than it is for cylindrical involute gearing. Firstly, the meshing conditions vary along the flank width, requiring a three-dimensional approach. Secondly, no clear description of a tooth profile, equivalent to the involute for planar gearing, is known for face-cut spiral bevel and hypoid gears [31]. Although it should be mentioned that with the latest cutting machines it has become theoretically possible to manufacture conjugate face-cut spiral bevel gears by optimization of the machine settings.

With the purpose of defining a metric that can be used in the optimization of the tooth flank form modifications of spiral bevel and hypoid gears, the concept of ease-off has been introduced [10, 117]. The ease-off topography is defined as the overall geometrical mismatch between a pair of mating pinion and gear flanks. As mentioned, this flank mismatch does not only correlate with the applied flank form modifications but it also depends on the spatial (mis)alignment of the gear pair. Therefore, the tooth flank form modifications are no longer considered as deviations from the basic rack - which is the case for cylindrical gears - but are rather related to the tooth contact characteristics of the mating wheel and pinion flanks of a spiral bevel or hypoid gear pair [62].

Methodology

Two different methodologies can be used to construct the ease-off topography. The first method simulates the load-free meshing of the tooth flanks, while keeping track of the distances along the instantaneous contact curves [10, 115, 117]. The enveloping surface of all the instantaneous ease-off curves results in a surface of minimum contact distances, which is the ease-off topography. However, in this case the ease-off topography is only a result of the UTCA and another methodology is required to detect contact between the mating flanks. An alternative approach relies on the computation of the flank that is conjugate to a (chosen) flank of the flank pair in contact [63]. The ease-off topography is then constructed by comparing the conjugate to the chosen flank with the other flank with which this chosen flank is in contact.

Ease-off topography The ease-off topography is either expressed with respect to the real gear flank (gear-based) or with respect to the real pinion flank (pinion-based). In a *gear-based* ease-off approach, the ease-off topography is constructed by comparing the gear flank with the flank that is conjugate to the chosen pinion flank. When a *pinion-based* ease-off approach is adopted, the conjugate to the chosen gear flank is computed and the topography is constructed by comparison with the pinion flank. Depending on the definition, the ease-off topography is either visualized on a *gear-based* or *pinion-based* projection plane, which can be constructed by a circular projection of the involved gear flanks onto a plane that includes the rotational axis. An example of gear-based ease-off topography is provided in Fig. 2.3. A comparison between gear-based and pinion-based ease-off topography is found in Appendix C.
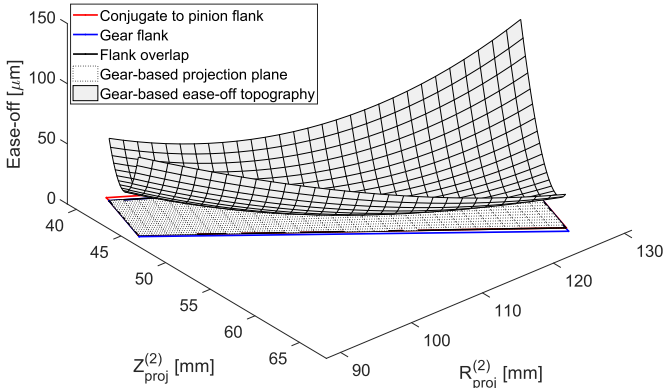
Figure 2.3: An example of gear-based ease-off topography.

Conjugate flanks In unloaded conditions each contact point on a pair of conjugate (gear tooth) surfaces transfers the motion according to the prescribed kinematic law (i.e. the gear ratio). Thus, neither penetration nor gap exists between any of those points in contact for an incremental surface rotation ϕ_z. Differential Geometry formulates these conditions with the *equation of meshing*:

$$f(u, v, \phi_z) = \left(\frac{\partial \boldsymbol{r}}{\partial u} \times \frac{\partial \boldsymbol{r}}{\partial v}\right) \cdot \frac{\partial \boldsymbol{r}}{\partial \phi_z} = 0 \tag{2.14}$$

Starting from a known (tooth) surface $\mathcal{S}(u, v)$, where the curvilinear coordinates u and v describe the coordinates $\boldsymbol{r}$ of a point P on $\mathcal{S}(u, v)$, the conjugate to the surface is found by solving Eq. (2.14). The vector product of the partial derivatives of $\boldsymbol{r}$ to u and v denotes the surface normal $\boldsymbol{N}$. The partial derivative of $\boldsymbol{r}$ to ϕ_z has the same direction as the relative velocity $\boldsymbol{v}$ between a point on surface $\mathcal{S}(u, v)$ and a coincident point on the surface, conjugate to $\mathcal{S}(u, v)$. Consequently, Eq. (2.14) is often written in a more practical form:

$$\boldsymbol{N} \cdot \boldsymbol{v} = 0 \tag{2.15}$$

Eq. (2.15) reflects the no-gap/penetration condition, as it requires the relative velocity $\boldsymbol{v}$ to be perpendicular to the surface normal $\boldsymbol{N}$ at the contact point P.

Surface of roll angles The roll angle is the value of ϕ_z for which a point P on the surface $\mathcal{S}(u, v)$ satisfies Eq. (2.15). The surface of roll angles $\mathcal{R}_\phi$ is the set of roll angles $\phi_{z,i}$ for $\mathcal{S}(u, v)$, of which each value belongs to a point on $\mathcal{S}(u, v)$. More details on the surface of roll angles and its usage are given are Chapter 4.
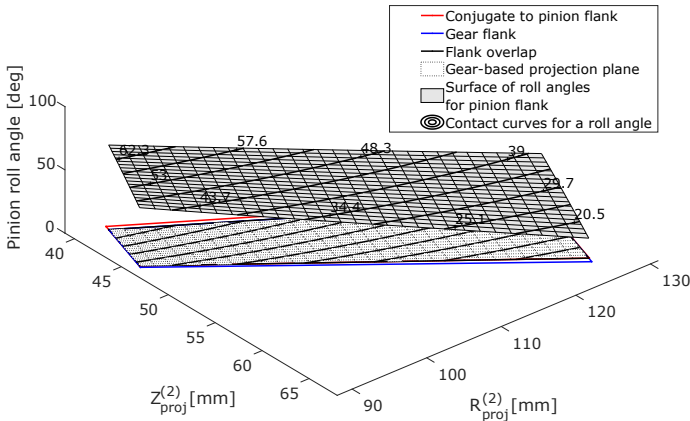
Figure 2.4: An example of surface of pinion roll angles.

Contact detection By combining both the surface of roll angles and the ease-off topography an efficient contact detection methodology was developed in [63]. The different steps of the method can be summarized as follows:

- **Construction of the projection plane.** A gear-based ease-off approach is adopted in [63]. The required gear-based projection plane is created by applying a discretized grid of $n \times m$ points to the projected flank overlap.

- **Computation of the real gear surface points.** Using the machine settings and a mathematical model that simulates the machining process, the surface points for the gear flank are computed for each of the points on the discretized projection plane. An example of such a mathematical model that simulates the machining process can be found in Chapter 3.

- **Computation of the real pinion surface points.** A pinion projection plane is created, starting from the the points of the gear projection plane. To guarantee coincident grids, the projected conjugate flank points are defined to coincide with those of the projected real gear. The conjugate surface points can be computed by combining Eq. (2.15) with the mathematical model that simulates the machining process of the pinion flanks. To account for potential gear pair misalignments, these equations are solved in an auxiliary reference frame that is similar to the earlier introduced base frame S_B.

- **Construction of the EO topography and surface of roll angles.** By solving Eq. (2.15) for each point on the projection plane, the pinion's surface of roll angles is automatically obtained. In addition, the gear-based ease-off topography can be computed as the difference between the real gear flank and the flank that is conjugate to the real pinion flank. To visualize the flank form modification, both flanks are rotated to have them in contact in at least one point (see Fig. 2.5). This rotation is removed to have an ease-off topography that is zero in at least one point (see Fig. 2.3).

- **Computation of the UTE and CPP.** For a given orientation of the pinion, a potential contact curve is computed between the real pinion flank and its conjugate flank. To determine the true contact state, the ease-off values that belong to each point on the potential contact curve are computed. The point where the ease-off values of the contact curve reach a minimum point is identified as the instantaneous contact point. The ease-off value at the ICP indicates the rotation that is required for the gear to contact the pinion and thus is the UTE value for this mesh cycle configuration. Assuming a marking compound with thickness δ_e, the instantaneous contact curve is defined by all points for which the ease-off is within a value δ_e from the ICP.

Contrary to the continuous tangency approach, the roll surface and ease-off methodology does not consider the gear teeth flanks to be arbitrary surfaces. In fact, it embeds the knowledge that the gear teeth are designed to transmit near-conjugate motion to attain an increased numerical performance. Moreover, the assumption of near-conjugate tooth surfaces holds also for real gear pairs where the tooth profiles have both global (e.g. manufacturing errors) and local (e.g. wear) deviations [65]. The methodology does not require the solution of a system of nonlinear equations to identify the contact point, nor are the relative curvatures required to determine the direction and the length of the contact line. The method only requires the tooth surfaces to be defined by their position vectors and corresponding normal vectors to solve Eq. (2.15), prior to the actual contact detection. A more accurate and more natural contact curve - instead of a line - is found through the use of the surface of roll angles in combination with the ease-off topography and the threshold value δ_e.

Challenges

Because of these advantages, other researchers have also used the methodology or its ideas. A similar method for ease-off based TCA was used by Fan to optimize the pinion tip line to avoid root-tip interference [35]. Artoni et al. developed a TCA variant that expressed the ease-off topography w.r.t. the pinion element, allowing corrective modifications to the behavior of the gear pair by only correcting the pinion [8]. While the methodology, as formulated in [63], has proven its worth in TCA, a direct adaptation to a contact detection strategy within a multibody application is not without its challenges.

The methodology's main limitation is tied to how it uses the projection plane for contact detection in the presence of gear pair misalignment. The gear projection plane is defined to be bounded by the overlap between the contacting flank pair (pinion and gear). This flank overlap varies depending on the misalignment, as shown in Fig. 2.6. As a result, only a gear pair misalignment that remains constant during the mesh cycle can be analyzed. For TCA purposes this is sufficient, since this is what TCA tends to accomplish. However, during a multibody simulation the gear pair configuration should not be expected to remain constant but should be assumed to vary continuously as the result of component compliance and component interactions within the system. Under such conditions the projection plane, the surfaces of roll angle and the ease-off topography should be reestablished each time the gear pair deviates from its original configuration. One of the greatest advantages of this methodology lies in the fact that the contact locations can be determined as part of a preprocessing step (offline). A recalculation of the contact data, each time the configuration changes (online), would significantly reduce its computational efficiency.
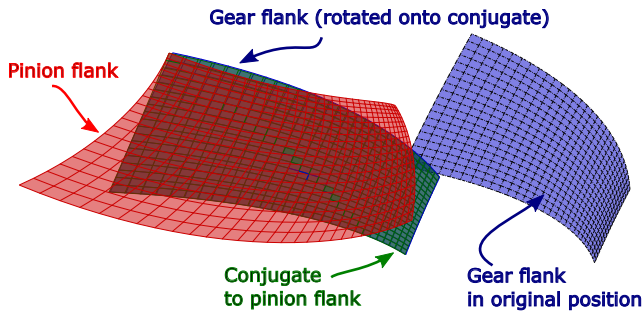
Figure 2.5: An illustration of the pinion (red), conjugate to pinion (green) and gear (blue) flanks in contact, displaying the rigid body rotation that generally exists between the gear flank and the conjugate to the pinion.

An approximation may be to assume that the misalignments remain relatively small and therefore do not affect the flank overlap all that much. Still another challenge, directly related to the way how contact is detected, should be overcome when considering variable misalignments. While the gear-based approach determines the potential contact curves between the real pinion flank and its conjugate flank by using the surface of roll angles, the ease-off topography is required to determine the gap between the real pinion flank and the real gear flank. Naturally, the opposite holds for a pinion-based approach. However, the shape and value of the ease-off topography, reveal a much higher sensitivity to changes of the local (relative) geometry, as shown in Fig. 2.6. As mentioned, the construction of the ease-off topography is performed by determining the difference between the real gear flank and the conjugate to the pinion flank. Since both flanks are generally not yet in contact (see Fig. 2.5), the first step of this process rotates both flanks to have them make contact in at least one point. To compute this rigid body rotation the complete conjugate flank needs to be evaluated, which leads to an additional (online) computational cost.

KOLIVAND and KAHRAMAN show in [66] that their methodology can be applied to other geared geometries, given that the manufacturing process is known in order to compute the data on the projection plane. Therefore, a somewhat specific and minor challenge can be encountered when extending their methodology to geometries for which the manufacturing process is not known or not available to the user. Such an extension can be particularly useful when a multibody application is considered. Multibody models are often created by starting from the CAD-files and by (often different) users that have no direct access to additional information, regarding the manufacturing process of the components.
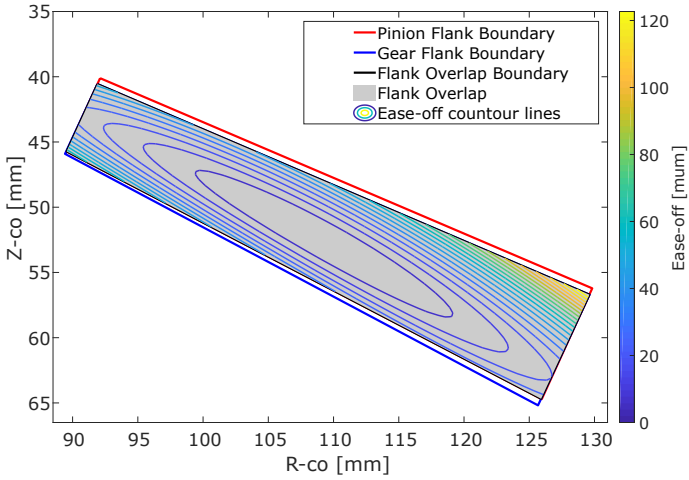
(a) An example of the ease-off topography in a aligned configuration.
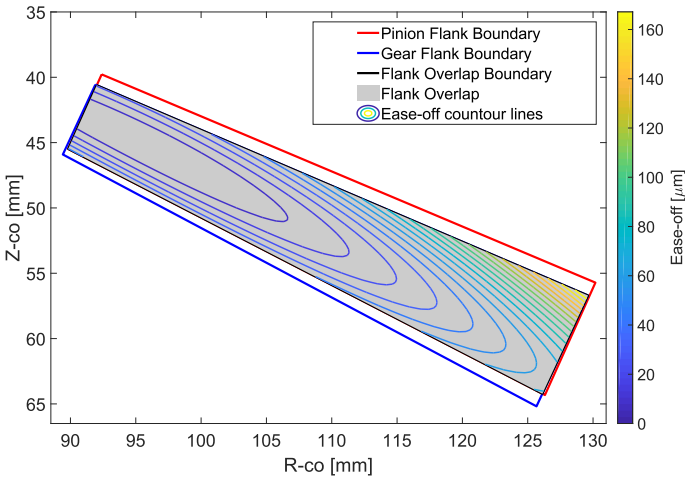
(b) An example of the ease-off topography in a misaligned configuration.

Figure 2.6: Example of the flank overlap and the ease-off topography for an aligned and misaligned configuration.

2.2   Models for loaded tooth contact analysis

Where UTCA mainly focuses on providing an accurate description of the geometrical aspects that govern the contact between meshing surfaces, loaded tooth contact analysis (LTCA) shifts its focus to correctly capturing the deformation effects that occur due to contact loads. In LTCA, an assessment of the gear pair's performance under load is usually obtained, based on the loaded transmission error (LTE), the (instantaneous and overall) contact pressure and the root bending stresses. However, a prediction of the latter is not always included in the different methodologies.

Models for LTCA of spiral bevel and hypoid gears are relatively scarce. Most of the models, which are currently described in literature, can be divided into two fundamental groups: analytical and FE-based semi-analytical models. LTCA models are often tailor-made for the purpose of gear analysis and can make use of the contact detection methodologies that were developed for UTCA. Alternatively, NL-FEA methods are also applied to the loaded analysis of spiral bevel gear pairs. Because of the general formulation that these methodologies adopt, they are considered as a separate family of modeling tools in this work.

2.2.1   Analytical models

Depending on the assumed behavior and applied boundary conditions, different approximate solutions can be derived to analytically model a problem. For this reason, this work limits itself to providing only a brief description of some analytical models that have been described in the literature. The reader is referred to the referenced work for more information.

KRENZER proposed a methodology for LTCA in which the overall tooth deformation was modeled as a combination of Hertzian contact theory and beam theory. In his work a TCA program, based on continuous tangency, was used to describe the tooth geometry and no-load contact analysis [68].

ELKHOLY et al. used an analytical procedure to calculate the transmitted load distribution for straight bevel gears by dividing the teeth into different slices with varying cross-section [34]. Using TREDGOLD's approximation [18] he assumed that the cross-section of each slice could be well represented by involute tooth profile, for which he computed the deflection using analytical formulas developed by NAKADA and UTAGAWA [87].

SCHLECHT et al. also applied a slicing method to approximate spiral bevel and hypoid gear teeth as cylindrical gear teeth, obtained by fitting of a square polynomial tooth profile [101]. ZIEGLER and BAUMANN developed this

methodology to estimate the bending, compressive and shear deformation of cylindrical [141] and bevel [13] gears, for which they in turn used the deformation energy based approach, formulated by WEBER and BANASCHEK [135].

The relatively inexpensive computational cost of analytical load distribution models enable them to provide good impressions of the gear pair's loaded behavior within an acceptable simulation time. Yet, correctly capturing coupled deformation effects that occur between different teeth pair in contact, remains difficult within an analytical model. Therefore, limitations to these models are expected when load sharing between multiple gear teeth pair is predominant. Such situations can occur in high contact ratio gears[1], or under high operating loads where the coupling effects should not be neglected.

2.2.2 Semi-analytical models

Where analytical models approximate the deformation of the teeth with expressions that have been derived for a simpler geometry, semi-analytical models use a combination of numerical and analytical methods to compute the gear pair's mesh stiffness. An example of such a numerical method is the *finite element method* (FEM), which is commonly applied to discretize complex geometries, like spiral bevel gear teeth, to obtain a more accurate description of the structural behavior. The deformation field that is computed with FEM also allows to correctly include all the relevant coupling effects. However, to accurately represent the correct stress-strain field and its high gradients near the contact zone, FEM requires locally refined meshes. The number of finely meshed contact zones that are required to accurately model the contacting gear teeth, would result in FE models with hundreds of thousands of *degrees of freedom* (DOFs). Using only FEM would result in simulation times that would make design and optimization processes extremely cumbersome. Therefore, semi-analytical models try to combine the best of both worlds by typically using a FE model to describe the linear deformation of the gear (body and crown), while using analytical expressions to capture the local nonlinear (Hertzian) contact deformation accurately.

Without any claim on completeness, this subsection provides a brief overview of some relevant semi-analytical LTCA models that have been described in literature. In light of the modeling strategy that this work wants to adopt, ideas that were proposed by ANDERSSON-VEDMAR [5] and FERNANDEZ DEL RINCON [38] for the analysis of spur and helical gears, are also mentioned.

---

[1]No clear definition of a high contact ratio spiral bevel gear is given in the gear literature. Since most spiral bevel gears have a contact ratio between 2 and 3, in this work a high contact ratio spiral bevel gear is said to have a contact ratio greater than 3.

GOSSELIN et al. developed an LTCA program for spiral bevel and hypoid gears and included tooth compliance by precomputing the tooth stiffness along the surface normal with a 3D FE model of a single tooth. Weighting functions were used to translate the tooth compliance values, computed on the FE nodes, to the contact points [46].

FAN and WILCOX presented a methodology for loaded TCA where the loaded contact is assumed to take place along the conjugate line of tooth contact. The concept of a combined flexibility matrix is used to model the compliance of the gear, the pinion and the housing. Load sharing is included through the use of FEA-based meshing models with multiple teeth [37].

HEMMELMANN also developed an FE-based LTCA model for spiral bevel and hypoid gears where he computed tooth compliance from a three-dimensional FE model that included multiple teeth [50]. He used the spring model by NEUPERT [89], to include the coupling effects between teeth.

KOLIVAND and KAHRAMAN used a semi-analytical approach, developed by VAIDYANATHAN et al. [123], to model the tooth stiffness by using a Rayleigh-Ritz based shell model with linearly varying tooth thickness along the toe, heel and top [63].

ANDERSSON and VEDMAR developed a FEM-based methodology to compute the load distribution between two rotating helical gears [5, 124]. They proposed to divide the *total deformation* field of the gear tooth into a *global deformation* and a *local deformation* component. In accordance with the principle of Saint-Venant[2] they reasoned that outside of the contact zone the gear's deformation field could be approximated well by a linear FEA model. In a preprocessing phase, the global deformation field was computed as a superposition of two load cases. During the first load case a unit force is applied to each of the contact nodes, which results in a deformation field that is globally correct but incorrectly represents the tooth's deflection inside the contact zone. To eliminate this locally incorrect solution, a second load case is computed under different essential boundary conditions on displacements, which allow to isolate the locally incorrect displacement field. Finally, the total deformation of the gear is correctly described by adding a local contact deformation, which is nonlinearly dependent on the magnitude fo the contact load. By locally approximating the contacting tooth surfaces as cylinders in contact and by using the closed-form expression that was derived by WEBER and BANASCHEK [135], they were able to well-approximate the local contact deformation under the assumption of a Hertzian contact pressure distribution.

---

[2]Principle of Saint-Venant: The difference between the strain-stress fields, generated by two different but statically equivalent loads, becomes very small at a sufficiently large distance from the load application zone.

In order to eliminate the need for highly refined FE-meshes of the contacting surfaces, VIJAYAKAR introduced a similar approach to separate the deformation field of flexible gears. By combining the FE deformation field of the bodies with a surface integral form of the Boussinesq half space solution for the contact zone, he developed a hybrid approach that allows for precise LTCA simulations [126]. Although the developed program is considered to be a reference for LTCA of cylindrical, bevel and hypoid gears, the use of large FE models and a computationally expensive FE-based contact detection method, limits its applicability to efficient system-level simulations.

Using the methodology of [5] to model the gear pair compliance, FERNANDEZ DEL RINCON described an advanced model to simulate the quasi-static behavior of spur gear transmissions [38]. By exploiting the concept of line of action for cylindrical involute gear teeth, he developed a penetration-based contact algorithm. The *compatibility* condition was then imposed to translate the measured penetration into contact loads under the assumption that the flank penetration matches the deformation of the flexible gear teeth. Finally, by guaranteeing that the *complementary* condition was satisfied, he limited the active contact locations to those on which compressive contact forces acted.

Recently the methodology by ANDERSSON and VEDMAR was also successfully adopted by other researchers for the simulation of cylindrical gear pair [22, 120] and bearing [39] dynamics.

2.2.3   FE-based contact formulations, applied to TCA

When it comes to the contact analysis of spiral bevel and hypoid gears, the application of FEA has become a widely used technique. The reason for its success can be found in the main idea of the FEM. By dividing the complete domain into a set of simple subdomains (finite elements) and then applying an approximate solution to the problem on an element level, the FEM lends itself very well to the structural analysis of complex geometries, such as spiral bevel and hypoid gears. Within the design process of gear drives, FEA offers an extension to TCA by allowing a detailed investigation into the load transfer between the contacting gear teeth, as well as the determination of areas where severe contact and bending stresses occur during the mesh cycle [41].

In this work FEA-based contact simulations are mainly performed to validate the modeling techniques that are developed. For this purpose a commercially available software package is used (See Chapters 5 and 6). The goal of this subsection is to provide a concise overview of the methods that are used to detect contact and establish the contact conditions.

Methodology

In FEA the contact between two surfaces is usually treated as a kinematic nonlinearity or a boundary nonlinearity, since the displacement boundary conditions are determined by the structure's deformation [59]. To avoid that two colliding bodies penetrate each other, the contact constraints need to be enforced along the contact boundary. However, while it is expected that the displacements along the contact boundary remain small, it is usually not known in advance which part of the boundary will be in contact. Therefore, before the contact constraints can be enforced, a contact search is required to identify the location of potential contact points on both surfaces in contact.

Contact detection   Earlier presented techniques to determine contact locations, such as continuous tangency or ease-off based methods, have found little to no application in FEA because they either require a continuous description of the contacting surfaces or because they are so specific that they can only be applied to near-conjugate surfaces. Considering that NL-FEA methods are not only used to analyze gear-related contact problems, they require a contact detection strategy that is applicable to surfaces of arbitrary shape.

One of the most widely used techniques that is applied to large deformation 3D contact problems of discretized bodies, is the *node-to-surface* (NTS) algorithm. To determine potential contact locations this method makes use of a *gap-function* that expresses the perpendicular distance between the FE-nodes of a chosen slave surface $\mathcal{S}^{(S)}$ and the FE-surfaces (elements) of the opposing master surface $\mathcal{S}^{(M)}$. For each of the node-element combinations, the shortest distance (or gap) between the slave node $P^{(S)}$ with coordinates $\boldsymbol{r}^{(S)}$ and a to-be-computed point $P^{(M)}$ on the master surface with coordinates $\boldsymbol{r}^{(M)}(\xi^{(cont)}, \eta^{(cont)})$ has to be found to determine whether the surfaces are locally penetrating (See Fig. 2.7). The location of this point $P^{(M)}$ is found by minimizing the distance function $\left\| \boldsymbol{r}^{(S)} - \boldsymbol{r}^{(M)}(\xi, \eta) \right\|$, which corresponds to solving the following system of nonlinear equations in terms of quadrilateral surface coordinates ξ and η:

$$\begin{cases} \dfrac{\partial \boldsymbol{r}^{(M)}(\xi, \eta)}{\partial \xi} \cdot \left(\boldsymbol{r}^{(S)} - \boldsymbol{r}^{(M)}(\xi, \eta) \right) = 0 \\ \dfrac{\partial \boldsymbol{r}^{(M)}(\xi, \eta)}{\partial \eta} \cdot \left(\boldsymbol{r}^{(S)} - \boldsymbol{r}^{(M)}(\xi, \eta) \right) = 0 \end{cases} \tag{2.16}$$

The coordinates of the point $\boldsymbol{r}^{(M)}(\xi, \eta)$ in Eq. (2.16) are defined by the coordinates $\boldsymbol{r}_l^{(M)}$ of the corner points $P_l^{(M)}$ and the corresponding shape functions N_j^e. Assuming that the contacting bodies have been discretized with 8-noded hexahedron finite elements of which each face is defined by a
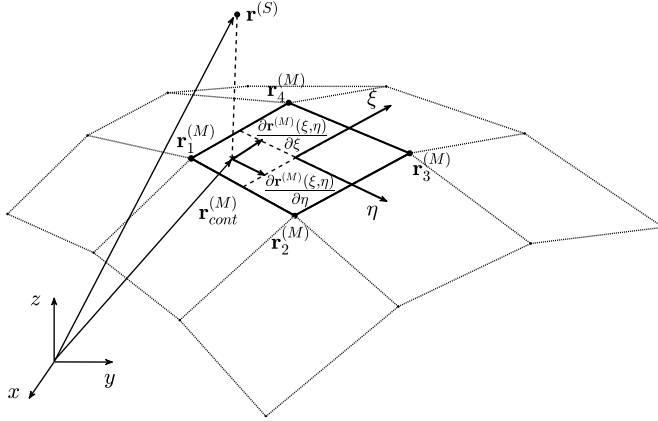
Figure 2.7: Contact detection using the node-to-surface algorithm.

4-noded quadrilateral surface, as shown in Fig. 2.7, any point $\boldsymbol{r}^{(M)}(\xi, \eta)$ on the quadrilateral master element is described by Eq. (2.17) for which the shape functions can be found in Appendix D.

$$\boldsymbol{r}^{(M)}(\xi, \eta) = \sum_{l=1}^{4} N_l^e(\xi, \eta) \, \boldsymbol{r}_l^{(M)} \tag{2.17}$$

Finally, with the quadrilateral parameters $(\xi^{(cont)}, \eta^{(cont)})$ of the perpendicular projection determined, the gap value g_N is computed as:

$$g_N = \boldsymbol{N}^{(M)} \cdot \left(\boldsymbol{r}^{(S)} - \boldsymbol{r}^{(M)}(\xi^{(cont)}, \eta^{(cont)}) \right) \tag{2.18}$$

where the $\boldsymbol{N}^{(M)}$ is the normal vector of the master surface, evaluated at the contact point, that points outwards of the material. According to this definition, contact will not be detected when $g_N \geq 0$.

Using the master-slave concept, the contact constraints are imposed in such a way that the slave surface cannot penetrate the master surface. However, since such a requirement is not imposed on the master surface, it is still possible that both surfaces penetrate. To reduce this type of numerical error, it is recommended to select the master and slave surfaces in such a way that the overall penetration is minimized. Practically speaking, this means of two contacting surfaces, the surface with either the highest curvature, the finest mesh size or the highest compliance, should be best chosen as the slave surface and the opposing surface as the master surface. Consequently, when FEA-based contact analysis is considered for a spiral bevel gear pair, it is recommended to select the tooth surfaces of the pinion and the gear as the slave and master surfaces, respectively.

Contact constraints   For elastic systems, contact can be considered as a constraint optimization problem where a displacement field has to be found that minimizes the potential energy while satisfying the contact constraints [59]. In case of frictionless contact, the HERTZ-SIGNORINI-MOREAU conditions for the contact force f_N and gap g_N, given by Eq. (2.19), can be used to prevent the bodies from penetrating each other along the normal direction [138].

$$f_N \geq 0, \qquad g_N \geq 0, \qquad f_N g_N = 0 \qquad (2.19)$$

In FEA the constrained optimization problem is usually converted into an unconstrained one for which one of the following techniques can be used: the *penalty* method, the *Lagrange* method or the *augmented Lagrange* method, which is a combination of the two former methods. In the penalty method the potential energy is penalized proportionally to the magnitude of constraint violation that is allowed [59, 71]. The effect of the penalty factor ϵ_P can best be compared by adding a one-directional spring with stiffness ϵ_P between the contacting surfaces, such that $|f_N| = |\epsilon_P g_N|$ when $g_N < 0$. As a result, the contact constraints are only satisfied approximately and an amount of penetration between the contacting surfaces is allowed. Choosing the optimal value for the penalty factor ϵ_P comes down to making a trade-off between allowing a magnitude of nonphysical penetration and creating an ill-conditioned problem ($\epsilon_P \rightarrow \infty$).

In contrast, the Lagrange method supplements the potential energy by a product of the contact constraint and an unknown Lagrange multiplier λ, such that the impenetrability requirement is exactly satisfied. In this case the Lagrange multiplier λ correspond to the value of the contact force f_N [71]. Depending on the level of interest, the reader is referred to the textbooks by KIM [59], WRIGGERS [138] or LAURSEN [71] for a more detailed discussion.

To conclude, the *constraint function* method [11, 12] is briefly discussed. To improve the computational efficiency, the constraint function method replaces the inequality constraints of Eq. (2.19) by a constraint function $w(g_N, \lambda) = 0$ that provides a continuous and differentiable relation between the gap g_N and contact force λ. For the normal contact condition such a function is given by:

$$w(g_N, \lambda) = \frac{g_N + \lambda}{2} - \sqrt{\left(\frac{g_N + \lambda}{2}\right) + \epsilon_N} \qquad (2.20)$$

where ϵ_N is a small user-defined parameter ($\epsilon_N \ll 1$) [11, 107]. Compared to the ideal contact constraints of Eq. (2.19), the constraint function relaxes the constraints as a function of ϵ_N (See Fig. 2.8). The constraint of Eq. (2.20) can be imposed through either the above mentioned penalty or Lagrange multiplier method [12]. In this work, NX Nastran's implicit nonlinear solution (SOL 601) [107], which makes use of the ADINA solver [106] to solve the contact problem, is used for validation purposes. The ADINA solver has the constraint function method implemented through the use of Lagrange multipliers [12].

(a) Ideal contact constraints.

(b) Constraint function.
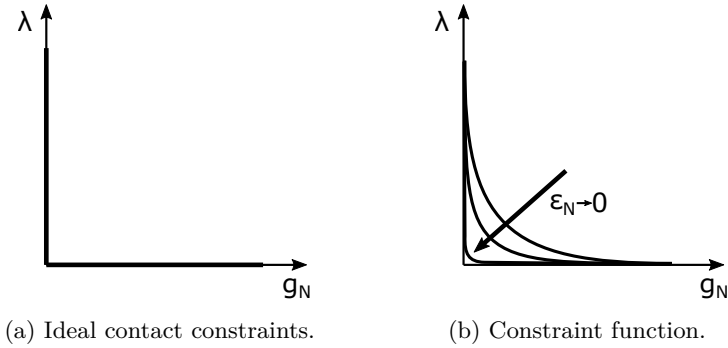
Figure 2.8: Comparison between ideal contact constraints of Eq. (2.19) and the constraint-function method of Eq. (2.20).

2.3 Multibody contact models for spiral bevel gears

The field of mechanics that studies the dynamic behavior of mechanical systems is called multibody system dynamics (MBSD) [48]. A multibody system can here be considered as a collection of components (e.g. shafts, gears, ...) that undergo large translational or rotational motion, while being held together by a number of kinematic constraints and having forces (e.g. a contact force) acting between them. While in theory the components (or bodies) can be either rigid or deformable, all the models that are mentioned here consider the bodies as rigid. This implies that the deformation of each body is assumed to be small such that the body deformation does not affect the overall body motion. The motion of each body in space can thus be completely described by six generalized coordinates [105]. The *equations of motion* for a dynamic system of rigid bodies can be derived using Hamilton's principle [105], leading to:

$$\begin{cases} \mathbf{M}(\boldsymbol{q})\ddot{\boldsymbol{q}} + \mathbf{G}_{\boldsymbol{q}}^T(\boldsymbol{q})\boldsymbol{\lambda} & = \boldsymbol{Q}(\boldsymbol{q},\dot{\boldsymbol{q}},t) \\ \boldsymbol{G}(\boldsymbol{q}) & = 0 \end{cases} \tag{2.21}$$

where $\mathbf{M}$ is the mass matrix, $\boldsymbol{G}(\boldsymbol{q})$ the vector of applied holonomic kinematic constraints, $\mathbf{G}_{\boldsymbol{q}}$ is the constraint Jacobian matrix and $\boldsymbol{\lambda}$ is the vector of Lagrange multipliers. The vectors $\boldsymbol{q}$, $\dot{\boldsymbol{q}}$ and $\ddot{\boldsymbol{q}}$ represent the system's generalized coordinates, generalized velocities and generalized accelerations, respectively. The generalized forces $\boldsymbol{Q} = \boldsymbol{Q}_v + \boldsymbol{Q}_e + \boldsymbol{Q}_{cont}$ that act on the system are subdivided into: $\boldsymbol{F}_v$ for the generalized quadratic velocity forces (gyroscopic and Coriolis components), $\boldsymbol{Q}_e$ for the generalized externally applied forces and $\boldsymbol{Q}_{cont}$ for the generalized contact forces. An in-depth treatment of the equations of motion of an MB-system, is found in the works of HAUG [48] or SHABANA [105].
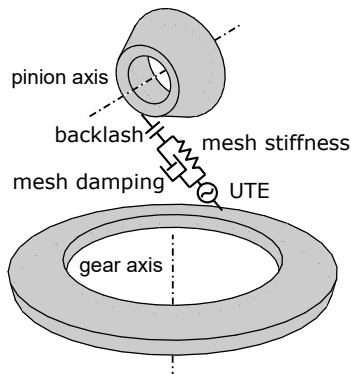
Figure 2.9: An example of a spiral bevel gear mesh model for dynamic analysis.

Methodology

Of all the generalized forces that act on the system, only the gear mesh contact forces that contribute to the generalized contact force $\boldsymbol{Q}_{cont}$ are considered in this discussion. Compared to parallel axis gears, the dynamic analysis of spiral bevel and hypoid gears is significantly more challenging due to the tooth geometry and the resulting unique time- and spatial-varying mesh characteristics.

For this reason, general purpose multibody codes often still include a tessellation-based contact detection method, comparable to the NTS method for FEA, and Hertzian-based contact models to simulate spiral bevel and hypoid gears [86].

Alternatively, dynamic mesh models that are described in the literature have adopted a simplified mesh model, similar to the one of Fig. 2.9. These models also rarely define the problem as a set of differential-algebraic equations (DAE), given by (2.21), but rather eliminate the constraints to obtain a system of ordinary differential equations (ODE) in terms of the system's DOFs. Similar to some models for parallel axis gears [92, 125], the simplified dynamic mesh force for spiral bevel and hypoid gears is modeled through the use of a spring-damper system that shows a nonlinear behavior when backlash is considered [24, 25, 95, 133]. By making use of LTCA programs that correctly include the gear tooth geometry, time- (i.e. mesh cycle) and spatially-varying mesh data, such as the mesh point, direction of the surface of action (here simplified to a line), mesh stiffness and mesh damping values, are precomputed and stored in so-called look-up tables that are accessed during the dynamic simulation. However, the approximation of a spring-damper model inevitably reduces the gear meshing process from a complex spatially distributed contact problem to a single point, that is obtained by averaging the precomputed LTCA results.

Challenges

Besides studies into the dynamic transmission error (DTE) of spiral bevel and hypoid gears in dry-contact conditions [57, 95, 133], the above-mentioned lumped parameter models also prove fruitful in the development of elastohydrodynamic lubrication (EHL) models for lubricated hypoid gears [58, 85], and in the investigation of system influences (e.g. bearing compliance and preload) on the transmission's DTE, vibration spectra and efficiency [83]. In addition, UDF routines, which are commonly available in general-purpose multibody simulation software packages, allow for the integration of look-up table based contact models for spiral-bevel and hypoid gears [84, 100].

Besides reducing the spatial meshing process to a single time- and spatially-varying mesh point, the TCA-based contact model is not without its drawbacks. For instance, while the effects of the gear tooth geometry are correctly captured by using LTCA results, the behavior of the gear pair under load is always the result of two components: the EO topography (unloaded) and the tooth deformation (loaded). Therefore, at least two TCA simulations are required: an unloaded analysis to identify the UTE and one loaded analysis to isolate the mesh stiffness based on LTE and UTE [95]. Moreover, while the equivalent spring-damper model for the mesh force is capable of introducing gear pair misalignments due to system compliance, the lack of an actual 3D contact detection makes that the model can only correctly approximate those misaligned conditions that were precomputed and stored in the look-up tables.

For this reason some researchers have proposed a co-simulation approach to the dynamic simulation of spiral bevel gears [132], where two simulation tools (i.e. a multibody solver and a LTCA program) work together to solve the problem. At each iteration/time-step, the multibody solver communicates the position and orientation of the gear pair to the LTCA program that simulates the 3D tooth meshing. The LTCA program in its turn provides the multibody solver with the resulting contact forces, which are applied to the MB model to solve the equations of motion. However, the feasibility of co-simulation, heavily depends on the numerical efficiency of the TCA program, since numerous calls by the multibody solver are required. In addition, the extra time that is needed for the different programs to communicate with each other becomes another bottleneck.

All things considered, it is recognized in [95] that the development of a three-dimensional mesh model to simulate the meshing process with an acceptable level of accuracy and simulation time, remains one of the major challenges for the dynamic analysis of spiral bevel gears.

2.4   Proposed modeling strategy

While the introduction of this dissertation identified a clear need for accurate and numerically efficient modeling methods for spiral bevel gears to allow both dynamic and system-level analysis, an overview of the current state of the art has shown a noticeable gap in terms of modeling fidelity between the methodologies that are used for tooth contact analysis and dynamic analysis. To help bridge the gap between both modeling methodologies, this work proposes a modeling strategy (see Fig. 2.10) that enables the development of a accurate and numerically efficient gear contact model, applicable to multibody simulations

Similar to TCA methods, the proposed modeling strategy also places an emphasis on the accurate description of the tooth surfaces to correctly describe the effects of flank form modifications. To this end the methodology creates a virtual model of the tooth geometry by either simulating the manufacturing process or by importing a predefined geometry (Chapter 3). The latter aspect, however, is not directly illustrated in the dissertation.

Of all the discussed methods for contact detection, the methodology proposed by KOLIVAND [63], shows to be the most computationally efficient and most suited for adaption to a multibody framework. Therefore, the theory of conjugate surfaces is used to analyze the gear pair kinematics and to determine the surface of roll angles of the gear teeth (Chapter 4). In addition to computing the required data for the contact model, these efforts lead to the creation of a tool for the unloaded tooth contact analysis of (spiral bevel) gear pairs.

Adopting a multibody approach to LTCA, the surfaces of roll angles of the gear teeth are used to develop an efficient and accurate algorithm for contact detection over multiple tooth pairs (Chapter 5). As the surface of roll angles defines the surface of action - a generalization of the line of action for cylindrical gears - the contact between teeth flanks is established based on penetration, similar to the model that was proposed by FERNANDEZ DEL RINCON [38]. To translate the measured penetration into distributed contact loads, an uncoupled analytical tooth stiffness model is proposed as a first level of modeling fidelity. The effects of varying gear pair misalignments due to assumed system compliance are then included by interpolating a new surface of roll angles based on the misaligned state (Chapter 6).

In parallel, starting from the virtual model of the gear teeth, an automated process for the generation of detailed FE spiral bevel gear models is created (Chapter 3). Using this process, NL-FEA contact simulations are performed to validate the different aspects of the proposed methodology (Chapters 5 and 6).

With one of the research objectives being modular architecture, the proposed modeling strategy is defined to allow a level of scalability. Drawing another analogy to the model by FERNANDEZ DEL RINCON, the proposed contact model can be extended with FEA-based gear stiffness models, similar to the one by ANDERSSON and VEDMAR. Such improvements, together with the implementation of the proposed model within a multibody (system) dynamics simulation code, are considered future work (Chapter 7).
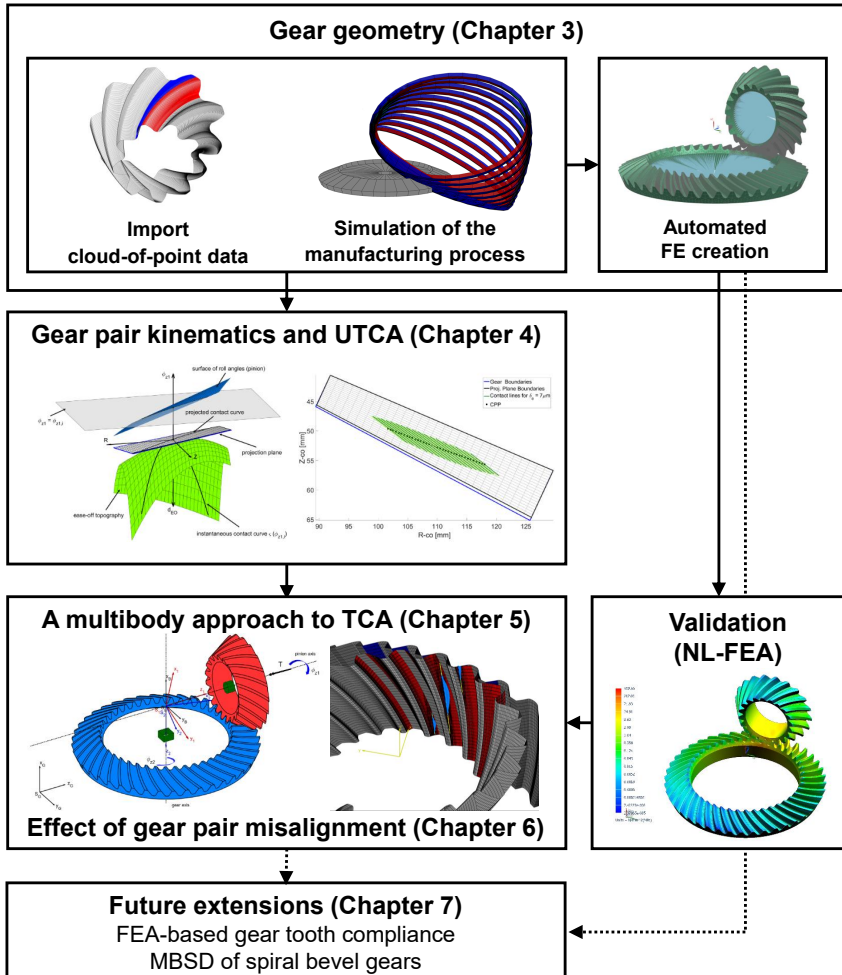
Figure 2.10: Overview of the proposed modeling strategy.

Chapter 3

Spiral bevel gear geometry

Most of the fundamental principles for today's spiral bevel gear design and manufacturing were established during the first part of the previous century in notable works by BUCKINGHAM [19], WILDHABER [137] and BAXTER [14], to name only a few. Yet, present-day research [8, 35, 41, 77, 115] still focuses intensively on the identification of the optimal machine settings and cutter parameters, since significant improvements in contact performance can be achieved by local modifications to the gear tooth flank geometry. For this reason an accurate contact modeling methodology cannot but include a detailed description of the contacting surfaces.

An overview of the geometrical aspects of the modeling strategy is provided in this chapter. The basics to spiral bevel gear geometry are presented in Section 3.1. These concepts are meant to provide a limited but necessary background to understand the remainder of the dissertation. Section 3.2 focuses on the mathematical procedures that are used to construct the tooth flank geometry. Common to most types of spatial gears, is a geometrical complexity of the tooth flank surfaces that cannot be described by a closed-form expression but has to be obtained through simulation of the manufacturing process. In addition, the resulting tooth flank geometry will also depend on the applied manufacturing process and shape of the cutter blades. Through simulation of the manufacturing process a discrete model of the tooth flank geometry is created that will serve as input for the contact detection methods, developed in Chapters 4 and 5. Starting from a discretized surface, a general procedure to determine the local surface curvature in terms of principal curvature and directions is described in Section 3.3. Finally, an automated procedure for the creation of FEM-based spiral bevel gear models is described in Section 3.4.

(a) Tooth numbers and spiral handedness.   (b) Tooth flank convention.
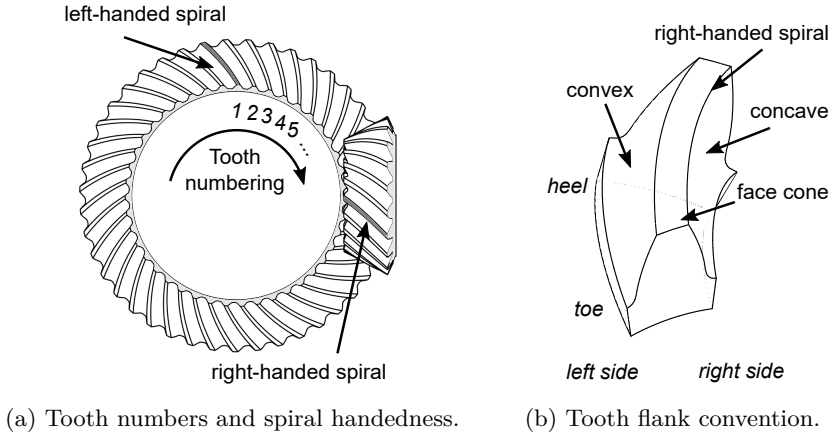
Figure 3.1: Convention for tooth numbers, hand of spiral and gear flanks.

3.1 Basic concepts of spiral bevel gear geometry

The conical shape of spiral bevel gears is explained by the shape of their axodes, which are generated by the loci of the instantaneous rotational axis with respect to each of the rotational axes. When motion is transferred between intersecting rotational axes, these axodes will take on a conical shape. Correspondingly, the design of a bevel gear set is based on a set of characteristic cones that help in defining the gear tooth geometry (see Fig. 3.2). For example, the *face* and *root cones* are used to indicate the boundaries of the gear teeth, while the *pitch cone* can be used as a reference point when designing the tooth geometry. In the case of intersecting rotational axes, the pitch cones and the axodes coincide. When discussing the axodes of a gear pair, a comment to hypoid gears can also be made. Since hypoid gears transfer motion between crossed rotational axes, their axodes are hyperboloids of revolution. Yet, the concept of axodes has found limited use in the design of hypoid gear [31, 76]. In practice the hyperboloids of revolution are approximated as cones, leading to the concept of operating pitch cones and a simplified conical shape for hypoid gear elements. As such, some textbooks on gear geometry classify hypoid gears as a special case of spiral bevel gears [62], while others make a distinction [31, 76]. In this dissertation only spiral bevel gears with intersecting axes will be analyzed, although the developed techniques are also applicable to gears with crossing rotational axes.

The face cone can be used as a reference to establish a convention for the tooth numbers and the direction of the tooth spiral, as illustrated in Fig. 3.1. The teeth of a (spiral) bevel gear are numbered from 1 to Z in ascending order by observing the face cone of the gear and moving in a clockwise direction along
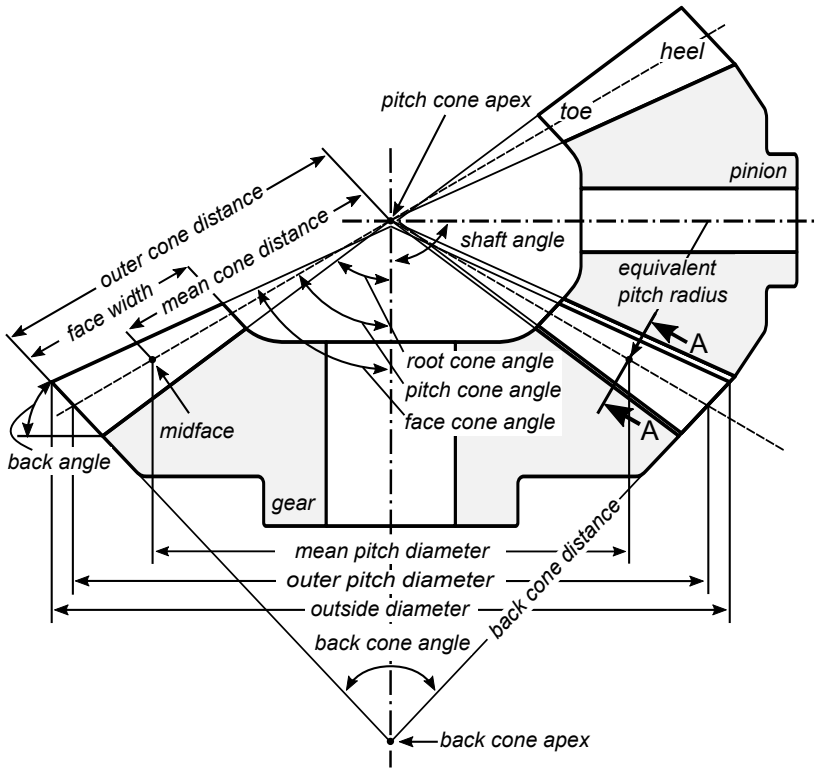
(a) Axial cross-section view.
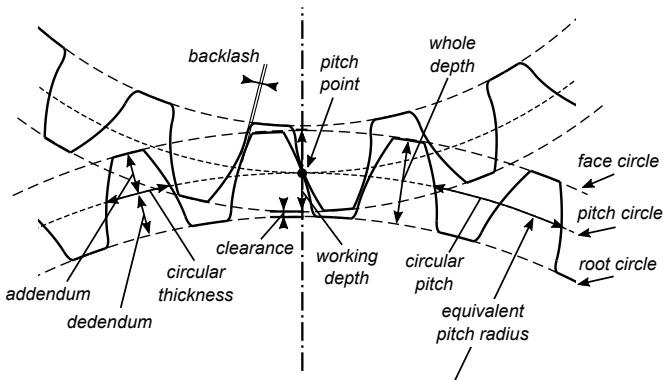
(b) Mean transverse cross-section view (Section view A-A in Fig. 3.2a).

Figure 3.2: Cross-sectional views for a spiral bevel gear pair.

the cone's circumference. A spiral bevel gear is said to be *right-handed* when the outer half of the tooth is inclined in a clockwise direction when viewed by an observer that looks onto the face cone of the gear. Similarly, for a *left-handed* spiral bevel gear the outer half of the tooth is inclined in counter-clockwise direction when viewed from the same position [2, 52]. For a right-handed spiral bevel gear the left tooth flank is the convex flank, while the right flank is the concave flank, as shown in Fig. 3.1b. The opposite is true for a left-handed spiral bevel gear. Meshing between the gear flanks is only feasible if a contacting flank pair contains a convex and a concave flank side. As such a spiral bevel gear pair always contains a pinion and a gear that is opposite in spiral hand.

The remaining parameters that determine the gear geometry are defined through the use of three cross-sections. The axial section is created by sectioning the gear pair by a plane that is spun by a projection of the gear pair's rotational axes (see Fig. 3.2a). It is in this section that most of the gear blank's dimensions are defined. Two additional sectional views, the normal and transverse sections, are defined perpendicular to the tooth surface and the pitch cone, respectively. Both sections are predominantly used to dimension the gear teeth. The presence of the spiral angle and the conical shape of the gear blank cause the shape and size of gear teeth to vary from the inside (toe) to the outside (heel) of the tooth. When designing the gear blank, approximate calculations that regard the size of the gear teeth are therefore made at the midface of the gear. The dimensions of the gear teeth are computed in the mean transverse plane under the assumption that the bevel gear geometry can be approximated in the transverse plane by an equivalent spur gear (see Fig. 3.2b) These calculations have been described in the international standards by the AGMA [2] or the ISO [52]. It should also be noted that, while the calculations are made in the mean transverse plane, the literature often reports the geometrical parameters of Fig. 3.2b in the outer transverse plane, where they are easier to measure.

Unlike cylindrical gears, the shape of spiral bevel gear teeth is not standardized but depends completely on the manufacturing process that is used to cut the gear pair. Not only do the manufacturing parameters, such as the machine settings and cutter blade geometry, dictate the tooth's shape in the transverse plane, but also the curvature of the tooth spiral is determined by the kinematics of the machining process. The two most common methods to manufacture spiral bevel gears on an industrial scale are discussed in the next section.

3.2   Face-cut spiral bevel gears

Intensive research in the field of design and manufacturing of bevel gears has resulted in not less than twelve different cutting methods, which are currently available for the manufacturing of spiral bevel gears [62]. The majority of these methods can be attributed to THE GLEASON WORKS or THE KLINGELNBERG GROUP, which played a pivotal role in the development of spiral bevel gear generators, capable of mass-production [75]. Metal cutting processes for spiral bevel gear production are commonly grouped, based on how the gear blank indexes w.r.t. the cutter blades. In a *single indexing* process, the cutter head withdraws once a tooth slot is created, so that the blank can be rotated to cut the next tooth slot. Alternatively, *continuous indexing* processes, where both the gear blank and the cutter blades rotate according to predefined kinematic relations, were also developed. The first generation of spiral bevel gear generators made use of a so-called cradle system that, combined with the other machine settings, provided the required degrees of freedom to produce gears by either the single or continuous indexing method. An example of a cradle-based generator and its available machine settings are provided in Fig. 3.3. While current generation cutting machines have evolved into numerically controlled machines, their working principles and machine settings have remained equivalent to those of the cradle-based ones.
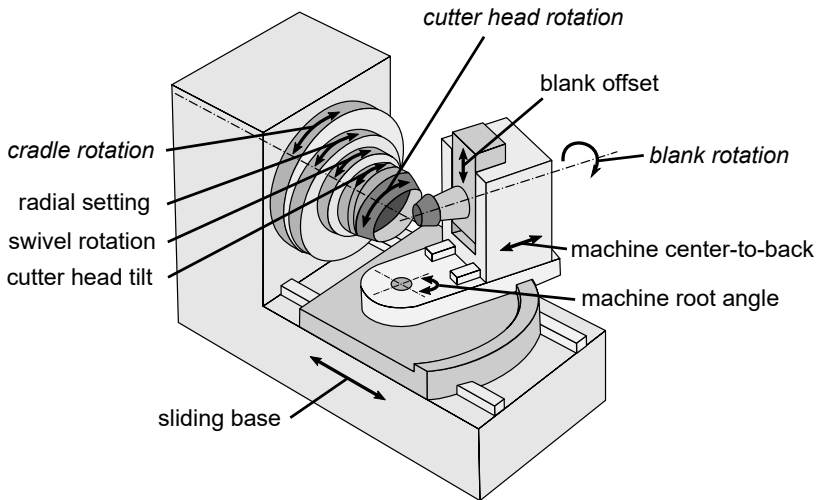
Figure 3.3: Cradle-based bevel gear generator.

3.2.1   Manufacturing processes: face-milling and face-hobbing

Although the design of the gear blank is described in standards, the final tooth geometry can vary significantly, depending on the cutting process that is adopted. The single indexing and continuous indexing processes, also referred to as *face-milling* (FM) and *face-hobbing* (FH) respectively, are two families of cutting methods that allow to produce spiral bevel gears on an industrial scale. For both the face-milling and face-hobbing processes, the rotation of the cradle (onto which the gear head cutter is mounted), will have an important influence on the resulting tooth geometry. When this additional rotation is included (see Fig. 3.4), the cradle is allowed to rotate according to a predefined *roll ratio* that kinematically determines the rotation of the cradle as a function of the gear blank. This *generating process* for face-milling or face-hobbing produces a tooth profile with an increased curvature due to the additional generating motion [62, 76]. Alternatively, in a *non-generating* cutting process the cradle is held at rest during operation and the teeth are created by a plunge cut process that leads to a shorter machining time. Since there is no generating motion between the cutter head and the work-piece, the ratio of roll is zero and the tooth profile is an exact reproduction of the cutter tool [62]. While the generating process can be used to produce both pinion and gear elements, the non-generating process is only applied to the manufacturing of gear wheels.

Varying the different machine settings directly affects the tooth's geometry in terms of the tooth profile, the tooth spiral trace or the tooth's height variation. As such different types of FM and FH processes have been developed and it is generally not possible to pair a pinion, created by one manufacturing process, with a gear that has been created by another process; not even if both of these cutting processes belong to the same family of methods (i.e. FM or FH). Given the number of available cutting methods, the dissertation limits itself to highlighting the main differences between the single and the continuous indexing method. The interested reader is referred to a textbook by KLINGELNBERG [62], which provides an extensive overview of the fundamentals spiral bevel gear design and manufacturing.

The face-milling process   In this group of manufacturing processes the gear teeth are created by cutting one tooth slot at a time, as shown in Fig. 3.4a. Once a tooth slot is cut, the cutter head retracts and the gear blank rotates by one angular pitch ($\tau = \frac{2\pi}{Z}$) so that the next tooth slot can be created (single-indexing). Two types of cutter blades are mounted onto the cutter head in altering fashion so that each set cuts one side of the tooth. The *inside blades* are used to cut the convex side of the tooth, while the *outside blades* create the concave side. Both blade groups are positioned along a circle, giving the
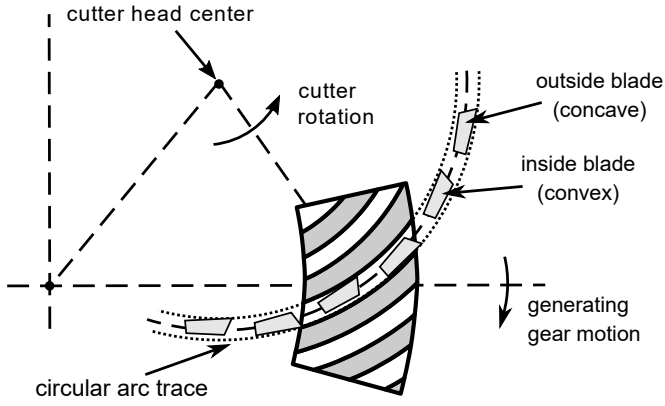
(a) Single indexing process (face-milling).
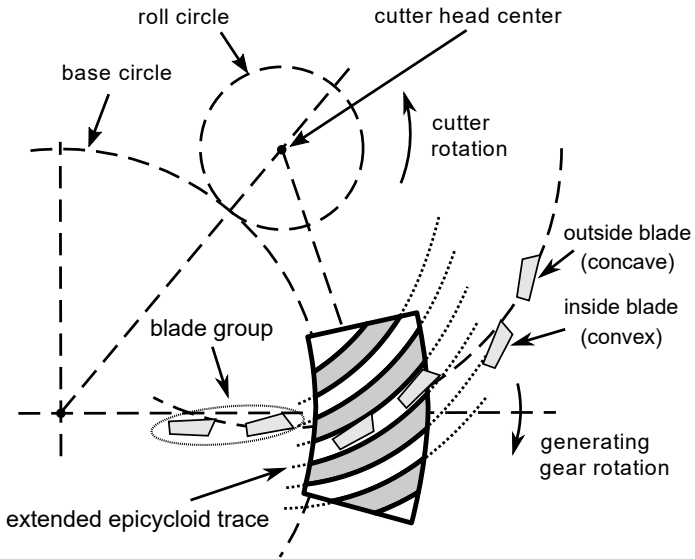
(b) Continuous indexing process (face-hobbing).

Figure 3.4: Face cutting methods: the single and continuous indexing process.

impression of a conical cup when rotated at high speed. While the circular installment of the tool's cutting edges leads to a tooth spiral that traces a circular arc, it also allows for an accurate installment of the blades and ensures that the inactive regions of the cutting edges will never make contact with the gear blank [62]. FM spiral bevel gears are most commonly found with tapered teeth along the face width (see Fig. 3.5a). The face-milling process is still used on a large scale within the aerospace industry.

The face-hobbing process By coupling the rotation of the cutter head and the gear blank, a group of manufacturing methods for spiral bevel gears was developed that allows to machine the gear teeth almost quasi-simultaneous. The required kinematic relation is defined by envisioning the cutter head to roll together with the gear blank such that at any time one blade group will pass through one tooth slot, as shown in Fig. 3.4b. By correctly positioning the blade groups onto the cutter head, they are able to simultaneously cut different parts of multiple tooth slots, resulting in a continuous indexing process [62]. Each blade group contains an inside and an outside blade, which again are used to cut the convex and concave side of the tooth slot, respectively. The rolling of the work-piece and the cutter head can be seen as the meshing between the to-be-created gear element and a virtual crown gear, created by various blade groups of the cutter head. The correct kinematic relation is obtained by defining the ratio of the number of gear teeth and the number of blade groups, which is equivalent to the ratio of the base circle radius and the roll circle radius [62]. When the cutting edges of the blade groups are positioned on a radius that is greater than the roll circle radius, the trace of the created tooth spiral will be that of an extended epicycloid. FH spiral bevel gears have a constant tooth height (see Fig. 3.5b). The face-hobbing process is mostly applied for the manufacturing of automotive gear sets.

(a) Variabled tooth height.   (b) Constant tooth height.
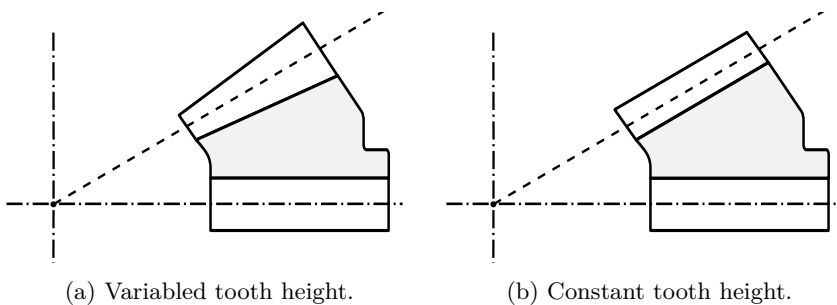
Figure 3.5: Bevel gears with variable (tapered) and constant tooth height.

3.2.2 A mathematical model for face-milled spiral bevel gears

Since it is this dissertation's main objective to develop a numerically efficient and accurate contact model for spiral bevel gears in multibody applications, a correct description of the contacting geometry can not be overlooked. However, while various manufacturing processes have been developed, not every methodology is accurately described in the literature. Because the *five-cut* method is a historically relevant face-milling process [62, 117], it is rather well described in the literature and has complete data sets published [6, 40, 76]. Therefore, this method is implemented in this work to create a reference model that can be used for intermediate verification of the developed techniques.

The five-cut method   This method derives its name from the five independent steps that are required to produce an FM spiral bevel gear pair. The gear wheel is created using only two cuts: a roughing and a finishing cut, since both tooth flanks can be cut simultaneously. The machining of the pinion involves the remaining three cuts: a roughing cut for both flanks, which is followed by a finishing cut for the convex flanks and another for the concave flanks. This allows flank form modifications to be defined independently for each flank by variation of the machine and tool settings. Lengthwise crowning is obtained by altering the cutter radii. Profile crowning can be achieved by modifying the machine kinematics, e.g. by the inclusion of *modified roll* to modify the ratio of roll during the generating process [62].

A computer model, which is used to compute tooth flank surfaces, should only simulate the finishing steps of the manufacturing process. Following the steps in Fig. 3.6, the creation of such a virtual model for gear and pinion can be achieved. By describing the motion of the cutting edges (Fig. 3.6a) w.r.t. the gear blank, a family of surfaces is obtained (Fig. 3.6b). The envelope to this family of surfaces defines the tooth geometry (Fig. 3.6c) and can be computed with the earlier-introduced equation of meshing (Eq. (2.14)).
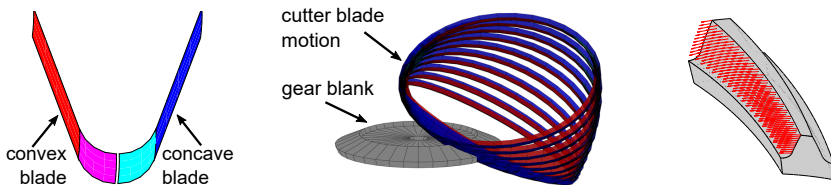
(a) Blade definition.   (b) Kinematics of cutting process.   (c) Gear tooth surface.

Figure 3.6: Steps for the simulation of the manufacturing process.
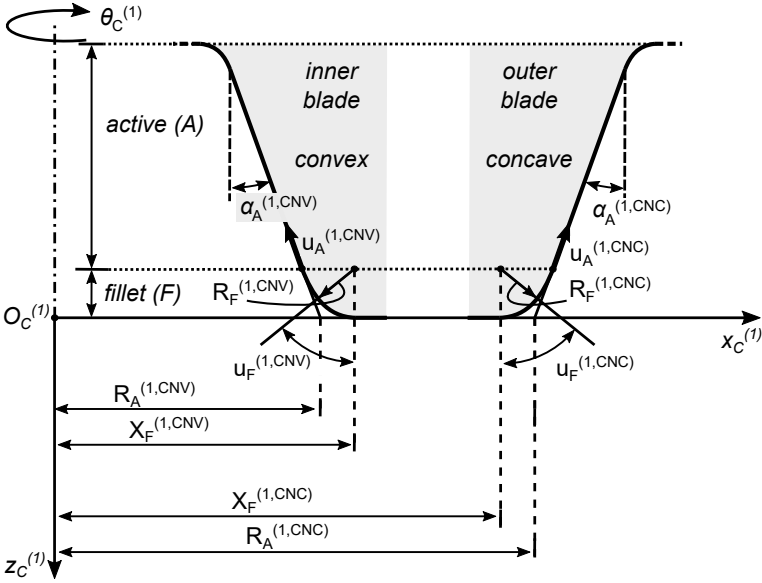
(a) Convex and concave blades of a straight-line head cutter for the pinion.
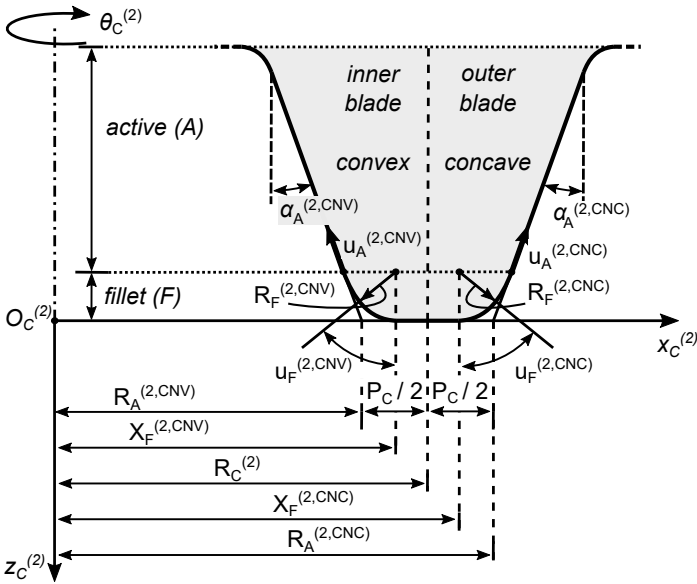
(b) Convex and concave blades of a straight-line head cutter for the gear.

Figure 3.7: Straight-line head cutter for the pinion and the gear.

Description of a straight-line cutter blade

The model for tooth flank generation makes use of a straight-line blade with circular arc to cut the active part and root fillet of the tooth, respectively. The geometrical parameters that define the blade edges, used to manufacture the pinion and the gear element, are given in Fig. 3.7. As shown in Fig. 3.7a and Fig. 3.7b, these parameters are almost identical for the pinion and gear blades. The differences that exist are introduced to allow the simulation of the two independent finishing cuts for the concave and convex pinion flanks.

The cross-sectional geometry of the blade edges is defined in the XZ-plane of the local reference frame S_C for the cutter head and then rotated by an angle θ_C about the cutter head's rotational axis (local z-axis). Due to the rotation, the straight-line or active part of the blade describes the conical surface $\mathcal{S}^{(A)}$, while the circular arc of fillet part of the blade describes the surface $\mathcal{S}^{(F)}$ that is part of a torus (see Fig. 3.6a). In practical applications, the rotational speed of the cutter head is high enough that it can be considered independent from the machine kinematics. As such the rotational speed of the cutter head can be chosen to allow for optimal machining conditions. However, the rotation angle of the cutter head θ_C still defines the point on the tooth flank that is created.

The equations that define the mathematical model for a straight-bladed face-milling process are presented in a condensed form. The parameters of the blades that cut the concave (CNC) flank and convex (CNV) flank of the tooth slot are indicated by the corresponding superscripts in Fig. 3.7. These superscripts have been omitted in the presented equations for clarity and compactness of notation. Where a double sign ($\pm$ or $\mp$) is used, the *upper sign* refers to the CNC blade, while the *lower sign* should be used to define the CNV blade. A detailed description of these equations can also be found in [76].

Active part of the cutter blade   Under normal operational conditions the gear pair is designed so that the active part of the pinion tooth flank ($g = 1$) contacts the active part of the gear tooth flank ($g = 2$). The active part of the tooth flank is generated by the straight blade edge of the cutter tool. When viewed in the XZ-plane of the local reference frame S_C (see Fig. 3.7), the position along the straight part of the blade is defined by $u_A^{(g)}$, while the *profile angle* $\alpha_A^{(g)}$ defines the inclination of the tool's edge. Due to the rotation of the cutter head, defined by the angle $\theta_C^{(g)}$ about its rotational axis, a conical surface $\mathcal{S}^{(A)}$ is described by the straight part of the blade. Eq. (3.1) is used to define the coordinates of any point on the surface $\mathcal{S}^{(A)}$ in the frame S_C as a function of the *surface parameters* $u_A^{(g)}$ and $\theta_C^{(g)}$.

$$\boldsymbol{r}_C^{(g,A)}(u_A^{(g)}, \theta_C^{(g)}) = \begin{bmatrix} \left[R_A^{(g)} \pm u_A^{(g)} \sin\left(\alpha_A^{(g)}\right) \right] \cos\left(\theta_C^{(g)}\right) \\ \left[R_A^{(g)} \pm u_A^{(g)} \sin\left(\alpha_A^{(g)}\right) \right] \sin\left(\theta_C^{(g)}\right) \\ -u_A^{(g)} \cos\left(\alpha_A^{(g)}\right) \end{bmatrix}, \quad (g = 1, 2) \quad (3.1)$$

The installment of the blades onto the cutter head is defined by the *cutter point radius* $R_A^{(g)}$. To allow for an independent motion of the cutter blades (i.e. for two finishing cuts), the blade edges of the pinion are specified by a separately defined cutter point radius $R_A^{(1)}$ for the CNC and CNV blade. Since the gear wheel is finished with a single cut, the cutter point radius $R_A^{(2)}$ for the CNC and CNV blades are linked by the *point width* $P_C^{(2)}$ of the cutter and (mean) radius $R_C^{(2)}$ of the cutter head, onto which the blades are installed. The cutter point radii for the gear cutters are therefore defined by:

$$R_A^{(2)} = R_C^{(2)} \pm \frac{P_C^{(2)}}{2} \tag{3.2}$$

Additionally, the unit normal $\boldsymbol{N}_C^{(g,A)}$ to the generating surface $\mathcal{S}^{(A)}$ for the pinion ($g = 1$) or gear ($g = 2$) at the corresponding point $\boldsymbol{r}_C^{(g,A)}$ is obtained from:

$$\boldsymbol{N}_C^{(g,A)} = \frac{\dfrac{\partial \boldsymbol{r}_C^{(g,A)}}{\partial u_A^{(g)}} \times \dfrac{\partial \boldsymbol{r}_C^{(g,A)}}{\partial \theta_C^{(g)}}}{\left\| \dfrac{\partial \boldsymbol{r}_C^{(g,A)}}{\partial u_A^{(g)}} \times \dfrac{\partial \boldsymbol{r}_C^{(g,A)}}{\partial \theta_C^{(g)}} \right\|} = \begin{bmatrix} \cos\left(\alpha_A^{(g)}\right) \cos\left(\theta_C^{(g)}\right) \\ \cos\left(\alpha_A^{(g)}\right) \sin\left(\theta_C^{(g)}\right) \\ \pm \sin\left(\alpha_A^{(g)}\right) \end{bmatrix}, \quad (g = 1, 2) \quad (3.3)$$

Fillet part of the cutter blade   The root of the gear tooth connects the active part of the tooth to the root cone of the gear blank and is created by the second part of the cutter blade. In the XZ-plane of the local reference frame S_C (see Fig. 3.7), the rounding of the cutter, which is used to create the root fillet, is described as part of a circle with radius R_F, the *cutter point radius*. Due to the rotation of the cutter head, this blade segment describes a toroidal surface $\mathcal{S}^{(F)}$, when viewed in the local reference frame S_C. A possible parametrization for the coordinates of a point on the surface $\mathcal{S}^{(F)}$ is given by Eq. (3.4), in which $u_F^{(g)}$ and $\theta_C^{(g)}$ are the *surface parameters*. The *cutter point angle* $u_F^{(g)}$ defines an acute angle within the interval $0 \leq u_F^{(g)} \leq \frac{\pi}{2} - \alpha_A^{(g)}$ to allow a continuous connection with the straight part of the blade. The *center of the cutter point* $X_F^{(g)}$ defines the center of the blade's circular arc and is computed by Eq. (3.5).

$$\boldsymbol{r}_C^{(g,F)}\left(u_F^{(g)}, \theta_C^{(g)}\right) = \begin{bmatrix} \left[X_F^{(g)} \pm R_F \sin\left(u_F^{(g)}\right)\right] \cos\left(\theta_C^{(g)}\right) \\ \left[X_F^{(g)} \pm R_F \sin\left(u_F^{(g)}\right)\right] \sin\left(\theta_C^{(g)}\right) \\ -R_F \left[1 - \cos\left(u_F^{(g)}\right)\right] \end{bmatrix}, \quad (g = 1, 2) \quad (3.4)$$

$$X_F^{(g)} = R_A^{(g} \mp R_F \frac{1 - \sin\left(\alpha_A^{(g)}\right)}{\cos\left(\alpha_A^{(g)}\right)}, \quad\quad\quad (g = 1, 2) \quad (3.5)$$

The unit normal $\boldsymbol{N}_C^{(g,F)}$ to the generating surface $\mathcal{S}^{(F)}$ for the pinion $(g = 1)$ or gear $(g = 2)$ at the corresponding point $\boldsymbol{r}_C^{(g,F)}$ is defined by:

$$\boldsymbol{N}_C^{(g,F)} = \frac{\frac{\partial \boldsymbol{r}_C^{(g,F)}}{\partial u_F^{(g)}} \times \frac{\partial \boldsymbol{r}_C^{(g,F)}}{\partial \theta_C^{(g)}}}{\left\| \frac{\partial \boldsymbol{r}_C^{(g,F)}}{\partial u_F^{(g)}} \times \frac{\partial \boldsymbol{r}_C^{(g,F)}}{\partial \theta_C^{(g)}} \right\|} = \begin{bmatrix} \sin\left(u_F^{(g)}\right) \cos\left(\theta_C^{(g)}\right) \\ \sin\left(u_F^{(g)}\right) \sin\left(\theta_C^{(g)}\right) \\ \pm \cos\left(u_F^{(g)}\right) \end{bmatrix}, \quad (g = 1, 2) \quad (3.6)$$

Machine kinematics of the generating process

While the previous section focused on a description of the different edges of the cutter blade, this section focuses on a parametrization of the machine kinematics that are used for the finishing motion. The presented model includes the motions of a cradle-based spiral bevel gear generator to simulate the five-cut manufacturing process of generated spiral bevel gear pairs. The same machine settings that are displayed in Fig. 3.3 are present in the model, with the exception of *cutter head tilt* and *swivel rotation*. The swivel and tilt rotational settings allow other - mostly FH - manufacturing methods to introduce lengthwise crowning, whereas the five-cut FM process is able to achieve lengthwise crowning through variation of the cutter head radius [62].

To describe the machining process, the motion of the head cutter is expressed w.r.t. the gear blank as a series of elementary rotations or translations, for which the transformation matrix method is used [76]. An overview of the required reference frames and elementary transformations is provided in this section, while the corresponding transformation matrices can be found in Appendix B. With the machining motion established, the correct kinematic relations for a generating FM process are then imposed by defining the (modified) ratio of roll between the head cutter and the gear blank.
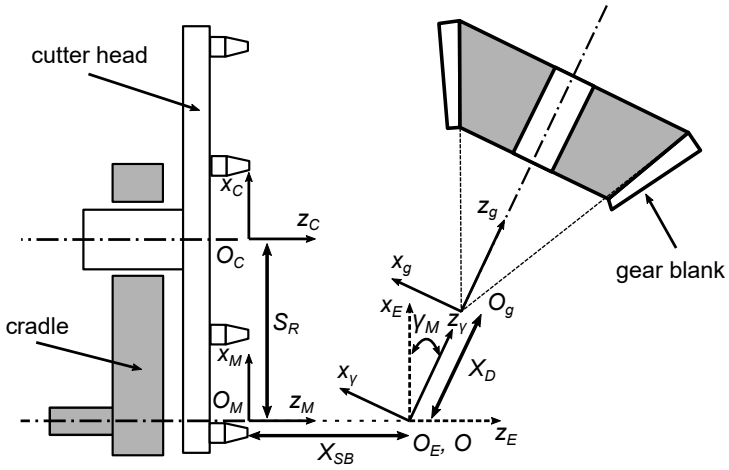
(a) Top-down view of the cutter head and of the gear blank.
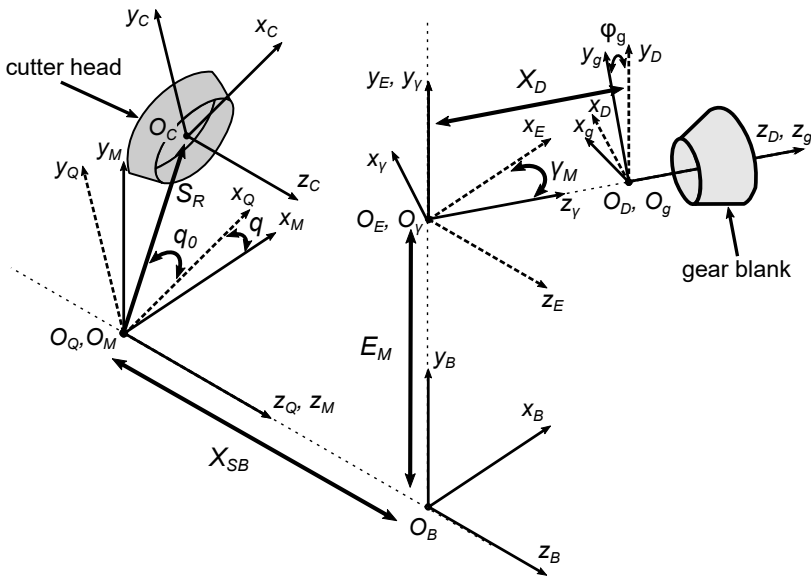
(b) Schematic representation of a cradle-based gear generator for the FM process.

Figure 3.8: Reference frames that are used to describe the machining motions.

Machine settings A schematic representation of the cradle-based spiral bevel gear generator of Fig. 3.3 is shown in Fig. 3.8, where Fig. 3.8a shows the simplifications to the head cutter's installment due the exclusion of cutter head tilt and swivel rotation. The remaining machine settings are described through a series of reference frames that allow to parameterize the gear cutting process. The head cutter, described by equations (Eqs. (3.1) - (3.6)), is connected to the machine's cradle such that its position can be defined by the *radial setting of the cradle* S_R and the *basic cradle angle* q_0, which reflects the initial orientation of the cradle. The *rotation of the cradle*, represented by q, is specified w.r.t. to the machine's reference frame S_M. This fixed reference frame is then also used to describe the position and orientation of the gear blank, which is defined by the following machine settings: a translation along the direction of the *sliding base* X_{SB}, a translation along the direction of the *blank offset* E_M, a rotation that defines the *machine-root angle* γ_M and a translation along the gear blank's rotational axis to set the *machine-center-to-back* X_D. The *rotation of the gear blank* about its rotational axis is represented by ϕ_g.

The homogeneous transformation matrix $\mathbf{T}_{gC}$ can be defined to combine all of these sequential translations and rotations into a single matrix that expresses the motion of any point $\boldsymbol{r}_C$ on the cutter head (in the reference frame S_C) w.r.t. the gear blank (in the local reference frame S_g). The definition of the individual transformation matrices can be found in Appendix B.

$$\mathbf{T}_{gC}(\phi_g, X_D, E_M, X_{SB}, q, q_0, S_R) = \mathbf{T}_{gD}(-\phi_g)\,\mathbf{T}_{D\gamma}(-X_D)\,...$$

$$\mathbf{T}_{\gamma E}\big(-(\frac{\pi}{2} - \gamma_M)\big)\,\mathbf{T}_{EB}(E_M)\,... \quad (3.7)$$

$$\mathbf{T}_{BM}(-X_{SB})\,\mathbf{T}_{MQ}(q)\,\mathbf{T}_{QC}(S_R, q_0)$$

By applying Eq. 3.7 to the generating process of a pinion ($g = 1$) or a gear wheel ($g = 2$), a family of cutter surfaces for the active part of the blade and of the fillet part of the blade, given by Eq. (3.8) and (3.9) respectively, can be defined w.r.t. the work-piece in S_g. To perform the transformation, the vectors $\boldsymbol{r}_g^{(g,A)}$ and $\boldsymbol{r}_g^{(g,F)}$, which represent the points on the cutter surfaces, are expanded to their homogeneous vector equivalents $\bar{\boldsymbol{r}}_g^{(g,A)}$ and $\bar{\boldsymbol{r}}_g^{(g,F)}$.

$$\bar{\boldsymbol{r}}_g^{(g,A)} = \mathbf{T}_{gC}(\phi_g^{(g)}, X_D^{(g)}, E_M^{(g)}, X_{SB}^{(g)}, q^{(g)}, q_0^{(g)}, S_R^{(g)})\quad...$$

$$\bar{\boldsymbol{r}}_C^{(g)}(u_A^{(g)}, \theta_C^{(g)}) \qquad\qquad (g = 1, 2) \qquad (3.8)$$

$$\bar{\boldsymbol{r}}_g^{(g,F)} = \mathbf{T}_{gC}(\phi_g^{(g)}, X_D^{(g)}, E_M^{(g)}, X_{SB}^{(g)}, q^{(g)}, q_0^{(g)}, S_R^{(g)})\quad...$$

$$\bar{\boldsymbol{r}}_C^{(g)}(u_F^{(g)}, \theta_C^{(g)}) \qquad\qquad (g = 1, 2) \qquad (3.9)$$

The unit normal vectors to the surfaces that are described by $\bar{r}_g^{(g,A)}$ and $\bar{r}_g^{(g,F)}$ are given by Eqs. (3.10) and (3.11), respectively, where $\mathbf{L}_{gC}$ corresponds to the rotational part of the homogeneous transformation matrix $\mathbf{T}_{gC}$.

$$\boldsymbol{N}_g^{(g,A)} = \mathbf{L}_{gC}(\phi_g^{(g)}, X_D^{(g)}, E_M^{(g)}, X_{SB}^{(g)}, q^{(g)}, q_0^{(g)}, S_R^{(g)}) \quad \cdots$$

$$\boldsymbol{N}_C^{(g)}(u_A^{(g)}, \theta_C^{(g)}) \qquad\qquad (g = 1, 2) \qquad (3.10)$$

$$\boldsymbol{N}_g^{(g,F)} = \mathbf{L}_{gC}(\phi_g^{(g)}, X_D^{(g)}, E_M^{(g)}, X_{SB}^{(g)}, q^{(g)}, q_0^{(g)}, S_R^{(g)}) \quad \cdots$$

$$\boldsymbol{N}_C^{(g)}(u_F^{(g)}, \theta_C^{(g)}) \qquad\qquad (g = 1, 2) \qquad (3.11)$$

Kinematics and modified roll When defining the motion of the cutter head w.r.t. to the gear blank in Eq. (3.7), the rotation of the cradle and the rotation of the gear blank were considered to be independent. In case of the non-generating process both the cradle and the gear blank are kept fixed, removing both parameters as variables in the above equations. If the generating process is applied to cut the spiral bevel gear, a kinematic relation is imposed such that the rotation of the gear blank $\phi_g^{(g)}(q^{(g)})$ becomes a function of the cradle rotation $q^{(g)}$. In addition, when also the concept of *modified roll* is used to introduce additional flank form modifications, both rotational angles are defined by means of a polynomial function [76]:

$$\phi_g^{(g)} = m_{gc}\left(q^{(g)} - C_2^{(g)}\big(q^{(g)}\big)^2 - C_3^{(g)}\big(q^{(g)}\big)^3\right) \quad (g = 1, 2) \qquad (3.12)$$

In Eq. (3.12), the coefficients $C_2^{(g)}$ and $C_3^{(g)}$ are considered constants that determine the higher order contributions, while m_{gc} determines the so-called *ratio of roll* or *velocity ratio* that is defined as [76]:

$$m_{gc} = \left.\frac{\mathrm{d}\phi_g^{(g)}/\mathrm{d}t}{\mathrm{d}q^{(g)}/\mathrm{d}t}\right|_{q^{(g)}=0} \qquad (3.13)$$

Although it would theoretically be possible to manufacture both elements of the gear pair by using the modified roll method, it is more practical to apply the modified roll method only to the pinion (lower number of teeth) and to produce a generated gear wheel with a constant ratio of roll. In this case, the following kinematic relations are usually used for pinion and gear, respectively:

$$\phi_1^{(1)} = m_{1c}\left(q^{(1)} - C_2^{(1)}\big(q^{(1)}\big)^2 - C_3^{(1)}\big(q^{(1)}\big)^3\right) \qquad (3.14)$$

$$\phi_2^{(2)} = m_{2c}\, q^{(2)} \qquad (3.15)$$
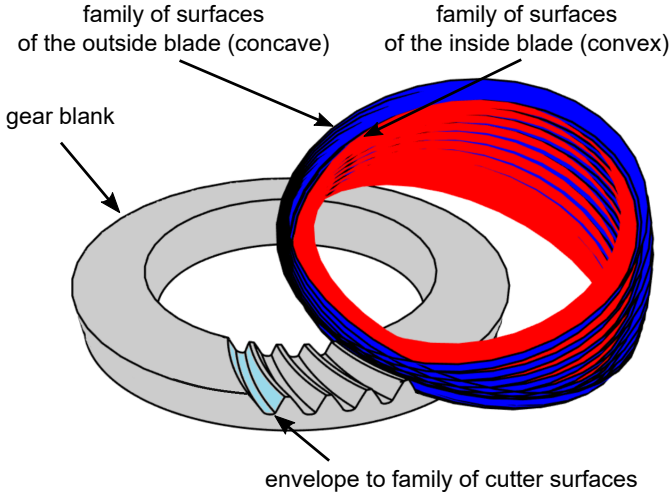
Figure 3.9: Gear teeth are created as the envelope to family of cutter surfaces.

Envelope to family of cutter surfaces

By substituting Eq. (3.12) into Eqs. (3.8) and (3.9), the family of cutter surfaces, described by the active part of the blade and the fillet part of the blade, can be expressed as a function of three variables: the cutter head rotation θ_C, the blade edge coordinate u (i.e. u_A or u_F), and the cradle rotation q. Fig. 3.9 illustrates this family of cutter surfaces for the active parts of the inside (convex) and the outside blade (concave) edges during the cutting simulation of the ring gear.

The resulting tooth surface geometry can be defined by the surface that envelopes the respective family of cutter surfaces. This enveloping surface is obtained as the solution to the *equation of meshing* between the moving cutter surface and the gear blank, where the tooth flank takes to role of conjugate flank to the cutter blade. Starting from Eq. (2.14), while using Eqs. (3.10) and (3.11) to replace the vector product, the equation of meshing can be simplified to:

$$f(q, u, \theta_C) = \boldsymbol{N}_g(q, u, \theta_C) \cdot \frac{\partial \boldsymbol{r}_g(q, u, \theta_C)}{\partial q} = 0 \qquad (3.16)$$

Since the tooth flank geometry is a surface that is described by two independent curvilinear coordinates, Eq. (3.16) defines the additional constraint that allows one of the three surface variables to be defined as a function of the other two. One possible choice could be to express the blade parameter $u(q, \theta_C)$ as a function of the rotations q and θ_C, such that it becomes possible to determine the position $\boldsymbol{r}_g(q, \theta_C)$ on the tooth flank analytically.

However, depending on the complexity of the manufacturing process and the resulting nonlinear nature of the equations, it is not always possible to derive these equations in a closed form. In that case the tooth flank surface is computed in an iterative way. When considering the family of cutter surfaces that are described by the active part of the blade, the resulting set of nonlinear equations that has to be solved numerically is given as by Eq. (3.17) for both pinion ($g = 1$) and gear ($g = 2$).

$$\begin{cases} \bar{\boldsymbol{r}}_g^{(g,A)}(q^{(g)}, u_A^{(g)}, \theta_C^{(g)}) &= \mathbf{T}_{gC}(q^{(g)})\, \bar{\boldsymbol{r}}_C^{(g,A)}(u_A^{(g)}, \theta_C^{(g)}) \\ f^{(g,A)}(q^{(g)}, u_A^{(g)}, \theta_C^{(g)}) &= 0, \qquad\qquad (g = 1, 2) \end{cases} \tag{3.17}$$

In addition, a similar set of equations has to be derived for the fillet part of the blade edge to compute surface that defines the root of the gear tooth.

The gear tooth surfaces are computed as an ordered set of points and their corresponding surface normal vectors, which requires two additional constraints that define the location on the tooth flank. The active parts of the tooth surfaces are computed based on a discretization of the projected tooth flank (see Fig. 3.10). The tooth root surfaces are obtained from the discretization of the interval $[0, \frac{\pi}{2} - \alpha_A^{(g)}]$, in which u_F exists, while imposing that the root points lie along the direction of the tooth profile section, which is determined by the active flank points.
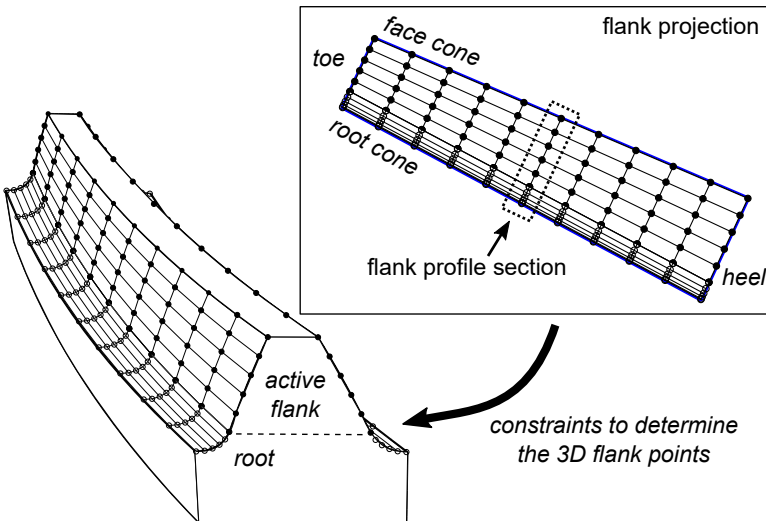
Figure 3.10: Discretization of the gear tooth surfaces in 3D.

3.3 Tooth surface curvature

The normal curvature of a surface depends on the directions along which the surface is observed. Consequently, for any point on the surface there exists a direction along which the normal curvature reaches its maximum value and a direction along which the normal curvature is minimal. These extreme values of normal curvature are referred to as the *principal curvatures* and *principal directions* of the surface at that point. When the principal curvatures and corresponding directions are known in a point on the surface, it becomes possible to reconstruct the normal curvature along any given direction in that point. In Chapter 5 this approach is used to compute the normal curvature along the direction of the instantaneous contact curves, based on precomputed curvature data. Therefore, this dissertation adopts the methodology of [90] to estimate the contact surfaces' principal curvature and directions, based on the curvature of fitted spatial circles and Mohr's circle of curvature.

3.3.1 Normal curvature of a spatial circle

In the vicinity of a point P on the surface $\mathcal{S}$, the curvature along a given direction t that is tangent to the surface $\mathcal{S}$ can be well-approximated by fitting a spatial circle through P. Considering that the gear tooth surfaces were generated as discretized surfaces, for which the surface points and surface normal vectors are stored on ordered grids, a local 3-by-3 grid that has P as its central point is defined on the tooth flank. In this local grid, four spatial circles c_i are then constructed through P along the different directions of the grid, as shown in Figure 3.11. Each circle c_i is defined by a center point C_i and a radius R_i and runs through P where a local reference frame is defined. The unit vectors n_i, t_i and b_i are the curve normal vector, the curve tangent vector and the curve binormal vector of the circle c_i, respectively.

The curvature of each spatial curve $\kappa_{\mathcal{C},i}$ is computed from Eq. (3.18), where the spatial curve's radius of curvature is given by $\rho_{\mathcal{C},i} = R_i$.

$$\kappa_{\mathcal{C}} = \frac{1}{\rho_{\mathcal{C}}} \tag{3.18}$$

The surface normal curvature $\kappa_{n,i}$ is obtained for each circle c_i by projecting the curvature of the curve $\kappa_{\mathcal{C},i}$ onto the surface normal vector N, where Γ_i represents the projection angle between the vectors n_i and N (see Fig. 3.11).

$$\kappa_{n,i} = \kappa_{\mathcal{C},i} \; n_i \cdot N \tag{3.19a}$$

$$= \kappa_{\mathcal{C},i} \; \cos(\Gamma_i) \tag{3.19b}$$
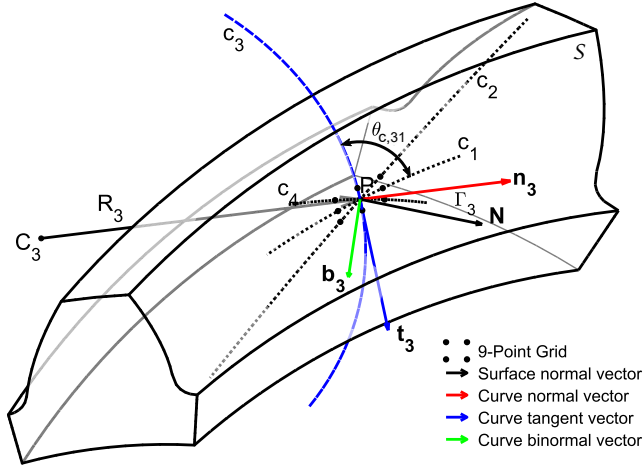
Figure 3.11: Surface normal curvature calculation at the Point P by fitting circles c_i along different directions. The process is illustrated for circle c_3 ($i = 3$).

3.3.2 Surface principal curvatures and directions

The principal directions $\boldsymbol{e}_{min}$ and $\boldsymbol{e}_{max}$ are defined as those directions through each point P on a smooth surface $\mathcal{S}$ for which the surface torsion τ_g is zero [90]. The normal surface curvatures κ_{min} and κ_{max} along these directions are then said to the minimum and maximum principal curvatures of the surface at P. The *Circle of Mohr* for surface curvature relates the surface normal curvature κ_n and the surface torsion τ_g with the principal curvatures κ_{max} and κ_{min} [90]:

$$
\begin{cases}
\kappa_n = \dfrac{\kappa_{max} + \kappa_{min}}{2} + \dfrac{\kappa_{max} - \kappa_{min}}{2} \cos(2\theta_t) & \text{(3.20a)} \\[2ex]
\tau_g = \dfrac{\kappa_{max} - \kappa_{min}}{2} \sin(2\theta_t) & \text{(3.20b)}
\end{cases}
$$

In Eq. (3.20) the Circle of Mohr is defined by the center $\frac{\kappa_{max}+\kappa_{min}}{2}$ and the radius $\frac{\kappa_{max}-\kappa_{min}}{2}$, while the θ_t represents angle between the maximum principal curvature direction $\boldsymbol{e}_{max}$ and the curve tangent $\boldsymbol{t}$ direction that yields (κ_n, τ_g).

The curvature parameters κ_{max}, κ_{min} and $\boldsymbol{e}_{max}$ are found from a tensor rotation (see Appendix E), once at least three normal curvatures along three different directions at P are known [73, 74]. The process is shown in Fig. 3.12.
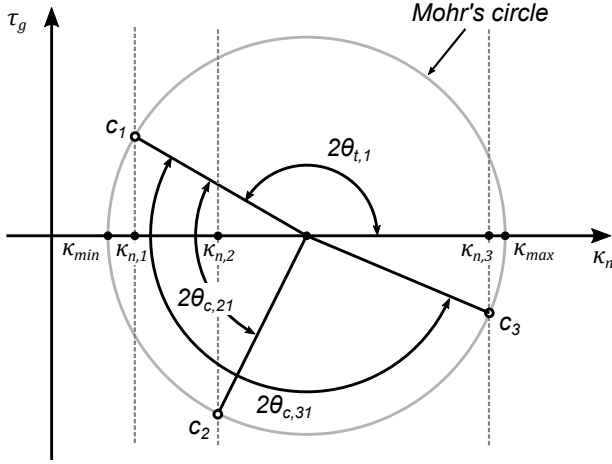
Figure 3.12: Principal curvature calculation using the Mohr circle.

Using a circle fitting approach, illustrated in Fig. 3.11 for $i = 3$, three spatial circles c_i $(i = 1, 3)$ with spatial curve curvature $\kappa_{\mathcal{C},i}$ are fitted through a point P of the gear tooth surface $\mathcal{S}$ along three known tangent directions $\boldsymbol{t}_i$. Using Eq. (3.19), the corresponding surface normal curvatures $\kappa_{n,i}$ along directions $\boldsymbol{t}_i$ are obtained by projecting onto the surface normal $\boldsymbol{N}$ at P. With only the surface normal curvatures $\kappa_{n,i}$ in three different directions $\boldsymbol{t}_i$ known, the tensor rotation is found by solving the following system for κ_{max}, κ_{min} and $\theta_{t,1}$:

$$
\begin{cases}
\kappa_{n,1} & = \dfrac{\kappa_{max} + \kappa_{min}}{2} + \dfrac{\kappa_{max} - \kappa_{min}}{2} \cos(2\ \theta_{t,1}) \\[2mm]
\kappa_{n,2} & = \dfrac{\kappa_{max} + \kappa_{min}}{2} + \dfrac{\kappa_{max} - \kappa_{min}}{2} \cos(2\ (\theta_{t,1} + \theta_{c,21})) \\[2mm]
\kappa_{n,3} & = \dfrac{\kappa_{max} + \kappa_{min}}{2} + \dfrac{\kappa_{max} - \kappa_{min}}{2} \cos(2\ (\theta_{t,1} + \theta_{c,31}))
\end{cases}
\qquad (3.21)
$$

The angle $\theta_{t,1}$ provides the orientation of $\boldsymbol{e}_{max}$ w.r.t. the tangent direction $\boldsymbol{t}_1$ of the curve c_1, while the angles $\theta_{c,i1}$ express the orientation of the tangent direction of a curves c_i w.r.t. $\boldsymbol{t}_1$.

To reconstruct the normal curvature along any direction $\boldsymbol{t}$ at the point P of the surface, Euler's formula for normal curvature, given in Eq. (2.5), is written as:

$$
\kappa_n = \kappa_{min} + (\kappa_{max} - \kappa_{min})\ \cos^2(\theta_t) \quad \text{with} \quad \cos(\theta_t) = \boldsymbol{t} \cdot \boldsymbol{e}_{max} \qquad (3.22)
$$

3.4 Finite element model creation

Starting from a CAD model, the creation of FEM-based spiral bevel gear models can become a time-expensive process, especially when the same operations have to be (manually) repeated for each design case. Therefore, numerous researchers have dedicated their time on advancing tools that allow the automatic creation of FE models of spiral bevel gears [6, 77, 40, 41]. Similar to the TCA tools, these automated tools also include the equations that govern the manufacturing process of spiral bevel and hypoid gears, to assure the correct description of the tooth geometry. Once the FE models have been created, commercially available FEA software can then be used to perform the contact simulations [6, 41].

Within this research and related activities [1, 23, 26] a set of procedures is developed to automatically generate detailed spiral bevel gear FE models. While the main focus of these efforts is turned towards enabling NL-FEA-based contact simulations to validate the developed contact model (see Chapter 5 and 6), future extensions of the contact model with FE-based tooth stiffness data are already considered. Fig. 3.13 shows the process. By simulating the manufacturing kinematics with the models of Section 3.2.2, the tooth surfaces are generated as a set of points that are stored on a regular grid. The gear blank geometry is then created, as described in Section 3.1, and the tooth volume is defined and discretized with finite elements. These routines are integrated into a dedicated tool, which are developed for the automated FE mesh creation of cylindrical gears [16, 21]. The process supports the generation of fully parametric 3D spiral bevel gear elements, of which the geometry is discretized by linear hexahedral elements. The model files are written in the Nastran format.

In addition, specific procedures have been developed for the purpose of FEA-based contact simulations. Due to their high computational cost, these analyses rarely focus on more than one mesh cycle since the behavior is expected to repeat itself. Accordingly, models for FEA-based tooth contact analysis require only those teeth that are expected to be in contact over the course of one mesh cycle, to be finely meshed so that accurate contact detection is guaranteed. The remaining section of the gear, for which the teeth are not expected to be in contact, can either be excluded from the model or replaced by a coarsely meshed FE model. Within the scope of this dissertation, the decision was made to use 3D FE models of complete gear pairs. To reduce the size of the model, each gear's FE mesh is constructed out of three sections, to which a *fine*, *coarse* and *intermediate mesh*[1] is applied. The intermediate section is used to assure a smooth transition between the finely and coarsely meshed sections.

---

[1]In Fig. 3.13, 1 fine tooth has 36750 el. (100 %), 1 intermediate tooth has 6150 el. (17 %) and 1 coarse tooth 1200 el. (3 %). Within the complete FE gear model with 36 coarse, 2 intermediate and 5 fine teeth their respective contributions are 18 %, 5 % and 77 %.

3D model of the tooth surface

create tooth volume,
discretize the tooth,
create finite elements

3D FE model of the tooth

copy,
rotate,
assemble

coarse   *intermediate*   *fine*
mesh   *mesh*   *mesh*

3D FE Gear model
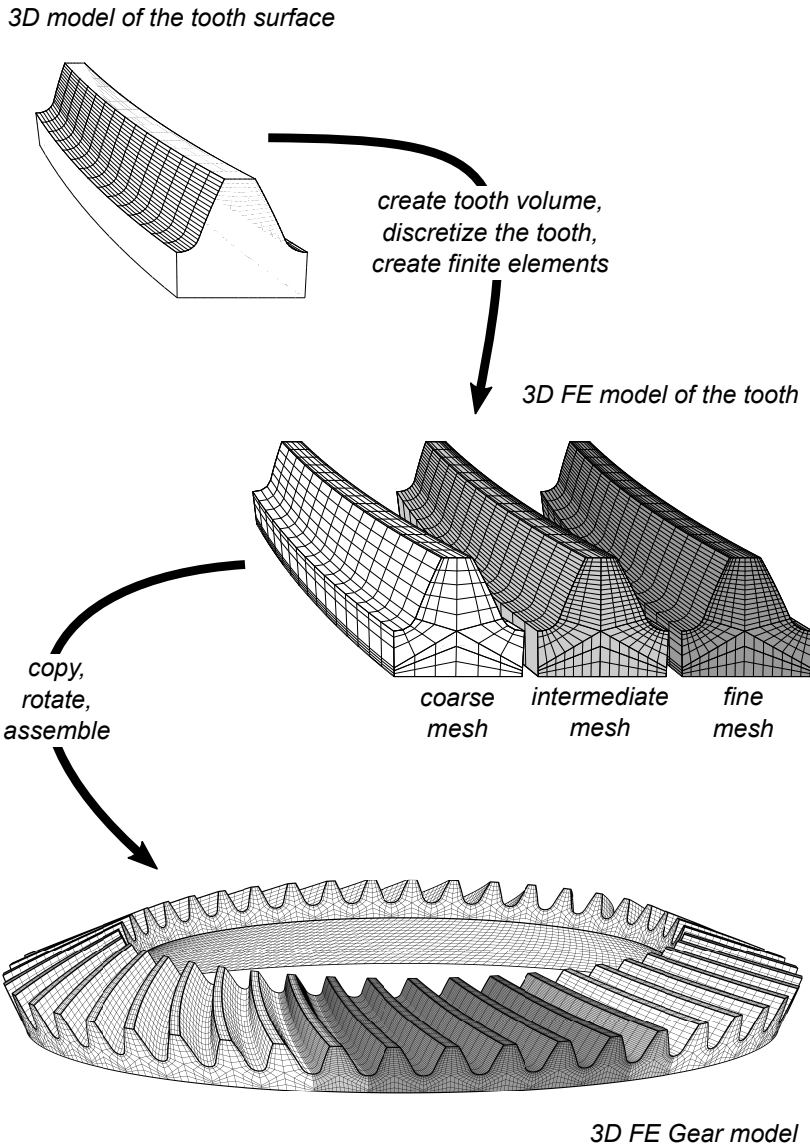
Figure 3.13: Finite element model generation process for spiral bevel gears.

3.5   Conclusion

This chapter focuses on the geometrical aspects of the developed modeling methodology for spiral bevel gears. In Section 3.1 the basic concepts and terminology of spiral bevel gear geometry are discussed. Section 3.2 provided an overview of the most common methods to manufacture spiral bevel gears on an industrial scale. Since the shape of a spiral bevel gear tooth is not standardized, it is completely dictated by the blade geometry and machine settings that are used during the machining process. Depending on how the gear blank rotates w.r.t. to the cutter blades, the available machining processes are typically divided into single indexing (face-milling) and continuous indexing (face-hobbing) methods. A mathematical model of the five-cut method (a face-milling process) is described and used to generate the spiral bevel gear's tooth flank geometry as an ordered set of points and surface normal vectors. The model simulates the motion of the cutter blades during the finishing cut, while using the equation of meshing to determine the tooth flanks as the envelope to a family of cutter surfaces. Building upon the discrete representation of the tooth surfaces, a general methodology is developed in Section 3.3 that estimates the tooth flank curvature. By combining the curvature of surface-fitted spatial circles with the circle of Mohr for curvature, the principal curvatures and principal directions are determined. Finally, the developed procedures for the creation of detailed FEM-based spiral bevel gear models are briefly described in Section 3.4. The discrete tooth surfaces, obtained by simulating the cutting process, serve as input for this automated process.

Chapter 4

Gear pair kinematics and unloaded TCA

This chapter lays the groundwork for the contact detection strategy that is used in Chapter 5 to develop a novel gear contact force model for spiral bevel gears. From the discussion of the different contact detection methods in Chapter 2, it becomes clear that - besides their accuracy - the numerical efficiency with which the potential contact locations are detected significantly impacts the overall effectiveness of the methodology. While conventional methods, such as the continuous tangency approach (see Section 2.1.1) or the NTS method for discretized surfaces (see Section 2.2.3), have proven to be adequate for contact detection, they consider the mating flanks to be arbitrary, which in turn impacts the numerical efficiency of the methodology. The knowledge that the contacting tooth flanks of the gear pair are designed to be near-conjugate to ensure motion transmission with minimal transmission error, can be exploited to improve the efficacy and accuracy of the contact detection method. This additional information is embedded in the ease-off approach (see Section 2.1.2) through the use the theoretical conjugate surfaces.

To attain a superior performance in terms of contact detection, the methodology adopts a conjugate surface approach. Building upon the theory of conjugate surfaces, the kinematic relations between a given tooth flank and its theoretical conjugate flank are determined in Section 4.1. The predefined tooth flank surfaces (see Chapter 3) are the starting point for this computation in order to develop a methodology that is general and independent from the manufacturing process. The equation of meshing, which determines the conjugate motion, is solved for each point of the discrete flank to determine that flank's surface of roll
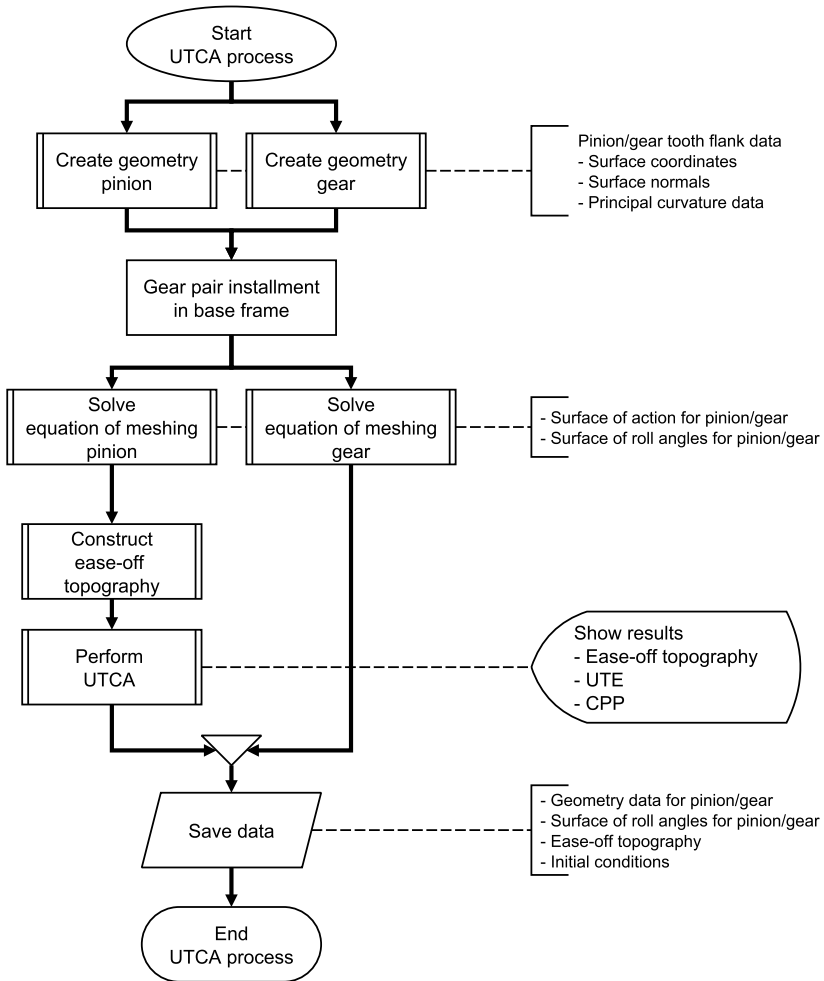
Figure 4.1: Overview of the process for unloaded tooth contact analysis (UTCA).

angles. The surface of roll angles is of major importance for the methodology as it not only defines the conjugate to a given flank but also allows to determine the location of the contact points on the surface of action. Once the complete surface of roll angles has been obtained, the ease-off topography for that flank pair is constructed. By combining the surface of roll angles and ease-off topography an accurate and performant UTCA process, similar to the one of [63], is developed in Section 4.2. A schematic overview of this process is provided in Fig. 4.1.

4.1 Gear pair kinematics

Although current generation computer-controlled face cutting machines are capable of producing fully conjugate tooth pair surfaces, no direct geometrical relation exists between the mating flanks that would allow an a priori definition of a conjugate flank pair. Current spiral bevel gear design therefore does not start from conjugate flanks - as it is the case for cylindrical gears - but is dependent on TCA procedures to determine a gear pair's contact performance and to identify optimized machining parameters. Additionally, flank form modifications that result in close-to-conjugate surfaces are introduced to ensure the desired quality of motion transfer when tooth deformation and misalignments occur. Such considerations explain why a conjugate surface based methodology, such as the ease-off approach, can be applied to the gear contact analysis. Inherent to the methodology is the assumption that for a given flank pair the difference between the real mating surface to a selected flank and its conjugate remain small (up to a few hundred micrometers), such that contact detection can be simplified based on the kinematic motion of the selected flank and its computed conjugate. The ease-off topography can then be used to account for the differences that exist between the real mating surface and the conjugate to the selected surface.

4.1.1 Conjugate motion transfer

Conjugate motion transfer so far is defined as perfect motion transfer between two contacting surfaces without providing a proper definition. In case of a gear pair this means that the resulting motion is conveyed according to the *gear ratio* m_{21}, which can be defined as the ratio between the angular velocities of the gear (gear 2) and of the pinion (gear 1) or the ratio between the number of gear teeth of the pinion Z_1 and of the gear Z_2:

$$m_{21} = \frac{\omega^{(2)}}{\omega^{(1)}} = \frac{\mathrm{d}\phi_z^{(2)}/\mathrm{d}t}{\mathrm{d}\phi_z^{(1)}/\mathrm{d}t} \tag{4.1a}$$

$$= \frac{Z_1}{Z_2} \tag{4.1b}$$

Assuming that the gear rotational axis coincides with the z-axis of a local reference frame that is attached to the gear body, integration of Eq. (4.1a) results into the expression for the *transmission error*, given by Eq. (2.4). A common simplification of Eq. (2.4) is obtained as: $TE = \phi_z^{(2)} - m_{21}\phi_z^{(1)}$, when both gears are rotated such that the flanks are in contact at the start of the analysis and the initial gear rotation $\phi_{z0}^{(1)}$ and $\phi_{z0}^{(2)}$ can be omitted. In case of conjugate motion the resulting transmission error is zero.

A pair of gear teeth in mesh does not have to be (fully) conjugate to transmit motion with zero transmission error. This can be achieved as long as at least one contact point on both flanks is capable of conveying the rotation according to the prescribed gear ratio. However, when computing the conjugate surface to a chosen tooth flank, the equation of meshing ensures that the gear ratio is enforced for every point on the surface.

4.1.2 The equation of meshing

Similarly to how the cutter blade meshes perfectly with the gear blank when it performs the cutting of the tooth flank, a real tooth flank also meshes perfectly with its conjugate when it rotates about its rotational axis. The conjugate to a given flank is therefore defined as the envelope to a family of real tooth flank surfaces and can be computed with the *equation of meshing* for the flank while taking into account the relative position and orientation of the gear pair. When a continuous parametrization of the selected surface is available, its conjugate surface is obtained by both Eqs. (2.14) and (2.15). In case of a discrete surface the latter equation is best adopted, since it avoids the computation of the partial derivatives by replacing them with their geometric and kinematic counterparts.

A real world spiral bevel gear pair is created with manufacturing errors, e.g. flank form errors or tooth pitch errors. However, the modeling and the effects of such errors are not studied in this work. The following assumptions are made regarding the gear geometry when solving the equation of meshing: (i) all teeth of the pinion are identical without indexing errors, (ii) all teeth of the gear are identical without indexing errors and (iii) the gear geometry is predefined. The first two assumptions allow to solve the equation of meshing for the flanks of a single tooth pair, the *reference tooth pair*, and to translate the results to other tooth pairs when needed. The final assumption allows to write Eq.(2.15) as:

$$\boldsymbol{N}(\phi_z) \cdot \boldsymbol{v}(\phi_z) = 0 \tag{4.2}$$

provided that the discrete surface is described as a set of surface coordinates $\boldsymbol{r}$ with accompanying surface normal vectors $\boldsymbol{N}$ and that the correct kinematic relations are available. The required kinematic relation is prescribed by the relative velocity $\boldsymbol{v}$ between the coincident contact points on both the chosen surface and its conjugate counterpart. As additional advantage, solving Eq. (4.2) is simplified to finding the solution in terms of gear rotational angle ϕ_z to a single nonlinear equation for each point of the gear flank surface.
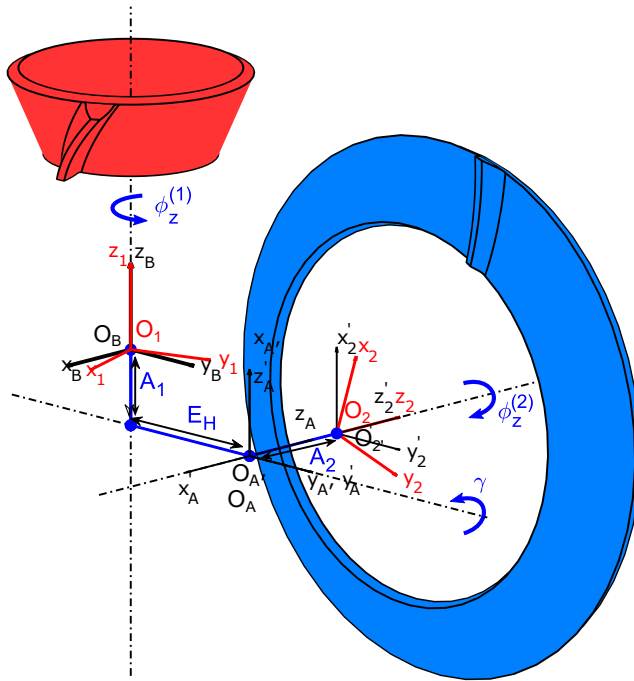
Figure 4.2: Relative orientation of pinion (gear 1) and gear (gear 2) w.r.t. the base frame, displayed for installment parameters $A_1 > 0$, $E_H > 0$, $A_2 > 0$ and $\gamma = -90 \deg$.

Position and orientation of the gear pair

The different reference frames that are used to describe the position and orientation of the gear pair are shown in Fig. 4.2. The surface points of the pinion flank (*gear 1*) are expressed in a local reference frame S_1, while the points of both the conjugate to the pinion flank and the gear flank (*gear 2*) are expressed in the local reference frame S_2. The gear pair installment is defined through the shaft offset E_H, the pinion axial offset A_1, the gear axial offset A_2 and shaft angle γ. The angles $\phi_z^{(1)}$ and $\phi_z^{(2)}$ represent the rotation about the rotational axes of the pinion and of the gear w.r.t. the base frame, respectively. The base frame S_B is introduced as an auxiliary reference frame to describe the relative position and orientation of the gear and the pinion. It is defined in such a way that its origin stays the same as that of S_1 while the pinion is only allowed to rotate about their common z-axis. The homogeneous transformation matrix $\mathbf{T}_{B1}$ expresses the position and orientation of the reference frame S_1

w.r.t. the base frame S_B, while matrix $\mathbf{T}_{B2}$ expresses the position and orientation of the reference frame S_2 w.r.t. the base frame S_B. The two transformation matrices are given by Eqs. (4.3) and (4.4), respectively.

$$\mathbf{T}_{B1} = \mathbf{T}_z\left(\phi_z^{(1)}\right) \tag{4.3}$$

$$\mathbf{T}_{B2} = \mathbf{T}_{B2'}\left(A_1, \gamma, E_H, A_2\right) \mathbf{T}_z\left(\phi_z^{(2)}\right) \tag{4.4}$$

The transformation matrix $\mathbf{T}_z$ represents the rotation about the gear rotational axis for either the pinion in Eq. (4.3) or for the gear in Eq. (4.4).

$$\mathbf{T}_z(\phi_z) = \begin{bmatrix} \cos(\phi_z) & -\sin(\phi_z) & 0 & 0 \\ \sin(\phi_z) & \cos(\phi_z) & 0 & 0 \\ 0 & 0 & 1 & 0 \\ 0 & 0 & 0 & 1 \end{bmatrix} \tag{4.5}$$

The considered gear pair installment parameters are combined in a single transformation matrix $\mathbf{T}_{B2'}$, given by Eq. (4.6).

$$\mathbf{T}_{B2'} = \begin{bmatrix} \cos(\gamma) & 0 & \sin(\gamma) & 0 \\ 0 & 1 & 0 & 0 \\ -\sin(\gamma) & 0 & \cos(\gamma) & -A_1 \\ 0 & 0 & 0 & 1 \end{bmatrix} \begin{bmatrix} 1 & 0 & 0 & 0 \\ 0 & 1 & 0 & E_H \\ 0 & 0 & 1 & A_2 \\ 0 & 0 & 0 & 1 \end{bmatrix} \tag{4.6}$$

The conjugate to the pinion flank

The conjugate to the pinion flank is obtained by solving the equation of meshing for the real pinion flank while taking into account the relative position and orientation of the gear pair. Expressing Eq. (4.2) w.r.t. the base frame S_B results in Eq. (4.7) for the real pinion flank.

$$\boldsymbol{N}_B^{(1)} \cdot \boldsymbol{v}_B^{(12)} = 0 \tag{4.7}$$

The relative velocity $\boldsymbol{v}_B^{(12)}$ defines the correct kinematic relation between the surface points of the pinion and its conjugate flank and is defined by Eq. (4.8).

$$\boldsymbol{v}_B^{(12)} = \left(\boldsymbol{\omega}_B^{(1)} \times \boldsymbol{r}_B^{(1)}\right) - \left(\boldsymbol{\omega}_B^{(2)} \times \boldsymbol{\rho}_B\right) \tag{4.8}$$

The vector $\boldsymbol{\rho}_B = \boldsymbol{r}_B^{(1)} - \boldsymbol{R}_B^{(2)}$ accounts for the rotational moment that arises when either the shaft offset E_H or the axial offset A_1 are non-zero for the configuration in Fig. 4.2. The vector $\boldsymbol{R}_B^{(2)}$ expresses the arm of the rotational moment and is defined as the vector that points from the origin of S_B to the

origin of S_2. The position and orientation of the corresponding surface normal for any point on the surface of the pinion w.r.t. the frame S_B is given by:

$$\bar{\boldsymbol{r}}_B^{(1)} = \mathbf{T}_{B1}\big(\phi_z^{(1)}\big)\ \bar{\boldsymbol{r}}_1^{(1)} \tag{4.9}$$

$$\boldsymbol{N}_B^{(1)} = \mathbf{L}_{B1}\big(\phi_z^{(1)}\big)\ \boldsymbol{N}_1^{(1)} \tag{4.10}$$

The vectors $\bar{\boldsymbol{r}}_1^{(1)}$ and $\bar{\boldsymbol{r}}_B^{(1)}$ are used to express the homogeneous form of the position vectors $\boldsymbol{r}_1^{(1)}$ and $\boldsymbol{r}_B^{(1)}$. The matrices $\mathbf{L}_{B1}$ and $\mathbf{L}_{B2}$ correspond to the rotational part of the homogeneous transformation matrices $\mathbf{T}_{B1}$ and $\mathbf{T}_{B2}$. The angular velocity vectors $\boldsymbol{\omega}_B^{(1)}$ and $\boldsymbol{\omega}_B^{(2)}$ of Eq. (4.8) for the pinion and the gear are defined as:

$$\boldsymbol{\omega}_B^{(1)} = \mathbf{L}_{B1} \begin{bmatrix} 0 \\ 0 \\ \omega^{(1)} \end{bmatrix} \tag{4.11}$$

$$\boldsymbol{\omega}_B^{(2)} = \mathbf{L}_{B2} \begin{bmatrix} 0 \\ 0 \\ -\omega^{(2)} \end{bmatrix} \tag{4.12}$$

The magnitudes $\omega^{(1)}$ and $\omega^{(2)}$ of the corresponding angular velocity vectors for the pinion and its conjugate are defined by the gear ratio m_{21} in Eq. (4.1).

Surface of roll angles and surface of action

Solving the equation of meshing for one particular point P on the tooth flank of the pinion yields a specific value of pinion *roll angle* $\phi_z^{(1)}$. The *surface of roll angles* $\mathcal{R}_\phi^{(1)}$ of the real pinion flank is the complete set of pinion roll angles that are obtained by solving Eq. (4.7) for each point on the flank. The roll angle $\phi_z^{(1)}$ of a point on the pinion flank corresponds to the rotation that the pinion has to undergo for that point to reach its mating point on the conjugate flank.

The location where this contact takes place is a point on the *surface of action* of the pinion flank. Similarly to the plane of action for involute cylindrical gears, the surface of action describes the family of contact curves between two conjugate flanks that are represented in a fixed reference frame [76]. The action surface of a left pinion flank is given in Fig. 4.3 by using Eq. (4.9) to express all the contact locations of the pinion flank w.r.t. the base frame S_B. Similarly to cylindrical gears the tooth flank will intersect the surface of action when it comes in contact with its conjugate for a given value of pinion roll angle $\phi_z^{(1)}$. For those points that belong to the (instantaneous) contact curve between

pinion flank and its conjugate the two contact conditions, given by Eq. (2.1), are satisfied. The resulting conditions for (i) coincidence of contact points and (ii) collinearity of surface normal vectors can be written as:

$$\boldsymbol{r}_B^{(1)} = \boldsymbol{r}_B^{(2c)} \tag{4.13a}$$

$$\boldsymbol{N}_B^{(1)} = -\boldsymbol{N}_B^{(2c)} \tag{4.13b}$$

where the position vector $\boldsymbol{r}_B^{(2c)}$ is used to represent the points on the conjugate flank, while the vector $\boldsymbol{N}_B^{(2c)}$ expresses the surface normal vector at $\boldsymbol{r}_B^{(2c)}$.

Finally, the surface coordinates $\boldsymbol{r}_2^{(2c)}$ of a point on the *conjugate to the pinion flank* are obtained from Eq. (4.14). The resulting homogeneous transformation expresses the coordinates $\boldsymbol{r}_1^{(1)}$ of the point on the pinion flank w.r.t. to the local reference frame S_2 that is attached to the gear, while imposing the kinematic relation that is prescribed by the gear ratio m_{21}.

$$\bar{\boldsymbol{r}}_2^{(2c)} = \mathbf{T}_{B2}^{-1}\big(-m_{21}\,\phi_z^{(1)}\big)\,\mathbf{T}_{B1}\big(\phi_z^{(1)}\big)\,\bar{\boldsymbol{r}}_1^{(1)} \tag{4.14}$$

In this transformation the vectors $\bar{\boldsymbol{r}}_1^{(1)}$ and $\bar{\boldsymbol{r}}_2^{(2c)}$ are the homogeneous versions of the position vectors $\boldsymbol{r}_1^{(1)}$ and $\boldsymbol{r}_2^{(2c)}$, respectively.
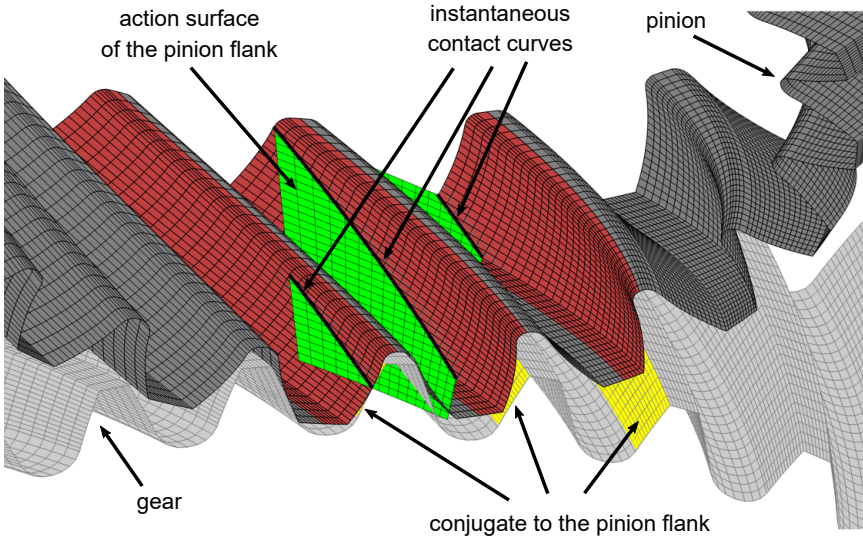
Figure 4.3: Example of the surface of action of the left pinion flanks.

The conjugate to the gear flank

The conjugate to a given real tooth flank is computed without changing its relative configuration w.r.t. the pinion. This way the obtained surface of roll angles allows a direct description of the real gear flank's action surface in S_B. Similarly to Eq. (4.7), the equation of meshing between the real gear flank and is conjugate is defined as:

$$\boldsymbol{N}_B^{(2)} \cdot \boldsymbol{v}_B^{(21)} = 0 \qquad (4.15)$$

Considering that $\boldsymbol{v}_B^{(21)} = -\boldsymbol{v}_B^{(12)}$, the relative velocity $\boldsymbol{v}_B^{(21)}$ can be replaced by Eq. (4.8), since its sign does not affect the required perpendicularity to the surface normal $\boldsymbol{N}_B^{(2)}$. However, Eq. (4.8) expresses the relative velocity $\boldsymbol{v}_B^{(12)}$ in function of the vector $\boldsymbol{r}_B^{(1)}$, which in the current case would correspond to the coordinates $\boldsymbol{r}_B^{(1c)}$ of a point on the surface that is *conjugate to the gear flank.* By relying on the contact conditions, which are valid for any point on the surface of action of the real gear flank, it is possible to replace $\boldsymbol{r}_B^{(1c)}$ by $\boldsymbol{r}_B^{(2)}$. The equation of meshing between the real gear flank and its conjugate is then found as:

$$\boldsymbol{N}_B^{(2)} \cdot \left[\left(\boldsymbol{\omega}_B^{(1)} \times \boldsymbol{r}_B^{(2)} \right) - \left(\boldsymbol{\omega}_B^{(2)} \times \left(\boldsymbol{r}_B^{(2)} - \boldsymbol{R}_B^{(2)} \right) \right) \right] = 0 \qquad (4.16)$$

The surface of roll angles $\mathcal{R}_\phi^{(2)}$ of the real gear flank is then constructed by solving Eq. (4.16) for the gear roll angle $\phi_z^{(2)}$ for each point on the real gear flank. The coordinates $\boldsymbol{r}_1^{(1c)}$ of the points on the conjugate surface to the real gear flank are defined in the pinion reference frame S_1 and can be obtained from the following transformation:

$$\bar{\boldsymbol{r}}_1^{(1c)} = \mathbf{T}_{B1}^{-1}\left(-\phi_z^{(2)}/m_{21} \right) \, \mathbf{T}_{B2}\left(\phi_z^{(2)} \right) \, \bar{\boldsymbol{r}}_2^{(2)} \qquad (4.17)$$

4.1.3   Ease-off topography

In the actual gear pair the real pinion flanks do not mesh perfectly with the real gear flanks. This amount of flank mismatch is expressed through the *ease-off* (EO) *topography,* which is defined as the amount of deviation of a real flank from the conjugate to its real mating flank. Therefore, it is a property of the flank pair that includes all possible types of small deviations, such as changes in the flank's micro-geometry, misalignments and manufacturing errors. To determine the ease-off topography, a point-by-point comparison between the real flank and the theoretical conjugate to its mating flank is performed on a region that is bounded by the flank overlap of the real flanks. This region can be identified by projecting both the real flank and the conjugate to its mating flank onto a common plane.

The *gear-based* ease-off topography that is constructed in this work is only created to optimize the UTCA process and to provide a metric that enables an evaluation of the tooth flank form modifications during data preprocessing. In following chapters the computed *penetration* between the real tooth flanks (of both the pinion and the gear) is used to determine contact and to compute the resulting contact forces.

The projection plane

To construct the gear-based ease-off topography of a given flank pair, the real gear tooth surface has to be compared with the *conjugate gear* surface, i.e. the surface that is conjugate to the mating pinion tooth surface. Considering that the real tooth flanks of both the pinion and the gear are discretized during the geometry generation process, a direct comparison between the real gear flank and the conjugate gear surface is difficult to obtain without the use of interpolation or surface fitting techniques. For example, if both pinion and gear flanks are discretized with a different number of points, a common coincident grid cannot be created. In addition, it should also be noted that the points on the surface that is conjugate to the pinion flank are obtained by solving the equation of meshing. Therefore, their distribution resembles that of the movement of the distributed pinion flank points as they mesh with the to-be-computed conjugate surface. While the points on this conjugate surface are still stored on an ordered grid, due to the meshing motion there is no guarantee that the points will keep their regular distribution. By projecting the points of both the real gear tooth flank and the conjugate gear surface onto a common plane, an interpolation strategy was developed to compute the points of both flanks onto a common grid, which is bounded by the resulting flank overlap.

The conjugate to the real pinion flank and the real gear flank are first projected onto a plane in S_2 that includes the gear rotational axis. Such a projection is feasible without loss of accuracy due to the similarity between both flanks in terms of size and flank curvature. This so-called *projection plane* is bounded by the flank overlap of the conjugate to the real pinion and the real gear, as illustrated in Fig. 4.4. The projection is carried out as the rotation along a circular arc about the gear rotational axis, for which the parametrization is given by Eq. (4.18).

$$\begin{cases} x_2 & = R_{proj} \ \cos(\theta_{proj}) \\ y_2 & = R_{proj} \ \sin(\theta_{proj}) \\ z_2 & = Z_{proj} \end{cases} \qquad (4.18)$$

The projection plane is then discretized with a new grid to enable a one-to-one comparison of the real gear flank ($g = 2$) and the conjugate gear surface ($g = 2c$).
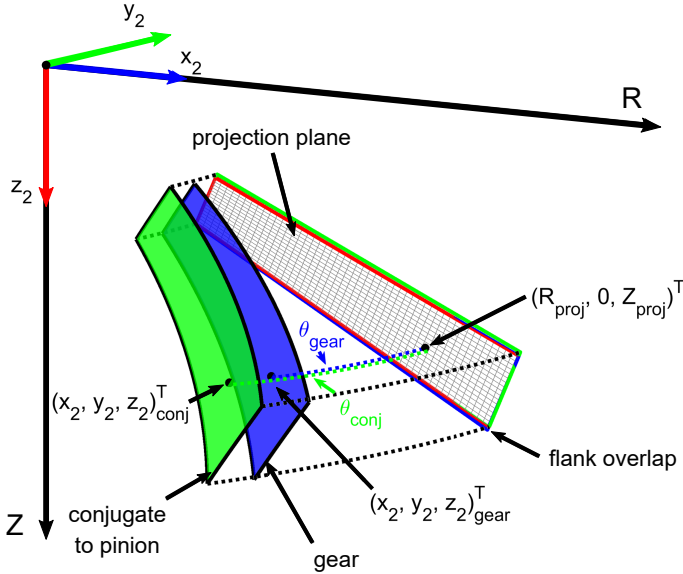
Figure 4.4: Projection plane creation.

For each point of the *projection plane grid*, the 3D surface coordinates of both surfaces are computed in the gear reference frame S_2 through a shape-function based interpolation method. While both bilinear and biquadratic shape functions can be used, the latter is here preferred since the point distribution of the conjugate (gear) surface can be nonlinear due to the motion of the real (pinion) flank. The process is visualized in Fig. 4.5, while the most important steps are summarized below.

- A local grid of nine projected surface points (of either the gear flank or the conjugate gear flank) is identified for each point P_{ppg} on the projection plane grid, such that the distance between P_{ppg} and the central node of the local grid P_9 is minimized.

- The local nine-noded grid is used to define a biquadratic element that is defined by the surface's projected coordinates $(R_{proj,l}^{(g)}, Z_{proj,l}^{(g)})$ of the corner points $P_l^{(g)}$ and the shape functions $N_l^e(\xi, \eta)$. The position of any point on this nine-noded element is then found by the following

interpolation function:

$$
\begin{cases}
R_{proj}^{(g)}(\xi,\eta) &= \displaystyle\sum_{l=1}^{9} N_l^e(\xi,\eta)\ R_{proj,l}^{(g)} \\[2em]
Z_{proj}^{(g)}(\xi,\eta) &= \displaystyle\sum_{l=1}^{9} N_l^e(\xi,\eta)\ Z_{proj,l}^{(g)}
\end{cases}
\qquad (g = 2, 2c) \qquad (4.19)
$$

- Since the position of the grid point P_{ppg} is known from the imposed discretization, the corresponding natural coordinates ξ_{ppg} and η_{ppg} are determined by solving the system of nonlinear equations of Eq. (4.19).

- The required 3D surface coordinates are found by evaluating the function:

$$
r_2^{(g)}(\xi_{ppg}, \eta_{ppg}) = \sum_{l=1}^{9} N_l^e(\xi_{ppg}, \eta_{ppg})\ r_{2,l}^{(g)} \qquad (g = 2, 2c) \qquad (4.20)
$$

- To completely define the projection plane data, this process is repeated for each of the projection plane grid points and for both the real gear flank and the conjugate gear flank.
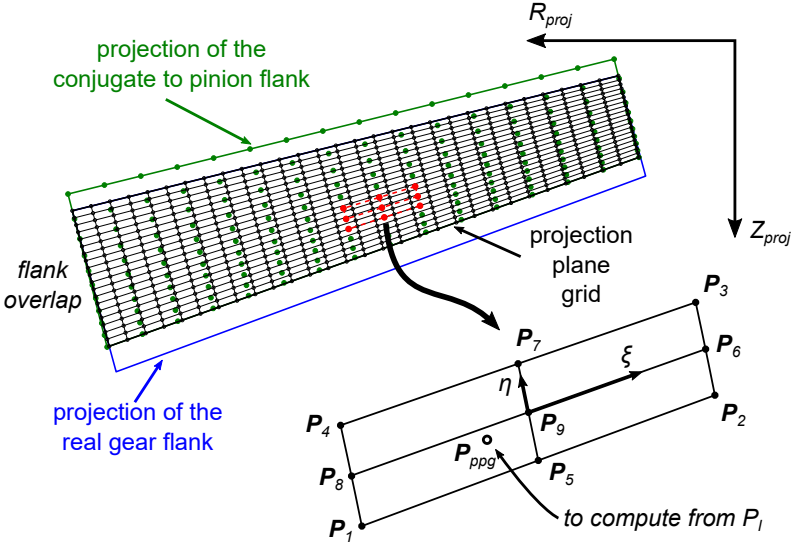
Figure 4.5: Interpolation of the real gear flank data and the conjugate to pinion flank data onto a common projected grid that is bounded by the flank overlap.

Gear-based ease-off topography

Once all the data is defined onto the projection plane, the ease-off topography is constructed as the difference in projection angle $\theta_{proj}^{(2)}$ of the gear flank and of the conjugate flank $\theta_{proj}^{(2c)}$. The gear-based ease-off topography definition is given in Eq. (4.21) in terms of angular deviations or in Eq. (4.22) in terms of distance by multiplying the angular ease-off value with the radius $R_{proj}^{(2)}$ of the corresponding point on the projection plane:

$$\mathcal{E}_{\theta}^{(2)} = \theta_{proj}^{(2)} - \theta_{proj}^{(2c)} \tag{4.21}$$

$$\mathcal{E}_{\delta}^{(2)} = R_{proj}^{(2)} \; \mathcal{E}_{\theta}^{(2)} \tag{4.22}$$

The rigid body rotation between both flanks (see Fig. 2.5) that translates into an offset of the ease-off topography is automatically removed. The resulting ease-off topography is 0 μm or 0 μrad in at least one point to indicate that both pinion and gear flank are conjugate in this point.

An example of gear-based ease-off topography is found in Fig. 2.3, while an example for pinion-based ease-off topography has been added to Appendix C.

4.2   Unloaded tooth contact analysis

The UTCA process focuses on the geometrical analysis of the tooth flank pairs in contact. Inherent to such a process is the assumption that all the contacting teeth pairs are identical and that flank-related manufacturing errors are absent. Since load sharing does not occur in unloaded conditions, the results obtained for a single flank pair can be extrapolated to the neighboring teeth flank pairs. Therefore, the results of a *single flank analysis* provide sufficient information to determine the unloaded contact behavior of the gear pair.

As mentioned in Section 2.1.2, typical results for unloaded TCA, such as the unloaded transmission error (UTE) and the contact point path (CPP), can be elegantly obtained by combining the surface of roll angles and the ease-off topography of a single flank pair. This process has been described in [63] and is briefly illustrated in the following subsection.

4.2.1   Unloaded transmission error and contact point path

The main idea behind an ease-off topography-based approach to UTCA is that the contact detection can be simplified by first establishing the contact between a chosen flank and its conjugate flank. In the described procedure the pinion flank is selected as the input flank such that the ideal instantaneous contact curve is computed based on this pinion flank's surface of roll angles. The true instantaneous contact curve is computed in a second phase by accounting for the difference between the conjugate gear surface and the real gear flank, which is captured in the gear-based ease-off topography. Both steps of this procedure are illustrated in Fig. 4.6 for an instantaneous value of roll angle $\phi_{z,i}^{(1)}$.

For any value $\phi_{z,i}^{(1)}$ of the pinion's roll surface $\mathcal{R}_\phi^{(1)}$ it is possible to define an *instantaneous contact curve* such that all the contact points have the same value of pinion roll angle, as shown in Fig. 4.6. First, an *instantaneous curve of potential contact points* is computed from the intersection of a plane with constant pinion roll angle $\phi_{z,i}^{(1)}$ and the surface of pinion roll angles $\mathcal{R}_\phi^{(1)}$, which is defined on the gear-based projection plane. Such a contact search is numerically more efficient compared to finding the contact points as the solution to a system of nonlinear equations, in which the surfaces are considered to be arbitrary. The potential contact points are projected onto the projection plane to determine the contact locations on the tooth flank. The instantaneous contact curves ς_θ (angular units) and ς_δ (linear units) are established by computing the ease-off value for each point of the projected contact curve, using the ease-off topographies $\mathcal{E}_\theta^{(2)}$ and $\mathcal{E}_\delta^{(2)}$ respectively. Depending on the ease-off topography, the line contact, present for the instantaneous curve of potential contact points, evolves into a point contact for the instantaneous contact curve ς. The *instantaneous contact point* (ICP) is the first point on the real pinion flank that contacts the real gear flank for an incremental pinion rotation. As shown in Fig. 4.6b, it is computed from the contact curve ς_θ as the point where the ease-off $\mathcal{E}_\theta^{(2)}$ reaches an (absolute) minimum. Since this ease-off value represents the angle that the conjugate to the pinion flank has to rotate about the gear axis to come into contact with (a point on) the real gear flank, it directly represents the instantaneous transmission error value $TE(\phi_{z1,i})$ in unloaded conditions. To illustrate the contact zone under load, the contact curve length L_c is computed by moving from the ICP along the direction of the contact curve ς_δ (linear scale) within a predefined distance δ_e, (see Section 2.1.1).

By repeating the above process for all values $\phi_{z,i}^{(1)}$ of the pinion roll surface $\mathcal{R}_\phi^{(1)}$, the unloaded transmission error and contact point path of a single flank pair can be determined. The UTE and CPP of the gear pair, analyzed in this work, are presented in Fig. 4.7 and Fig. 4.8 of the next subsection.
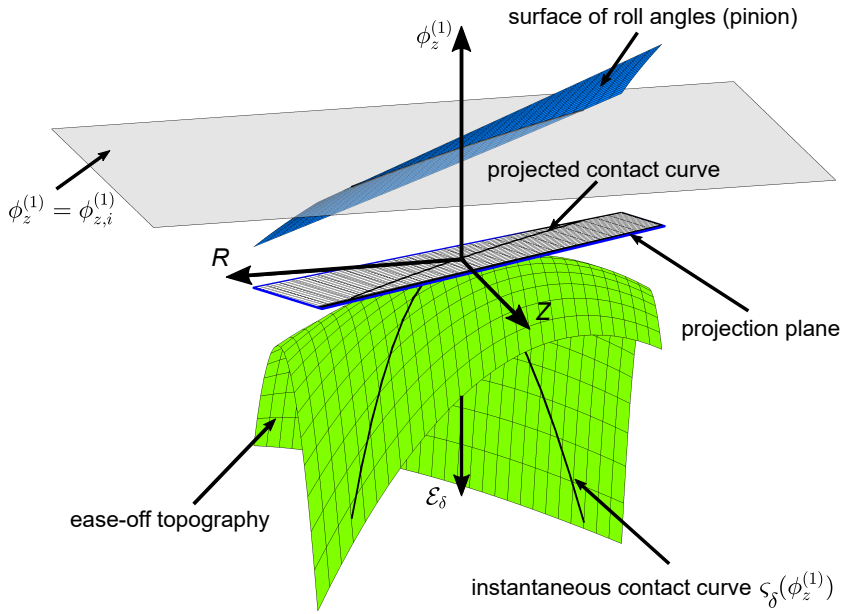
(a) Creation of the instantaneous contact curve ς_δ.
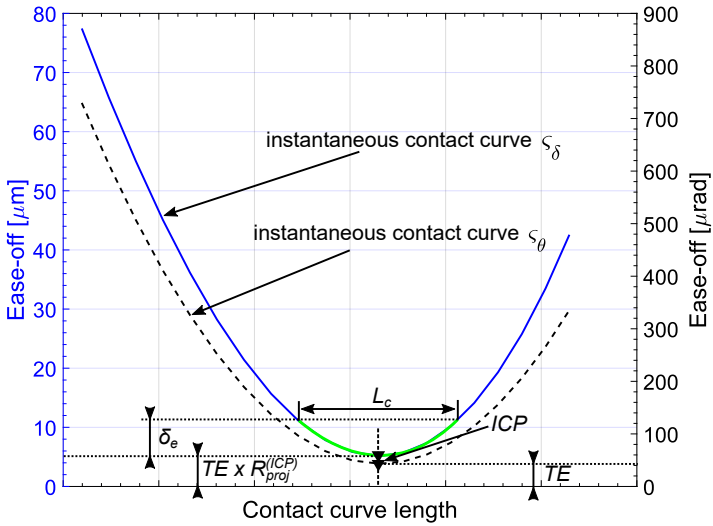
(b) Instantaneous UTE and contact width L_c.

Figure 4.6: UTCA based on the surface of roll angles and the ease-off topography.

4.2.2 UTCA Results

Gear pair data

The unloaded contact behavior of a FM spiral bevel gear pair is analyzed with the developed process for ease-off-based UTCA. The data that defines the analyzed gear pair was taken from the literature [6] to have an additional level of validation during the development process. In the literature this gear pair has been analyzed with the continuous tangency method (see Section 2.1.1). An overview of the required data can be found in Appendix A.

Results for UTE and CPP

Results for unloaded transmission error and contact point path are reported for the left flank pair in Fig. 4.7 and for the right flank pair in Fig. 4.8. Given pinion's right-handed spiral, the *left flank pair* consists of the convex side of the pinion tooth and the concave side of the gear tooth, while for *right flank pair* contains the concave side of the pinion and the convex side of the gear tooth.

The UTE curves, shown in Fig. 4.7a and Fig. 4.8a, can be determined in two ways. Either a single flank analysis, as described in Section 4.2.1, can be used to compute the UTE of a single flank pair (*tooth pair 0*) and then translated to the neighboring flank pairs (*tooth pairs +1* and *+2*) under the assumption that the periodicity of the UTE corresponds to the angular pitch. Alternatively, the computed surface of roll angles of a single pinion flank can be translated in a similar fashion to the neighboring pinion flanks to simulate a roll test in unloaded conditions. In this case the contact is detected between multiple pinion flanks and their conjugate surface, while the same ease-off topography is used to establish the different instantaneous contact curves. Assuming that each flank has only one instantaneous contact curve, the flank that has the lowest ease-off value on its contact curve will be in contact. This minimum value corresponds directly to the UTE value for the considered roll angle. The resulting UTE curve is described by the envelope to the family of UTE curves that are computed for the individual flank pairs.

The obtained CPP for both tooth pair flanks is shown in Fig. 4.7b and Fig. 4.8b. Since the neighboring tooth pairs can take over the contact as the gear pair rotates, the CPP has to be computed by considering multiple tooth pairs in contact. If this were not the case, the CPP would span the complete gear flank, leading to an unnatural representation of the contact pattern. Besides an indication of the instantaneous contact points, a predefined marking thickness of $\delta_e = 5~\mu m$ is used to illustrate the contact width.
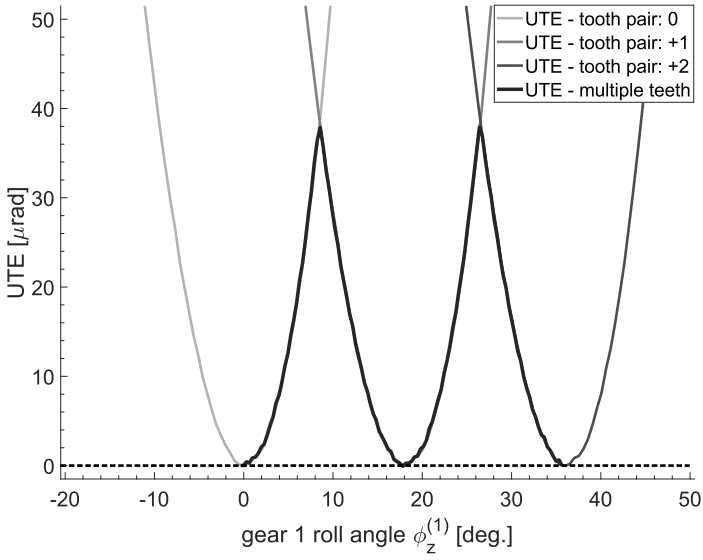
(a) Unloaded tooth transmission error (UTE) for the left flank pair
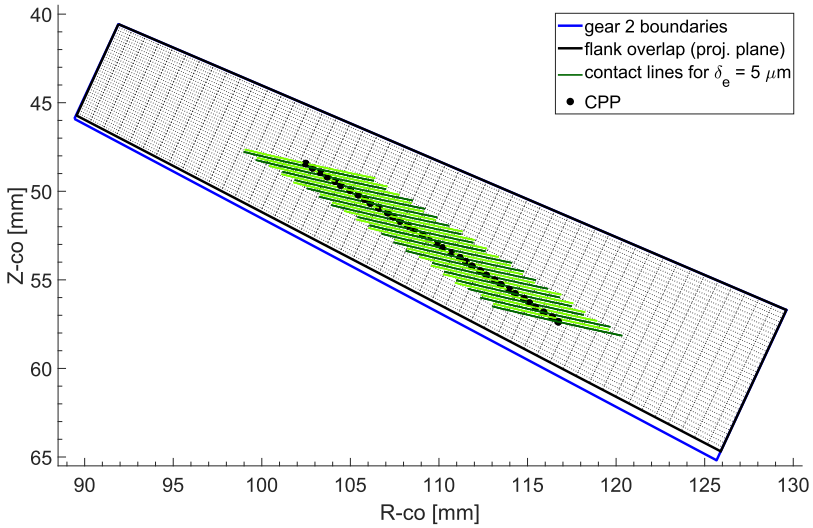
(b) Contact point path (CPP) on the projected left flank of the gear.

Figure 4.7: UTCA results for the analyzed gear pair: left flank pair in contact.
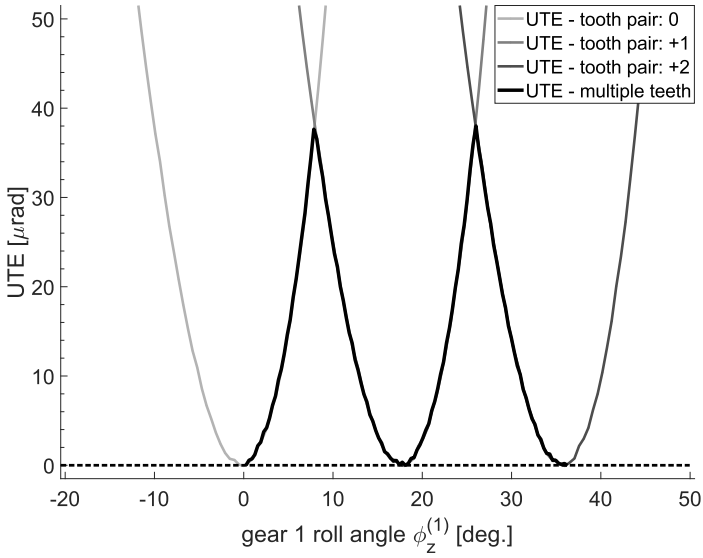
(a) Unloaded tooth transmission error (UTE) for the right flank pair
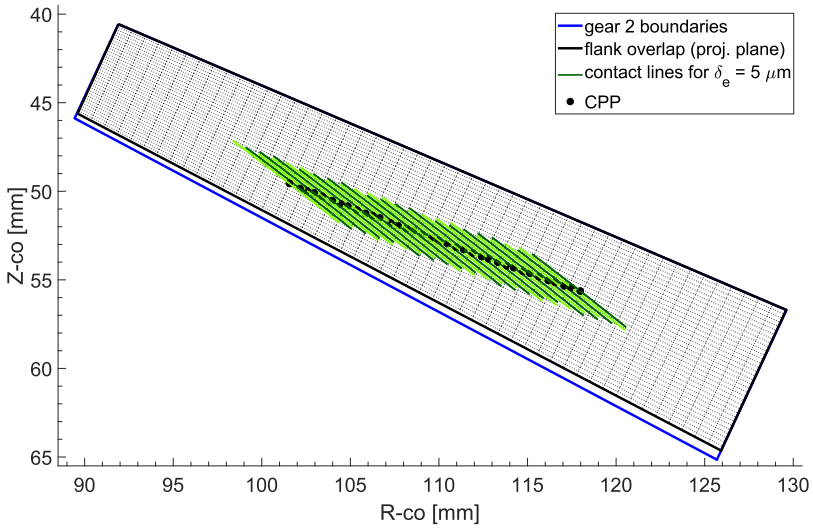
(b) Contact point path (CPP) on the projected right flank of the gear.

Figure 4.8: UTCA results for the analyzed gear pair: right flank pair in contact.

4.3   Conclusion

This chapter lays the emphasis on a correct description of the gear pair's kinematics. Current spiral bevel gear design depends on tooth contact analysis to optimize the machine settings and flank form modifications such that the desired quality of motion transmission can be obtained. Although an a priori definition of the ideal conjugate surfaces is not known, the resulting contact flanks are designed to be close-to-conjugate surfaces. Embedding this knowledge into the contact detection is essential for the computational efficiency of the gear contact model that is developed in the next chapter.

Therefore, the theory of conjugate surfaces is used in Section 4.1 to establish the kinematic relation between a chosen real tooth flank and its computed theoretical conjugate flank. The equation of meshing is used to define the surface that is conjugate to the selected flank and to construct the surface of roll angles for this flank. The surface of roll angles defines the location of the contact points on the surface of action such that it can be used to identify curves of potential contact points. Once the conjugate surface to the real tooth flank is computed, the ease-off topography is constructed to account for the differences that exist between the real mating tooth flank and the conjugate to the selected surface. Since the tooth flank geometry is considered to be predefined, an interpolation strategy was developed to compute the ease-off topography on a newly defined grid that is bounded by the projected flank overlap. By combining the surface of roll angles of the pinion flank with the gear-based ease-off topography for its mating real gear flank, Section 4.2 builds upon the established concepts to create an efficient and accurate procedure for unloaded tooth contact analysis of spiral bevel gear pairs. The process is used to determine the unloaded transmission error and contact point path for both tooth flank pairs of a face-milled spiral bevel gear pair that is also further analyzed in the following chapters.

Chapter 5

A novel spiral bevel gear contact force element

The content of this chapter is based on the following research papers:

- VIVET, M., MUNDO, D., TAMAROZZI, T., AND DESMET, W. An analytical model for accurate and numerically efficient tooth contact analysis under load, applied to face-milled spiral bevel gears. *Mechanism and Machine Theory 130* (Dec. 2018), 137–156

In this chapter a spiral bevel *gear contact force element* (GCFE) is developed that has the potential to be included in a multibody simulation environment. In Section 5.1 a conceptual overview of the GCFE is provided together with the required input data. By taking advantage of the earlier established concepts such as the surfaces of roll angles and the action surfaces for each flank pair, an accurate and computationally efficient penetration-based contact detection algorithm is developed in Section 5.2. In Section 5.3 a load distribution model is developed to translate the detected penetration into resulting contact forces, under the assumption that the flank penetration matches the deformation of the teeth if they were flexible. To model the overall tooth compliance the deformation field is decomposed in a global and a local component. While the global tooth deformation is approximated with a set of expressions that are based on beam theory, the local contact deformation is modeled based on Hertzian contact theory. In Section 5.4 a multibody approach to tooth contact analysis is proposed to validate the GCFE against NL-FEA simulations in terms of transmission error, contact patterns and contact pressure distribution.

5.1 Design of the gear contact force element

A schematic representation of the novel gear contact force element for spiral bevel gears is presented in Fig. 5.1. The force element models the gear pair as two rigid bodies but assumes that the contacting gear teeth deform quasi-statically. Therefore, the inputs to the element are the generalized coordinates $q^{(1)}$ and $q^{(2)}$, which represent the rigid-body DOFs of the pinion and gear, respectively. Each set of rigid-body coordinates contains three translational coordinates and three (e.g. Euler angles or Bryant angles) or four rotational coordinates (e.g. Euler parameters), depending on the parametrization that is used [44]. A specific Bryant angles convention is used by the GCFE to internally describe the rotational motion where needed (see Section 5.2). The outputs of the force element are the generalized contact forces $Q_c^{(1)}$ and $Q_c^{(2)}$ that act on the body-attached frames of the pinion and the gear, respectively.
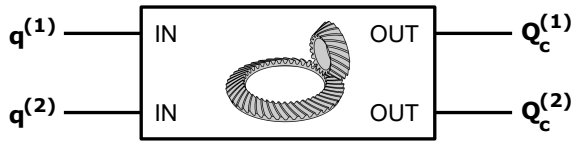
Figure 5.1: Schematic representation of the gear contact force element.

Besides the material-related parameters that are used to compute the load distribution, the force element also requires the following UTCA-related data to perform the three-dimensional contact detection efficiently:

- **Tooth flank geometry.** The GCFE internally represents the contact surfaces of the pinion and of the gear as a 3D crown of gear teeth. Both the left and the right tooth flanks are included and each flank surface contains both the active and the root sections of the tooth flank. The tooth flank surfaces are discretized according to the procedures of Chapter 3.

- **Surface of roll angles.** Unlike in the UTCA procedure, the gear-based ease-off topography is not used by the GCFE to determine contact since it depends on the instantaneous configuration of the gear pair. In the GCFE the ease-off is replaced by a penetration-based contact detection algorithm that uses the surfaces of roll angles of both the pinion and gear flanks. The required surfaces are computed during preprocessing for the active parts of the tooth flanks. Updating the surface of roll angles allows to efficiently include effects of gear pair misalignments in Chapter 6.

- **Initial values.** The initial rotation of the gear and pinion can be defined by the user in order to acquire the desired phasing of the gear pair. Alternatively, the rotation of the gear pair can also be determined automatically by using the pinion's surface of roll angles to reconstruct the gear-based ease-off topography of the reference tooth flank pair for the initial flank overlap. In the latter case the gear pair is rotated such that the reference flank pair is in contact (i.e. where the ease-off is minimal) at the start of the simulation.

The working principle of the gear contact force element can be divided into two major tasks: (i) detection of the contact for multiple and varying flank pairs, and (ii) a correct translation of the detected penetration into contact loads. Both aspects are addressed in the remainder of this chapter.

5.2 Penetration-based contact detection

Similarly to cylindrical gears, where the (roll) angle of the involute is used to express the position of the contact points on the line/plane of action [54], the surface of roll angles can be used to accurately and efficiently compute the contact location on the surface of action for spiral bevel gears. This methodology was already illustrated in Chapter 4 for the UTCA process and is now extended to loaded conditions. To this end, the gear-based ease-off topography is replaced by the surface of roll angles of the real gear flanks during the development of the novel GCFE for spiral bevel gears.

The contact detection methodology is described by considering only one type of flank pairs, i.e. either the right or the left flank of the tooth, since the process to include the other flank pairs is identical.

5.2.1 The challenge of ease-off topography in a general gear contact force element

By including the surfaces of roll angles for both the real pinion and the real gear flanks, a contact detection methodology, similar to the ones that exist for cylindrical gears [38], is developed. As such, the contact locations are directly identified on the real teeth flanks (for both the pinion and the gear) without the requirement of the ease-off topography but rather based on the computed penetration of the real flank geometry. The choice to include the surfaces of roll angles of both the real flanks rather than the ease-off topography of the flank pair proves highly relevant for a general case, in which the gear pair's relative

configuration and rotations are no longer predetermined but rather the result of the component compliance, external forces and arising contact forces.

Although both the gear-based ease-off topography and the surface of roll angles of the gear flank contain equivalent information; nl. they allow to compute the contact line on the gear flank and indicate the geometrical error between the real gear and pinion flanks, the ease-off topography poses a challenge when the general case is considered. In this dissertation, gear pair misalignments that can occur during a multibody simulation are considered as an example of such a case. In sections 2.1.2 and 4.1.3 it has been explained that to determine the geometrical error of a mating set of tooth flanks, the ease-off topography is computed on the projected flank overlap using the conjugate to a chosen flank and its real mating flank. When the flank overlap changes due to misalignments (see Section 2.1.2), the complete conjugate flank should be computed to determine its location w.r.t. to the real mating flank and to reestablish the ease-off topography. Performing such an analysis during the contact simulation significantly reduces the computational efficiency of the GCFE. Using both surfaces of roll angles allows to determine the contact points on the real teeth flanks (both for the gear and the pinion) without the requirement of ease-off topography but rather through the penetration of the real flank geometry.

5.2.2 Position and orientation of the gear pair

Within the envisioned multibody simulation environment, the position and the orientation of the pinion and the gear element are defined by their respective generalized coordinates $\boldsymbol{q}^{(1)}$ and $\boldsymbol{q}^{(2)}$. Although the teeth are assumed to deform quasi-statically to compute the resulting contact forces, it is assumed that both gears can be represented as rigid bodies, such that their generalized coordinates only contain the rigid body coordinates.

In the proposed GCFE the position and orientation of each geared body g (e.g. $g = 1$ for the pinion and $g = 2$ for the gear wheel) is expressed w.r.t. the global reference frame S_G. Any point on the tooth surface of the geared body, defined by $\boldsymbol{r}_g^{(g)}$ in the body-attached reference frame S_g, is then expressed in the world frame S_G by:

$$\boldsymbol{r}_G^{(g)} = \boldsymbol{R}_G^{(g)} + \mathbf{A}_g \boldsymbol{r}_g^{(g)} \qquad (g = 1, 2) \qquad (5.1)$$

The global position of the origin of the body-attached reference frame S_g is given by the vector $\boldsymbol{R}_G^{(g)}$. while its orientation w.r.t. S_G is given by the rotation matrix $\mathbf{A}_g$ [105]. The GCFE internally makes use of a set of Bryant angles to parameterize the rotational motion of the geared bodies [44].

An auxiliary reference frame S_B, referred to as the *Base frame*, is computed based on the position and orientation of the body-attached frames S_1 and S_2 to describe the relative position and orientation of the gear pair. The set of Bryant angles $(\phi_x^{(g)}, \phi_y^{(g)}, \phi_z^{(g)})$ is used to express the rotation of each geared body w.r.t. S_B. Since the Bryant angle $\phi_z^{(g)}$ corresponds to the roll angle of each gear, the base frame S_B has to define the relative orientation of the gear pair in correspondence with the equation of meshing, which was used to compute the surface of roll angles during preprocessing (see Fig. 4.2). Conform to the spiral bevel gear literature, which defines the shaft angle γ as a rotation about the Y-axis, the rotational convention *Y-X-Z* is chosen. This allows the rotations about the Y- and Z-axis of S_B to be described in the range of $[0, 2\pi]$, while having its singularity for $\phi_x = \pm\pi/2$.

5.2.3 Contact curves over multiple flank pairs

Using the expressions in [30], the instantaneous rotation angles $\phi_z^{(1)}$ for the pinion and $\phi_z^{(2)}$ for the gear are computed based on the orientation of S_1 and S_2 w.r.t. S_B. Once the instantaneous rotational angles $\phi_z^{(1)}$ and $\phi_z^{(1)}$ for pinion and gear are known, their respective surfaces of roll angles $\mathcal{R}_\phi^{(1)}$ and $\mathcal{R}_\phi^{(2)}$ can be used to determine the potential contact curves on the real tooth flanks.

Number of teeth in contact　In a loaded contact simulation different teeth pair can come into contact as the result of either the rotation of the gears or due to increased loading. An estimate for the number of teeth N_T that are potentially in contact is determined based on the contact ratio ϵ_γ for spiral bevel gears and includes the profile contact ratio ϵ_α and face contact ratio ϵ_β [2]. The calculation of the contact ratio involves the approximation of the spiral bevel gear pair as an equivalent spur gear pair that is seen from the back cone (Tredgold's approximation). Therefore the contact ratio only offers a rough approximation and a safety factor is introduced to overestimate N_T as:

$$N_T = 2\lceil \epsilon_\gamma \rceil + 1 \tag{5.2}$$

Tooth flank pair identification　At the start of each new rotational configuration it is a priori not known which tooth numbers of each geared body forms the tooth flank pairs that are potentially in contact. Therefore, an estimate is made by first identifying combinations of the N_T closest tooth flank pairs, which are computed by evaluating the distance between each pinion flank and each gear flank at the middle of the flank. Since all the teeth of a gear are
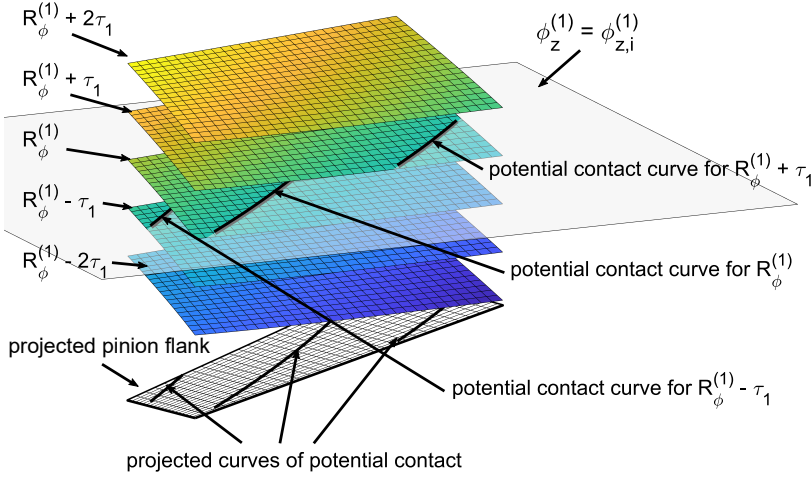
Figure 5.2: Curves of potential contact are created for different pinion flanks, starting from the reference roll surface $\mathcal{R}_\phi^{(1)}$. The contact curves are computed as the intersection of the surfaces of roll angle $\mathcal{R}_{\phi,k}^{(1)}$ with a plane of constant roll angle ϕ_{z1}.

assumed to be identical, the roll surface of each flank k of the gear pair can be computed based on the tooth number T_k and the angular pitch τ. Adopting a clock-wise tooth numbering when looking at the face cone of the spiral bevel gears (see Fig. 3.1a), the roll surfaces for tooth pair k are found by Eqs. (5.3) and (5.4) for the pinion and the gear flanks.

$$\mathcal{R}_{\phi,k}^{(1)} = \mathcal{R}_\phi^{(1)} - (T_k^{(1)} - 1)\,\tau_1 \qquad\qquad \tau_1 = \frac{2\pi}{Z_1} \qquad\qquad (5.3)$$

$$\mathcal{R}_{\phi,k}^{(2)} = \mathcal{R}_\phi^{(2)} - (T_k^{(2)} - 1)\,\tau_2 \qquad\qquad \tau_2 = \frac{2\pi}{Z_2} \qquad\qquad (5.4)$$

Curves of potential contact points   While in Chapter 4 a common projection plane was used onto which the ease-off topography and surface of roll angles had been defined, the GCFE works directly with the discretized flank geometry such that the flank's surface of roll angles is stored directly onto the grid of the respective flank. However, the procedure to compute the potential contact curves remains the same as explained in Section 4.2.2. As illustrated in Fig. 5.2 for a pinion flank, multiple potential contact curves are created

onto the projected pinion flank as the intersection of a plane with constant roll angle ϕ_z and the surfaces of roll angle $\mathcal{R}_{\phi,k}$. Since N_T is defined to be an overestimation of the number of teeth in contact, it is more than likely that a curve of potential contact points cannot be created for certain flank pairs k. In Fig. 5.2 these flanks are the ones that have roll surfaces $\mathcal{R}_\phi^{(1)} - 2\tau_1$ and $\mathcal{R}_\phi^{(1)} + 2\tau_1$. The same procedure can be established for the gear flanks by using the gear's surface of roll angles $\mathcal{R}_\phi^{(2)}$ and the gear's rotational angle $\phi_z^{(2)}$.

Slicing of the flank overlap For a general mismatched flank pair (non-conjugate) the use of two surfaces of roll angles, one for each of the real flanks, results into two curves of potential contact points, which do not coincide when projected onto the flank overlap, as illustrated in Figure 5.3. Therefore, KOLIVAND [65] proposed to replace the contact line of the real gear with the one of the conjugate to the real pinion when solving for the conditions of compatibility and equilibrium, since it would change the orientation and shape of the contact curve very little due to the high level of conformity between the mating flanks. In that case contact is determined based on the pinion's roll surface and the gear-based ease-off topography. Since in this work the contact forces are computed from the computed penetration between the real
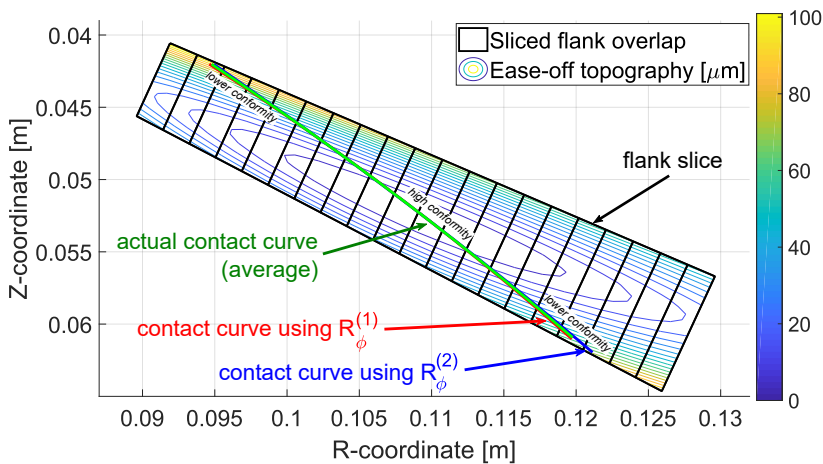
Figure 5.3: Actual contact curve (green) computed as the average of the contact curves, determined with roll surfaces $\mathcal{R}_\phi^{(1)}$ (red) and $\mathcal{R}_\phi^{(2)}$ (blue). The ease-off contours are added to indicate zones of high conformity.

tooth flanks, a new *actual contact curve* is determined as the average of both contact curves by dividing the flank overlap into a finite number of slices and by computing maximum one actual contact point for each of the tooth slices.

This extension fits well in the philosophy of the envisioned multibody approach, where the system's behavior is influenced by each individual body (i.e. gear). Geometrical effects of both real tooth surfaces in mesh are included to better approximate of the contact curve in low conformity regions. Moreover, this approach correlates naturally with commonly adopted concepts that simplify the contact detection between cylindrical involute gear teeth. There, the concept of the roll angle of the involute is used to express the contact position on the tooth flank along the line/plane of action for each gear [38]. The methodology, as it is formulated here, generalizes these well-known concepts for contact detection.

Furthermore, it will be shown in Chapter 6 that the surfaces of roll angles, computed for an aligned gear pair, can still provide a good approximation for the contact locations when the gear flanks become misaligned. Consequently, transmission error and contact pattern remain well-approximated, since the gear contact force model always accounts for the actual position and orientation of the (misaligned) real gear tooth surfaces, when computing the contact loads. An ease-off based contact detection method cannot provide a similar prediction without computing the ease-off topography for the misaligned gear flank pair.

5.2.4 Flank penetration

For each of the actual contact points (2D) the corresponding pinion and gear points (3D) are computed in order to determine the penetration between the mating flanks. The *flank slice penetration δ* is then computed by first calculating the distance between the point in the pinion flank $\boldsymbol{r}_G^{(1)}$ and the corresponding point on the gear flank $\boldsymbol{r}_G^{(2)}$, both expressed in the global reference frame S_G. The distance between the flank slices is then projected onto the local contact normal $\boldsymbol{N}_G^{cont}$ to obtain the flank slice penetration δ.

$$\delta = \left(\boldsymbol{r}_G^{(1)} - \boldsymbol{r}_G^{(2)} \right) \cdot \boldsymbol{N}_G^{cont} \tag{5.5}$$

$$\boldsymbol{r}_G^{cont} = \frac{1}{2} \left(\boldsymbol{r}_G^{(1)} + \boldsymbol{r}_G^{(2)} \right) \tag{5.6}$$

$$\boldsymbol{N}_G^{cont} = \frac{1}{2} \left(\boldsymbol{N}_G^{(1)} - \boldsymbol{N}_G^{(2)} \right) \tag{5.7}$$

The contact location $\boldsymbol{r}_G^{cont}$ is defined in the global frame S_G as the average of the contact point on the pinion and on the gear. The direction of the contact

normal $\boldsymbol{N}_G^{cont}$ is also computed in S_G as the average of the directions of the respective surface normal vectors $\boldsymbol{N}_G^{(1)}$ and $\boldsymbol{N}_G^{(2)}$, given by Eqs. (5.8) and (5.9). The surface normal vectors are evaluated at the contact points on the respective flanks. Since both flanks are penetrating their respective contact points are not coincident and their surface normal will not be collinear. Although such deviations are expected to be small, the averaging is still performed to compute a common contact point and contact direction along which the contact force can be applied to both gears.

$$\boldsymbol{N}_G^{(1)} = \mathbf{A}_1 \boldsymbol{N}_1^{(1)} \tag{5.8}$$

$$\boldsymbol{N}_G^{(2)} = \mathbf{A}_2 \boldsymbol{N}_2^{(2)} \tag{5.9}$$

5.3   Tooth compliance modeling

The tooth contact forces that act on the individual tooth slices, are computed under the assumption that the measured penetration between two rigid tooth surfaces is identical to the deformation that these surfaces would experience if they were flexible. Adopting the idea of ANDERSON and VEDMAR [5], the deformation between the contacting tooth slices is modeled as the result of two contributions; (i) a local contribution that describes the deformation in the region of contact between the two bodies, and (ii) a set of global contributions that describe the deflection of the individual teeth outside the contact zone. In the presented model each of the contributions is modeled in an analytical way.

5.3.1   An analytical model for local tooth compliance

For a general case of mismatched flanks the instantaneous contact between two meshing flanks can be described as a point contact under no-load conditions. Under load this point contact spreads into a line contact that runs over a part of the tooth flanks. Therefore, a Hertzian line contact, oriented along the direction of the contact curve, is assumed for each of the contacting tooth slices. The nonlinear *contact deformation d_c*, which represents the combined deformation of the pinion and gear flanks near the contact zone due to the contact load F_c that is distributed over a contact curve segment of length l_c, can be described with a closed-form formula that was derived by WEBER and BANASCHEK [135].

$$d_c = \frac{F_c}{\pi l_c} \left(\frac{1 - \nu_1^2}{E_1} + \frac{1 - \nu_2^2}{E_2} \right) \left[\ln \left(\frac{4\, h_C^{(1)} h_C^{(2)}}{a^2} \right) - \frac{1}{2} \left(\frac{\nu_1}{1 - \nu_1} + \frac{\nu_2}{1 - \nu_2} \right) \right] \tag{5.10}$$
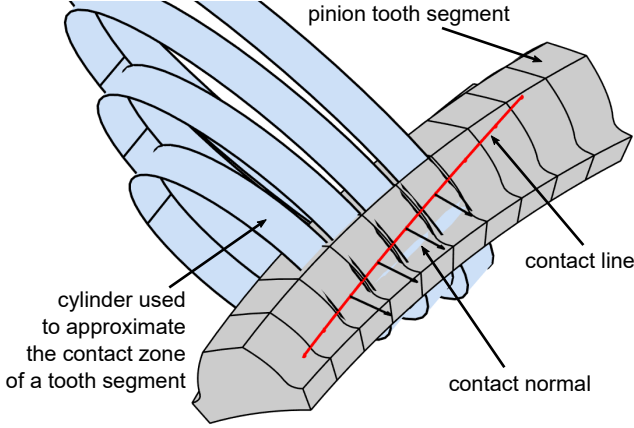
Figure 5.4: A Hertzian line contact is adopted to describe the contact deformation of each pair of tooth segments. The line contact is oriented along the contact direction, while the surfaces are locally approximated as cylinders.

Eq. (5.10) was derived under the assumption that in the proximity of the contact the two contacting flanks can be well represented as cylinders with radii of curvature $\rho^{(1)}$ and $\rho^{(2)}$, as illustrated in Fig. 5.4. The parameters $h_C^{(1)}$ and $h_C^{(2)}$ correspond to the distance along the contact direction from the point of contact to the center of the tooth slice for the pinion and the gear, respectively. An example for a general h_C is given in Fig. 5.5b. HERTZ derived the analytical formulas that allow to approximate the half contact width a and the maximum contact pressure p_0 at the surface as functions of a contact load F_c [56].

$$a = \left[\frac{4F_c}{\pi l_c} \rho^* \left(\frac{1 - \nu_1^2}{E_1} + \frac{1 - \nu_2^2}{E_2} \right) \right]^{1/2} \tag{5.11}$$

$$p_0 = \frac{2F_c}{\pi a l_c} \tag{5.12}$$

The material characteristics are taken into account through the Young's moduli E_1 and E_2 and the Poisson's ratios ν_1 and ν_2 of the pinion and of the gear, respectively. The relative radius of curvature ρ^* accounts for the relative curvature of the two cylinders at the contact point [56].

$$\frac{1}{\rho^*} = \frac{1}{\rho^{(1)}} + \frac{1}{\rho^{(2)}} = \kappa_n^{(1)} + \kappa_n^{(2)} \tag{5.13}$$

The normal curvatures $\kappa_n^{(1)}$ and $\kappa_n^{(2)}$ in Eq. (5.13) are obtained for each of the contact points by evaluating Euler's curvature formula, given by Eq. (3.22), along the direction $\boldsymbol{t}$ of each local contact segment.

5.3.2 An analytical model for global tooth compliance

The global deformation d_g of a single tooth is approximated by assuming that the gear body remains undeformed, while the crown of gear teeth are deformable. Tredgold's approximation is applied to each tooth slice, where penetration is detected, to estimate the global compliance of a single gear tooth in contact. Within this simplification the (spiral) bevel gear pair is approximated by an equivalent spur gear pair when viewed from the back cone, as shown in Fig. 5.5a. For each tooth slice of the spiral bevel gear element the tooth flank geometry is modeled in the transverse plane by fitting an involute profile onto the existing tooth flank geometry. Each equivalent involute tooth profile is then projected to the local normal plane to determine the required tooth slice dimensions.

To match the direction of the contact force, defined by the contact normal $\boldsymbol{N}_G^{cont}$, the deformation of the tooth segment is computed in a plane that is local to the tooth surface at the contact point. Based on the dimensions of the resulting tooth profile in the normal plane (see Fig. 5.5b), the tooth segment's global compliance is estimated by using a set of expressions that were derived by NAKADA and UTAGAWA [87]. The bending d_b, shear d_s and gear body foundation d_f deformation contributions are computed by approximating each tooth slice of width w_s as a beam with variable thickness.

$$
\begin{aligned}
d_b = {} & \frac{12 F_c s_F \cos^2(\alpha_n)}{E\ w_s\ t_F^3} \left[s_M + \frac{s_F^3}{3} - s_F s_M \right] \\
& + \frac{6 F_c (s_0 - s_F)^3 \cos^2(\alpha_n)}{E\ w_s\ t_F^3} \left[\frac{s_0 - s_M}{s_0 - s_F} \left(4 - \frac{s_0 - s_M}{s_0 - s_F} \right) \right. \\
& \hspace{6cm} \left. - 2 \ln\left(\frac{s_0 - s_M}{s_0 - s_F} \right) - 3 \right]
\end{aligned}
\tag{5.14}
$$

$$
d_s = \frac{2(1 + \nu) F_c \cos^2(\alpha_n)}{E\ w_s\ t_F} \left[s_F + (s_0 - s_F) \ln\left(\frac{s_0 - s_F}{s_0 - s_M} \right) \right] \tag{5.15}
$$

$$
d_f = \frac{24 F_c s_M^2 \cos^2(\alpha_n)}{\pi\ E w_s\ t_F^2} \tag{5.16}
$$

$$
s_0 = \frac{s_T t_F - s_F t_T}{t_F - t_T} \tag{5.17}
$$

The resulting *global deformation* d_g at the contact point of the segment is found as the sum of the individual contributions:

$$
d_g = d_b + d_s + d_f \tag{5.18}
$$
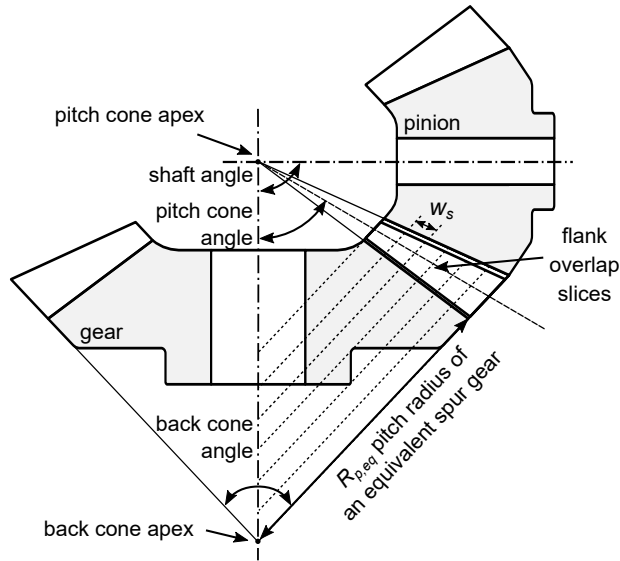
(a) Tooth slicing, viewed in the axial plane
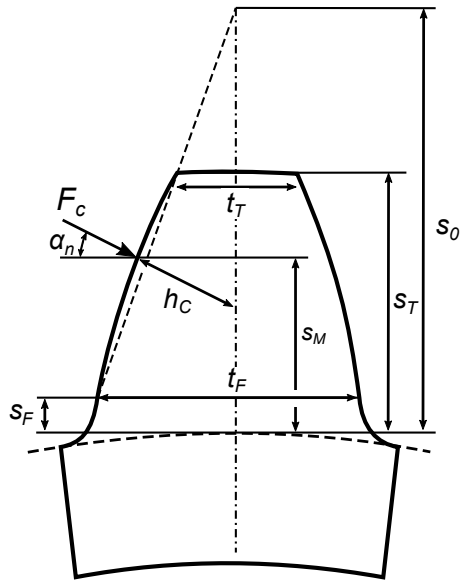
(b) Tooth dimensions, viewed in the normal plane

Figure 5.5: To compute the global compliance components each tooth slice profile is approximated as an equivalent involute tooth in the transverse plane and the dimensions are projected onto the local normal plane.

The tooth thickness in the normal plane at the bottom t_F and top t_T of the active flank are computed by projecting the transverse tooth thickness values of the equivalent spur gear onto the normal plane. The transverse tooth thicknesses for the equivalent spur gear are computed based on the actual tooth geometry. The tooth thickness is computed at the front and the back of the gear tooth and assumed to vary linearly across the face width. The tooth heights s_F, s_T, s_0 at the bottom and the top of the active flank and at the intersection with the tooth's mid plane are directly computed from the tooth flank slice geometry.

Validity of the analytical global compliance model

NAKADA and UTAGAWA originally formulated Eqs. (5.14) to (5.17) to estimate the tooth stiffness of spur cylindrical gears [87]. ELKHOLY applied their model, combined with Tredgold's approximation, to analyze straight bevel gears [34]. Within the scope of the dissertation the presence of the spiral angle is included by locally projecting the equivalent spur tooth geometry onto the normal plane.

While the model can offer a good first estimation of the spiral bevel gear tooth stiffness, some considerations are made to identify its validity and limitations.

Since the analytical global compliance model does not include the gear blank, inherently the blank is assumed rigid with only the teeth deforming under load. Therefore, in case of lightweight blank design or under high operational loading, where the gear blank's deformation is non-negligible, the model lacks accuracy.

Furthermore, the gear teeth deflections are also described uncoupled, meaning that the loading of one tooth slice does not deform the other teeth slices. Consequently, the model cannot predict the deformation of surrounding gear teeth due to the loading of an adjacent tooth. Here, it can only offer an estimate of the load sharing between multiple gear teeth pairs in contact at high loads. Although the global slice deformation is computed in the normal plane and in the direction of the contact load, the absence of coupling between the neighboring tooth slices on the same tooth flank is expected to affect the accuracy of the load transfer along the tooth spiral direction in case of highly curved gear teeth.

Finally, the linearly varying tooth height assumption seems to better suit slender gear teeth, although further investigation is required to confirm this assumption.

Improving the global compliance's modeling fidelity can address such limitations, e.g. change the analytical model with a numeric FEM-based one (see Chapter 7).

5.3.3   Computation of the gear contact forces

The contact forces for pinion and gear are computed as the result of the individual contact forces that are acting between the different tooth segments. The *total deformation d_t* of two contacting flank segments is found as the combination of the global deformation of the pinion $d_g^{(1)}$ and of the gear $d_g^{(2)}$, and the contact deformation d_c. Considering that at a given moment during the simulation N_T tooth pairs are possibly in contact (i.e. penetrating or not) and that each flank of the tooth pair is discretized into N_S segments, the total deformation $d_{t,ki}(F_{c,ki})$ for a single flank pair slice s of tooth pair t becomes:

$$d_{t,ts}(F_{c,ts}) = d_{g,ts}^{(1)}(F_{c,ts}) + d_{g,ts}^{(2)}(F_{c,ts}) + d_{c,ts}(F_{c,ts}) \qquad (5.19)$$

The contact force F_{ki} that acts on the flank pair segment is found by assuming that the total deformation $d_{t,ts}$ is the same as the penetration δ_{ts} that is computed by Eq. (5.5) under the assumption that contacting flanks are rigid surfaces.

$$\delta_{ts} = d_{g,ts}^{(1)}(F_{c,ts}) + d_{g,ts}^{(2)}(F_{c,ts}) + d_{c,ts}(F_{c,ts}) \qquad (5.20)$$

If no penetration between the flank segments is detected, the contact force F_{ts} for that segment pair is considered to be zero. Otherwise the contact force is computed by numerically inverting Eq (5.20). The resulting contact forces $\boldsymbol{Q}_c^{(1)}$ and $\boldsymbol{Q}_c^{(2)}$ that act on the pinion and gear body, respectively, are found as the result of the individual contact forces magnitudes $F_{c,ts}$ of each segment.

5.4   A multibody approach to TCA

To validate the proposed methodology and to demonstrate its capabilities, the novel gear contact force element is applied to the loaded tooth contact analysis of the spiral bevel gear pair, whose unloaded contact behavior was already analyzed in Section 4.2. Appendix A contains an overview of all the important gear geometry and material-related data. To acquire the reference data that is needed to validate the methodology, a FEM-based model of the spiral bevel gear pair is created. The FE-based LTCA of the gear pair is conducted as a series of static contact simulations, which are computed by using NX Nastran (SOL 601), a commercial software package for NL-FEA [107]. The validation of the GCFE is based on a comparison of the obtained results in terms of static transmission error, contact curves and contact pressure.

5.4.1 A multibody representation of the spiral bevel gear pair

By using the developed gear contact force element, a multibody (MB) approach to tooth contact analysis is achieved that can be used to simulate the static contact behavior of spiral bevel gears. While the force element could also be applied to the dynamic simulation of spiral bevel gear pairs, dynamic studies are postponed for future work since this dissertation focuses on the the development and validation of the static behavior of the gear pair. A representation of the multibody model of the spiral bevel gear pair under analysis is shown in Fig. 5.6.

Model setup

The gear pair is modeled as a set of rigid bodies such that position and orientation of each body in space are defined by 6 DOFs. To correctly validate the GCFE the LTCA is performed by constraining the MB model in such a way that it is easily compared in Section 5.4.3 with the NL-FEA results. Therefore, both geared bodies are connected to a ground body to remove their respective DOFs. The pinion is constrained so that it can only rotate about the z-axis of the body-attached frame S_1, whereas the gear body is clamped to ground to remove all of its DOFs during each step of the contact simulation. The deflections of the gear teeth under load are taken into account by the GCFE that is defined by using the body-attached frames of the pinion S_1 and the gear S_2. An external torque is applied to the pinion in the global reference frame S_G, such that the spiral bevel gear pair can be loaded with a desired constant load.
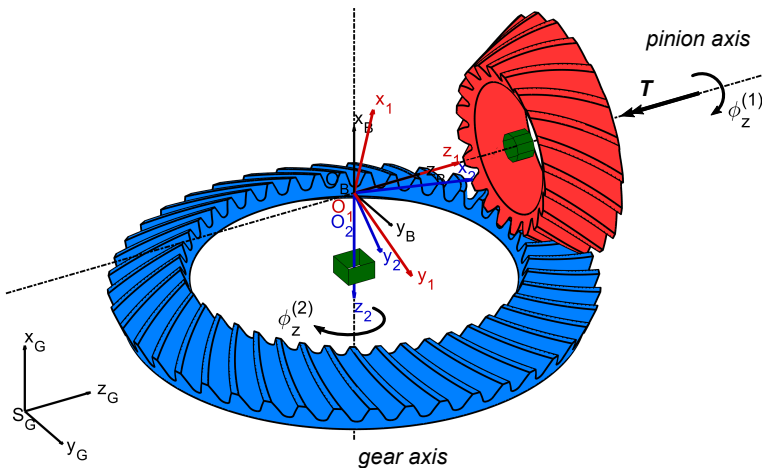
Figure 5.6: Multibody model of the analyzed spiral bevel gear pair.
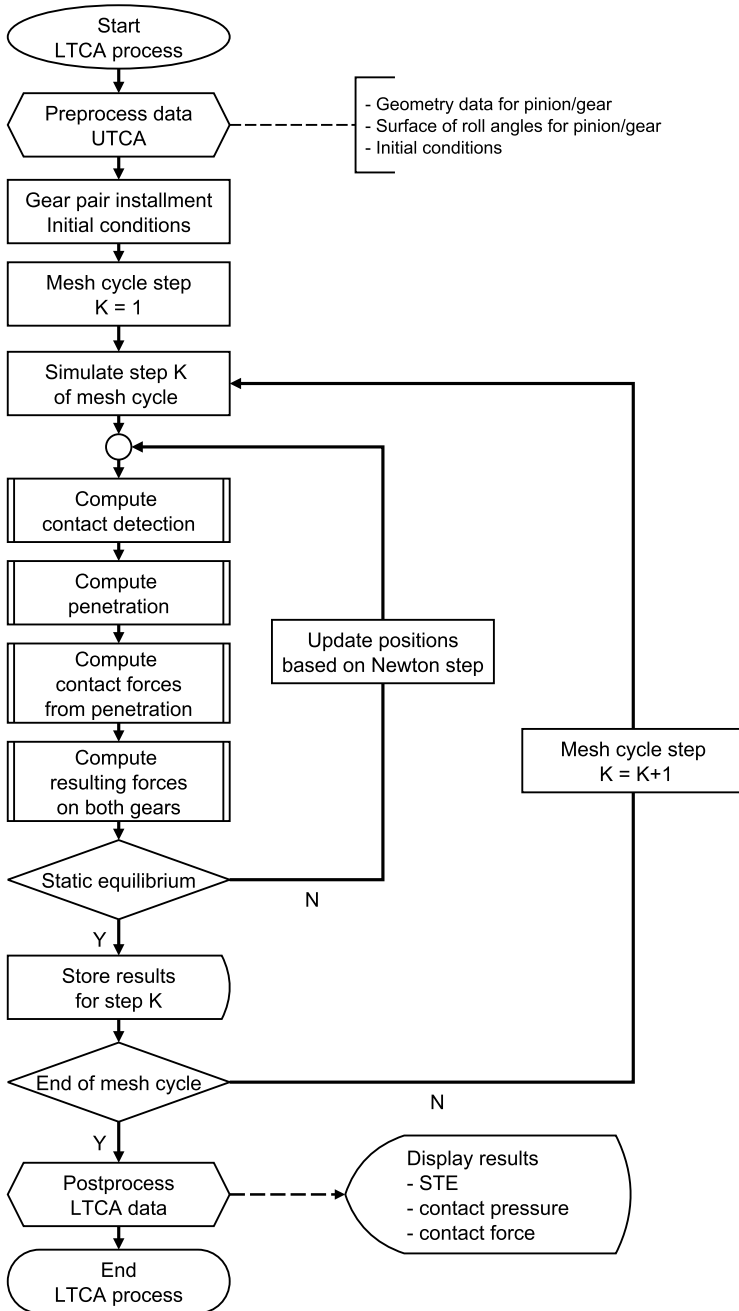
Figure 5.7: Schematic overview of the multibody approach to loaded tooth contact analysis (LTCA), using the proposed gear contact force element (GCFE).

LTCA process

A schematic overview of the working principles of the GCFE during the LTCA process is shown in Fig. 5.7. The initial values that place both real gear flanks in contact at their conjugate point at the start of the simulation, are computed through the use of the gear-based ease-off topography and the surface of roll angles for the pinion flank, using the methodology of Chapter 4 for the predefined tooth flank geometry. Using an iterative procedure the pinion's rotation about its rotational axis is updated until static equilibrium is achieved for the applied constant load. The arising contact forces are computed as the result of the gear tooth flank penetration, which is measured during the contact simulation by the developed contact detection algorithm. At the end of each static simulation the contact points, the contact forces and the contact pressures are stored for postprocessing. Based on the pinion rotation angle $\phi_z^{(1)}$ and gear rotation angle $\phi_z^{(2)}$ at equilibrium, the instantaneous value for the static transmission error (STE) is computed with Eq. (2.4). The next step of the mesh cycle is simulated by appropriately updating the generalized coordinates of both the pinon and the gear, such that the GCFE can compute the contact forces for the next step. The process is repeated until a full mesh cycle is simulated.

5.4.2 Creation of the FEM-based reference model

The FEM-based contact simulations purpose the creation of reference LTCA data sets to validate the presented bevel gear contact model at component-level. Results of interest are the STE curves, the overall contact pressure distribution and the local contact curves to provide both global and local evaluation of the gear contact model. Such metrics are commonly used in the gear literature to rate the performance of a spiral bevel gear set [7, 64, 77].

Finite element model creation

A FEM-based representation of the gear pair is created to serve as a reference model for the validation of the developed spiral bevel gear contact force element. Using the procedures that are described in Section 3.4, both the pinion and gear geometry (blank and teeth) are discretized as a set of connected 3D solid elements (HEXA8) for which the tooth flank nodes are directly computed during the simulation of the manufacturing process. The mixed-mesh approach of Fig. 3.13 is used to reduce the overall model size and thus the required computation time. Fig. 5.9 shows the resulting FE-model.
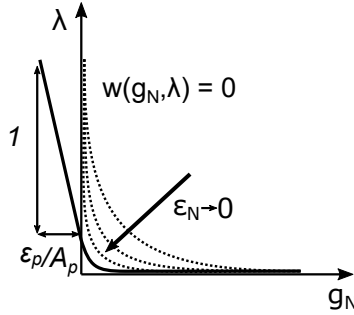
Figure 5.8: Effect of contact compliance on the constraint function $w(g_N, \lambda) = 0$.

Contact solver parameters

The contact simulations are computed with NX Nastran's implicit nonlinear solution (SOL 601). The accuracy of this commercial NL-FEA software package is evaluated for application within LTCA of cylindrical and bevel gears in [26].

NX Nastran's SOL 601 uses the ADINA solver to solve the contact problem. Section 2.2.3 explains that this solver uses the constraint function method in combination with Lagrange multipliers to enforce the contact constraints. The contact detection is performed with the NTS method, for which the master and slave contact interfaces are defined on the FE-model's finely meshed gear teeth. Conform to Section 2.2.3, the pinion tooth flanks are selected as the slave surfaces, while the gear tooth flanks are assigned to be the master surfaces within the NTS formulation. With exception of those listed in Table 5.1, the contact solver parameters are kept to the default values (see also [107]).

To reduce contact pressure concentrations, arising from the FEM-discretization, the contact compliance ϵ_p is specified to allow for a penetration magnitude δ between the contacting surfaces before enforcing the contact constraints, via:

$$\delta = \epsilon_p \, p_N \tag{5.21}$$

Fig. 5.8 illustrates the change to the constraint function $w(g_N, \lambda) = 0$ by introducing the contact compliance ϵ_p. Its working principle resembles that of the penalty method, as the contact compliance mimics the behavior of a one-directional spring with stiffness A_p/ϵ_p. The latter follows from the relation

Constraint function	ϵ_N	$[-]$	$1 * 10^{-12}$
Contact compliance	ϵ_p	$[\mu m / MPa]$	$1 * 10^{-03}$

Table 5.1: Contact solver parameters used in the NL-FEA simulations.

between the contact pressure p_N, the contact force λ and the contact area A_p:

$$\delta = \epsilon_p \left(\frac{\lambda}{A_p} \right) \rightarrow \lambda = \left(\frac{A_p}{\epsilon_p} \right) \delta \qquad (5.22)$$

The value for ϵ_p in Table 5.1 is chosen to allow for a penetration of $\delta = 1\ \mu$m in case of a maximum contact pressure $p_N = 1000$ MPa at 200 Nm (see Fig. 5.11).
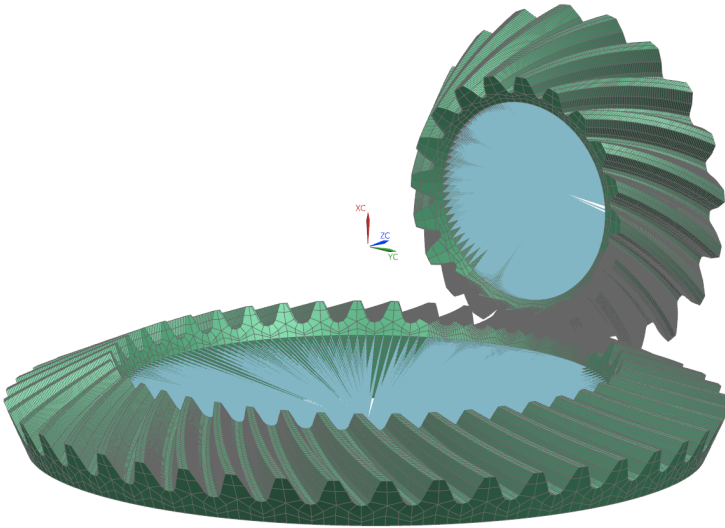
Figure 5.9: Finite element model of the spiral bevel gear pair, used to validate the proposed methodology through nonlinear finite element contact simulations.

	Number of elements [el.]	total	1 tooth (contact)	active profile	root profile	face width
Base	Pinion	242 250 el.	36 750 el.	35 el.	10 el.	75 el.
	Gear	269 850 el.	36 750 el.	35 el.	10 el.	75 el.
Refined	Pinion	329 760 el.	50 400 el.	42 el.	10 el.	90 el.
	Gear	362 880 el.	50 400 el.	42 el.	10 el.	90 el.

Table 5.2: Mesh convergence analysis: Overview of the number of finite elements that are used for the complete model (total) and for the contacting teeth of the *base* and *refined* FE model in specific.

Convergence analysis of the reference model

A mesh convergence analysis is performed to determine the required number of elements that provide the desired trade-off between the accuracy of the results and the computation time, required to obtain those results. Different models are created to study the mesh convergence, such that for each analysis a *Base* model can be compared with a *Refined* model. At each iteration the Refined model is created by increasing the the number of elements by 20 % along the directions of the active profile, the root profile and the face width. The resulting number of elements (el.), used to create the final iteration of the FE gear pair model, are listed in Table 5.2 for the Base and Refined versions. It includes the total number of elements for the complete model and for a single finely meshed gear tooth, together with the number of elements along the profile (active and root) and the face width directions of a single finely meshed gear tooth.

To verify the mesh size convergence of the Base model, its results for transmission error (Fig. 5.10) and overall contact pattern and contact pressure (Fig. 5.11) are analyzed and compared with the results of the Refined model. In this work the root bending stresses are not considered, since the analytical compliance model does not include them. Each static simulation is computed by applying the specified load to the pinion, while the gear element is kept fixed. Considering that mesh discretization effects are more noticeable at lower loads, the mesh convergence study addresses two cases: a nearly unloaded case at 0.01 Nm and a moderately loaded case at 200 Nm for which a clear contact pattern is identified.

Based on the STE curves in Fig. 5.10, and the overall contact pressure distribution in Fig. 5.11, it is concluded that both models produce similar results and that existing differences are small. Thus, allowing the Base model to serve as a good reference model for validating the GCFE.

5.4.3 Numerical validation

A total of eight load levels that range from unloaded contact (0.01 Nm) to highly loaded contact (700 Nm), are applied to validate the gear contact force element.

Using the Base model as the reference FE model, NL-FEA contact simulations are performed and the results for static transmission error, instantaneous contact curves, overall contact pattern and contact pressure distribution are extracted.
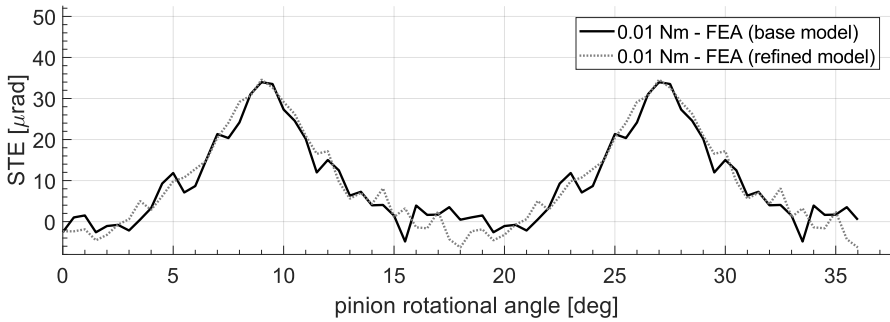
(a) Static transmission error for 0.01 Nm.
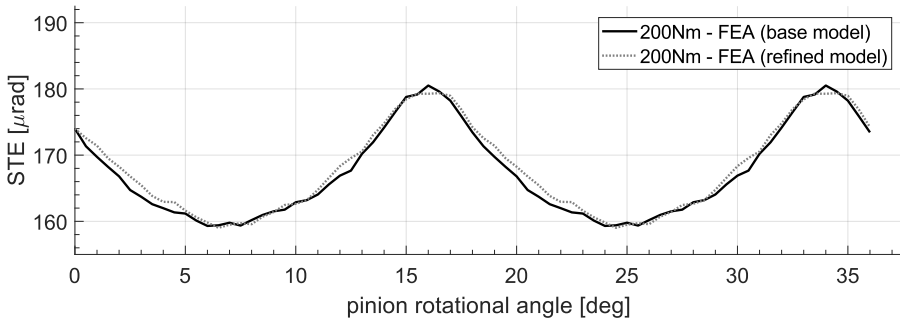
(b) Static transmission error for 200 Nm.

Figure 5.10: Mesh convergence analysis: Static transmission error comparison (right-handed flanks) for the *Base* and *Refined* model at 0.01 Nm and 200 Nm.
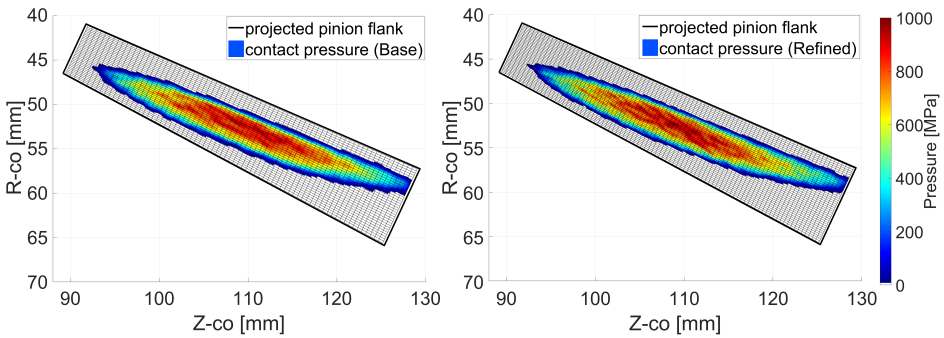
(a) Base FE model.

(b) Refined FE model.

Figure 5.11: Mesh convergence analysis: Contact pressure pattern at 200 Nm.

(a) Contact curves for 200 Nm.

(b) Contact curves for 700 Nm.
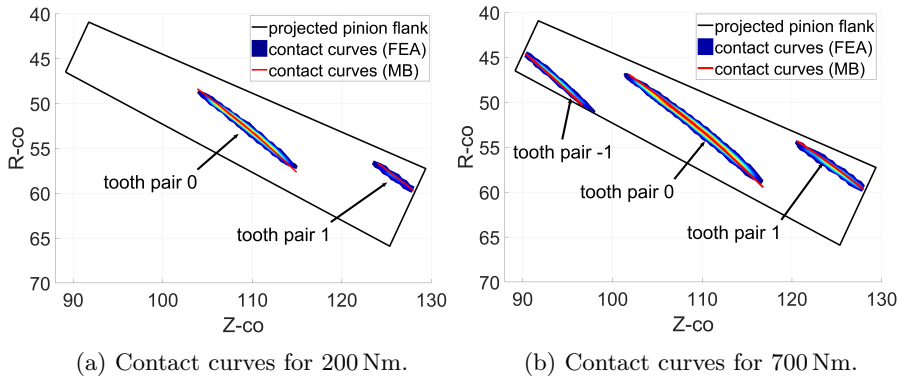
Figure 5.12: Comparison of instantaneous contact curves for 200 Nm and 700 Nm. The tooth flank pair that carries the majority of the load is given index 0, while the neighboring left and right flank pairs are given index -1 and 1, respectively.

Instantaneous contact curves   Figure 5.12 shows the evolution of the instantaneous contact curves for the different tooth flank pairs in contact at the start of the mesh cycle. Since ease-off topography is introduced to the gear pair, only a single tooth flank pair will be in contact for unloaded and lightly loaded conditions. As the load increases, multiple tooth flanks come into contact. Fig. 5.12a and Fig. 5.12b show that for this specific gear pair two and three tooth flank pairs carry the contact at a given load level of 200 Nm and 700 Nm. In order to visualize the results for different tooth flank pairs the contact points of the flank pairs in contact are projected onto a common flank projection for the pinion. The tooth flank that carries the majority of the load is identified through index 0, while the neighboring left and right flank pairs are given index -1 and 1, respectively. The obtained results show that a good correlation in terms of instantaneous contact location is obtained between the reference FE model and the analytical model for loaded contact conditions.

Overall contact pattern   Within experimental TCA a dye or paint is commonly applied to the gear teeth of the physical prototype to reveal the contact pattern that occurs during the roll test as the result of friction between the gear teeth. The shape, location and orientation of the region, where the paint is removed, then provides a natural way to evaluate the quality of the tooth contact. Within simulated LTCA the overall contact pattern is generated by keeping track of the instantaneous contact curves and contact pressures during a full mesh cycle. A comparison between the MB model and the FEA model in terms of overall loaded contact pattern and contact pressure distribution is provided in Fig. 5.13, Fig. 5.14 and Fig. 5.15 for loads of 200 Nm, 500 Nm and 700 Nm, respectively.

(a) GCFE - analyical compliance.

(b) NL-FEA contact simulation.
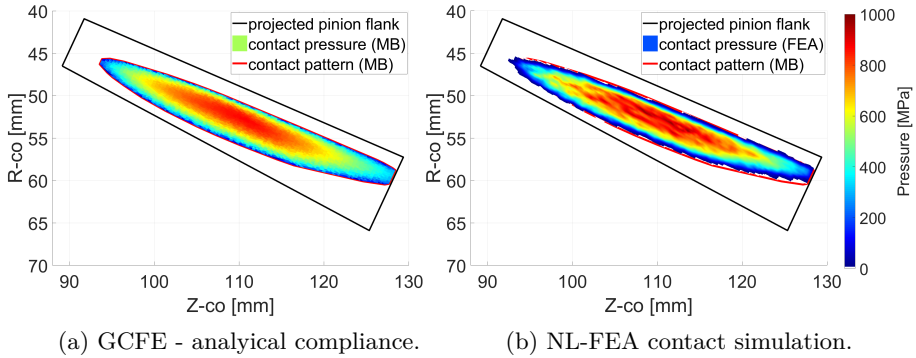
Figure 5.13: Comparison of the overall contact pressure pattern at 200 Nm.

(a) GCFE - analyical compliance.

(b) NL-FEA contact simulation.
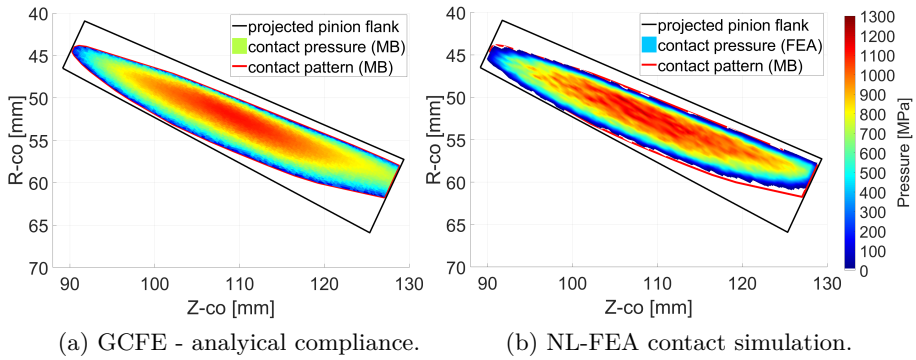
Figure 5.14: Comparison of the overall contact pressure pattern at 500 Nm.

(a) GCFE - analyical compliance.

(b) NL-FEA contact simulation.
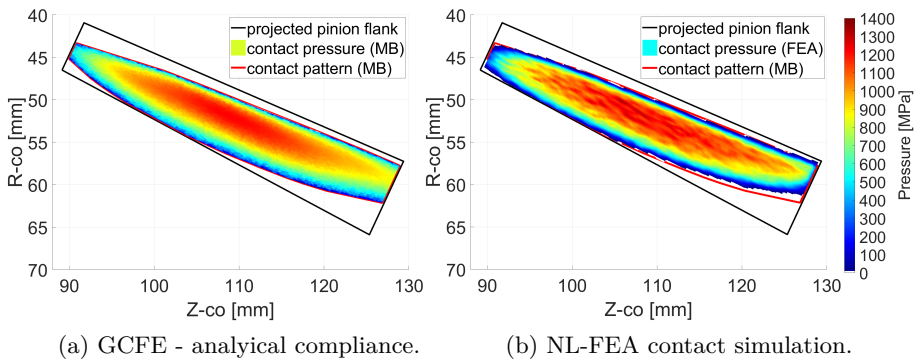
Figure 5.15: Comparison of the overall contact pressure pattern at 700 Nm.

To allow a one-to-one comparison of both models the maximum contact pressure during the mesh cycle is displayed on a projection of the pinion flank. The nodal contact pressure is computed on the nodes of the slave surfaces (pinion) during the NL-FEA contact simulation, while the contact pressure for the analytical model is computed using Eq. (5.12). Fig. 5.13a, Fig. 5.14a and Fig. 5.15a show the overall contact pressure distribution and the boundary of the contact pattern, which are computed with the analytical compliance model of the GCFE for the different load cases. Fig. 5.13b, Fig. 5.14b and Fig. 5.15b in their turn illustrate the overall contact pressure distribution that was obtained through NL-FEA simulations for the same load cases. The contact pattern boundary of the analytical model is also displayed on these figures to facilitate the comparison of the size of the contact patterns.

Results in terms of overall loaded contact pattern for the GCFE show a remarkably good correlation in terms of actual contact region and maximum contact pressure, when compared to the FEA results. While the contact pressure distribution for the FE results is accurately represented, it does show that the effect of mesh discretization is more pronounced for lower load cases (i.e. 200 Nm). The GCFE does not suffer from such effects, since the contact curves that are computed based on the surface of roll angles are less susceptible to mesh discretization. The local contact compliance of Eq. (5.10) also allows to model the contact pressure analytically by assuming that a Hertzian pressure distribution is present across the line load for each of the tooth slices in contact.

Static transmission error   The STE-curves, shown in Fig. 5.16, are analyzed in terms of shape and peak-to-peak value for each load case. Two STE cycles are shown with one cycle repeating itself every 18 deg, indicating that the error in motion transmission occurs according to the (pinion's) gear mesh frequency. Overall the STE curves, predicted by the GCFE, show a good correlation for curve's shape and for the peak-to-peak STE (PP STE) values of Table 5.3.

Similar to cylindrical gears, micro-modifications (ease-off) are also applied to bevel gear flank to counteract the deformation due to loading. Based on the obtained results the designed operating load, where the micro-modifications balance out the deformation and thus minimize the peak-to-peak TE, appears to be located around 100 Nm. Fig. 5.16c shows that for the lower torque ranges the STE is very well predicted, which is a good indicator for the correctness of the contact detection and the local contact compliance model. As the load increases and the teeth start to deform more, differences arise. Such differences are not unexpected since the assumption of an equivalent involute tooth geometry and the uncoupled global compliance formulas of Eqs. (5.14)-(5.18) do introduce some approximations into the model. The effect of load sharing, due to the
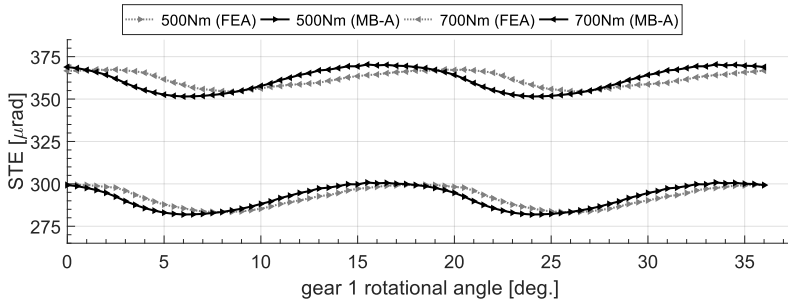
(a) STE curves under highly loaded conditions (500 Nm and 700 Nm).
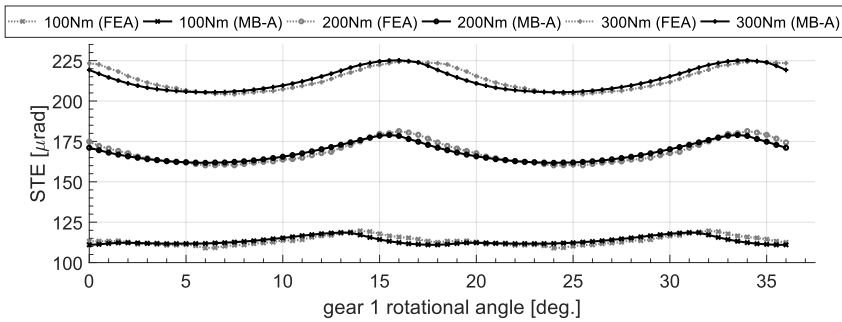
(b) STE curves under moderately loaded conditions (100 Nm, 200 Nm and 300 Nm).
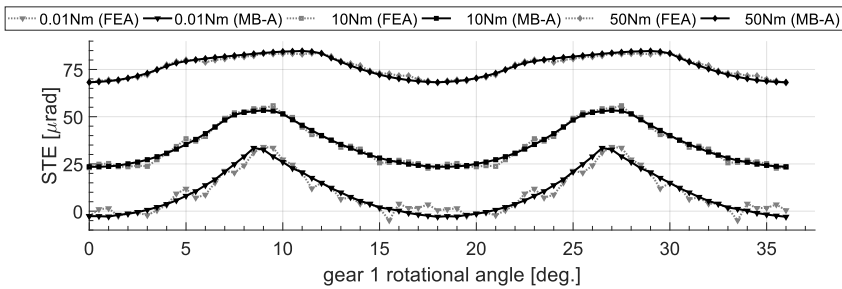
(c) STE curves under lightly loaded conditions (0.01 Nm, 10 Nm and 75 Nm).

Figure 5.16: Comparison of the STE curves from 0.01 Nm to 700Nm for the reference model (FEA) and the GCFE with the analytical tooth compliance formulation (MB-A).

coupled deformation of the neighboring teeth, is not yet included into the proposed contact force model. Since effects of load sharing are more pronounced with an increase of the load, they can most likely be connected with the noticeable increase in phase difference between the STE curves of both models for high loading conditions, as shown in Figure 5.16a.

	Load	[Nm]	0.01	10	50	100	200	300	500	700
PP STE	FEA	[μrad]	36.5	31.4	15.4	10.4	21.2	20.3	16.1	13.0
	MB-A	[μrad]	36.1	29.8	16.5	7.6	17.3	19.8	18.9	18.9
	Diff.	[μrad]	−0.4	−1.6	1.1	−2.8	−3.9	−0.5	2.8	5.9

Table 5.3: Peak-to-peak STE (PP STE), computed by the reference model (FEA) and the GCFE with the analytical tooth compliance formulation (MB-A).

Computational requirements   To benchmark the proposed model objectively, it is executed on the desktop computer (i7 @ 3.20 GHz with 32 GB RAM) that is used to perform the NL-FEA simulations. Table 5.4 provides an overview of the required computation time for both models.

The differences between both models are contributed to the methodology for contact detection that was used, and the number of DOFs of each model. The element size that is required to accurately model the contacting tooth geometry not only results in a higher number of elements that have to be included into the general contact search, but also increases the overall problem size (number of DOFs). The GCFE benefits from an optimized contact search that is based on precomputed surfaces of roll angles. In addition, the (rigid) MB model contains a minimal number of DOFs, since the penetration is computed between the tooth surfaces of rigid bodies and converted into contact loads by an analytical compliance formulation.

Computation time	Reference Model (NL-FEA)	MB Model (50 slices)	MB Model (100 slices)
Single step	10, 625 s	1.2 s	1.4 s
Mesh cycle (37 steps)	4 d 13 h	44 s	51 s

Table 5.4: Computation time for a single step and a full mesh cycle for the reference NL-FEA model and the developed GCFE (for 50 and 100 flank slices).

Validity of the gear contact model   Having correlated the LTCA results of the spiral bevel gear contact model (GCFE) with those of the NL-FEA simulations, a discussion w.r.t. the research objectives (Section 1.2) is given for completeness.

Table 5.4 is a strong indicator that the envisioned numerical efficiency for the GCFE, i.e. the solution of a static LTCA step in an order of seconds, is achieved.

In terms of accuracy the objectives are also sufficiently reached, yet there is room for further improvement. The statement is based on following motivations. A visual check of Figs. 5.13 to 5.15 shows the overall contact pressure distribution and pattern to be well predicted with differences being within the 15 % limit. Looking at the STE, it is concluded that the GCFE correctly captures the evolution of the STE shape and peak-to-peak value as a function of the load. Yet, limitations of the analytical compliance model result in a loss of correlation at higher loads (above 500 Nm), which explain the high error (17-45 %) in predicted PP STE. Nonetheless, on average the GCFE predicts the peak-to-peak STE within the desired 10-15 % error range for the analyzed loads up to 300 Nm.

5.5   Conclusion

This chapter develops a novel spiral bevel gear contact force element for application within a multibody framework. The requirements for this gear contact force are discussed in Section 5.1. The methodology's starting point is fact that the real contacting flanks are designed to transmit motion in a near-conjugate way (i.e. near 0 TE). This information, contained in the surface of roll angles of the real pinion and real gear flanks, allows to create a general, accurate and efficient penetration-based contact detection algorithm in Section 5.2. The contact forces are computed efficiently by assuming that the detected penetration between the rigid flanks matches the gear teeth deformation, if they were flexible. In Section 5.3 an analytical tooth compliance model is proposed that divides the total tooth compliance into a local and global contribution.

In Section 5.4 a multibody approach to loaded tooth contact analysis is used to validate the gear contact model against NL-FEA-based contact simulations. Overall, a good correlation is found for peak-to-peak static transmission error, contact pattern and contact pressure distribution, while the computational time of the proposed model is a fraction of that of the the NL-FEA simulations. Nevertheless, limitations of the contact force element, due to the analytical compliance model, are identified for highly loaded conditions. More advanced methods to model the global gear (tooth) compliance, e.g. FEM-based, are proposed as a future research track. Chapter 6 focuses on extending the contact detection methodology to accurately capture gear pair misalignments.

Chapter 6

Parametric modeling of gear pair misalignments

Errors in the alignment of a gear pair can prove detrimental for its contact performance, yielding an open-ended subject for many actual research activities [41, 42, 49, 64]. In general, any deviations from the designed relative configuration causes the overall contact pattern to move from the designed location - often around the flank middle - towards the edges of the gear tooth surfaces. In addition to an increased chance for edge contacts, this shift of contact pattern is usually also accompanied by an increase of both contact and bending stresses and a rise in transmission error. Consequently, these effects have the tendency to cause elevated noise and vibration levels, while also negatively impacting the operational life time of the gear pair. Therefore, a well-designed gear pair incorporates an optimized ease-off topography that counteracts the effects of alignment errors within a predefined range [42].

This chapter focuses on the correct modeling and efficient simulation of gear pair misalignment by means of the developed spiral bevel gear contact force element. In Section 6.1 the force element (GCFE), as described in Chapter 5 for the nominal alignment, is used to analyze a case of predefined alignment error. The performance of the nominal GCFE is evaluated by comparing its behavior with that of a GCFE that is updated with the surfaces of roll angles that corresponds to the misaligned configuration. Section 6.2 introduces the novel idea of interpolating new surfaces of roll angles based on the instantaneous misaligned state of the gear pair. This enables the simulation of varying misalignment in an accurate and efficient way. In Section 6.3 the proposed methodology is numerically validated against NL-FEA-based contact simulations.

6.1 Evaluation of the developed gear contact model in case of gear pair misalignment

To correctly predict the above-mentioned changes in gear pair performance under gear pair misalignment, the contact force model should be able to include all the relevant effects that arise at the contact interfaces. In this work special attention is given to those effects that concern the computation of the contact curves and the resulting penetration between the (real) gear tooth surfaces.

6.1.1 Approximations regarding the contact detection

Besides potential assembly and/or manufacturing errors, misalignment of the gear pair can also be caused by load-induced deflections of the supporting components (e.g. shafts, bearings, ...) [41]. The latter source can be of particular interest when analyzing power transmission in gear drive systems, since it can result in variable alignment errors.

The contact detection methodology within the developed spiral bevel gear contact force model is based on the instantaneous position and orientation of both the pinion and the gear body, providing it with the potential to correctly include each of these misalignment sources. However, since alignment errors alter the kinematics of the gear pair, they have a direct effect on the surfaces of action and the surfaces of roll angles that are used to determine the contact curves. Realizing that the alignment errors, which occur during a contact simulation, are not known beforehand but are rather the result of interactions with the supporting components, it is unfeasible to include the required data (i.e. the surfaces of roll angles) that would guarantee a correct contact detection.

Given that typical alignment errors remain relatively small[1], it is reasonable to assume that the surfaces of action are only slightly modified when compared to the nominal (i.e. non-misaligned) configuration. Consequently, the rotation (i.e. the roll angle) that each gear tooth surface needs to undergo to reach the corresponding surface of action is not altered much either. It is hypothesized that the developed spiral bevel GCFE with the surfaces of roll angles, which are computed for the nominal configuration, could very well provide accurate results when gear pair misalignments occur.

---

[1]Alignment errors occur due to the deflection of the supporting components, such as bearings or shafts. Although there is an application and load dependency, the order of magnitude for translational misalignments can range up to a few tenths of a millimeter or up to a few tenths of a degree for angular misalignments.

6.1.2   Studied case of gear pair misalignment

To verify whether the GCFE, developed in Chapter 5 with *nominal* surfaces of roll angles, would be directly applicable to the analysis of gear pair misalignments, its performance is evaluated against an updated GCFE that contains the *recalculated* and exact surfaces of roll angles for the misaligned configuration. A predefined case of gear pair misalignment is selected and kept fixed during the analysis to accommodate a clear comparison between both models. The corresponding installment parameters are listed in Table 6.1. Fig. 6.1 illustrates the effects of the gear misalignment in terms of flank overlap and ease-off topography. The alignment errors for the misaligned case are chosen based on three criteria: (i) the alignment error has to be sufficiently large to create a clear shift in contact pattern when compare to the nominal case, (ii) the alignment errors should be defined by all four installment parameters, and (iii) the resulting combination of parameters has to avoid double-sided tooth contact that would result in wedging of the gear teeth.

Installment data	γ [deg.]	E_H [mm]	A_1 [mm]	A_2 [mm]
Nominal case	-90.000	0.000	0.000	0.000
Misaligned case	-90.250	0.250	0.249	0.250

Table 6.1: Installment parameters for the nominal and misaligned configuration.

To quantify the effects of alignment errors on the nominal force element, the study focuses on the analysis of the right flank pairs of the gear pair, which were also analyzed in Chapter 5 for non-misaligned conditions. If the initial rotations are not specified, the GCFE computes the rotations such that the initial contact occurs at the minimum of the ease-off topography. To avoid that this contact point varies depending on the surfaces of roll angles that are used (e.g. nominal or recalculated), the initial contact is specified to take place at the midface of the right gear flank. The required rotations, listed in Table 6.2 are computed by using the UTCA procedures, described in Chapter 4.

Initial gear rotation	Pinion (gear 1) [deg.]	Gear (gear 2) [deg.]
ϕ_{z0}	179.802392	-7.538770

Table 6.2: Initial gear rotation to analyze the misaligned gear pair. The rotation angles bring the right flank pairs of both the pinion and the gear in contact. The contact point on the gear flank is situated at the midface.
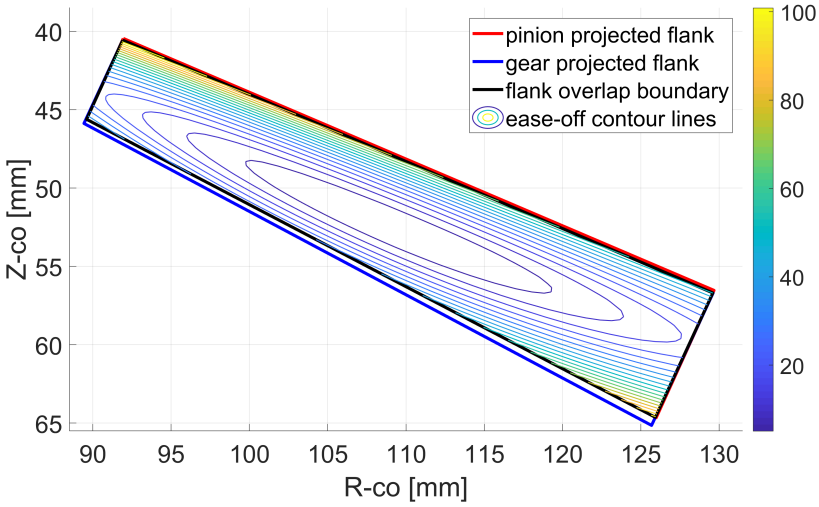
(a) Projected flank overlap and ease-off topography for the aligned case..
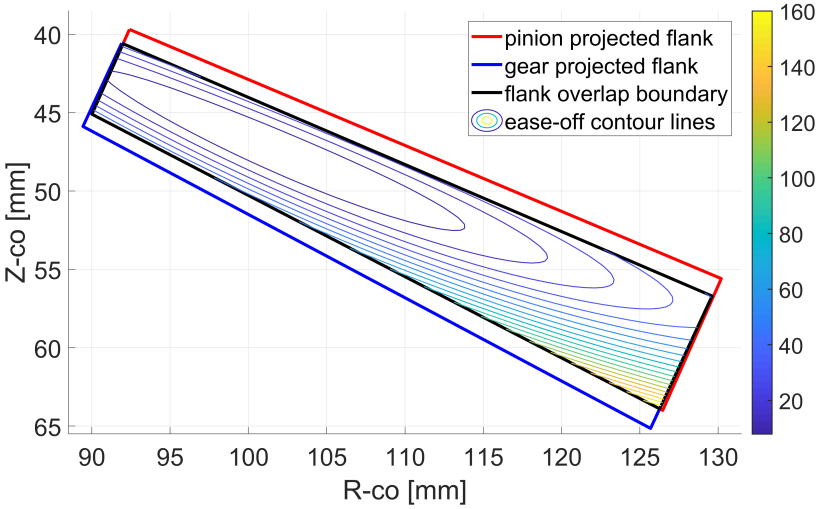
(b) Projected flank overlap and ease-off topography for the misaligned case.

Figure 6.1: Comparison between the nominal and misaligned cases of Table 6.1 in terms of projected flank overlap and ease-off topography to indicate the to-be-expected change of the contact pattern due to the gear misalignment.

6.1.3 Preliminary analysis of the UTCA-relevant data

Depending on the gear alignment error, the modified gear pair kinematics cause contact between the gear teeth to occur either earlier or later than in the non-misaligned configuration. This difference in tooth engagement timing is explained by the fact that the alignment error alters the shape of the surfaces of action of the gear teeth. Consequently, it also causes a change in the location and orientation of the instantaneous contact curves. Combined with the local geometry of the mating tooth flanks, these alterations are responsible for the shift of contact pattern towards the edges of the tooth surfaces due to a modification of the ease-off topography (see Figs. 2.6 and 6.1).

The goal of this subsection is to quantify the difference that exist between the nominal surface of roll angles and the newly calculated surface of roll angles under misalignment for the right flank pair. Additionally, the gear-based ease-off topographies are constructed for the misaligned configuration by using the nominal and recalculated surfaces of roll angles for the pinion flanks.

Effect of misalignments on the surface of roll angles

Even though the ease-off topography and the contact pattern can be significantly altered under gear pair misalignment, if one considers that typical alignment errors remain relatively small, the rotation that each of the flank points needs to undergo to reach its modified surface of action is only slightly changed. To verify this assumption the nominal and recalculated surfaces of roll angles of the right flanks of both the pinion and the gear are analyzed in Table 6.3. Each surface of roll angles is stored on the same underlying grid onto which the respective tooth surface points are defined, hence a direct comparison is easily

Roll angles	$\mathcal{R}_\phi$	$\mathcal{R}_{\phi,\min}$ [deg.]	$\Delta\mathcal{R}_{\phi,\min}$ [deg.]	$\mathcal{R}_{\phi,\max}$ [deg.]	$\Delta\mathcal{R}_{\phi,\max}$ [deg.]	RMSE [deg.]
Pinion	cal.	151.1755	—	203.7397	—	—
	nom.	151.9420	0.7665	204.5576	0.8179	0.7849
Gear	cal.	−20.9396	—	4.0437	—	—
	nom.	−20.0324	0.9072	4.9108	0.86702	0.8862

Table 6.3: Error analysis of the computed surface of roll angles for a right flank pair in the nominal (nom.) and the misaligned (cal.) configuration. The absolute error between the minimum and maximum value of the surface of roll angles is represented by $\Delta\mathcal{R}_{\phi,\min}$ and $\Delta\mathcal{R}_{\phi,\max}$, respectively.

obtained. Based on an analysis of the corresponding surfaces of roll angles, this assumption seems to be confirmed relatively well. The extreme values of each surface of roll angles, $\mathcal{R}_{\phi,\min}$ and $\mathcal{R}_{\phi,\max}$, show that the corresponding teeth indeed require a similar amount of rotation to reach and exit their action surface. The difference between in extreme values, $\Delta\mathcal{R}_{\phi,\min}$ and $\Delta\mathcal{R}_{\phi,\max}$, for the nominal and recalculated surfaces of roll angles amounts to less than 1 deg. Moreover, the root mean square error (RMSE) for both pinion and gear provides a similar estimate of the absolute error, providing a reliable estimate for the average absolute error. For an average (projected) gear radius of $R = 110\,\text{mm}$ and a face width of $41\,\text{mm}$, the estimated error on the position of the contact curve would result to $1.92\,\text{mm}$ or less than $5\,\%$. Although the estimated error is obviously misalignment dependent, this preliminary result is promising and shows the validity of the earlier-made assumption.

Effect of misalignments on the ease-off topography

Since the ease-off topography is determined by the local flank geometry, it is much more susceptible to gear alignment errors. This is confirmed by an evaluation of the iso-contour lines of the gear-based ease-off topography for the gear pair's right flank pair in the nominal configuration, shown in Fig. 5.3, and the studied misaligned configuration, shown in Fig. 6.2. However, the change in ease-off topography due to misalignment is of lesser concern, since it is not required by the developed GCFE. More relevant is an evaluation of how well the nominal surface of roll angles (of the pinion flank) can approximate the conjugate to the misaligned gear flank, since this indicates the quality with which the nominal GCFE can approximate the unloaded behavior of the misaligned gear pair. Table 6.4 provides a comparison of the ease-off topography for a right flank pair of the misaligned gear pair, computed once with the pinion flank's surface of roll angles for the nominal configuration and once with the

Ease-off	$\mathcal{E}_{\delta}^{(2)}$	$\mathcal{E}_{\delta,\min}^{(2)}$ $[\mu\text{m}]$	$\Delta\mathcal{E}_{\delta,\min}^{(2)}$ $[\mu\text{m}]$	$\mathcal{E}_{\delta,\max}^{(2)}$ $[\mu\text{m}]$	$\Delta\mathcal{E}_{\delta,\max}^{(2)}$ $[\mu\text{m}]$	RMSE $[\mu\text{m}]$
Gear	cal.	0.0000	—	165.1737	—	—
pair	nom.	0.0156	0.0156	159.5261	−5.6464	1.8284

Table 6.4: Error analysis: gear-based ease-off topography for a right flank pair in the misaligned configuration, computed with the surface of roll angles for the nominal (nom.) and misaligned (cal.) configuration. The absolute error between the minimum and maximum value of the ease-off topography is represented by $\Delta\mathcal{E}_{\delta,\min}^{(2)}$ and $\Delta\mathcal{E}_{\delta,\max}^{(2)}$, respectively.

pinion flank's surface of roll angles for the misaligned configuration. Overall, the gear-based ease-off topography is well-approximated by the nominal surface of roll angles with an RMSE value of 1.8282 µm. Analysis of the extreme values of both ease-off topographies, learns that: the maximum value $\mathcal{E}_{\delta,\max}^{(2)}$ can be easily identified in the same point for both the nominal and misaligned case due to the shape of the ease-off topography, while the minimum value $\mathcal{E}_{\delta,\min}^{(2)}$ is more influenced by the differences between the nominal and recalculated surfaces of roll angles. To evaluate the absolute error on $\mathcal{E}_{\delta,\min}^{(2)}$, the ease-off topography, created by the nominal surface of roll angles, is evaluated at the point where the ease-off topography, created by the recalculated surface of roll angles reaches its minimum value of 0 µm. While the absolute error in ease-off topography is the highest for the flank regions that have high ease-off values, it should be noted that in practice the resulting error on the UTE curve is lower, because the flank overlap restricts the contact zone to the lower ease-off regions, for which the absolute error is also lower.

6.1.4 Limitations of the nominal gear contact force element

A preliminary analysis of the surfaces of roll angles and the corresponding ease-off topographies in the previous section shows promising results towards the use of the nominal surfaces of roll angles for the analysis of gear pair misalignment. Obviously, the verification of this hypothesis cannot be completed without an actual analysis of the loaded behavior of the misaligned gear pair. Therefore, an in-depth analysis of the performance of the contact force element that once uses the nominal surfaces of roll angles (*RS nom.*) and once the exact roll surfaces (*RS cal.*) that correspond to the analyzed misalignment, is provided in terms of contact curves and pattern, transmission error and contact pressure.

Contact curves and overall contact pattern

A comparison between of the instantaneous contact curves and overall contact pattern, which has been obtained by both spiral bevel gear contact force models under an applied load of 200 Nm for the specified installment error of Table 6.1, is shown in Fig. 6.2. As predicted by Table 6.3, the difference between the nominal and recalculated surfaces of roll angles cause a noticeable shift in the location of the instantaneous contact curves. Moreover, Fig. 6.2a shows that the orientation of the contact curve is slightly altered. The shift in contact location causes the contact, approximated by the nominal GCFE, to lead w.r.t. the contact that is computed by the GCFE that uses the exact surfaces of roll angles. Consequently, the nominal GCFE predicts gear teeth to enter and exit
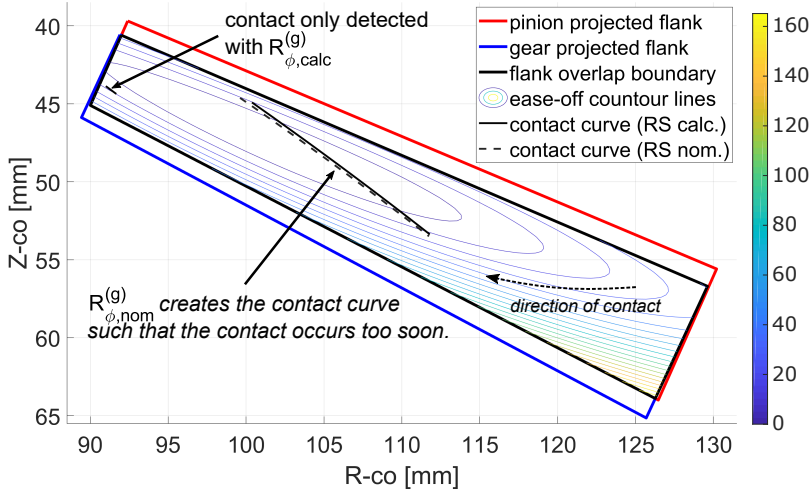
(a) Contact curves for 200 Nm.
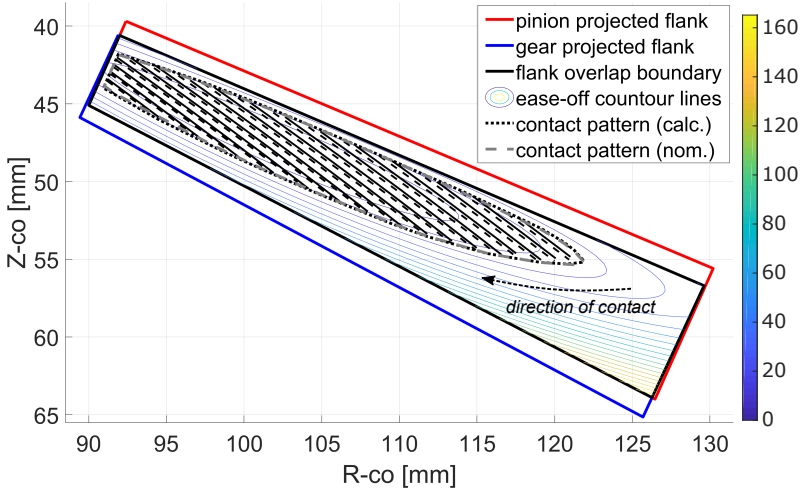
(b) Contact pattern for 200 Nm.

Figure 6.2: Error analysis: contact pattern under gear pair misalignments.

the contact too soon, such that it is not able to detect tooth contact at the edges of the contact pattern where there should actually be teeth in contact (see Fig. 6.2a) or vice versa. However, as shown in Fig. 6.2b, the latter effect seems to be minor, as the size of the overall contact pattern, computed as the convex hull to the family of instantaneous contact curves, remains almost unaffected. The size of the contact pattern under load is also directly linked to the misaligned gear pair's ease-off topography, which the nominal surface of roll angles is able to approximate well for the studied alignment error. This makes the area of the overall contact pattern less meaningful as a metric to evaluate the performance of the GCFE for spiral bevel gears.

Static transmission error

The GCFE with nominal surfaces of roll angles and the GCFE with recalculated and exact roll surfaces are used to perform a loaded tooth contact analysis of the gear pair in the studied misaligned configuration. The LTCA process that was used, corresponds to the one that is described in Fig. 5.7. The resulting STE curves for 0.01 Nm (unloaded) and 200 Nm are shown in Fig. 6.3a and Fig. 6.3b, respectively. A summary of the peak-to-peak TE and an evaluation of the absolute error that is introduced by the use of the nominal surfaces of roll angles is provided in Table 6.5. Overall, it can be concluded that the STE curves and especially the peak-to-peak STE value is well-predicted by the GCFE with nominal surfaces of roll angles. However, the obtained STE curves confirm that the differences in nominal and recalculated roll surfaces not only cause a shift in the location of the instantaneous contact curve but also lead to a noticeable angular shift of the resulting STE curve. Accordingly, the contact behavior of the GCFE with nominal roll surfaces leads w.r.t. the GCFE with recomputed surfaces of roll angles.

STE	RS	peak-to-peak [μrad]	error p-p [μrad]	shift p-p [deg.]	RMSE p-p [μrad]
0.01 Nm	cal.	45.6725	–	–	–
	nom.	47.0008	1.3283	0.5005	3.6552
200 Nm	cal.	19.3049	–	–	–
	nom.	18.4586	0.8463	0.5005	1.4600

Table 6.5: Error analysis: transmission error at 0.01 Nm and 200 Nm for the right flank pairs in the misaligned configuration, computed with the surface of roll angles for the nominal and misaligned configuration.
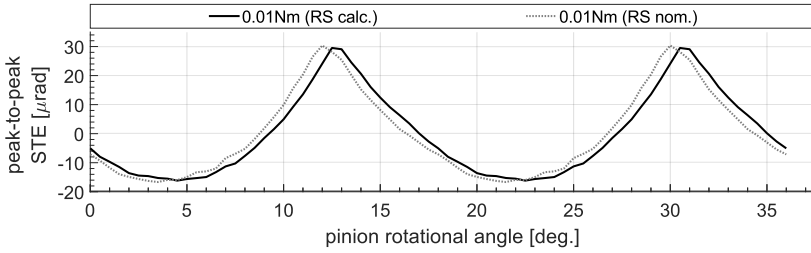
(a) Unloaded transmission error at 0.01 Nm.
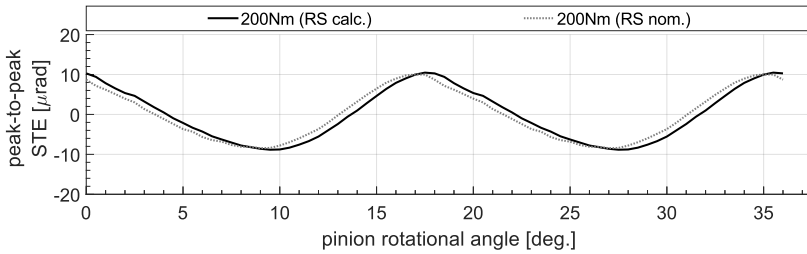
(b) Static transmission error at 200 Nm.
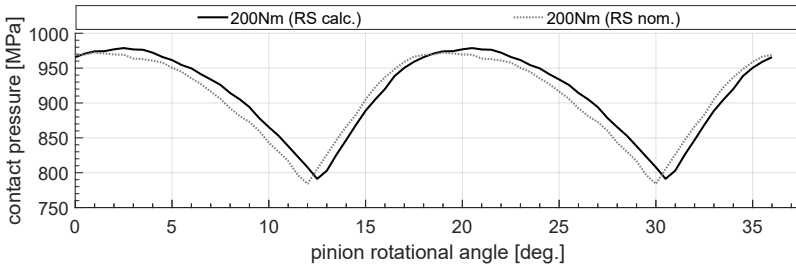
(c) Maximum contact pressure at 200 Nm.

Figure 6.3: Transmission error at 0.01 Nm and 200 Nm and maximum contact pressure at 200 Nm for the right flank pairs in the misaligned configuration, computed with the surfaces of roll angles for the nominal and misaligned configuration.

Maximum contact pressure

In addition to the static transmission error, the evolution of the maximum contact pressure throughout the mesh cycle is analyzed for both GCFE models. Fig. 6.3 shows that the GCFE with nominal surfaces of roll angles accurately predicts this evolution for the considered case of gear pair misalignment. An overview of the differences between both gear contact force models is summarized in Table 6.6. The differences in minimum and maximum contact pressures are situated between 6-7 MPa, which corresponds to less than 1 %. The relatively higher RMSE value of the contact pressure can be explained by the presence of an angular shift, similar to the one identified for the STE curves.

Contact pressure	RS	p_{min} [MPa]	Δp_{min} [MPa]	p_{max} [MPa]	Δp_{max} [MPa]	shift [deg.]	RMSE [MPa]
200 Nm	cal.	791.18	–	978.73	–	–	–
	nom.	784.11	7.07	972.29	6.44	0.5005	16.13

Table 6.6: Error analysis: contact pressure at 200 Nm for the right flank pairs in the misaligned configuration, computed with the surface of roll angles for the nominal and misaligned configuration.

6.1.5 Summary and findings of the study

The study investigates if the surfaces of roll angles of the aligned configuration would be viable approximations for the exact surfaces of roll angles of the misaligned gear pair. This endorses the use of the (nominal) gear contact force element for the analysis of gear misalignment. Preliminary analysis of the nominal surfaces of roll angles confirms the assumption that differences with the recomputed surfaces of roll angles remain small. Therefore, the nominal surfaces of roll angles accurately approximates the misaligned gear pair's ease-off topography. Furthermore, LTCA showed that a GCFE with nominal roll surfaces predicts the contact behavior of the misaligned gear pair with good accuracy, since the model computes the contact based on the actual location of the (misaligned) real gear tooth surfaces. This gives the penetration based GCFE, which uses the surfaces of roll angles of both pinon and gear flanks rather than the pinion's surface of roll angles and a gear-based ease-off topography, a higher versatility. A better approximation of the true surfaces of roll angles in case of gear misalignment is expected to reduce the spatial shift of the contact curves and to improve the GCFE's performance.

6.2 Improved contact detection by parametrically updating the surfaces of roll angles

This section proposes the novel idea to update the gear pair's surfaces of roll angles, based on the instantaneous alignment error of the gear pair and a set of surfaces of roll angles, computed for predefined misaligned configurations. Building upon the knowledge that the differences between a tooth flank's surface of roll angles for the aligned (nominal) configuration and the surface of roll angles of the misaligned configuration remain small, a multivariate but linear interpolation strategy is proposed. To describe this parametric surface of roll angles (pRS) a general parametrization of the gear pair misalignment is proposed. Although applicable to any gear type, the methodology is only applied to the analysis of spiral bevel gears in this dissertation. Aiming to better approximate the gear pair's exact surfaces of roll angles for the the misaligned configuration, the gear contact force element is then extended with the proposed methodology and its performance is reevaluated.

6.2.1 A parametric description of the surface of roll angles

The gear contact force element is developed to analyze the loaded contact behavior of spiral bevel gear pairs within a multibody multibody simulation environment. The contact force model assumes that the gear pair can be represented as a set of rigid bodies for which the tooth compliance has been modeled in an analytical fashion (See Chapter 5). Internally, the GCFE represents the rotation of each geared body by a set of Bryant angles, such that the position and orientation of each rigid body is defined by three translational and three rotational coordinates. An auxiliary reference frame S_B (the Base frame) is introduced to describe the relative position of the gear w.r.t. the pinion.

A general parametrization of the gear pair misalignment

The definition of the Base frame S_B determines the parametrization that is used to describe the relative position of the gear pair and the possible alignment errors. The straightforward choice within the GCFE is to parameterize the relative position of the gear w.r.t. the pinion in function of three translational and three rotational coordinates. This way the rotational misalignment of the gear pair can be expressed in terms of the adopted Bryant angle convention. Additionally, to correctly describe the gear pair kinematics, the definition of
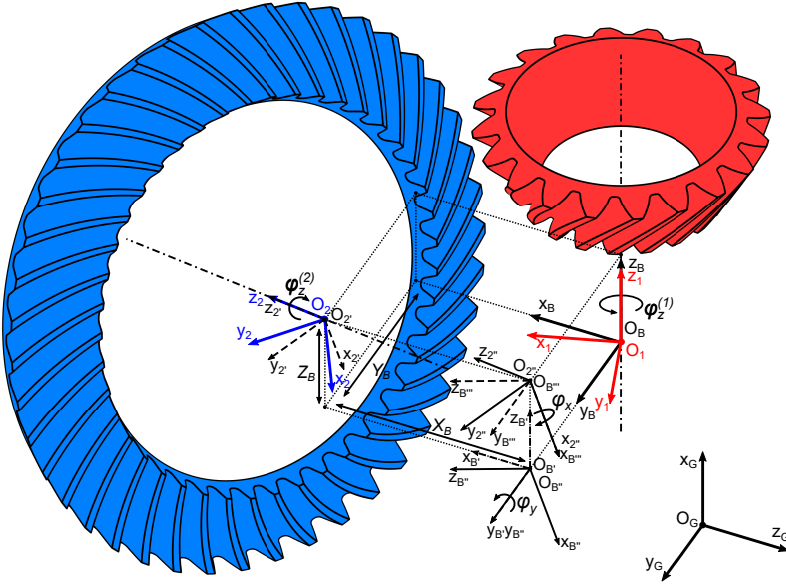
Figure 6.4: Relative orientation of a misaligned gear pair w.r.t. the global frame.

the Base frame has to correspond to the one that is used to define the equation of meshing for the gear tooth surfaces (see Chapter 4).

As described in Chapter 5, the position and the orientation of the gear pair w.r.t. to the global frame S_G are described by the body-attached frames S_1 for the pinion and S_2 for the gear wheel. An example of a misaligned configuration with an illustration of the proposed parametrization is shown in Fig. 6.4. To develop this parametrization, the Base frame S_B is defined to be coincident with the pinion's body-attached frame S_1 such that the pinion can only rotate about its local z-axis. The position vector $\boldsymbol{R}_G^{(B)}$ and the rotation matrix $\mathbf{A}_B$ define the position of the origin and the orientation of the reference frame S_B w.r.t. to the global frame S_G. The relative position and orientation of the pinion ($g = 1$) and the gear ($g = 2$) w.r.t. the Base frame S_B are then defined by:

$$\boldsymbol{R}_B^{(g)} = \mathbf{A}_B^T \big(\boldsymbol{R}_G^{(g)} - \boldsymbol{R}_G^{(B)} \big) \qquad (g = 1, 2) \qquad (6.1)$$

$$\mathbf{L}_{Bg} = \mathbf{A}_B^T \mathbf{A}_g \qquad (g = 1, 2) \qquad (6.2)$$

The position of the origin of body-attached pinion frame S_1 w.r.t. S_B is by definition given as $\boldsymbol{R}_B^{(1)} = \mathbf{0}$, while the rotation of the pinion is described by $\mathbf{L}_{B1} = \mathbf{L}_z(\phi_z^{(1)})$, which is in accordance with Eq. (4.3). The relative position of

the body-attached gear frame S_2 w.r.t. S_B and w.r.t. the body-attached pinion frame S_1 is simply derived from Eq. 6.1 and parameterized as:

$$\boldsymbol{R}_B^{(2)} = \mathbf{A}_B^T \big(\boldsymbol{R}_G^{(2)} - \boldsymbol{R}_G^{(B)} \big) = \begin{bmatrix} x_B^{(2)} \\ y_B^{(2)} \\ z_B^{(2)} \end{bmatrix} \tag{6.3}$$

The relative orientation of the body-attached gear frame S_2 w.r.t. S_B is defined by the rotation matrix $\mathbf{L}_{B2}$ as a series of successive rotations that are described by the adopted set of Bryant angles $\phi_x^{(2)}$, $\phi_y^{(2)}$ and $\phi_z^{(2)}$ (See Section 5.2), which can be found by combining Eqs. (6.2) and (6.4) with the expressions of [30].

$$\mathbf{L}_{B2} = \mathbf{L}_y(\phi_y^{(2)})\mathbf{L}_x(\phi_x^{(2)})\mathbf{L}_z(\phi_z^{(2)}) \tag{6.4}$$

where

$$\mathbf{L}_x(\phi) = \begin{bmatrix} 1 & 0 & 0 \\ 0 & \cos(\phi) & -\sin(\phi) \\ 0 & \sin(\phi) & \cos(\phi) \end{bmatrix}, \quad \mathbf{L}_y(\phi) = \begin{bmatrix} \cos(\phi) & 0 & \sin(\phi) \\ 0 & 1 & 0 \\ -\sin(\phi) & 0 & \cos(\phi) \end{bmatrix},$$

$$\mathbf{L}_z(\phi) = \begin{bmatrix} \cos(\phi) & -\sin(\phi) & 0 \\ \sin(\phi) & \cos(\phi) & 0 \\ 0 & 0 & 1 \end{bmatrix} \tag{6.5}$$

Adopting the Bryant-angles based parametrization, the position and orientation of the gear pair is described as a function of seven parameters. However, since both gear rotational angles $\phi_z^{(1)}$ and $\phi_z^{(2)}$ are used to computed the contact curves on the corresponding surfaces of roll angles $\mathcal{R}_\phi^{(1)}$ and $\mathcal{R}_\phi^{(2)}$, the five remaining parameters $(x_B^{(2)}, y_B^{(2)}, z_B^{(2)}, \phi_x^{(2)}$ and $\phi_y^{(2)})$ that define the configurational alignment can be used to interpolate the new surfaces of roll angles. Since the proposed parametrization describes the gear pair misalignment in terms of relative translation and a set of Bryant angle rotations, it has the potential to be generally applicable that is analyzed by using the concept surface of roll angles. Considering that the parametrization is used to update the surfaces of roll angles based on interpolation, the adopted Base frame definition guarantees that its position and orientation remain unchanged w.r.t. the installment of the gear wheel and pinion, This way the interpolation error is only introduced on the surfaces of roll angles that is relatively insensitive to small errors.

Multivariate interpolation of the surfaces of roll angles

To improve the contact detection in case of gear alignment errors a parametric surface of roll angles methodology is proposed that updates the gear teeth their surface of roll angle depending on the instantaneous misaligned configuration. Therefore, multiple roll surfaces, which correspond to different misaligned gear pair configurations, are computed in a preprocessing phase to the contact simulation. The gear contact force element is extended so that it identifies the correct parametrization of the gear pair's misaligned state at the start of the contact detection. If the gear pair's spatial configuration changes during simulation, the surfaces of roll angles of the gear teeth flanks are updated by using a linear multivariate interpolation strategy.

Parametric surface of roll angles   To interpolate the new surface of roll angles that better-approximates a flank's true surface of roll angles for the misaligned configuration, a basis of surfaces of roll angles, which correspond to predefined misaligned gear pair configurations, has to be computed during data preprocessing for each gear and for each tooth flank that is considered in the contact simulation. This basis is created by parametrically varying the alignment error around the given nominal configuration. Starting from the gear pair's nominal installment settings, defined by A_1, A_2, E_H and γ, it is possible to compute the equivalent parametrization in terms of $x_B^{(2)}, y_B^{(2)}, z_B^{(2)}, \phi_x^{(2)}$ and $\phi_y^{(2)}$.

Given that this parametrization is an input to derive the required surfaces of roll angles, the following renaming of the parametrization is adopted that simplifies the notation by omitting the superscript $\bullet^{(2)}$:

$$\{x_B^{(2)}, y_B^{(2)}, z_B^{(2)}, \phi_x^{(2)}, \phi_y^{(2)}\} \rightarrow \{X_B, Y_B, Z_B, \Phi_x, \Phi_y\}$$

The parameters that describe the nominal configuration are thus defined as $\tilde{X}_B, \tilde{Y}_B, \tilde{Z}_B, \tilde{\Phi}_x$ and $\tilde{\Phi}_y$. Within the scope of this dissertation, the level of alignment variations, represented by $\Delta X_B, \Delta Y_B, \Delta Z_B, \Delta \Phi_x$ and $\Delta \Phi_y$, is considered to be defined by the user. The parameters that define the resulting misaligned configuration are then given as:

$$X_B = \tilde{X}_B + \Delta X_B \qquad Y_B = \tilde{Y}_B + \Delta Y_B \qquad Z_B = \tilde{Z}_B + \Delta Z_B$$

$$\Phi_x = \tilde{\Phi}_x + \Delta \Phi_x \qquad \Phi_y = \tilde{\Phi}_y + \Delta \Phi_y$$

$$(6.6)$$

The surfaces of roll angles for the different user-defined misaligned configurations are obtained by solving the equation of meshing for the pinion and the gear, given by Eqs. (4.7) and (4.15) respectively. However, given the different

parametrization of the gear's installment w.r.t. the Base frame S_B, the transformation matrix $\mathbf{T}_{B2'}$ of Eq. (4.6) has to be replaced by Eq. (6.7).

$$\mathbf{T}_{B2'} = \left[\begin{array}{c|c} \mathbf{L}_y(\Phi_y)\mathbf{L}_y(\Phi_x) & \begin{array}{c} X_B \\ Y_B \\ Z_B \end{array} \\ \hline \mathbf{0}_{1\times 3} & 1 \end{array} \right] \tag{6.7}$$

Eqs. (4.7) and (4.15) should be solved for all possible combinations of the specified levels of alignment error to completely define the parametric surface of roll angles (pRS) of the tooth flanks for the pinion and for the gear.

Eq. (4.7): $f\big(\phi_z^{(1)}; X_B, Y_B, Z_B, \Phi_x, \Phi_y\big) \rightarrow \mathcal{R}_\phi^{(1)}\big(X_B, Y_B, Z_B, \Phi_y, \Phi_x\big)$

Eq. (4.15): $f\big(\phi_z^{(2)}; X_B, Y_B, Z_B, \Phi_x, \Phi_y\big) \rightarrow \mathcal{R}_\phi^{(2)}\big(X_B, Y_B, Z_B, \Phi_y, \Phi_x\big)$

Consequently, the dimensions of the pRS for a pinion flank ($g = 1$) and of the pRS for the gear flank ($g = 2$) are defined as:

$$\text{size}\Big(\mathcal{R}_\phi^{(1)}\Big) = N_1 \times N_X \times N_Y \times N_Z \times N_{\phi_y} \times N_{\phi_x} \tag{6.8}$$

$$\text{size}\Big(\mathcal{R}_\phi^{(2)}\Big) = N_2 \times N_X \times N_Y \times N_Z \times N_{\phi_y} \times N_{\phi_x} \tag{6.9}$$

where N_1 and N_2 correspond to the number of points on the respective pinion and gear flank and N_X, N_Y, N_Z, N_{ϕ_y} and N_{ϕ_x} are the number of specified alignment error variations for each parameter.

Eqs. (6.8) and (6.9) illustrate the the proposed pRS for the pinion and the gear flanks are data intensive. Assuming that all the misalignment parameters are considered during the contact simulation of a spiral bevel gear for which both sides of each gear tooth are included and that the nominal surface of roll angles and at least one variation for each alignment error parameter is specified, the minimal number of roll surfaces that have to be computed is: $2^5 \times 2$ gears $\times 2$ flanks = 128 RS. A more practical approach would consider an interval (e.g. $[-\Delta, 0, +\Delta]$) around the nominal configuration such that both positive and negative alignment error variations can be analyzed. For the latter case the total amount of required surfaces of roll angles rises to: $3^5 \times 2$ gears $\times 2$ flanks = 972 RS. Of course, depending on the applied constraints, it is not always required to include all dimensions. For example if only relative translations between the pinion and gear element are modeled, then it suffices to include only variations of the parameters X_B, Y_B and Z_B.

While the data preprocessing for the proposed approach may be intensive, the multivariate interpolation that is described in the next paragraph, results in a relative inexpensive update of the roll surfaces during actual simulation.

Multivariate interpolation   The contact detection algorithm of the GCFE is extended with a procedure that computes the instantaneous misalignment parametrization from Eqs. (6.1) to (6.4) in terms of $\{x_B^{(2)}, y_B^{(2)}, z_B^{(2)}, \phi_x^{(2)}, \phi_y^{(2)}\}$ each time the contact detection is performed.   This new misalignment parametrization is compared with the stored parametrization to determine whether the spatial configuration of the gear pair has changed sufficiently such that it is required to update the surfaces of roll angles of the gear tooth surfaces. Since the parametric surface of roll angles of a gear tooth surface is a function of five coordinates, a multivariate interpolation procedure, which is based on linear shape functions in each dimension, is adopted to compute the tooth flank's new surface of roll angles that approximates the current misaligned configuration.

To identify the surfaces of roll angles $\mathcal{R}_{\phi,l}$, which serve as data points for the interpolation algorithm, it is first required to determine in which interval of predefined alignment error variations each of the misalignment parameters lies. For each of the computed parameters X the lower bound and upper bounds are identified such that $X_1 \leq X \leq X_2$. Since FEM-based shape functions are used to interpolate the different dimensions, Eq. (6.10) is used to scale the misalignment parameter X such that its value ranges between -1 and $+1$.

$$g\big(X; X_1, X_2\big): \quad X \mapsto x = \frac{X - \mathrm{mean}(X_1, X_2)}{X_2 - \mathrm{mean}(X_1, X_2)} \tag{6.10}$$

For a misaligned configuration c, given by $\{x_{B,c}^{(2)}, y_{B,c}^{(2)}, z_{B,c}^{(2)}, \phi_{x,c}^{(2)}, \phi_{y,c}^{(2)}\}$, the scaled parameters within their respective interval are then defined as:

$$g\big(x_{B,c}^{(2)}; X_{B,1}, X_{B,2}\big): x_{B,c}^{(2)} \mapsto \xi_c \qquad g\big(y_{B,c}^{(2)}; Y_{B,1}, Y_{B,2}\big): y_{B,c}^{(2)} \mapsto \eta_c$$

$$g\big(z_{B,c}^{(2)}; Z_{B,1}, Z_{B,2}\big): z_{B,c}^{(2)} \mapsto \mu_c \qquad g\big(\phi_{y,c}^{(2)}; \phi_{y,1}^{(2)}, \phi_{y,2}^{(2)}\big): \phi_{y,c}^{(2)} \mapsto \upsilon_c \tag{6.11}$$

$$g\big(\phi_{x,c}^{(2)}; \phi_{x,1}^{(2)}, \phi_{x,2}^{(2)}\big): \phi_{x,c}^{(2)} \mapsto \zeta_c$$

Considering all five misalignment parameters, 32 RS data points are needed to cover all the possible combinations that are used in the pentalinear interpolation scheme. These 32 RS data points populate a five-dimensional regular grid for which two variations around the nominal value in each dimension are considered. The updated surface of roll angles for a tooth flank of the pinion ($g = 1$) or of the gear ($g = 2$) is computed by using Eq. (6.11) to evaluate Eq. (6.12).

$$\mathcal{R}_\phi^{(g)}(\xi_c, \eta_c, \mu_c, \upsilon_c, \zeta_c) = \sum_{l=1}^{32} N_l^e(\xi_c, \eta_c, \mu_c, \upsilon_c, \zeta_c)\, \mathcal{R}_{\phi,l}^{(g)} \qquad (g = 1, 2) \tag{6.12}$$

An overview of the shape functions that allow to interpolate linearly in each of the misalignment dimensions (up to five), is provided in Appendix D. The shape functions in Eq. (6.12) correspond to those that are defined by Eq. (D.7).

6.2.2 Updated results for the studied gear alignment error

The predefined case of gear pair misalignment, which was intensively studied during Section 6.1, is analyzed with the *extended* GCFE to evaluate the proposed pRS-methodology for contact detection under gear pair misalignment.

Parametrization of the studied gear pair alignment

The misaligned gear pair configuration, defined for the installment parameter A_1, A_2, E_H and γ in Table 6.1, can be translated into the misalignment parametrization for X_B, Y_B, Z_B, Φ_x and Φ_y. The resulting values of the equivalent parametrization are listed in Table 6.7.

Base frame parameters	X_B [mm]	Y_B [mm]	Z_B [mm]	Φ_x [deg.]	Φ_y [deg.]
Gear pair	-0.250	0.250	-0.250	0.000	-90.250

Table 6.7: Misalignment parametrization of the gear pair w.r.t. the Base frame.

Based on the specified alignment error variation in Table 6.8, a data set of parametric surface of roll angles $\mathcal{R}_\phi^{(1)}$ and $\mathcal{R}_\phi^{(2)}$ for both the left and right gear tooth surfaces of the pinion and the gear, are constructed during that data preprocessing phase of the extended GCFE. The magnitude of alignment error variation is chosen for two specific reasons. Since the interpolation function is linear along each dimension, the interpolation error evolves quadratically over the interval of each selected parameter. Therefore, the maximum interpolation error is achieved by evaluating the function for those parameters value that lie in the middle of the identified interval. Secondly, it illustrates that even though the parameter variation ranges are user-specified, it is still possible to obtain good results by selecting relatively wide ranges.

Base frame parameters	X_B [mm]	Y_B [mm]	Z_B [mm]	Φ_x [deg.]	Φ_y [deg.]
min. variation	-0.500	-0.500	-0.500	-0.500	-90.500
nominal	0.000	0.000	0.000	0.000	-90.000
max. variation	$+0.500$	$+0.500$	$+0.500$	$+0.500$	-89.500

Table 6.8: Nominal alignment and alignment error variations that are included in the precomputed parametric surfaces of roll angles.
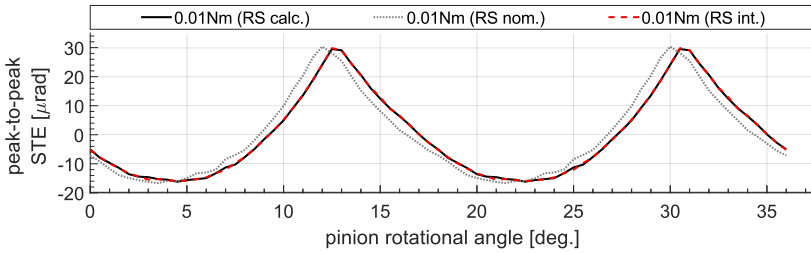
(a) Unloaded transmission error at 0.01 Nm.
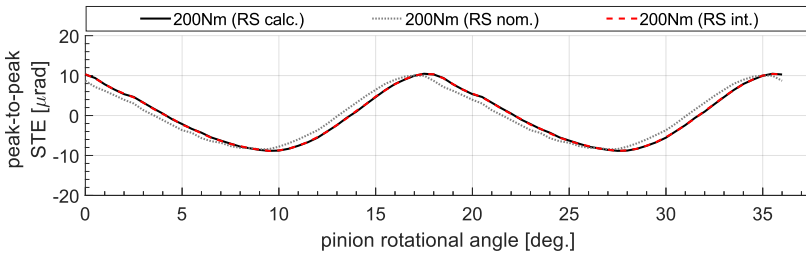
(b) Static transmission error at 200 Nm.
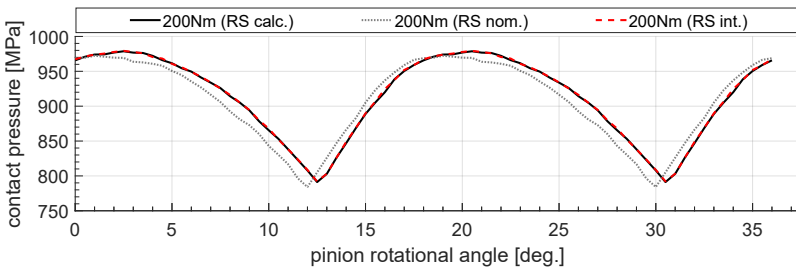
(c) Maximum contact pressure at 200 Nm.

Figure 6.5: Error analysis: TE at 0.01 Nm and 200 Nm and maximum contact pressure at 200 Nm for the rights flank pairs in the misaligned configuration, computed with the nominal and extended gear contact force element.

Evaluation of the LTCA results

To assess the accuracy of the pRS-based contact detection methodology the LTCA results for STE and maximum contact pressure, obtained with the extended GCFE (*RS int.*), are compared in Fig. 6.5 with the LTCA results of Fig. 6.3. The latter are computed by the nominal GCFE that used the surfaces of roll angles for the nominal configuration (*RS nom.*) and the recomputed surfaces of roll angles for the misaligned configuration (*RS calc.*).

Static transmission error The unloaded ($0.01\,\mathrm{Nm}$) and loaded ($200\,\mathrm{Nm}$) STE curves are provided in Fig. 6.5a and Fig. 6.5b. In both cases the STE curve, obtained the extended GCFE with interpolated surfaces of roll angles, is nearly identical to the GCFE with exact surfaces of roll angles for the misaligned configuration. Table 6.9 quantifies these results for the load case of $200\,\mathrm{Nm}$. When compared to the GCFE with nominal surfaces of roll angles, the extended GCFE predicts a peak-to-peak STE value of which the error is an order of magnitude lower for both the absolute error and the RMSE value. In addition, the results show that the interpolated surfaces of roll angles provide a better approximation of the true roll surfaces, such that the angular shift in the evolution of the STE curve disappears.

STE	RS	peak-to-peak [μrad]	error p-p [μrad]	shift p-p [deg.]	RMSE p-p [μrad]
	cal.	19.3049	–	–	–
$200\,\mathrm{Nm}$	nom.	18.4586	0.8463	0.4969	1.4600
	int.	19.2763	0.0287	0.0000	0.0738

Table 6.9: Error analysis: STE at $200\,\mathrm{Nm}$ for the rights flank pairs in the misaligned configuration, computed by the nominal and the extended GCFE.

Contact pressure	RS	p_{min} [MPa]	Δp_{min} [MPa]	p_{max} [MPa]	Δp_{max} [MPa]	shift [deg.]	RMSE [MPa]
	cal.	791.18	–	978.73	–	–	–
$200\,\mathrm{Nm}$	nom.	784.11	7.07	972.29	6.44	0.5004	16.13
	int.	792.07	-0.89	979.32	-0.59	0.0000	1.15

Table 6.10: Error analysis: contact pressure at $200\,\mathrm{Nm}$ for the rights flank pairs in the misaligned configuration, computed by the nominal and extended GCFE.

Maximum contact pressure   While the GCFE with nominal surfaces of roll angles already shows good results in terms of maximum contact pressure over the course of the mesh cycle, the main cause for the higher RMSE is attributed to the angular shift that results due to the differences between the nominal and recalculated surfaces of roll angles. Similar to the STE results, Fig. 6.5c and Table 6.10 illustrate that this angular shift of the contact pressure curve is not present for the extended GCFE. The interpolated surfaces of roll angles enable to approximate the true contact curves with such an accuracy that both the absolute error and RMSE value between the extended GCFE and the GCFE with exact surfaces of roll angles become negligible (order of $1\,\mathrm{MPa}$).

6.3   Numerical validation

To validate both the proposed parametric surface of roll angles methodology for contact detection and the gear contact force element that is developed in the dissertation, LTCA is performed to further evaluate the static behavior of the extended GCFE against NL-FEA contact simulations.

6.3.1   Model setup

FEM-based reference model   The FEM-based procedure for LTCA that is used in Chapter 5 to validate the nominal GCFE with analytical mesh compliance formulation, is used to validate the methodology for contact analysis in misaligned spiral bevel gears. The earlier-analyzed Base FE model of the spiral bevel gear pair is also used for this analysis. The details with regard to the NL-FEA-based contact simulations, the creation of the FEM-based gear pair model and the performed mesh convergence analysis, can be found in Subsection 5.4.2. The performed mesh convergence analysis for nominal gear pair alignment proves the Base model's mesh size convergence in terms of both contact pressure and STE. Since it is more than reasonable to assume that these findings can be extrapolated to the studied misaligned configuration of Table 6.1, a mesh convergence analysis under gear pair misalignment is omitted.

MB model with extended GCFE   The multibody approach to TCA, described in Subsection 5.4.1, is used to analyze the misaligned gear pair configuration of Table 6.1. The nominal GCFE is replaced with the extended force element to detect the contact in case of alignment errors, while the contact forces are computed based on the analytical gear mesh compliance model. The required pRS data, used to compute the contact curves, is defined by Table 6.8.
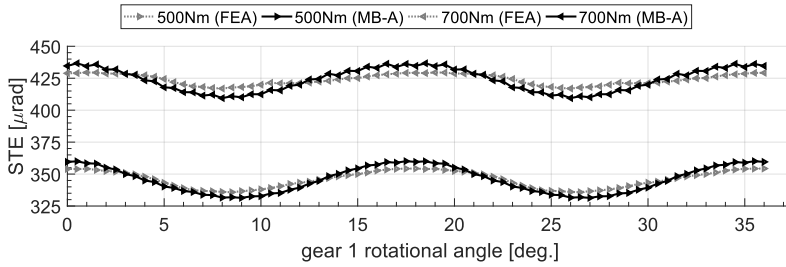
(a) STE curves under highly loaded conditions (500 Nm and 700 Nm).
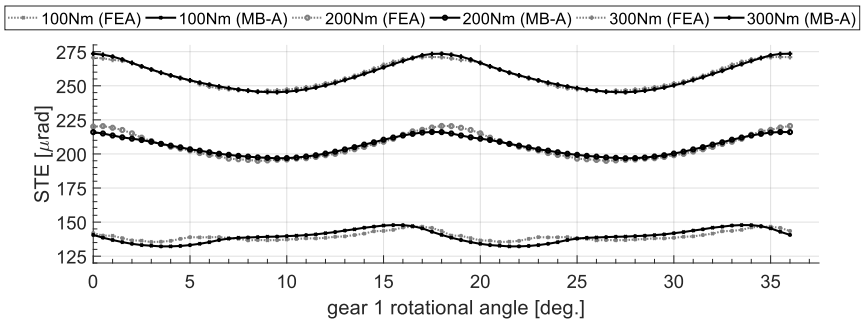
(b) STE curves under moderately loaded conditions (100 Nm, 200 Nm and 300 Nm).
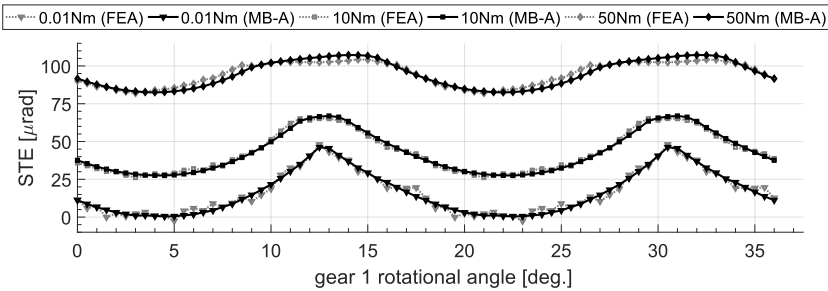
(c) STE curves under lightly loaded conditions (0.01 Nm, 10 Nm and 75 Nm).

Figure 6.6: STE curves for the misaligned gear pair from 0.01 Nm to 700 Nm for the reference model (FEA) and the extended GCFE with interpolated surfaces of roll angles and the analytical tooth compliance formulation (MB-A).

(a) GCFE - analyical compliance.

(b) NL-FEA contact simulation.
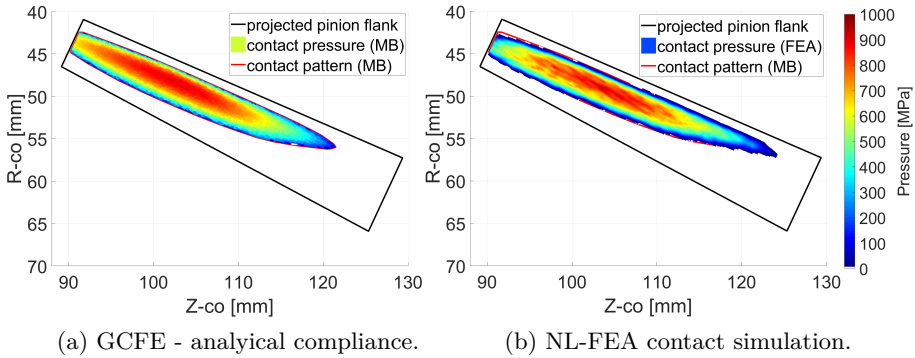
Figure 6.7: Overall contact pressure pattern for the misaligned case at 200 Nm.

(a) GCFE - analyical compliance.

(b) NL-FEA contact simulation.
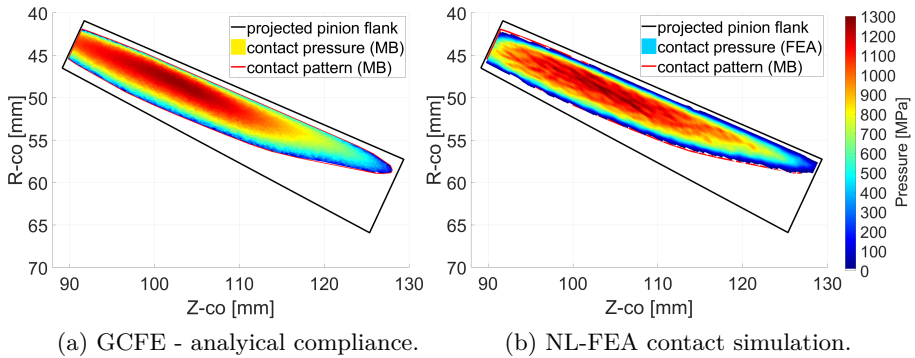
Figure 6.8: Overall contact pressure pattern for the misaligned case at 500 Nm.

(a) GCFE - analyical compliance.

(b) NL-FEA contact simulation.
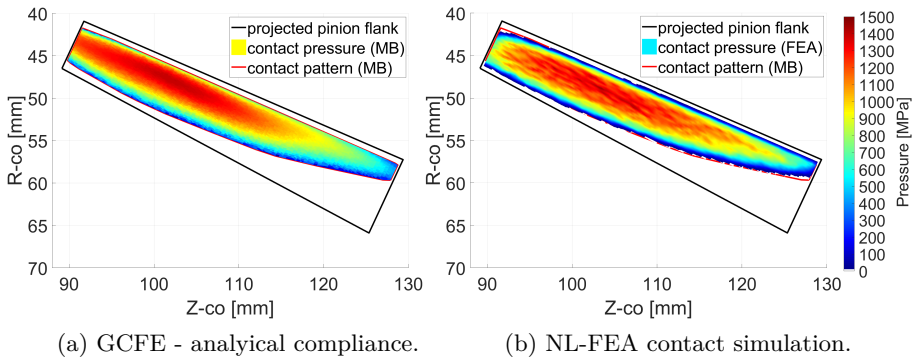
Figure 6.9: Overall contact pressure pattern for the misaligned case at 700 Nm.

6.3.2   Loaded tooth contact results

As with the numerical validation of the nominal GCFE, the accuracy of the extended force element is studied for eight load cases that vary from unloaded (0.01 Nm) to highly loaded (700 Nm). The STE, the contact pattern and the overall contact pressure distribution are compared against those of FEM-based LTCA for the right tooth flank pairs of the misaligned spiral bevel gear pair.

Static transmission error   Fig. 6.6 shows the STE curves for the misaligned gear pair. Each STE curve displays two cycles, which repeat themselves in correspondence with the pinion's tooth indexing. Table 6.11 provides an overview of the PP STE. The STE curves, predicted by the extended GCFE, provide a good correlation in terms of both shape and peak-to-peak value. Up to moderately high torque magnitudes, the STE is well correlated to the NL-FEA results, as shown in Fig. 6.6c and 6.6b. This suggests that the interpolated surfaces of roll angles approximate the true contact curves for the misaligned configuration with high accuracy. Comparing the STE curves of the aligned gear pair with those where misalignments are present, it can be noted the UTE value for the misaligned configuration is higher. This is easily explained by the change in ease-off topography (Fig. 5.3 vs. Fig. 6.2) that occurs due to the misalignment. At higher loads a loss of correlation is again noted (See also Subsection 5.4.3), although the shape of the STE curves is better preserved. This further indicates that at high load the uncoupled global compliance model reaches its limits and more advanced methodologies (e.g. FEM-based) are needed to improve the modeling of load sharing and gear blank deformation.

	Load	[Nm]	0.01	10	50	100	200	300	500	700
PP STE	FEA	[μrad]	47.3	39.0	22.3	11.3	25.6	24.6	18.5	12.6
	MB-A	[μrad]	45.7	39.4	24.7	15.6	19.3	28.3	27.6	23.7
	Diff.	[μrad]	−1.6	0.4	2.4	4.3	−6.3	3.7	9.1	11.1

Table 6.11: Peak-to-peak STE (PP STE) for the misaligned gear pair, computed by the reference model (FEA) and by the proposed GCFE model (MB-A).

Contact pattern   The contact pattern and overall contact pressure distribution, predicted by the extended GCFE, is shown in Fig. 6.7a, Fig. 6.8a and Fig. 6.9a. The contact pattern and contact pressure distribution, extracted from the NL-FEA contact simulations, are provided in Fig. 6.7b, Fig. 6.8b and Fig. 6.9b onto which the contact pattern boundary, predicted by the GCFE, is added to aid the evaluation of the size and direction of both contact patterns. The results are

displayed on a projection of the pinion flank to compare the analytical contact pressure with the maximum nodal pressure that is computed by the NL-FEA contact simulations. Besides a good correlation in terms of contact pattern location and contact pressure distribution, Figs. 6.7 to 6.9 predict the expected shift of contact pattern towards the toe of the flank edges (see Figs. 5.13 to 5.15). This is consistent with the change in ease-off topography, shown in Fig. 6.2.

Validity of the gear contact model   Given that the extended GCFE for misaligned spiral bevel gears uses the analytical tooth deformation model, its numerical efficiency and accuracy are in line with what is reported in Chapter 5.

The differences in overall contact pressure distribution and contact area are well within the 15 % error limit, as learned from a visual comparison of Figs. 6.7 to 6.9. For the studied case of gear misalignment, the extended GCFE also shows to correctly capture the evolution of the STE in function of the applied load. However, the listed limitations of the analytical tooth compliance model again cause a correlation loss in (peak-to-peak) TE at higher loads (above 500 Nm). While for loads up to 300 Nm the difference in PP STE for the misaligned gear pair is on average still around the envisioned 15 % limit, the results show that further improvements to the gear mesh compliance model have to be considered.

6.4   Conclusion

The correct and accurate modeling of gear alignment errors, using the tools that are developed in this dissertation, is the prime focus of this chapter. Latent in the discussion but important for the applicability of the developed gear contact force element, is the requirement to simulate variable gear pair misalignment, which occurs due to system interactions (e.g. bearing or shaft compliance, ...).

Section 6.1 shows the versatility of the penetration-based gear contact force element with surfaces of roll angles, computed for the non-misaligned (nominal) configuration, as it is capable of predicting the transmission error and the contact pressure for a misaligned gear pair rather accurately. However, comparing against LTCA with the exact surfaces of roll angles reveals small differences in the location and the orientation of the instantaneous contact curves.

In Section 6.2 a novel method that updates the surfaces of roll angles depending on the instantaneous misalignment, is proposed to further improve the contact detection under gear pair misalignment. Validation of this extended gear contact model against nonlinear finite element analysis in Section 6.3 shows a good correlation in terms of transmission error and contact pressure distribution.

Chapter 7

Conclusions and future work

The research that is presented in this dissertation, treats the development of an accurate and numerically efficient modeling strategy for spiral bevel gears. The proposed methodology aims at correctly predicting component behavior at a computational cost that constitutes further application within system-level analysis, while also creating a foundation to facilitate future research into the field of contact modeling for spiral bevel gears. Considering that present-day engineering challenges often arise from a pursuit of increased performance that is contrasted by a continued desire for lightweight design, the need for such solutions, which integrate into the system-level design process for mechanical transmissions, is evermore growing.

The complexity of the three-dimensional tooth surface geometry, which is required to guarantee near-conjugate motion transmission, poses a substantial obstacle for the design of spiral bevel gears. This has made the tooth contact analysis (TCA) based optimization of the contact characteristics common practice during the design. Yet, the numerical efficiency of TCA simulations is often hindered by the fact that they consider the contacting flanks to be arbitrary. The high computational cost, which results from applying general contact detection methods, limit their applicability to the study of component behavior. In contrast, dynamic models of spiral bevel gears are commonly based on three-dimensional TCA results that are condensed into a single mesh point.

The modeling strategy that is presented in this dissertation makes an attempt to bridge the gap between both modeling methods. A summary of the main contributions and findings is provided in Section 7.1. Notwithstanding the progress that is made, the nice thing about research is that improvements are always possible; some suggestions are made in Section 7.2.

7.1   Conclusions

7.1.1   A novel spiral bevel gear contact force model

This dissertation's main contribution is the development of a novel gear contact force model that allows the analysis of spiral bevel gear drives within a multibody simulation framework. The modeling methodology is devoted to the analysis of discretized contact surfaces to increase its versatility within the design process. Since an accurate representation of the contact interfaces is vital for the correct prediction of the contact phenomena during operation, the gear tooth surfaces are created by simulating the five-cut face-milling manufacturing process.

Given the complexity of the tooth surfaces and computational cost that characterizes general-purpose contact detection methods, the development of an accurate but also numerically efficient contact detection is accentuated. The contact detection methodology, which is proposed in [63] to improve the computational efficiency of TCA, is identified as one fo the most applicable methods to the system-level analysis of spiral bevel gears. Instead of enforcing contact between the real tooth surfaces, the detection process is simplified by determining contact between the (chosen) real pinion tooth flank and a (computed) theoretical flank that is conjugate to the pinion flank. The ease-off topography, which is computed during data preprocessing for a given mounting configuration, is used by this method to account for the differences between the conjugate to the pinion flank and the mating real gear flank. The key to the superior numerical efficiency of the methodology lies in the surface of roll angles, which enables to express the instantaneous contact curves between the real pinion flank and its conjugate surface as a function of the gear rotational angle (i.e. roll angle). The surface of roll angles are computed during data preprocessing by solving the equation of meshing, which determines the kinematics of the chosen pinion flank for a given alignment of the gear pair. The assumption that the contact curve between the pinion flank and its conjugate surface does not differ much from the one between the real pinion and the real gear flanks is considered justified, since the contacting tooth surfaces of real-world gear pairs are designed to transmit motion in a near-conjugate manner.

However, since the ease-off topography depends on both the geometry of the contacting tooth surfaces and the relative installment of the gear pair, it shows to be susceptible to gear alignment errors. In a system-level analysis, it is not uncommon that variations about the nominal mounting conditions are introduced due to interactions with and the compliance of the supporting components (e.g. shafts). Therefore, the dissertation proposes a spiral bevel gear contact model that does not rely on the ease-off topography to detect

contact but uses the surfaces of roll angles of the real contact flank pair, i.e. the real pinion and the real gear tooth surfaces. It is shown that this modification improves the versatility of the gear contact model (with surfaces of roll angles for the nominal gear pair configuration) to approximate the contact conditions of a misaligned gear pair with high accuracy. The surfaces of roll angles for the real pinion and the real gear flanks are used to develop a general, accurate and numerically efficient penetration based contact detection algorithm. Contact between a mating pair of gear tooth surfaces is determined based on the penetration between the discretized, rigid flanks. The resulting contact forces are computed based on the assumption that the flank penetration matches the deformation of the gear tooth surfaces if they were flexible. A tooth deformation model is used that formulates the total tooth deflection as the result of: a local contribution that represents the nonlinear deformation in the region of the contact zone between the two contact surfaces, and a global contribution that captures the linear deformation of the gear teeth outside of the contact zone.

The compliance model is designed to be modular, allowing future improvements of both the global and local compliance models. In this dissertation the local contact deformation is modeled based on Hertzian contact theory that assumes a line contact along a segmented contact curve. The global deformation, on the other hand, is modeled under the assumption that an equivalent involute tooth profile can be fitted onto the spiral bevel tooth geometry. Analytical expressions, derived from beam theory, are used to create an uncoupled model that approximates the linear component of the tooth deformation.

The envisioned computational efficiency of the proposed gear contact model, i.e. order of seconds for a single contact simulation step, is successfully achieved, thanks to the optimized contact detection (the surfaces of roll angles), and a minimum degrees of freedom (contact between tooth surfaces of rigid bodies).

7.1.2 Accurate contact detection in case of gear misalignment

Given that mechanical transmissions are used to transmit power under high operational loads or at high operational frequency, gear alignment errors are expected to occur due to deformation of the supporting components, such as shafts, spline connections or bearings. However, since these deflections remain small, it is assumed that the resulting alignment errors remain small and that they vary around the nominal (non-misaligned) configuration of the gear pair. Based on these assumptions, it is reasoned that even in case of gear pair misalignment the rotation of the tooth flanks to their respective surfaces of actions does not change significantly. Therefore, the surfaces of roll angles that are computed for the non-misaligned gear pair configuration, can serve

as reasonable approximations to detect contact between misaligned gear tooth surfaces. Investigation into the contact behavior of the nominal gear contact model for misaligned spiral bevel gear pairs, proves that this assumption is indeed acceptable. The overall contact pattern, contact pressure and peak-to-peak transmission error show to be well approximated by the contact force element with nominal surfaces of roll angles, when compared to contact force element that is updated with the exact surfaces of roll angles (i.e. computed for the misaligned configuration). Yet, small differences in the location and the orientation of the instantaneous contact curves are identified, which result in a notable angular shift of the transmission error curves.

To further improve the contact detection in the presence of gear pair alignment errors, the idea of parametrically defined surfaces of roll angles is proposed in this dissertation. A set of roll surfaces that correspond to parametrically defined configurations of gear pair misalignment, is computed during data preprocessing for each tooth surface of the gear pair. A linear multivariate interpolation strategy is developed that enables the extended spiral bevel gear contact model to automatically compute new surfaces of roll angles that better represent the kinematics of the misaligned gear pair. Evaluation of the TCA results for transmission error and contact pressure, obtained by the extended contact force element with interpolated surfaces of roll angles, demonstrates that the differences between the proposed methodology and the model with exact surfaces of roll angles are negligibly small.

7.1.3   Validation of the methodology and limitations

To validate the spiral bevel gear contact force model the dissertation proposes a multibody approach to loaded tooth contact analysis (LTCA) and compares its results against nonlinear finite element analysis (FEA) based contact simulations. The TCA is performed by modeling the studied spiral bevel gear pair as rigid bodies, while the developed gear contact force element is used to compute the forces that arise due to a prescribed load that is statically applied to the pinion. The FEM-based reference model of the spiral bevel gear pair is created with dedicated and automated procedures that are developed within this research. A commercially available software package for FEA (NX Nastran - SOL 601) is used to perform the contact simulations and to compute the reference data sets.

The accuracy of the nominal and extended gear contact model is evaluated against FEM-based contact simulations for an aligned and misaligned spiral bevel gear pair configuration. The analytical tooth compliance model is used to compute the contact loads. For each alignment case, eight loads that range from $0.01\,\mathrm{Nm}$ (unloaded) to $700\,\mathrm{Nm}$, are simulated.

Correlation against the FEA-based LTCA results shows that the spiral bevel gear contact model well predicts the overall gear pair's performance both in the absence and the presence of gear alignment errors. The results are compared for well defined metrics such as static transmission error (STE), location and orientation of the instantaneous contact curves, location and area of the overall contact pattern and the resulting contact pressure distribution. For both analyzed configurations of gear pair (mis)alignment and for loads up to 300 Nm, the metrics are correctly predicted with an averaged accuracy that is within the desired 10-15 % error range, when compared to the FEA-based contact results.

At higher loads (above 500 Nm) the results for both alignment configurations indicate a loss of correlation in terms of peak-to-peak STE, although the overall contact pressure distribution remains well predicted. When the gear tooth deflection of a single gear teeth pair is sufficiently high due to the applied load, multiple gear teeth pair enter in contact, giving rise to load sharing effects. However, the analytical global tooth deformation models is uncoupled, such that the loading of one tooth does not induce the deformation of neighboring teeth. Therefore, it only approximates the load sharing effects between multiple teeth. In addition, the model assumes the gear blank to be rigid, which becomes a less accurate assumption as the load increases. More advanced modeling methods (e.g. FEM-based), which correctly include such effects, are the preferred path for further research to increase the fidelity of the global gear deformation model.

Besides enabling the proposed methodology to be evaluated at a level that goes beyond what is commonly published in the literature, the FEA-based contact simulations also create data sets that can be used to validate future research.

7.1.4 Overall conclusion

The research and effort that went into the development of the novel spiral bevel gear contact force model, naturally unifies all the different building blocks into a dedicated toolchain that covers: (i) the creation of the tooth surface geometry, (ii) the automated creation of detailed parametric FEM-based spiral bevel gear models, (iii) the automated preprocessing of the required data for contact detection and (iv) dedicated procedures for unloaded and (v) loaded tooth contact analysis of spiral bevel gears. The decision to develop a modeling methodology that starts from an accurate but discrete representation of the gear tooth surfaces proves to be successful, since it enables the analysis of non-face-cut spiral bevel and hypoid gears without any additional knowledge of the manufacturing process. While these efforts are not described in this dissertation, a recently published article, which is co-authored by the author, explores the unloaded contact behavior of such spiral bevel gears [33].

7.2   Future work

7.2.1   Advanced methodologies for gear compliance modeling

Validation of the proposed spiral bevel gear contact model with analytical tooth compliance formulation reveals a loss of accuracy for higher levels of the applied load. In the developed compliance model the total tooth deflection of a set of gear teeth under load is described as the superposition of two contributions: the local contact deformation of the contacting gear teeth and a global deformation component for each gear tooth in contact. This leads to an uncoupled compliance model that lacks the ability to account for load sharing effects and gear blank deformation. Notwithstanding the overall excellent correlation that is obtained against FEA-based contact simulations, there is significant room for further improvement of the tooth compliance model within the proposed methodology.

The inclusion of a FEA-based approximation for the global tooth compliance, leads to the creation of a semi-analytical contact model (see Section 2.2.2) in line with what ANDERSSON and VEDMAR established for cylindrical gears [5]. The *flexibility matrix* approach and *model order reduction* are proposed in the literature as viable methods to include FEA-based compliance data.
The flexibility matrix includes the combined compliance of the pinion, the gear and potentially supporting component. Each column of the flexibility matrix reflects the FE model's deformation due to a unit normal load that is applied to one of the contact nodes. The deformation is evaluated along the surface normal direction for all the listed contact nodes. Since only the deformation fields of the contacting surfaces are of importance, the flexibility matrix is often generated based on partial FE models that only include a few gear teeth [36]. Alternatively, model order reduction methods (MOR) can be used to better represent the multibody contact problem. An example of such MOR techniques are project-based methods that approximate the unknown state vector by a basis of reduced dimension, while projecting the governing equations onto an appropriately defined subspace of lower dimension [16]. The added advantage of MOR lies in the fact that a statically complete basis can consist of both static deformations shapes and dynamically reacting eigenvectors of the flexible body, enabling a future integration of the proposed modeling methodology for spiral bevel gears into a flexible multibody (dynamics) simulation environment. Relevant parametric MOR-techniques are proposed in [119], [16] and [21], where the emphasis lies on the dynamic solution of gear contact problems, applied to cylindrical gears. These techniques can also be applied to spiral bevel gears and the contact detection methods, developed in this dissertation, can aid in improving the efficiency of the contact detection.

7.2.2 Improved simulation of gear alignment error

To improve the contact detection in case of gear alignment error, this dissertation proposes the novel idea of updating the surfaces of roll angles, depending on the instantaneous misalignment parametrization. While the idea proves to be successful, the required parametrization is data intensive. Investigating whether a parametrization in terms of spiral bevel gear installment settings provides equivalent results, might provide further improvements of the methodology. This way the maximum number of misalignment parameters is reduced to four. Alternatively, a sensitivity study is proposed to identify those parameters that contribute the most to the approximation of the exact surfaces of roll angles. Building on this information, improved sampling strategies can be investigated to minimize the number of precomputed surfaces of roll angles, used to cover a predefined range of gear pair misalignment. However, a suitable error criterion has to be identified to indicate how well the interpolated surface of roll angles approximates the exact surface. Since error criteria based on the surface of roll angles or the ease-off topography require the computation of the exact solution, their applicability might be limited. Evaluating how well a gear tooth flank's interpolated surface of roll angles satisfies the equation of meshing for a predefined gear alignment error, seems to be a good starting point.

7.2.3 Towards dynamic 3D simulation of spiral bevel gears

The ultimate goal of the established methodology is the dynamic simulation and analysis of spiral bevel gears, using the advanced three-dimensional gear contact models that are developed in this dissertation. The presented spiral bevel gear contact force model is an important first step towards this goal's realization. The further development of the gear force model within a dynamic multibody simulation context for spiral bevel gear pairs is considered the logical next step. The simulation of gear pair dynamics is a numerically challenging problem due to the non-smooth nature of the contact force, which requires a small enough time step during the (transient) time simulation to correctly capture its effects. Besides the efficient modeling of the gear pair's structural behavior, an efficient contact detection method is therefore essential to minimize the total computational load for each time step. Correct simulation of the gear dynamics also requires an extension of presented models to include additional effects between the contact interfaces, such as friction and gear mesh damping. The gear mesh damping accounts for the energy loss at the contact interfaces, lessening the dynamic effects that arise from the tooth impacts. Finally, the development of a three-dimensional dynamic gear contact model can also support the research towards more accurate lubrication models for spiral bevel gears.

Appendix A

Important data of the analyzed spiral bevel gear pair

To demonstrate the different aspects of the proposed methodology, a spiral bevel gear set is analyzed over the course of the different chapters of this dissertation. The gear pair data was taken from literature [6] to have a first level of validation during the development process for both the geometry and the UTCA results. A virtual model of the spiral bevel gear pair, visualized in Fig. A.1, is obtained by simulating the face-milling process. Other important data such as the blank data for the individual gear pair elements (Section A.1), the nominal installment data (Section A.2) and the manufacturing data (Section A.3) are also reported.
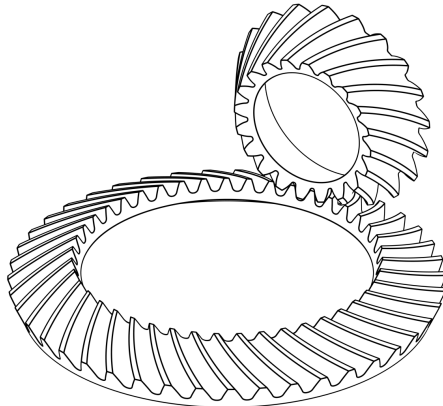

Figure A.1: A virtual model of the analyzed spiral bevel gear pair.

A.1 Gear blank data

The gear pair's blank geometry is derived according to the calculation procedures that are defined by international standards, such as AGMA [2] or ISO [52].

Blank data	symbol	units	Pinion	Gear
Number of teeth	Z	[-]	20	43
Face width		[mm]	41.0000	
Mean cone distance		[mm]	120.9400	
Mean spiral angle		[deg.]	32.0000	
Hand of spiral		[-]	RH	LH
Pitch cone angle		[deg.]	24.9439	65.0561
Root cone angle		[deg.]	23.1666	61.8166
Face cone angle		[deg.]	28.1833	66.8333
Outer addendum		[mm]	6.8900	3.2500
Outer dedendum		[mm]	4.3700	8.0100

Table A.1: Blank geometry the analyzed spiral bevel gear pair.

Material data	symbol	units	Pinion	Gear
Material			Steel	Steel
Young's modulus	E	[GPa]	210.00	210.00
Poisson's ratio	ν	[-]	0.30	0.30

Table A.2: Material properties of the analyzed spiral bevel gear pair.

A.2 Gear pair installment data

In absence of misalignments, the gear pair installment is defined by Table A.3.

Installment data	symbol	units	Gear Pair
Shaft angle	γ	[deg.]	-90.0000
Hypoid offset	E_H	[mm]	0.0000
Pinion axial offset	A_1	[mm]	0.0000
Gear axial offset	A_2	[mm]	0.0000

Table A.3: Nominal installment parameters of the spiral bevel gear pair.

A.3 Manufacturing data

The gear pair's tooth surface geometry is obtained by simulation of face-milling process. The mathematical model that is described in Section 3.2.2 was used to simulate the five-cut process. The required blade parameters and machine settings are listed in Tables A.4 and A.5.

A.3.1 Blade parameters

Blade parameters			Pinion		Gear	
			CNC	CNV	CNC	CNV
Profile angle	α_A	[deg.]	18.0000	22.0000	20.000	
Root fillet radius	R_F	[mm]	1.1016		2.413	
Cutter point diameter	$2R_A$	[mm]	305.3927	304.6986	n/a	
Head cutter diameter	$2R_C$	[mm]	n/a		304.800	
Point width	P_C	[mm]	n/a		3.556	

Table A.4: Blade parameters of the analyzed spiral bevel gear pair.

A.3.2 Machine settings

Machine settings			Pinion		Gear	
			CNC	CNV	CNC	CNV
Radial setting	S_R	[mm]	128.8831	140.9091	135.2870	
Basic cradle angle	q_0	[deg.]	73.4721	71.3245	−72.8081	
Sliding base	X_{SB}	[mm]	−0.8492	0.7376	0.0000	
Blank offset	E_M	[mm]	7.7182	−6.8138	0.0000	
Mach. center to back	X_D	[mm]	2.2066	−1.8271	0.0000	
Mach. root angle	γ_M	[deg.]	23.1666		61.8166	
Ratio of roll	m_{gc}	[-]	2.2941	2.4260	1.1011	
2nd roll constant	C_2	[-]	0.0000	0.0000	0.0000	
3rd roll constant	C_3	[-]	0.0000	0.0000	0.0000	

Table A.5: Machine settings of the analyzed spiral bevel gear pair.

Appendix B

Transformations to simulate the face-milling process

To acquire an accurate representation of the tooth flank geometry of a generated face-milling spiral bevel gear pair, created with the five-cut machining process, the cutting process is simulated in Chapter 3 by determining the enveloping surface to a family of cutter surfaces. This family of cutter surfaces describes the motion of the cutter head w.r.t. the work-piece as the cutter head cuts away material. The envelope to this family of surfaces represents the created tooth slot. The model of a cradle-based spiral bevel gear generator is used to incorporate the required machining motions, which are described as a series of elementary transformations (i.e. rotations or translations).

A homogeneous transformation matrix allows to express the general motion of a rigid body by combining the rotational and translational components in a single matrix. The homogeneous transformation matrix $\mathbf{T}_{gC}$ is used to express any point $\boldsymbol{r}_C$ on the cutter head, given in the cutter head's reference frame S_C, w.r.t. the reference frame S_g, fixed to the gear blank.

$$\bar{\boldsymbol{r}}_g = \mathbf{T}_{gC}\,\bar{\boldsymbol{r}}_C \tag{B.1}$$

In Eq. (B.1), $\bar{\boldsymbol{r}}_C$ and $\bar{\boldsymbol{r}}_g$ are the homogeneous vector equivalent of $\boldsymbol{r}_C$ and $\boldsymbol{r}_g$.

$$\mathbf{T}_{gC} = \left[\begin{array}{c|c} \mathbf{L}_{gC} & \Delta\boldsymbol{O}_{gC} \\ \hline \mathbf{0}_{1\times 3} & 1 \end{array}\right], \qquad \bar{\boldsymbol{r}}_C = \left[\begin{array}{c} \boldsymbol{r}_C \\ 1 \end{array}\right], \qquad \bar{\boldsymbol{r}}_g = \left[\begin{array}{c} \boldsymbol{r}_g \\ 1 \end{array}\right] \tag{B.2}$$

This 4×4 homogeneous transformation matrix is built, using the 3×3 rotation matrix $\mathbf{L}_{gC}$ to express the orientation of S_C w.r.t. S_g and the vector $\Delta\boldsymbol{O}_{gC}$ to express the translation from $\boldsymbol{O}_C$ (the origin of S_C) to $\boldsymbol{O}_g$ (the origin of S_g).

Given the layout of the cradle-based gear generator (see Fig. 3.8b), $\mathbf{T}_{gC}$ is found as a series of successive transformations, leading to Eq. (3.7). The required elementary transformation matrices of Eq. (3.7) are defined as follows:

The homogeneous transformation matrix from the *cutter head* reference frame S_C to the *cradle* reference frame S_C is defined as:

$$\mathbf{T}_{QC}(S_R, q_0) = \begin{bmatrix} 1 & 0 & 0 & S_R\cos(q_0) \\ 0 & 1 & 0 & S_R\sin(q_0) \\ 0 & 0 & 1 & 0 \\ 0 & 0 & 0 & 1 \end{bmatrix} \tag{B.3}$$

The homogeneous transformation matrix from the *cradle* reference frame S_C to the *machine* reference frame S_M is defined as:

$$\mathbf{T}_{MQ}(q) = \begin{bmatrix} \cos(q) & -\sin(q) & 0 & 0 \\ \sin(q) & \cos(q) & 0 & 0 \\ 0 & 0 & 1 & 0 \\ 0 & 0 & 0 & 1 \end{bmatrix} \tag{B.4}$$

The homogeneous transformation matrix from the *machine reference* frame S_M to the *sliding base* reference frame S_B is defined as:

$$\mathbf{T}_{BM}(-X_{SB}) = \begin{bmatrix} 1 & 0 & 0 & 0 \\ 0 & 1 & 0 & 0 \\ 0 & 0 & 1 & -X_{SB} \\ 0 & 0 & 0 & 1 \end{bmatrix} \tag{B.5}$$

The homogeneous transformation matrix from the *sliding base* reference frame S_B to the *blank offset* reference frame S_E is defined as:

$$\mathbf{T}_{EB}(E_M) = \begin{bmatrix} 1 & 0 & 0 & 0 \\ 0 & 1 & 0 & E_M \\ 0 & 0 & 1 & 0 \\ 0 & 0 & 0 & 1 \end{bmatrix} \tag{B.6}$$

The homogeneous transformation matrix from the *blank offset* reference frame S_E to the *machine root* reference frame S_γ is defined as:

$$\mathbf{T}_{\gamma E}(-(\tfrac{\pi}{2}-\gamma_M)) = \begin{bmatrix} \cos\!\left(-(\tfrac{\pi}{2}-\gamma_M)\right) & 0 & \sin\!\left(-(\tfrac{\pi}{2}-\gamma_M)\right) & 0 \\ 0 & 1 & 0 & 0 \\ -\sin\!\left(-(\tfrac{\pi}{2}-\gamma_M)\right) & 0 & \cos\!\left(-(\tfrac{\pi}{2}-\gamma_M)\right) & 0 \\ 0 & 0 & 0 & 1 \end{bmatrix}$$

$$= \begin{bmatrix} \sin(\gamma_M) & 0 & -\cos(\gamma_M) & 0 \\ 0 & 1 & 0 & 0 \\ \cos(\gamma_M) & 0 & \sin(\gamma_M) & 0 \\ 0 & 0 & 0 & 1 \end{bmatrix} \tag{B.7}$$

The homogeneous transformation matrix from the *machine root* reference frame S_γ to the *machine center-to-back* reference frame S_D is defined as:

$$\mathbf{T}_{D\gamma}(-X_D) = \begin{bmatrix} 1 & 0 & 0 & 0 \\ 0 & 1 & 0 & 0 \\ 0 & 0 & 1 & -X_D \\ 0 & 0 & 0 & 1 \end{bmatrix} \tag{B.8}$$

The homogeneous transformation matrix from the *machine center-to-back* reference frame S_D to the *gear blank* reference frame S_g is defined as:

$$\mathbf{T}_{gD}(-\phi_g) = \begin{bmatrix} \cos(-\phi_g) & -\sin(-\phi_g) & 0 & 0 \\ \sin(-\phi_g) & \cos(-\phi_g) & 0 & 0 \\ 0 & 0 & 1 & 0 \\ 0 & 0 & 0 & 1 \end{bmatrix}$$

$$= \begin{bmatrix} \cos(\phi_g) & \sin(\phi_g) & 0 & 0 \\ -\sin(\phi_g) & \cos(\phi_g) & 0 & 0 \\ 0 & 0 & 1 & 0 \\ 0 & 0 & 0 & 1 \end{bmatrix} \tag{B.9}$$
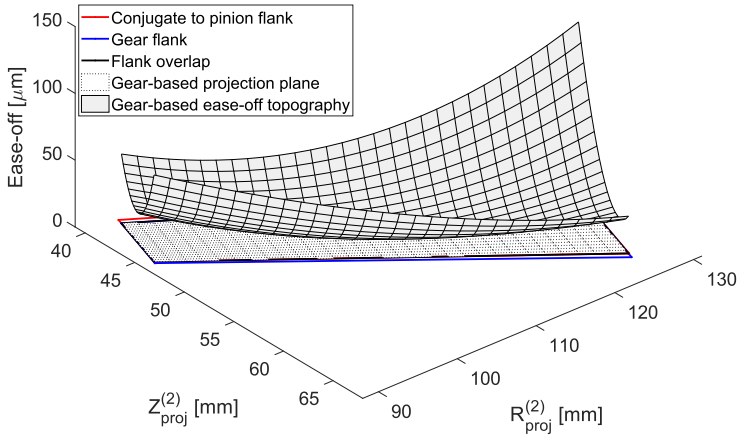
Appendix C

Ease-off topography definitions

For completeness, a comparison between the ease-off topography definitions is provided in Fig. C.1. Using the circular arc projection approach of Section 4.1.3, the gear-based (Fig. C.1a) and pinion-based (Fig. C.1b) ease-off topography has been created. The equations to compute the gear-based ease-off topography in units of angle and length are given by Eqs. (4.21) and (4.22), respectively. Similarly, the equations to construct the pinion-based ease-off topography are given by Eqs. (C.1) and (C.2).

$$\mathcal{E}_\theta^{(1)} = \theta_{proj}^{(1)} - \theta_{proj}^{(1c)} \tag{C.1}$$

$$\mathcal{E}_\delta^{(1)} = R_{proj}^{(1)} \, \mathcal{E}_\theta^{(1)} \tag{C.2}$$

In a general case of mismatched flanks the conjugate to the (real) pinion flank differs from the mating (real) gear flank. As a result, the flank overlap between the conjugate to the pinion flank and the gear will slightly differ from the flank overlap between the pinion and the gear. Due to this difference in flank overlap, small differences between the pinion-base and gear-based ease-off can be noticed at the edges of the flank overlap. However, as is seen from Fig. C.1 such that differences are negligible. When ease-off is expressed as an angular rotation, the pinion-based and gear-based ease-off relate to each other as a function of the gear ratio $m_{21} = \frac{Z_1}{Z_2}$.

(a) Gear-based ease-off topography.
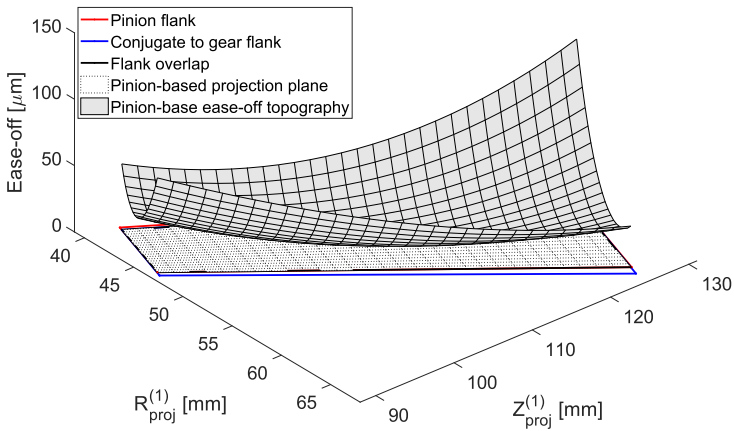
(b) Pinion-based ease-off topography.

Figure C.1: Illustration of gear-based and pinion-based ease-off topography onto the corresponding projection plane.

Appendix D

Shape functions

This appendix contains an overview of the different shape functions that are used in this dissertation to enable multivariate interpolation. Notable examples of the use of shape functions are found in Chapter 2 (Section 2.2.3) for the NTS contact detection method, in Chapter 4 (Section 4.1.3) to compute the ease-off topography on the projection plane and in Chapter 6 to update the surface of roll angles of the gear flanks, depending on the instantaneous position and orientation of the gear pair.

D.1   Linear element shape functions

D.1.1   Linear interpolation

Linear interpolation in one dimension (1D) requires two data nodes, which are spatially envisioned as two end points of a line. The general form of the shape functions that are used to perform the linear interpolation is written as:

$$N_l^e(\xi) = \frac{1}{2}(1 + \xi \xi_l) \tag{D.1}$$

The value of the shape function variable ξ varies between -1 and 1 along the line that connects both nodes. The parameters ξ_l correspond to the natural coordinates of the lth node of the element, such that the shape functions are defined by:

$$N_1^e(\xi, \eta) = \frac{1}{2}(1 - \xi), \qquad N_2^e(\xi, \eta) = \frac{1}{2}(1 + \xi) \tag{D.2}$$

D.1.2 Bilinear multivariate interpolation

Linear interpolation along two dimensions (2D) requires four data nodes, which can be spatially represented as four points that span a quadrilateral element. The general form of the shape functions that are required to perform the linear interpolation is written as:

$$N_l^e(\xi, \eta) = \frac{1}{4}(1 + \xi\xi_l)(1 + \eta\eta_l) \tag{D.3}$$

The shape function variables are ξ and η of which the values vary between -1 and 1 across the surface of the quadrilateral element. The parameters ξ_l and η_l denote the natural coordinates of the lth node of the element, according to the node numbering convention shown in Table D.1.

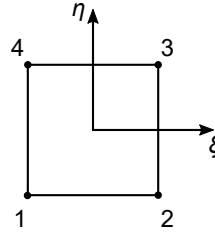| Node	ξ_l	η_l
1	-1	-1
2	$+1$	-1
3	$+1$	$+1$
4	-1	$+1$

Table D.1: Node numbering convention for a four-noded quadrilateral element.

Following the provided numbering convention the shape function that describe the bilinear quadrilateral element are found as:

$$N_1^e(\xi, \eta) = \frac{1}{4}(1 - \xi)(1 - \eta), \quad N_2^e(\xi, \eta) = \frac{1}{4}(1 + \xi)(1 - \eta)$$

$$N_3^e(\xi, \eta) = \frac{1}{4}(1 + \xi)(1 + \eta), \quad N_4^e(\xi, \eta) = \frac{1}{4}(1 - \xi)(1 + \eta) \tag{D.4}$$

D.1.3 Trilinear multivariate interpolation

Linear interpolation along three dimensions (3D) requires eight data points, which can be spatially represented by an eight-noded hexahedron element. The general form of the shape functions that are required to perform the linear interpolation is written as:

$$N_l^e(\xi, \eta, \mu) = \frac{1}{8}(1 + \xi\xi_l)(1 + \eta\eta_l)(1 + \mu\mu_l) \tag{D.5}$$

The values of the shape function variables ξ, η and μ again vary between -1 and 1 throughout the volume of the element. The parameters ξ_l, η_l and μ_l denote the natural coordinates of the lth node of the element. The node numbering convention for the trilinear hexahedron element is given in Table D.2.

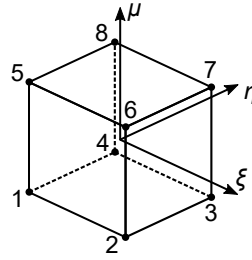| Node	ξ_l	η_l	μ_l
1	-1	-1	-1
2	$+1$	-1	-1
3	$+1$	$+1$	-1
4	-1	$+1$	-1
5	-1	-1	$+1$
6	$+1$	-1	$+1$
7	$+1$	$+1$	$+1$
8	-1	$+1$	$+1$

Table D.2: Node numbering convention for a eight-noded hexahedron element.

As can be derived from this table, the node numbering of the shape functions is obtained in similar fashion as was a done for the bilinear quadrilateral element.

D.1.4 Extension to higher dimensions

Linear interpolation along four dimensions (4D) requires 16 data nodes, while the linear interpolation along five dimensions (5D) requires 32 data nodes. The general form of the shape functions that are required to perform the linear interpolation in four and five dimensions are respectively given as:

$$N_l^e(\xi, \eta, \mu, \upsilon) = \frac{1}{16}(1 + \xi\xi_l)(1 + \eta\eta_l)(1 + \mu\mu_l)(1 + \upsilon\upsilon_l) \tag{D.6}$$

$$N_l^e(\xi, \eta, \mu, \upsilon, \zeta) = \frac{1}{32}(1 + \xi\xi_l)(1 + \eta\eta_l)(1 + \mu\mu_l)(1 + \upsilon\upsilon_l)(1 + \zeta\zeta_l) \tag{D.7}$$

The shape function variables ξ, η, μ, υ and ζ vary between -1 and 1 throughout the dimensions of the element. The parameters ξ_l, η_l, μ_l, υ_l and ζ_l denote the natural coordinates of the lth node of the element. Although both elements are more difficult to represent graphically, their node numbering is derived in a similar way as it was done for the the bilinear quadrilateral and trilinear hexahedron elements.

D.2 Quadratic element shape functions
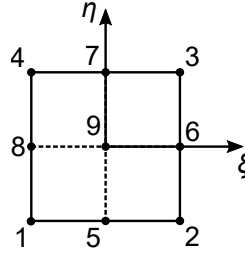
D.2.1 Biquadratic interpolation

Quadratic interpolation along two dimensions (2D) can be achieved when the data points are stored on a 3×3 grid. In this case the shape function elements of a nine-noded quadrilateral element are used to interpolate the data across the area of the element. The geometry of the element and its node configuration is given in Fig. D.1.
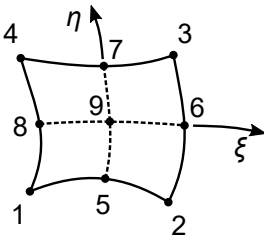
(a) Element geometry   (b) Reference element

Figure D.1: Node numbering convention for a nine-noded quadrilateral element.

According to the node numbering convention, the shape functions that describe this biquadratic quadrilateral element are as follows:

$$N_1^e(\xi, \eta) = \frac{1}{4}(1 - \xi)(1 - \eta)\xi\eta, \qquad N_2^e(\xi, \eta) = -\frac{1}{4}(1 + \xi)(1 - \eta)\xi\eta$$

$$N_3^e(\xi, \eta) = \frac{1}{4}(1 + \xi)(1 + \eta)\xi\eta, \qquad N_4^e(\xi, \eta) = -\frac{1}{4}(1 - \xi)(1 + \eta)\xi\eta$$

$$N_5^e(\xi, \eta) = -\frac{1}{2}(1 - \xi^2)(1 - \eta)\eta, \qquad N_6^e(\xi, \eta) = \frac{1}{2}(1 + \xi)(1 - \eta^2)\xi \qquad \text{(D.8)}$$

$$N_7^e(\xi, \eta) = \frac{1}{2}(1 - \xi^2)(1 + \eta)\eta, \qquad N_8^e(\xi, \eta) = -\frac{1}{2}(1 - \xi)(1 - \eta^2)\xi$$

$$N_9^e(\xi, \eta) = (1 - \xi^2)(1 - \eta^2)$$

The shape function variables are ξ and η of which the values vary between -1 and 1 across the surface of the quadrilateral element. The parameters ξ_l and η_l denote the natural coordinates of the lth node of the element.

Appendix E

Surface curvature tensor

The principal curvatures of a tooth surface $\mathcal{S}(u,v)$ are determined in Section 3.3 through the Circle of Mohr and the surface normal curvature, computed along various directions of the tooth surface. Here, the relation between the surface normal curvature, the surface torsion (or warping), the principal curvatures and the surface curvature tensor are briefly explained, based on the textbook [15].

Consider a regular surface $\mathcal{S}(u,v)$ that is defined by the independent coordinates u and v, such that the position of a point P on $\mathcal{S}(u,v)$ is expressed as $\boldsymbol{r}(u_P, v_P)$. The tangent vectors $\boldsymbol{t}_u$ and $\boldsymbol{t}_v$ along the u and v directions are then given as:

$$\boldsymbol{t}_u = \frac{\partial \boldsymbol{r}(u,v)}{\partial u}\bigg|_{(u_P, v_P)} \qquad \text{and} \qquad \boldsymbol{t}_v = \frac{\partial \boldsymbol{r}(u,v)}{\partial v}\bigg|_{(u_P, v_P)} \qquad (\text{E}.1)$$

The $u - v$ plane, spanned by unit tangent vectors $\boldsymbol{u}$ and $\boldsymbol{v}$, is the local tangent plane to $\mathcal{S}(u,v)$ at P, such that the (unit) surface normal $\boldsymbol{N}$ is given by:

$$\boldsymbol{u} = \frac{\boldsymbol{t}_u}{\|\boldsymbol{t}_u\|}, \qquad \boldsymbol{v} = \frac{\boldsymbol{t}_v}{\|\boldsymbol{t}_v\|}, \qquad \boldsymbol{N} = \boldsymbol{u} \times \boldsymbol{v} \qquad (\text{E}.2)$$

The surface curvature tensor $\mathcal{K}$, given by Eq. (E.3), then describes the curvature of the surface $\mathcal{S}$ at the point P along the perpendicular directions $\boldsymbol{u}$ and $\boldsymbol{v}$.

$$\mathcal{K} = \begin{bmatrix} \kappa_{uu} & \kappa_{uv} \\ \kappa_{vu} & \kappa_{vv} \end{bmatrix} \qquad (\text{E}.3)$$

The surface normal curvature κ_{uu} along the u-direction is well approximated by the curvature of the curve $\mathcal{C}_u$, defined by the intersection of the $(\boldsymbol{u}, \boldsymbol{N})$ plane and the surface $\mathcal{S}$. Similarly, the surface normal curvature κ_{vv} along

the v-direction is well described by the curvature of the curve $\mathcal{C}_v$, defined by the intersection of the (v, N) plane and the surface $\mathcal{S}$. The surface torsion (or warping) κ_{uv} expresses the rate with which the surface inclination in the v-direction changes when moving along the u-direction, and vice versa for κ_{vu}.

Assuming that in the vicinity of the point P the local surface geometry is well approximated by a quadratic function $f(u, v)$, the coordinates P in the frame S_N, defined by vectors u, v and N, are given as $r_N(u_P, v_P) = [u_P, v_P, f(u_P, v_P)]^T$. Then, the surface normal curvatures and surface torsion at P are found as [15]:

$$\kappa_{uu} = -\left.\frac{\partial^2 f(u, v)}{\partial u^2}\right|_{(u_P, v_P)} \tag{E.4}$$

$$\kappa_{vv} = -\left.\frac{\partial^2 f(u, v)}{\partial v^2}\right|_{(u_P, v_P)} \tag{E.5}$$

$$\kappa_{uv} = -\left.\frac{\partial^2 f(u, v)}{\partial u\, \partial v}\right|_{(u_P, v_P)} = -\left.\frac{\partial^2 f(u, v)}{\partial v\, \partial u}\right|_{(u_P, v_P)} = \kappa_{vu} \tag{E.6}$$

The surface curvature tensor $\mathcal{K}$ (along the u and v directions) can be used to compute the curvature along two new directions m and q, which also lie in the $u - v$ plane and are perpendicular ($m \cdot q = 0$). When the vector m is defined w.r.t. the vector u through a rotation about the N axis of angle θ, represented by the transformation matrix $\mathbf{L}(\theta)$, the directions of m and q are:

$$m = \begin{bmatrix} m_u \\ m_v \end{bmatrix} = \begin{bmatrix} \cos(\theta) \\ \sin(\theta) \end{bmatrix} \qquad \text{and} \qquad q = \begin{bmatrix} -m_v \\ m_u \end{bmatrix} = \begin{bmatrix} -\sin(\theta) \\ \cos(\theta) \end{bmatrix} \tag{E.7}$$

The surface normal curvature κ_{mm} and the corresponding surface torsion κ_{mq} along the newly defined m-direction are then found as:

$$\kappa_{mm} = m^T \mathcal{K} m \tag{E.8}$$

$$= \kappa_{uu} \cos(\theta)^2 + 2\kappa_{uv} \cos(\theta) \sin(\theta) + \kappa_{vv} \sin(\theta)^2 \tag{E.9}$$

$$\kappa_{mq} = m^T \mathcal{K} q \tag{E.10}$$

$$= (\kappa_{vv} - \kappa_{uu}) \cos(\theta) \sin(\theta) + \kappa_{uv}(\cos(\theta)^2 - \sin(\theta)^2) \tag{E.11}$$

The surface curvature tensor $\mathcal{K}'$ along the m and q directions is then found as:

$$\mathcal{K}' = \mathbf{L}^T \, \mathcal{K} \, \mathbf{L} \tag{E.12}$$

In Section 3.3 the normal curvature κ_{mm} along a direction m is replaced by κ_n. Similarly, the surface torsion κ_{mq} along a direction m is replaced by τ_g. When u and v are the principal directions of the surface, such that $\kappa_{uu} = \kappa_{max}$, $\kappa_{vv} = \kappa_{min}$ and $\kappa_{uv} = 0$, Eq. (E.9) reduces to Eqs. (2.5) and (3.22), and the equation for the Mohr Circle (Eq. (3.20)) is obtained from Eqs. (E.9) and (E.11).

Bibliography

[1] ADDUCI, R. Finite Element based stiffness calculation and contact detection for spiral bevel gears. MSc. Thesis, University of Calabria, 2016.

[2] AGMA. 2005-D03 design manual for bevel gears. Tech. rep., American Gear Manufacturers Association, 2003.

[3] AIRBUS HELICOPTERS. Redesigned vertical shaft on the ec225. Online Poster: www.EC225news.com, 2014.

[4] ANDERSON, N. Gear Industry Vision - A vision of the gear industry in 2025, developed by the gear community. In *Gear Industry Vision Workshop* (2004), Energetics, Inc., Ed.

[5] ANDERSSON, A., AND VEDMAR, L. A dynamic model to determine vibrations in involute helical gears. *Journal of Sound and Vibration 260*, 2 (2003), 195–212.

[6] ARGYRIS, J., FUENTES, A., AND LITVIN, F. L. Computerized integrated approach for design and stress analysis of spiral bevel gears. *Computer Methods in Applied Mechanics and Engineering 191*, 11 (2002), 1057–1095.

[7] ARTONI, A., GABICCINI, M., GUIGGIANI, M., AND KAHRAMAN, A. Multi-objective ease-off optimization of hypoid gears for their efficiency, noise, and durability performances. *Journal of Mechanical Design 133* (2011), 121007.

[8] ARTONI, A., GABICCINI, M., AND KOLIVAND, M. Ease-off based compensation of tooth surface deviations for spiral bevel and hypoid gears: Only the pinion needs corrections. *Mechanism and Machine Theory 61* (2013), 84–101.

[9] ARTONI, A., KOLIVAND, M., AND KAHRAMAN, A. An ease-off based optimization of the loaded transmission error of hypoid gears. *Journal of Mechanical Design 132* (2010), 011010.

[10] BÄR, G., AND LIEBSCHNER, B. Fitting flanks and contact properties of hypoid gears. In *Proceedings of 8th World Congress on the Theory of Machines and Mechanisms* (Prague, 1991), vol. 4, pp. 1095–1098.

[11] BATHE, K.-J. *Finite Element Procedures.* Klaus-Jürgen Bathe, 2014.

[12] BATHE, K. J., AND BOUZINOV, P. A. On the constraint function method for contact problems. *Computers & Structures 64*, 5-6 (sep 1997), 1069–1085.

[13] BAUMANN, V. *Untersuchungen zur Last- und Spannungsverteilung an bogenverzahnten Kegelrädern.* PhD thesis, TU Dresden, 1990.

[14] BAXTER, M. Basic geometry and tooth contact of hypoid gears. *Ind. Math. 11*, 2 (1961), 19–42.

[15] BEGHINI, M. *Lezioni ed esercitazioni di Tecnica delle Costruzioni Meccaniche.* Dipartimento di Ingegneria Meccanica, Nucleare e della Produzione, Universita di Pisa, 2011.

[16] BLOCKMANS, B. *Model reduction of contact problems in flexible multibody dynamics.* PhD Dissertation, KU Leuven - The Arenberg Doctoral School, 2018.

[17] BLOCKMANS, B., TAMAROZZI, T., NAETS, F., AND DESMET, W. A nonlinear parametric model reduction method for efficient gear contact simulations. *International Journal for Numerical Methods in Engineering 102*, 5 (dec 2015), 1162–1191.

[18] BUCHANAN, R., AND TREDGOLD, T. *Practical essays on mill work and other machinery.* John Weale, Architectural library, 59, High Holborn, London, 1841. Digitized by Google.

[19] BUCKINGHAM, E. *Analytical Mechanics of Gears.* McGraw-Hill, 1949.

[20] CAI, Y. Simulation on the rotational vibration of helical gears in consideration of the tooth separation phenomenon (a new stiffness function of helical involute tooth pair). *Journal of Mechanical Design 117*, 3 (1995), 460.

[21] CAPPELLINI, N. *System Level Simulation of Drivetrains by Advanced Gear Contact Techniques.* PhD Dissertation, KU Leuven - The Arenberg Doctoral School, 2018.

[22] CAPPELLINI, N., TAMAROZZI, T., BLOCKMANS, B., FISZER, J., COSCO, F., AND DESMET, W. Semi-analytic contact technique in a non-linear parametric model order reduction method for gear simulations. *Meccanica 53*, 1-2 (Jan. 2018), 49–75.

[23] CATERA, P. Development of an automated FE meshing tool for bevel and hypoid gear pairs for loaded tooth contact analysis. MSc. Thesis, University of Calabria, 2016.

[24] CHENG, Y., AND LIM, T. Dynamics of hypoid gear transmission with non-linear time-varying mesh. In *Proceedings of Design Engineering Technical Conferences and Computers and Information in Engineering Conference* (2000), pp. DETC2000/PTG–14432.

[25] CHENG, Y., AND LIM, T. C. Dynamics of hypoid gear transmission with nonlinear time-varying mesh characteristics. *Journal of Mechanical Design 125* (June 2003), 373–382.

[26] CONTARTESE, N. Loaded tooth contact analysis of cylindrical and spiral bevel gears using nonlinear FEA. MSc. Thesis, University of Calabria, 2017.

[27] COOX, L., VIVET, M., TAMAROZZI, T., GELUK, T., CREMERS, L., AND DESMET, W. Numerical assessment of the impact of vehicle body stiffness on handling performance. In *Proceedings of the 25th International Conference on Noise and Vibration Engineering (ISMA2012)* (Leuven, Belgium, Sept. 2012), vol. 5, pp. 3711–3723.

[28] DASSAULT SYSTÈMES. SIMULIA ABAQUS Unified CAE. Online: www.3ds.com/products-services/simulia/products/abaqus/, 2018.

[29] DASSAULT SYSTEMES DEUTSCHLAND GMBH. Multi-Body Simulation. SIMPACK MBS Software. Online: http://www.simpack.com/, 2018.

[30] DIEBEL, J. Representing attitude: Euler angles, unit quaternions, and rotation vectors, 2006.

[31] DOONER, D. B. *Kinematic Geometry of Gearing*, 2nd ed. John Wiley & Sons Ltd, 2012.

[32] DOONER, D. B., AND VIVET, M. Unloaded tooth contact analysis of hypoid gears for increased power density. In *Proceedings of the International Gear Conference 2018* (Lyon, France, Aug. 2018).

[33] DOONER, D. B., VIVET, M., AND MUNDO, D. Deproximating Tredgold's Approximation. *Mechanism and Machine Theory 102* (Aug. 2016), 36–54.

[34] ELKHOLY, A. H., ELSHARKAWY, A. A., AND YIGIT, A. S. Effect of meshing tooth stiffness and manufacturing error on the analysis of straight bevel gears. *Mechanics of Structures and Machines 26*, 1 (1998), 41–61.

[35] Fan, Q. Optimization of face cone element for spiral bevel and hypoid gears. *Journal of Mechanical Design 133* (2011), 091002.

[36] Fan, Q. Ease-off and application in tooth contact analysis for face-milled and face-hobbed spiral bevel and hypoid gears. In *Theory and Practice of Gearing and Transmissions*. Springer International Publishing, 2015, pp. 321–339.

[37] Fan, Q., and Wilcox, L. *New Developments in Tooth Contact Analysis (TCA) and Loaded TCA for Spiral Bevel and Hypoid Gear Drives*. Technical paper / FTM.: Technical paper. AGMA, 2005.

[38] Fernandez del Rincon, A., Viadero, F., Iglesias, M., García, P., de Juan, A., and Sancibrian, R. A model for the study of meshing stiffness in spur gear transmissions. *Mechanism and Machine Theory 61* (2013), 30–58.

[39] Fiszer, J. *Advanced Bearing Modelling for the Numerical Analysis of System - level Machine Dynamics*. PhD Dissertation, KU Leuven - The Arenberg Doctoral School, 2017.

[40] Fuentes, A., Litvin, F., Mullins, B., Woods, R., and Handschuh, R. Design and stress analysis of low-noise adjusted bearing contact spiral bevel gears. *Journal of Mechanical Design 124* (2002), 524–532.

[41] Fuentes, A., Ruiz-Orzaez, R., and Gonzalez-Perez, I. Compensation of Errors of Alignment Caused by Shaft Deflections in Spiral Bevel Gear Drives. In *Theory and Practice of Gearing and Transmissions*. Springer International Publishing, aug 2015, pp. 301–319.

[42] Gabiccini, M., Bracci, A., and Guiggiani, M. Robust Optimization of the Loaded Contact Pattern in Hypoid Gears With Uncertain Misalignments. *Journal of Mechanical Design 132*, 4 (2010), 041010.

[43] GearLab - The Ohio State University. GearLab Software for Consortium Members. Online: www.gearlab.osu.edu/research/gearlab-software-consortium-members, 2018.

[44] Géradin, M., and Cardona, A. *Flexible multibody dynamics: a finite element approach*. John Wiley & Sons, LTD, 2001.

[45] Gleason Corporation. Computer Aided Gear Engineering (CAGE™). Online: www.gleason.com/products/154/120/computer-aided-gear-engineering-cage, 2018.

[46] GOSSELIN, C., CLOUTIER, L., AND NGUYEN, Q. A general formulation for the calculation of the load sharing and transmission error under load of spiral bevel and hypoid gears. *Mechanism and Machine Theory 30*, 3 (1995), 433–450.

[47] GRUNWALD, A. Systematic optimization of gear boxes for hybrid and electric vehicles in terms of efficiency, NVH and durability. In *20th Aachen Colloquium Automobile and Engine Technology* (2011).

[48] HAUG, E. J. *Computer aided kinematics and dynamics of mechanical systems*, vol. 1. Allyn and Bacon, 1989.

[49] HE, D., DING, H., AND TANG, J. A new analytical identification approach to the tooth contact points considering misalignments for spiral bevel or hypoid gears. *Mechanism and Machine Theory 121* (2018), 785.

[50] HEMMELMANN, J. E. *Simulation des lastfreien und belasteten Zahneingriffs zur Analyse der Drehübertragung von Zahnradgetrieben.* PhD Dissertation, RWTH Aachen, 2007.

[51] HOUSER, D. R. Gear noise and vibration prediction and control methods. In *Handbook of Noise and Vibration Control.* John Wiley & Sons, Inc., 2017, pp. 847–856.

[52] INTERNATIONAL ORGANIZATION FOR STANDARDIZATION (ISO). *ISO 23509, Bevel and hypoid gear geometry.* ISO, 2006.

[53] INTERNATIONAL ORGANIZATION FOR STANDARDIZATION (ISO). *ISO 6336-1, Calculation of load capacity of spur and helical gears - P.1: Basic principles, introduction and general influence factors*, 2 ed. ISO, 2006.

[54] INTERNATIONAL ORGANIZATION FOR STANDARDIZATION (ISO). *ISO 21771, Gears - Cylindrical Involute Gears and Gear Pairs - Concepts and Geometry.* ISO, 2007.

[55] JOACHIM, F. J., BÖRNER, J., AND KURZ, N. How to minimize power losses in transmissions, axles and steering systems. In *VDI International Conference on Gears, Munich (Germany)* (2011).

[56] JOHNSON, K. L. *Contact mechanics.* Cambridge University Press, 1987.

[57] KARAGIANNIS, I., AND THEODOSSIADES, S. An alternative formulation of the dynamic transmission error to study the oscillations of automotive hypoid gears. *Journal of Vibration and Acoustics 136*, 1 (2013), 011001.

[58] KARAGIANNIS, I., THEODOSSIADES, S., AND RAHNEJAT, H. On the dynamics of lubricated hypoid gears. *Mechanism and Machine Theory 48* (feb 2012), 94–120.

[59] KIM, N.-H. *Introduction to Nonlinear Finite Element Analysis*. Springer US, 2015.

[60] KISSoft AG. KISSoft Products - KISSoft calculation program. Online: www.kisssoft.ch/english/products/kisssoft.php, 2018.

[61] KLINGELNBERG. Kimos: Zahnkontakt-analyse für kegelräder. Tech. rep., Klingelnberg Gruppe, 1996.

[62] KLINGELNBERG, J., Ed. *Bevel Gear - Fundamentals and Applications*. Springer Berlin Heidelberg, 2016.

[63] KOLIVAND, M. *Development of tooth contact and mechanical efficiency models for face-milled and face-hobbed hypoid and spiral bevel gears*. PhD Dissertation, Graduate School of The Ohio State University, 2009.

[64] KOLIVAND, M., AND KAHRAMAN, A. A load distribution model for hypoid gears using ease-off topography and shell theory. *Mechanism and Machine Theory 44*, 10 (2009), 1848–1865.

[65] KOLIVAND, M., AND KAHRAMAN, A. An ease-off based method for loaded tooth contact analysis of hypoid gears having local and global surface deviations. *Journal of Mechanical Design 132* (2010), 071004.

[66] KOLIVAND, M., AND KAHRAMAN, A. A General Approach to Locate Instantaneous Contact Lines of Gears Using Surface of Roll Angle. *Journal of Mechanical Design 133*, 1 (2011), 014503.

[67] KOLIVAND, M., LI, S., AND KAHRAMAN, A. Prediction of mechanical gear mesh efficiency of hypoid gear pairs. *Mechanism and Machine Theory 45*, 11 (2010), 1568–1582.

[68] KRENZER, T. J. Tooth contact analysis of spiral bevel and hypoid gears under load. In *SAE Technical Paper* (04 1981), SAE International.

[69] KRENZER, T. J. Understanding tooth contact analysis. *The Gleason Works Publication*, SD3139B/3-81/GMD (1981).

[70] KUANG, J. H., AND YANG, Y. T. An estimate of mesh stiffness and load sharing of a spur gear pair. In *Proceedings of International Power Transmission and Gearing Conference* (1992), vol. 43-1, pp. 1–9.

[71] LAURSEN, T. A. *Computational Contact and Impact Mechanics*. Springer Berlin Heidelberg, 2003.

[72] LIN, C.-H., AND FONG, Z.-H. Numerical tooth contact analysis of a bevel gear set by using measured tooth geometry data. *Mechanism and Machine Theory 84* (2015), 1–24.

[73] LISLE, R. J., AND RAGAN, D. M. Strain from three stretches: a simple Mohr circle solution. *Journal of Structural Geology 10*, 8 (1988), 905.

[74] LISLE, R. J., AND ROBINSON, J. M. The Mohr circle for curvature and its application to fold description. *Journal of Structural Geology 17*, 5 (1995), 739–750.

[75] LITVIN, F. L. *Theory of Gearing*. RP-1212. NASA, 1989.

[76] LITVIN, F. L., AND FUENTES, A. *Gear Geometry and Applied Theory*, 2nd ed. Cambridge University Press, 2004.

[77] LITVIN, F. L., FUENTES, A., AND HAYASAKA, K. Design, manufacture, stress analysis, and experimental tests of low-noise high endurance spiral bevel gears. *Mechanism and Machine Theory 41*, 1 (2006), 83–118.

[78] LITVIN, F. L., AND GUTMAN, Y. Methods of synthesis and analysis for hypoid gear-drives of formate and helixform - part 1. calculations for machine settings for member gear manufacture of the formate and helixform hypoid gears. *Journal of Mechanical Design 103* (1981), 83–88.

[79] LITVIN, F. L., AND GUTMAN, Y. Methods of synthesis and analysis for hypoid gear-drives of formate and helixform - part 2. machine setting calculations for the pinions of formate and helixform gears. *Journal of Mechanical Design 103* (1981), 89–101.

[80] LITVIN, F. L., AND GUTMAN, Y. Methods of synthesis and analysis for hypoid gear-drives of formate and helixform - part 3. analysis and optimal synthesis methods for mismatch gearing and its application for hypoid gears of formate and helixform. *Journal of Mechanical Design 103* (1981), 102–110.

[81] LITVIN, F. L., SHEVELEVA, G. I., VECCHIATO, D., GONZALEZ-PEREZ, I., AND FUENTES, A. Modified approach for tooth contact analysis of gear drives and automatic determination of guess values. *Computer Methods in Applied Mechanics and Engineering 194*, 27 (2005), 2927–2946.

[82] MICHAELIS, K., HÖHN, B.-R., AND HINTERSTOISSER, M. Influence factors on gearbox power loss. *Industrial Lubrication and Tribology 63*, 1 (feb 2011), 46–55.

[83] MOHAMMADPOUR, M., JOHNS-RAHNEJAT, P. M., THEODOSSIADES, S., AND RAHNEJAT, H. Effect of tapered roller bearing supports on the dynamic behaviour of hypoid gear pair differentials. *Proceedings of the Institution of Mechanical Engineers, Part D: Journal of Automobile Engineering 230*, 8 (aug 2015), 1090–1104.

[84] MOHAMMADPOUR, M., THEODOSSIADES, S., AND RAHNEJAT, H. Multiphysics Investigations on the Dynamics of Differential Hypoid Gears. *Journal of Vibration and Acoustics 136*, 4 (apr 2014), 041007.

[85] MOHAMMADPOUR, M., THEODOSSIADES, S., RAHNEJAT, H., AND KELLY, P. Transmission efficiency and noise, vibration and harshness refinement of differential hypoid gear pairs. *Proceedings of the Institution of Mechanical Engineers, Part K: Journal of Multi-body Dynamics 228*, 1 (aug 2013), 19–33.

[86] MULSKI, S. Multi-Body Dynamics Simulation. In *Wind and Drivetrain Conference 2015* (2015).

[87] NAKADA, T., AND UTAGAWA, M. The dynamic loads on gears caused by the varying elasticity of the mating teeth. In *Proc. of the 6th Jap. Nat. Cong. for Appl. Mech.* (1956).

[88] NAUNHEIMER, H., BERTSCHE, B., RYBORZ, J., AND NOVAK, W. *Automotive Transmissions: Fundamentals, Selection, Design and Application.* Springer Berlin Heidelberg, 2011.

[89] NEUPERT, B. *Berechnung der Zahnkräfte, Pressungen und Spannungen von Stirn- und Kegelradgetrieben.* PhD Dissert., RWTH Aachen, 1983.

[90] NUTBOURNE, A. W., AND MARTIN, R. R. *Differential Geometry Applied to Curve & Surface Design - Foundations V.1.* Prentice Hall, 1988.

[91] OTTMAN, J. A. *The new rules of green marketing: strategies, tools, and inspiration for sustainable branding*, 1 ed. Routledge Taylor & Francis Group, 2010.

[92] ÖZGÜVEN, H. N., AND HOUSER, D. R. Mathematical models used in gear dynamics—a review. *Journal of Sound and Vibration 121*, 3 (mar 1988), 383–411.

[93] PARK, D., KOLIVAND, M., AND KAHRAMAN, A. Prediction of surface wear of hypoid gears using a semi-analytical contact model. *Mechanism and Machine Theory 52* (2012), 180–194.

[94] PEARS, J. The modern approach to transmission system design and analysis. Online: www.geartechnology.com/issues/0915x/transmission.pdf, 2015.

[95] PENG, T. *Coupled Multi-body Dynamic and Vibration Analysis of Hypoid and Bevel Geared Rotor System.* PhD Dissertation, University of Cincinnati, 2010.

[96] Radzevich, S. P. *Dudley's Handbook of Practical Gear Design and Manufacture*, 2 ed. CRC Press Taylor & Francis Group, 2012.

[97] Rezayat, A., Shweiki, S., Park, D., Vivet, M., Donders, S., Flock, S., Jiranek, P., and Tamarozzi, T. A novel efficient high fidelity approach to gear contact simulation in multibody systems. In *Proceedings of the International Gear Conference 2018* (Lyon, 2018).

[98] Romax Technology Ltd. RomaxDESIGNER - Romax Technology. Online: www.romaxtech.com/software/romaxdesigner/, 2018.

[99] Sanchez-Marin, F., Iserte, J. L., and Roda-Casanova, V. Numerical tooth contact analysis of gear transmissions through the discretization and adaptive refinement of the contact surfaces. *Mechanism and Machine Theory 101* (2016), 75–94.

[100] Saxena, M., Raviprolu, P., Bredl, B., Wlezek, K., and Grandl, B. Rear Axle Whine Simulation using SIMPACK. In *2nd European SIMULIA User Group Meeting for Multibody Simulations* (2017).

[101] Schlecht, B., Schaefer, S., and Hutschenreiter, B. BECAL - Programm zur Berechnung der Zahnflanken- und Zahnfußbeanspruchung an Kegel- und Hypoidgetrieben bei Berücksichtigung von Relativlage und Flankenmodifikationen (Version 4.1.0). Tech. rep., TU Dresden, 2012.

[102] Schottel GmbH. Schottel Rudderpropeller - The Superior Propulsion System. Online: www.schottel.de/fileadmin/data/pdf/eng/SRP_EN_0913_web.pdf, 2013. Accessed: 2018-07-24.

[103] Scurria, L., Fiszer, J., Tamarozzi, T., Jiranek, P., and Desmet, W. An advanced modeling technique for rolling element bearings in elastohydrodynamic (EHL) field. In *EUROMECH COLLOQUIUM 578 - Rolling Contact Mechanics for Multibody System Dynamics* (2017).

[104] Scurria, L., Tamarozzi, T., Jiranek, P., and Fauconnier, D. A transient EHL contact model capturing system-level spur gears dynamic behavior. In *The 5th Joint Conference on Multibody System Dynamics* (2018).

[105] Shabana, A. A. *Dynamics of Multibody Systems*, 3 ed. Cambridge University Press, 2005.

[106] Siemens PLM Software. NX Nastran Advanced Nonlinear - Solution 601/701. Online: www.adina.com/NX_Nastran_Uses_ADINA.pdf, 2007.

[107] Siemens PLM Software. NX Nastran 10. Advanced Nonlinear Solution - Theory and Modeling Guide. Online: https://docs.plm.automation. siemens.com/data_services/resources/nxnastran/10/help/en_US/custom/ advanced_nonlinear/advanced_nonlinear_tmg.pdf, 2014.

[108] Siemens PLM Software. Boosting productivity in gearbox engineering: efficiently build and effectively simulate multibody simulation models. White paper: www.fp7demetra.eu/images/files/Siemens-PLM-Boosting-Productivity-in-Gearbox-Engineering-wp-65217-A20.pdf, 2017.

[109] Siemens PLM Software. LMS Samcef Solver Suite. Online: www.plm.automation.siemens.com/fr/products/lms/samtech/samcef-solver-suite/, 2018.

[110] Siemens PLM Software. Motion Analysis. Online: www.plm.automation.siemens.com/global/en/products/simulation-test/ motion-analysis.html, 2018.

[111] Siemens PLM Software. Structural Analysis: Linear analysis, Nonlinear analysis and Structural dynamics. Online: www.plm.automation.siemens.com/global/en/products/simulation-test/structural-analysis.html, 2018.

[112] Simon, V. Load distribution in hypoid gears. *Journal of Mechanical Design 122* (2000), 529–535.

[113] Simon, V. Optimal tooth modifications in hypoid gears. *Journal of Mechanical Design 127* (2005), 646–655.

[114] Simon, V. Computer simulation of tooth contact analysis of mismatched spiral bevel gears. *Mechanism and Machine Theory 42*, 3 (2007), 365–381.

[115] Simon, V. Influence of tooth modifications on tooth contact in face-hobbed spiral bevel gears. *Mechanism and Machine Theory 46*, 12 (2011), 1980–1998.

[116] Simon, V. Optimization of face-hobbed hypoid gears. *Mechanism and Machine Theory 77* (2014), 164–181.

[117] Stadtfeld, H. J. *Handbook of bevel and hypoid gears: calculation, manufacturing and optimization.* Rochester Institute of Technology, 1993.

[118] Stadtfeld, H. J. The ultimate motion graph. *Journal of Mechanical Design 122* (2000), 317–322.

[119] Tamarozzi, T. *Efficient Numerical Simulation Strategies for Flexible Multibody Systems with Variable Topology.* PhD Dissertation, KU Leuven - The Arenberg Doctoral School, 2014.

[120] Tamarozzi, T., Jinarek, P., Park, D., Vivet, M., Donders, S., and Flock, S. Democratization of simulation in the design engineering of gear boxes. In *Proceedings of NAFEMS Conference: Simulation Based Engineering* (Neuendettelsau, Germany, Nov. 2017).

[121] Toso, A., van Wermeskerken, F., Cappellini, N., and Heirman, G. On the effect of lightweight gear blank topology on transmission dynamics. In *ASME 2015 Power Transmission and Gearing Conference: 23rd Reliability, Stress Analysis, and Failure Prevention Conference* (2015), vol. 10, ASME.

[122] TU Dresden. Kegelradverzahnungen. Online: www.tu-dresden.de/ing/ maschinenwesen/imm/me/forschung/kegelradverzahnungen/Kegelradverzahnungen, 2018.

[123] Vaidyanthan, S., Busby, H., and Houser, D. *A Rayleigh-Ritz approach to determine compliance and root stresses in spiral bevel gears using shell theory.* AGMA, 1993.

[124] Vedmar, L. *On the Design of External Involute Helical Gears.* PhD Dissertation, Lund Technical University, 1981.

[125] Velex, P., and Ajmi, M. On the modelling of excitations in geared systems by transmission errors. *Journal of Sound and Vibration 290*, 3-5 (2006), 882–909.

[126] Vijayakar, S. A combined surface integral and finite element solution for a three-dimensional contact problem. *International Journal for Numerical Methods in Engineering 31*, 3 (1991), 525–545.

[127] Vijayakar, S. Calyx. Online: www.ansol.us/Products/Calyx/, 2018.

[128] Vivet, M., Acinapura, A., Dooner, D. B., Mundo, D., Tamarozzi, T., and Desmet, W. Loaded tooth contact analysis of spiral bevel gears with kinematically correct motion transmission. In *Proceedings of the International Gear Conference 2018* (Lyon, France, Aug. 2018).

[129] Vivet, M., Adduci, R., Catera, P., Heirman, G. H. K., Mundo, D., Tamarozzi, T., and Desmet, W. Global mesh stiffness calculation for lightweight spiral bevel gears. In *Proceedings of the 27th International Conference on Noise and Vibration Engineering (ISMA2016)* (Leuven, Belgium, Sept. 2016), vol. 27, pp. 1417–1429.

[130] Vivet, M., Heirman, G. H. K., Tamarozzi, T., Desmet, W., and Mundo, D. An Ease-off Based Methodology for Contact Detection and Penetration Calculation. In *Power Transmissions: Proceedings of the*

International Conference on Power Transmissions 2016 (ICPT 2016) (Chongqing, PR China, Oct. 2016), pp. 167–173.

[131] VIVET, M., MUNDO, D., TAMAROZZI, T., AND DESMET, W. An analytical model for accurate and numerically efficient tooth contact analysis under load, applied to face-milled spiral bevel gears. *Mechanism and Machine Theory 130* (Dec. 2018), 137–156.

[132] WAGNER, W., SCHUMANN, S., AND SCHLECHT, B. Co-simulation of the tooth contact of spiral bevel gears within a multibody simulation. In *Proceedings of the International Gear Conference 2018* (2018).

[133] WANG, J. *Nonlinear Time-varying Gear Mesh and Dynamic Analysis of Hypoid and Bevel Geared Rotor Systems.* PhD Dissertation, University of Cincinnati, 2007.

[134] WANG, X. C., AND GHOSH, S. K. *Advanced Theories of Hypoid Gears.* Elsevier Science Ltd., 1994.

[135] WEBER, C., AND BANASCHEK, K. Formänderung und Profilrücknahme bei gerad-und schrägverzahnten Rädern. Tech. rep., VDMA, 1955.

[136] WENSING, J. *On the Dynamics of Ball Bearings.* PhD Dissertation, University of Twente, 1998.

[137] WILDHABER, E. Basic relationships of hypoid gears. *American Machinist 90*, 4 (1946), 108–111.

[138] WRIGGERS, P. *Computational Contact Mechanics*, 2nd ed. Springer Berlin Heidelberg, 2006.

[139] XU, H. *Development of a generalized mechanical efficiency prediction methodology for gear pairs.* PhD Dissertation, Graduate School of The Ohio State University, 2005.

[140] YANG, J. J., SHI, Z. H., ZHANG, H., LI, T. X., NIE, S. W., AND WEI, B. Y. Dynamic analysis of spiral bevel and hypoid gears with high-order transmission errors. *Journal of Sound and Vibration 417* (2018), 149–164.

[141] ZIEGLER, H. *Verzahnungssteifigkeit und Lastverteilung schrägverzahnter Stirnräder.* PhD thesis, TH Aachen, 1971.

[142] ZIEGLER, P., AND EBERHARD, P. Investigation of Gears Using an Elastic Multibody Model with Contact. In *Multibody Dynamics: Computational Methods and Applications*, K. Arczewski, W. Blajer, J. Fraczek, and M. Wojtyra, Eds. Springer Netherlands, Dordrecht, 2011, pp. 309–327.

Curriculum Vitae

Personal Data

Name	Mathijs Vivet
Date of birth	March 6, 1989
Place of birth	Rumst, Belgium
Nationality	Belgian
E-mail	mathijs.vivet@gmail.com

Professional Experience

2014 - 2019	**PhD Researcher, Department of Mechanical Engineering, KU Leuven, Leuven (Belgium)**
2014 - 2019	**PhD Researcher, Department of Mechanical, Energy and Management Engineering, University of Calabria, Rende (Italy)**
Topic	Advanced techniques for numerical contact analysis in spiral bevel gears
Research Focus	Multibody simulations; advanced gear modeling; contact models for spiral bevel gears; gear mechanics; contact mechanics
Educational Activities	Advisor in 4 Master's Theses and 1 Integrated Project
Comment	Dual degree

2015 - 2017	**Research Engineer, Siemens Industry Software, Leuven (Belgium)**
Topic	Multibody simulations; advanced gear modeling; contact models for spiral bevel gears
Project	Two year secondment as part of the European research project FP-7 DEMETRA (Grant no. 324336).

2012 - 2014	**Customer Services Engineer, Siemens PLM Software, Leuven (Belgium)** former LMS International
Description	Application Engineer for LMS Virtual.Lab Motion and LMS Virtual.Lab Durability with a main focus on automotive applications.

Education

2010 - 2012	**Master of Science in Engineering (M.Sc.), KU Leuven, Leuven (Belgium)**
Degree	M.Sc. in Mechanical Engineering (Cum Laude), option: Automotive Engineering.
Thesis	Numerical assessment of the impact of vehicle body stiffness on ride and handling performance.

2007 - 2010	**Bachelor of Science in Engineering (B.Sc.), KU Leuven, Leuven (Belgium)**
Degree	B.Sc. in Mechanical Engineering, with a minor in Chemical Engineering.

2001 - 2007	**Secondary school, Sint-Theresiacollege, Kapelle-op-den-Bos (Belgium)**
Degree	Latin-Mathematics.

List of publications

Articles in reviewed academic journals

- VIVET, M., MUNDO, D., TAMAROZZI, T., AND DESMET, W. An analytical model for accurate and numerically efficient tooth contact analysis under load, applied to face-milled spiral bevel gears. *Mechanism and Machine Theory 130* (Dec. 2018), 137–156

- DOONER, D. B., VIVET, M., AND MUNDO, D. Deproximating Tredgold's Approximation. *Mechanism and Machine Theory 102* (Aug. 2016), 36–54

Articles in scientific conference proceedings

- VIVET, M., ACINAPURA, A., DOONER, D. B., MUNDO, D., TAMAROZZI, T., AND DESMET, W. Loaded tooth contact analysis of spiral bevel gears with kinematically correct motion transmission. In *Proceedings of the International Gear Conference 2018* (Lyon, France, Aug. 2018)

- VIVET, M., HEIRMAN, G. H. K., TAMAROZZI, T., DESMET, W., AND MUNDO, D. An Ease-off Based Methodology for Contact Detection and Penetration Calculation. In *Power Transmissions: Proceedings of the International Conference on Power Transmissions 2016 (ICPT 2016)* (Chongqing, PR China, Oct. 2016), pp. 167–173

- VIVET, M., ADDUCI, R., CATERA, P., HEIRMAN, G. H. K., MUNDO, D., TAMAROZZI, T., AND DESMET, W. Global mesh stiffness calculation for lightweight spiral bevel gears. In *Proceedings of the 27th International Conference on Noise and Vibration Engineering (ISMA2016)* (Leuven, Belgium, Sept. 2016), vol. 27, pp. 1417–1429

- DOONER, D. B., AND VIVET, M. Unloaded tooth contact analysis of hypoid gears for increased power density. In *Proceedings of the International Gear Conference 2018* (Lyon, France, Aug. 2018)

- REZAYAT, A., SHWEIKI, S., PARK, D., VIVET, M., DONDERS, S., FLOCK, S., JIRANEK, P., AND TAMAROZZI, T. A novel efficient high fidelity approach to gear contact simulation in multibody systems. In *Proceedings of the International Gear Conference 2018* (Lyon, 2018)

- TAMAROZZI, T., JINAREK, P., PARK, D., VIVET, M., DONDERS, S., AND FLOCK, S. Democratization of simulation in the design engineering of gear boxes. In *Proceedings of NAFEMS Conference: Simulation Based Engineering* (Neuendettelsau, Germany, Nov. 2017)

- COOX, L., VIVET, M., TAMAROZZI, T., GELUK, T., CREMERS, L., AND DESMET, W. Numerical assessment of the impact of vehicle body stiffness on handling performance. In *Proceedings of the 25th International Conference on Noise and Vibration Engineering (ISMA2012)* (Leuven, Belgium, Sept. 2012), vol. 5, pp. 3711–3723

FACULTY OF ENGINEERING SCIENCE
DEPARTMENT OF MECHANICAL ENGINEERING
PRODUCTION ENGINEERING, MACHINE DESIGN AND AUTOMATION
Celestijnenlaan 300B
B-3001 Leuven
mathijs.vivet@kuleuven.be
http://www.mech.kuleuven.be

FACOLTÀ DI IGNEGNERIA
DIPARTIMENTO DI IGNEGNERIA MECCANICA ENERGETICA E GESTIONALE
GRUPPO DI MECCANICA APPLICATA ALLE MACCHINE
Ponte P. Bucci 45C
87036 Rende (CS) Italy
www.unical.it/dimeg/